Boiling Enhancement on Engineered Surfaces

A Dissertation

Submitted to the Faculty

of

Drexel University

by

Md Mahamudur Rahman

in partial fulfillment of the

requirements for the degree

of

Doctor of Philosophy

July 2016

DREXEL UNIVERSITY
Graduate College

DISSERTATION/THESIS APPROVAL FORM

This form is for use by all doctoral and master's students with a dissertation/thesis requirement. Please print clearly as the library will bind a copy of this form with each copy of the dissertation/thesis. All doctoral dissertations must conform to university format requirements, which is the responsibility of the student and supervising professor. Students should obtain a copy of the Thesis Manual located on the Graduate College or library website.

Dissertation/Thesis Title: Boiling Enhancement on Engineered Surfaces

Author: Md Mahamudur Rahman

This dissertation/thesis is hereby accepted and approved.

Signatures:

Examining Committee

Chair

Members

Academic Advisor

Department Head

DEDICATIONS

I dedicate this dissertation first to my best friend, my guide and my biggest supporter who held my hand in every stage of my life, my mother, Hasina Bakool. Next I would like to dedicate this dissertation to my father (Md Muslim Ali) who worked very hard to raise me up and supported me on my future. I also dedicate this dissertation to my brother (Mahabubur Rahman) who acted as a role model for me throughout my career, and who has always motivated and supported me to achieve my goals and ambitions. I would like to dedicate this to my sister-in-law (Nadia Jabin Rahman) and my only nephew (Raveev Rahman) as well who kept me smiling and encouraged me to keep working hard for my career. I would like to dedicate this dissertation to the people of Bangladesh, the taxpayers whose contributions helped me to nurture my knowledge through preliminary and higher studies, and my relative and friends who have been holding my hand throughout my life. Finally, I would like to dedicate this dissertation to my wife (Mehnaz Tabassum Rahman) who has continuously acted as a friend, philosopher, supporter, and encouraged me to successfully complete this dissertation.

ACKNOWLEDGMENTS

At the very beginning, I would like to thank our creator for providing me such great opportunities of studying and learning till now. Also, I would like to thank all the people around me who have made this dissertation possible.

Next I would like to thank my supervisor Professor Matthew McCarthy for allowing me to work with him as a PhD student and in his *Multiscale Thermofluidics Laboratory* as a graduate research assistant. For the last five years, he has enriched my knowledge by continuously providing me guidance regarding how to work for a project, what things are required to be considered, how to do those things. He has always suggested me to work hard, try to learn more to achieve the success in life. He is always inspiring me to communicate with people, to try to learn from everywhere to build a successful career. He spent huge time with me to show me how to write a paper, how to present in front of people, even in the weekends. He showed me the way how to organize a paper, even this dissertation also. I am extremely thankful to him for his technical and theoretical support.

A special thank goes to all my MTL lab friends, especially Mr. Emre Ölçeroğlu, who and I were the first PhD students of Prof. Matthew McCarthy, and worked all together to build this MTL lab. He has also worked in my projects as a co-author, and I am very grateful to him also for giving me technical, especially with his excellent SEM imaging skills, and mental support all the time. I would also like to thank Mr. Stephen King and Mr. Donald Fehlinger for giving me technical and mental support all the time, and even they helped me in my project.

I would like to thank Prof. Moses Noh for training me and allowing me to utilize his Microfabrication facilities throughout my PhD career. I would also like to thank Drexel University Machine Shop people Mr. Mark Shiber and Mr. Scott for giving me huge support in building my experimental setup, and some macro-machined test surfaces. I am really grateful to all the Mechanical Engineering Department staffs for their kind help that they provided me to make this dissertation possible.

Finally, I am grateful for the financial support provided by the National Science Foundation (Grants Numbers 1454407, 1264958, and 1357918).

TABLE OF CONTENTS

Page

LIST OF TABLES x

LIST OF FIGURES xi

ABSTRACT xx

CHAPTER 1: INTRODUCTION 1

1.1 Background 1

1.1.1 Pool Boiling Heat Transfer 1

1.1.2 Pool Boiling Regimes 1

1.1.3 Critical Heat Flux (CHF) 4

1.1.4 Heat Transfer Coefficient (HTC) 5

1.2 Overview of Dissertation 5

CHAPTER 2: MOTIVATIONS AND OBJECTIVES 7

2.1 Motivations 7

2.1.1 Manufacturability 7

2.1.2 Physical Mechanism of Enhancement on Structured Surfaces 7

2.1.3 Robustness and Long-term Reliability 8

2.2 Objectives and Contributions to the Field 9

2.2.1 Development of Scalable Nanomanufacturing Techniques 9

2.2.2 Characterization of Individual Effects of Structured Surfaces on Boiling Heat Transfer 9

2.2.3 Demonstration of Novel and Robust Enhancement Mechanisms 10

2.2.4 Design and Engineering of High Performance Surfaces 10

CHAPTER 3: LITERATURE REVIEW 11

3.1 Boiling on Planar Surfaces 11

3.1.1 Nucleation 11

3.1.2 Heat Transfer Coefficient (HTC) 12

3.1.3 Critical Heat Flux (CHF) 14

3.2 Boiling of Water on Engineered Surfaces 18

3.2.1 Nanostructured Surfaces 19

3.2.2 Micro structured Surfaces 24

3.2.3 Hierarchical Surfaces 26

3.2.4 Macro-machined Surfaces 28

3.2.5 Heterogeneous Surfaces 30

3.3 Boiling of Dielectric Fluids on Engineered Surfaces 31

CHAPTER 4: POOL BOILING EXPERIMENTAL APPARATUS 36

4.1 Experimental Apparatus for Boiling of Saturated Water 36

4.1.1 Experimental Apparatus 36

4.1.2 Experimental Method 37

4.2 Experimental Apparatus for Boiling of Dielecteic Fluids 38

4.2.1 Experimental Apparatus 39

4.2.2 Experimental Method 40

4.3 Experimental Uncertainty 42

4.3.1 Experimental Uncertainty during Pool Boiling 42

4.3.2 Experimental Uncertainty during Wicking 43

4.3.3 Experimental Uncertainty with Roughness Factor Estimation 44

CHAPTER 5: SCALABLE NANOMANUFACTURING OF SURFACE COATINGS FOR BOILING APPLICATIONS 45

5.1 Introduction and Overview 45

5.2 Biotemplated Nanofabrication 46

5.2.1 The Tobacco mosaic virus (TMV) and its Genetic Modification 46

5.2.2 Virus Harvesting and Replication 48

5.2.3 Biotemplated Nanostructured Sample Preparation 50

5.2.4 Scalability of TMV Biotemplating.....54

5.3 Pool Boiling Characterization.....55

5.3.1Pool Boiling Results.....56

5.3.2 In-situ Deposition and Fouling Mitigation 57

5.3.3 Surface Wettability and Comparison with CHF Predictions.....60

5.4 Conclusions.....61

CHAPTER 6: WICKABILITY AND CHF ON STRUCTURED SUPERHYDROPHILIC SURFACES 63

6.1 Introduction and Overview.....63

6.2 CHF correlation and Surface Wickability 64

6.3 Wickability Characterization.....69

6.3.1 Wickability of Water.....69

6.3.2 Wickability of FC 72 73

6.4 Structured Surfaces.....78

6.4.1TMV on Silicon Substrates..... 78

6.4.2 Copper Oxide Nanostructures (CuO).....80

6.4.3 Estimation of Roughness Factor 81

6.5 Results: Boiling of Saturated Water 86

6.5.1 Silicon Substrates.....86

6.5.2 Effect of Substrate, Nanostructure Density, and Fouling 89

6.5.3 Effect of Nanostructure Material and Morphology 91

6.5.4 Effect of Wickability on CHF..... 92

6.5.5 Optimization of Biotemplated Nanofabrication for Boiling Applications 95

6.6 Results: Boling of Saturated FC 72 98

6.6.1 Wicking Results for FC 72 101

6.6.2 Boiling Results for FC 72 103

6.6.3 Effect of Wickability on CHF 105

6.7 Conclutions 106

CHAPTER 7: BOILING ENHANCEMENT ON MULTISCALE AND HETEROGENEOUS STRUCTURED SURFACES 108

7.1 Introduction and Overview 108

7.2 Effect of Engineered Nucleation Sites 109

7.2.1 Super-bi-philic Surfaces 109

7.2.2 Nanostructured Surfaces with Engineered Nucleation Sites 111

7.2.3 Pool Boiling Results 113

7.2.4 Effect of Engineered Nucleation Sites on HTC 115

7.2.5 Effect of Engineered Nucleation Sites on Wickability and CHF 116

7.3 Multiscale Surfaces 117

7.3.1 Microchannel Surfaces 117

7.3.2 Nanostructured CuO Surfaces 118

7.3.3 Multiscale Surface 120

7.3.4 Boiling Results on Single Length Scale Surfaces 121

7.3.5 Boiling Results on Multiscale Surfaces 123

7.3.6 Effect of Channel on CHF and HTC 127

7.4 Conclusions 129

CHAPTER 8: BOILING ENHANCEMENT USING ENGINEERED THEMAL GRADIENTS 132

8.1 Introduction and Overview 132

8.2 Bi- Conductive Surfaces for Tailoring Bubbble Dynamics during Boiling 133

8.3 High speed Imaging 136

8.4 Pool Boiling Results 138

8.5 Enhancement Mechanism 139

8.5.1 Preferential Nucleation 139

8.5.2 Resonance – like Enhancement 143

8.6 Conclusions 150

CHAPTER 9: BOILING ENHANCEMENT ON NANOSTRUCTURED SURFACES WITH ENGINEERED VARIATIONS IN WETTABILITY AND THAMAL CONDUCTIVITY 153

9.1 Introduction and Overview 153

9.2 Nanostructured Surfaces and Wickability 154

9.3Mixed Wettability and Nuclation 157

9.4 Bi-Conductive Surfaces 160

9.5 Nanostructured Surfaces with Engineered Variations in Wettability and Thermal Conductivity 161

9.6 Conclusions 165

CHAPTER 10: SUMMARY AND CONTRIBUTIONS 168

10.1 Overall Summary 168

10.2 Specific Contributions 173

10.2.1 Scalable Nanomanufacturing of Surface Coatings for Boiling Applications 174

10.2.2 Role of Wickability on CHF for Structured Superhydrophilic Surfaces 174

10.2.3 Boiling Enhancement on Multiscale and Heterogeneous Structured Surfaces 174

10.2.4 Boiling Enhancement using Engineered Thermal Gradients 175

10.2.5 Boiling Enhancement on Nanostructured Surfaces with Engineered Variations in Wettability and Thermal Conductivity 175

10.3 Recommendations for Future Research 176

10.3.1 Scalable Nanomanufacturing of Surface Coatings for Boiling Applications 176

10.3.2 Role of Wickability on CHF for Structured Superhydrophilic Surfaces 176

10.3.3 Boiling Enhancement using Engineered Thermal Gradients 177

BIBLIOGRAPHY 178

VITA.....187

LIST OF TABLES

Page

Table 6.1: Summary of selected pool boiling CHF models 65

LIST OF FIGURES

Page

Figure 1.1: A representative pool boiling curve with different boiling regimes 3

Figure 3.1: Prediction of active nucleation sites..... 12

Figure 3.2: Prediction of bubble departure diameter 13

Figure 3.3: Representative pool boiling curves with saturated water at atmospheric conditions..... 16

Figure 3.4: Effect of surface equilibrium contact angle on pool boiling critical heat flux with saturated water at atmospheric conditions [9] 17

Figure 3.5: : Scanning electron microscopy (SEM) images of nanowire surfaces (a) top view of Si Nanowires, (b) cross sectional view of Si Nanowires, (c) top view of Cu Nanowires, (d) cross sectional view of Cu nanowires, (e) equilibrium contact angles of a on Si, SiO2, and Si and Cu nanowire surfaces. [9]..... 20

Figure 3.6: Pool boiling heat flux as a function of wall superheat for silicon and copper nanowire structures [9] 21

Figure 3.7: Scanning Electron Microscope images of Silicon Nanowires with average heights of (a) 35 mm and (b) 20 mm [12]..... 21

Figure 3.8: Scanning Electron Microscope images of Copper Nanowires with average heights of (a) 20 mm, (b) 10 mm, (c) 5 mm and (d) 2 mm [12] 22

Figure 3.9: Pool boiling heat flux as a function of wall superheat for SiNW and CuNW surfaces with different heights [12]. 23

Figure 3.10: Visualization results of bubble dynamics during boiling. The surfaces with nanorods are shown to active 30 fold greater nucleate site densities in 5–10 K superheat range than that for bare surfaces [28] 23

Figure 3.11: SEMs of the surfaces with silicon microstructures showing the geometries of pillars. The pillars heights are (a) 10 μm and (b)-(f) 20 μm, the center-to-center spacing of microposts (a) and (f) 15 μm, (b) and (d) 5 μm, and (c) and (e) 10 μm; and varied diameters of (a) and (d)-(f) 10 μm and (b) and (c) 5 μm [8] 25

Figure 3.12: CHF as function of a surface roughness for microstructure surfaces [8].... 26

Figure 3.13: SEM images of the silica and CuO based hierarchical surfaces. (a) Microstructures coated with EPD (b) microstructures coated with CuO nanostructures (c)

zoomed view of the silica-based micropillar and the inset is EPD-coated SiO_2 nanoparticles (d) Magnified view of the CuO hierarchical surfaces and the inset is CuO nanostructures (e) cross-sectional view of hierarchical silicon and (f) cross-sectional view hierarchical copper surface. [37]..... 27

Figure 3.14: CHF as function of a roughness for hierarchical surfaces 28

Figure 3.15: Enhanced surface details (a) single channel with rectangular geometry, and (b) cross-section of the channel, and (c) pool boiling heat transfer performance of enhanced surface designs compared to bare surfaces showing significant enhancement in both CHF and HTC. [27]. 29

Figure 3.16: Schematic of enhanced surface design with controlled bubble dynamics showing separate liquid and vapor flow pathways during pool boiling. [27]..... 29

Figure 3.17: SEM images of bi-philic and super-bi-philic surfaces showing contact angle measures of hydrophilic, hydrophobic, superhydrophilic, and superhydrophobic surfaces. [10]..... 31

Figure 3.18: Scanning Electron Microscope images of CuNW at different heights. [44]... 32

Figure 3.19: CHF as a function of nanowire height for pool boiling of PF-5060. [44]... 32

Figure 3.20: SEM images of fabricated copper microstud surfaces coated with CNT. [44] 33

Figure 3.21: Heat flux as a function of wall superheat for fully CNT-coated, CNT-patterned, and bare silicon surfaces [44]..... 33

Figure 3.22: (a) Pool boiling heat transfer performance for silicon surfaces fully coated with CNT, and (b) corresponding images of during boiling photographs at various heat flux conditions [44]..... 34

Figure 4.1: Schematic of pool boiling experimental setup for water..... 37

Figure 4.2: Schematic of pool boiling experimental setup for dielectric fluids 40

Figure 4.3: Optical image of pool boiling experimental setup for dielectric fluids..... 41

Figure 5.1: The Tobacco mosaic virus (TMV) and genetic modification. (a) Schematic representation of the TMV structure showing the RNA strand and coat proteins and (b) A TEM image of the wild-type virus. (c)-(d) Schematic representations of the cysteine residues introduced during genetic modification and the C-terminus shielding the cysteines. (a) Reprinted with permission from The Encyclopedia Britannica [12], Copyright 1996. (b) Reprinted with permission from Elsevier [13], Copyright 1999. (c-d) Reprinted witrh permission from IOP [14], Copyright 2008..... 47

Figure 5.2: Replication of Tobacco mosaic virus (TMV). (a) Many seedlings initially grown in a single pot then (b) transplanted to individual trays where (c) they are manually infected. (d) Full grown infected leaf showing the mosaic pattern..... 49

Figure 5.3: Extraction of Tobacco mosaic virus (TMV). (a)-(b) Preparation of blended leaf and extraction buffer solution for centrifugation. (c) Coarse separation of TMV after first centrifugation. (d) TMV pellet after second centrifugation. (e) Insertion of TMV solution into sugar solution. (f) Gradient layer formation of TMV after swinging angle centrifugation. 50

Figure 5.4: Scalable nanomanufacturing using self-assembled Tobacco mosaic virus (TMV). (a) TEM image of the wild-type TMV [13]. (b) Tobacco plants are grown in the lab and infected with the TMV, leading to (c) the characteristic mosaic pattern. (d) The three-step solution-based biotemplating process where the TMV assembles onto a metallic surface and is coated with palladium nanoclusters and then electrolessly plated to form a nickel shell. (e) SEM images of the surface-bound nickel nanostructured coating. (a) Reprinted with permission from Elsevier, Copyright 1999. 52

Figure 5.5: (a) TEM image of nickel coated TMV nanostructure and (b) XPS analysis results for the surface-bound nickel-coated TMV nanostructures [15] (b) Reprinted with permission from ACS [15], Copyright 2008..... 53

Figure 5.6: Biotemplated superhydrophilic nanostructured nickel coatings on various metallic surfaces. Fabrication results for virus-structured coatings on (a) gold, (b) aluminum, (c) stainless steel, (d) and copper showing 1cm x 1cm samples before and after deposition, as well as SEM images at various magnifications. Side-view and orthogonal SEM images were obtained by (a) cleaving a silicon sample or (b,c) masking and etching the nanostructures using photolithography..... 55

Figure 5.7: Pool boiling results for nanostructures on different substrate materials (a) CHF as a function of wall superheat, and (b) HTC as a function of heat flux. 57

Figure 5.8: (a) Pool boiling curves showing repeatable performance and the effects of reversible fouling and pre-cleaning. (b) Results for copper and stainless steel samples after stripping and re-deposition of TMV nanocoatings, showing repeatable performance and a means to retrofit existing equipment as well as mitigate the effects of fouling. (c) SEM images showing that the TMV nanostructures remain intact with no mechanical failure after 24 hours of sustained nucleate boiling. 59

Figure 5.9: Comparison with CHF Predictions. Experimental pool boiling results showing good agreement for non-structured surfaces as compared to other work [4, 5, 9] and Kandlikar's CHF model 61

Figure 6.1: Schematic representation of the role of wickability in enhancing the critical heat flux. The wicked liquid is drawn into the nanostructures in the wetted areas, transported underneath the apparent liquid−vapor interface, and evaporated. 67

Figure 6.2: The characterization of surface wickability. Schematic of capillary wicking experimental setup to measure initial wicked volume flux for structured surfaces using water. 70

Figure 6.3: The characterization of surface wickability. (a) Schematic of the wicking measurement technique, where a structured surface is raised to touch a pendant droplet attached to a capillary tube. The droplet first quickly deforms to a constant wetted area, AW, and then liquid is wicked through the surface structures. (b) The apparent wetted area as a function of time, where the droplet spreading phase (-5 ms $< t < 0$) occurs entirely before the liquid wicking phase ($t > 0$). (c) Wicked volume as a function of time, calculated by tracking the high-speed images of the displaced meniscus in the tube. 71

Figure 6.4: Experimental measurement of wickability. (a) High-speed imaging of water being drawn from a 500 μm inner diameter capillary tube after a structured surface is raised into contact with a pendant droplet resulting in wicking across the surface. (b) Experimental results of wicked volume as a function of time (for three select surfaces), calculated by tracking the displacement of the water level in the tube, showing the initial. 72

Figure 6.5: Schematic of capillary wicking experimental setup to measure initial wicked volume flux for structured surfaces using low surface tension fluids. 74

Figure 6.6: Comparison of capillary wicking results using water for both with and without syringe (a) wetted area as a function of time, and (b) wicked volume as a function of time demonstrating that the added syringe backpressure has negligible effect on the initial wicked volume flux measurements. 75

Figure 6.7: Capillary wicking results of FC 72 compared with water using syringe wicking method (a) wetted area as a function of time and (b) wicked volume as a function of time. 76

Figure 6.8: Micro, nano, and hierarchically structured silicon surfaces fabricated to characterize the effect of wickability on pool boiling CHF. (a-d) SEM images of four representative microstructure geometries fabricated using deep reactive ion etching. (e-f) Hierarchical surfaces at three different magnifications composed of the microstructures shown in (a-d) conformally coated with TMV-templated nickel nanostructures. 79

Figure 6.9: Copper oxide nanostructured coatings. (a-e) SEM images of five different CuO nanostructured coatings and the corresponding fabrication conditions, including solution temperature, time, and composition 81

Figure 6.10: SEM images used for roughness estimation of TMV-structured surfaces including (a) less densely packed, and (b) more densely packed cylindrical nanostructures 83

Figure 6.11: TMV aggregation on hierarchical surfaces 84

Figure 6.12: Roughness estimation of CuO nanostructures on (a) rectangular and (b) triangular shaped structures 85

Figure 6.13: Experimental characterization of the CHF and wickability of structured silicon surfaces. (a) Boiling curves for six selected samples, where CHF is signified with an arrow. (b) Experimental results of CHF plotted against the wicked volume flux for all twenty silicon surfaces, showing a linear trend. (c) Details of the twenty micro, nano, and hierarchical silicon surfaces including sample name, microstructure geometry (diameter x pitchxheight), roughness factor, r, wicked volume flux, and CHF……..... 87

Figure 6.14: Wicked volume as a function of time for all twenty micro, nano, and hierarchical silicon surfaces Figure 6.11: TMV aggregation on hierarchical surfaces..... 88

Figure 6.15: Pool boiling results for structured surfaces (a) CHF as a function of wall superheat and (b) HTC as a function of heat flux.Figure 6.11: TMV aggregation on hierarchical surfaces..... 88

Figure 6.16: Effect of substrate material, TMV morphology, and fouling on wicking-enhanced CHF. (a) SEM images showing high-concentration and low-concentration TMV coatings. (b) CHF as a function of wicked volume flux for TMV nanostructures on multiple metallic substrates, showing variations in performance due to differences in morphology as well as fouling after repeated testing. The results are compared to the corresponding bare surfaces as well as the micro, nano, and hierarchal silicon surfaces. 90

Figure 6.17: Results for copper oxide nanostructured coatings. (a) Boiling curves and (b) CHF as a function wicked volume flux, showing consistency with TMV-structured micro, nano, and hierarchical coatings on silicon and metallic substrates (light grey symbols)..... 91

Figure 6.18: Effect of wickability on CHF. Experimentally measured CHF as a function of (a) wicked volume flux and (b) receding contact angle for over forty individual surfaces, showing the importance of wickability for structured superhydrophilic surfaces. The data includes variations in scale (micro, nano, hierarchical), morphology, fouling, structure material, and substrate material, as well as data from other researchers [8]. (c) CHF enhancement as a function of wicking number, Wi, for superhydrophilic surfaces showing excellent agreement with the developed correlation given by Eq 6.13..... 92

Figure 6.19: CHF as a function of surface roughness factor and receding contact angle 95

Figure 6.20: Effect of nickel deposition time on nanostructure size. (a) SEM images of various samples fabricated with different nanostructure thicknesses. (b) Diameter of biotemplated nanorods as a function of nickel coating deposition time..... 96

Figure 6.21: Experimental results (a) wicked volume as a function of time and (b) pool

boiling heat flux as a function of wall superheat for nickel nanostructures showing the effect of nickel deposition time..... 97

Figure 6.22: Comparison of measured and predicted CHF values showing the effect of nickel deposition time on pool boiling performance and mechanical failure of TMV coatings for deposition times of less than five minutes. 98

Figure 6.23: SEM image of structured surfaces fabricated to analyze the effect of capillary wicking on pool boiling CHF using dielectric fluid. 100

Figure 6.24: Capillary wicking results of FC 72 compared with water using syringe wicking method (a) wetted area as a function of time and (b) wicked volume as a function of time. 101

Figure 6.25: Capillary wicking results for the micro, nano and hierarchical structured surfaces using FC 72. (a) Wicked volume as a function of time and (b) Wetted area as a function of time..... 102

Figure 6.26: Pool boiling heat flux as a function of time for micro, nano and hierarchical surfaces compared with bare silicon and bare copper surfaces 104

Figure 6.27: Pool boiling heat flux as a function of time for (a) bare copper and (b) bare silicon surfaces compared with literature 104

Figure 6.28: Effect of wickability on CHF using water (gray data) and FC 72 (color data) as the working fluid. Experimentally measured CHF enhancement as a function of wicking number, Wi, for structured surfaces showing excellent agreement with the developed correlation..... 105

Figure 7.1: Fabrication and designs of super-bi-philic nickel nanostructured surfaces. (a) Steps of standard microfabrication, (b) SEM image of a super-bi-philic design where dark regions are superhydrophobic nickel nanostructures and lighter regions are superhydrophilic nickel nanostructures, and (c) different super-bi-philic designs with varied hydrophobic dot size and center-to-center spacing.....110

Figure 7.2: Fabrication and designs of engineered nucleation sites on copper nanostructured surfaces. (a) SEM images of CuO micro/nanostructured surfaces (b) machined cavities onto the structured surface, and (c) different engineered nucleation site designs..... 112

Figure 7.3: Fabrication and designs of engineered nucleation sites on nanostructured aluminum surfaces. (a) SEM images of nickel nanostructures (b) machined cavities onto the structured surface, and (c) different engineered nucleation site designs 112

Figure 7.4: Pool boiling heat transfer performance of super-bi-philic surfaces. (a) Heat flux as a function of wall superheat. (b) HTC as a function of heat flux..... 113

Figure 7.5: Pool boiling heat transfer performance of super-bi-philic surfaces. (a) Heat flux as a function of wall superheat. (b) HTC as a function of heat flux..... 114

Figure 7.6: Maximum HTC as a function of CHF for all engineered nucleation surfaces. 115

Figure 7.7: Effect of wickability on CHF enhancement for surfaces with engineered nucleation sites. Previously reported data is shown with light grey symbols..... 116

Figure 7.8: Channels patterned using Wire EDM. (a) Digital camera image of 4-channels and 10-channels designs (b) optical microscope image of a channel showing channel width and channel maximum depth, and (c) the dimensions of all five channel surface designs..... 118

Figure 7.9: SEM images and chemical bath composition, reaction temperature and time for different CuO nanostructures (CuO-1 to CuO-4)..... 119

Figure 7.10: Different CuO superhydrophilic nanocoatings on various channel surfaces. Fabrication results for different CuO nano coatings on bare copper (a) CuO-1, (b) CuO-2, (c) CuO-3, (d) and CuO-4 at various magnifications. Side-view SEM images of (e) CuO-3 nanocoated channel and side wall, and (f) CuO-4 nanocoated channel surface..... 120

Figure 7.11: Enhanced heat transfer during pool boiling using all CuO nanocoatings and channel surfaces. Experimental results of (a) heat flux as a function of superheat, and (b) heat transfer coefficient as a function of heat flux..... 122

Figure 7.12: CHF as a function of liquid initial volume flux for CuO nanostructured surfaces 122

Figure 7.13: Pool boiling curves for CuO-1 based surfaces (a) heat flux as a function of wall superheat, and (b) HTC as a function of heat flux..... 123

Figure 7.14: Pool boiling curves for CuO-2 based surfaces (a) heat flux as a function of wall superheat, and (b) HTC as a function of heat flux..... 124

Figure 7.15: Pool boiling curves for CuO-3 based surfaces (a) heat flux as a function of wall superheat, and (b) HTC as a function of heat flux..... 124

Figure 7.16: Pool boiling curves for CuO-4 based surfaces (a) heat flux as a function of wall superheat, and (b) HTC as a function of heat flux..... 125

Figure 7.17: Heat transfer mechanism for (a) CuO-3 and (b) CuO-4 based hierarchical channel surfaces showing rapid bubble explosion in the channel dominated boiling regimes and nanostructure wicking dominated delayed dry-out regimes..... 127

Figure 7.18: Heat transfer enhancement for hierarchical channel surfaces (a) CHF as a function of number of channels, and (b) maximum HTC as a function of number of

channels..... 129

Figure 8.1: The fabricated surfaces showing (a) samples with two and twelve divisions per centimeter, and (b–d) scanning electron microscope (SEM) images of the low-conductivity epoxy divisions embedded in high-conductivity copper. (e) Schematic of the resulting flow field where spatial variations in wall superheat temperature, $\Delta T(x)$, promotes spatial ordering. Nucleation sites, as well as the liquid and vapor flow paths, are tailored to coincide with the wavelength of the in-plane temperature variations given by the pitch, P. (f) Image of the onset of nucleate boiling ($\Delta T \sim 5$ K), where bubbles preferentially nucleate in the center of the copper segments resulting in (g) control over the nominal bubble diameter during lateral coalescence 134

Figure 8.2: Nucleate boiling on bi-conductive surfaces. High-speed imaging of nucleate boiling at ~10-15 W/cm2 on (a) a bare copper surface and bi-conductive surfaces with (b) N = 4 cm-1, (c) N = 6 cm -1, and (d) N = 12 cm-1 designs. For each bi-conductive surface, nucleation is seen in the center of the high-temperature copper and no lateral motion of the three-phase contact lines beneath vapor bubbles is observed. The low-temperature epoxy divisions remain wetted at all times providing ordered pathways near the surface for replenishing liquid to feed the bubble ebullition cycles 137

Figure 8.3: Experimental results for (a) heat flux and (b) heat transfer coefficient as a function of wall superheat temperature. Increased performance is seen for five of the six bi-conductive surfaces, corresponding to those with wavelengths of P = 1.2–3.7 mm. A decrease in performance is seen for the P = 0.96 mm design..... 139

Figure 8.4: Thermal circuit diagram for a segment of a bi-conductive surface showing the relevant conductive and convective resistances between the base copper and the saturated fluid..... 141

Figure 8.5: Lateral coalescence, contact line motion, and bubble departure. High-speed time lapse imaging of the lateral coalescence of attached vapor bubbles on (a) bi-conductive surfaces, and (b) bare copper surfaces at ~10-15 W/cm2. (a) When two bubbles laterally coalesce over an epoxy division, the cold epoxy remains wetted and no contact line motion is observed. By remaining wetted at all times, the epoxy divisions promote departure at small diameters and maintain ordered flow paths for replenishing liquid. (b) Conversely, lateral coalescence on bare copper surfaces typically includes the lateral motion of contact lines, and merging of non-wetted base areas beneath the vapor bubbles 144

Figure 8.6: Experimental results showing the percent increase in (a) critical heat flux (CHF), and (b) heat transfer coefficient (HTC) for bi-conductive surfaces as compared to bare copper surfaces. Optimal performance is seen at Bond numbers of unity with a 2x increase in CHF and a 5x increase in HTC. These results highlights the importance of tuning the wavelength of spatial temperature variations, P, with the capillary length of the working fluid, λC, resulting in enhanced boiling performance over all stages of boiling.. 148

Figure 9.1: The effects of nanostructured coatings on pool boiling. (a) SEM images showing nanostructured CuO surfaces at two different magnifications, as well as (b) heat flux and (c) heat transfer coefficient results, as compared to bare copper surfaces 155

Figure 9.2: The effects of nanostructured surfaces with mixed wettability on pool boiling. (a) SEM images of nanostructured nickel coatings, fabricated using biotemplating, as well as patterned conformal PTFE films (~ 10-20 nm thick) creating an array of superhydrophobic dots on an otherwise superhydrophilic surface. Boiling results for (b) heat flux and (c) heat transfer coefficient, as compared to the performance of superhydrophilic nanostructured surfaces..... 158

Figure 9.3: The effects of bi-conductivity on pool boiling. (a) Heat flux and (b) heat transfer coefficient, as compared to bare copper surfaces with no epoxy divisions..... 161

Figure 9.4: Heterogeneous surface designs combining nanostructures, mixed-wettability, and bi-conductivity. Schematic representations of (a) the nanostructured bi-conductive surfaces, and (b) the nanostructured bi-conductive biphilic surfaces. (c) SEM image of a nanostructured bi-conductive biphilic surface showing the CuO nanostructures, two embedded epoxy divisions separated by 2.33 mm, and a 50-60 μm wide line of superhydrophobic nanostructures in between them. (d) Magnification of the interface separating the superhydrophilic CuO nanostructures, and the superhydrophobic PTFE-coated nanostructures. (e) Schematic representation of the desired flow field..... 162

Figure 9.5: Pool boiling performance of the heterogeneous surface designs, showing (a) heat flux and (b) heat transfer coefficient, as compared against the performance of bare copper, surface with nanostructured CuO only, and surfaces with bi-conductivity only… 163

ABSTRACT

Boiling Enhancement on Engineered Surfaces

Md Mahamudur Rahman
Matthew McCarthy, Ph.D.

The realization of next generation technologies to enhance boiling heat transfer is of critical importance due to its impact on energy, the environmental, and water resources, as well as thermal management needs of high-power electronics. Recent studies have shown that high surface area coatings comprised of micro and nano scale structures can be used to substantially increase performance during boiling. While exciting results have been reported in the literature, there is little understanding, and even less consensus, on the fundamental underlying mechanisms by which structured coatings enhance boiling. Additionally, the fabrication schemes used in the lab setting to create these structures are not scalable to large areas, complex geometries, or materials traditionally used in heat transfer applications. The focus of the Ph.D. dissertation research is on: (1) a detailed characterization of the effects of structured surfaces on boiling performance, including the role of capillary wicking, as well as the effects of surface morphology, material, and length scales; (2) scalable nanomanufacturing of structured coatings using nanoscale biological templates, and (3) the realization of novel surfaces for boiling enhancement that are resistant to degradation.

The *Tobacco mosaic virus* (TMV) has been used as a nanoscale building block to create nanostructured and hierarchically structured surfaces with a wide variety of morphologies. Utilizing a simple technique for characterizing surface wicking, an

experimentally validated model relating the maximum heat flux from a boiling surface to its inherent "wickability" has been shown for the first time. For structured superhydrophillic surfaces with characteristic lengths much smaller than the inherent flow structures (~ 1mm), capillary wicking through surface structures is the single factor determining the critical heat flux (CHF). Separately, it has been shown that hierarchically structured surfaces with length scales comparable to the flow yield more complicated enhancement mechanisms with each length scale contributing differently. Nanoscale structures enhance CHF, while micro-to-milli scale structures enhance nucleation and therefore heat transfer coefficient (HTC). The combination of the two has been show to enhance CHF and HTC by over 238% and 540% respectively.

TMV biotemplating has been leveraged not only for fundamental studies of boiling enhancement but also demonstrated here for the scalable nanomanufacturing of structured coatings. Biotemplating has been used to conformally coat a variety of materials using a cheap and sustainable room-temperature solution-based procedure. Repeatable boiling heat transfer enhancements of over 200% have been demonstrated on aluminum, silicon, copper, and stainless steel surface. Such solution-based techniques are easily extended to complex surfaces and large areas using in-situ depositions for retro-fittings existing systems and rejuvenating surfaces that have fouled and degraded.

Finally, the use of engineered thermal gradients across surfaces comprised of heterogeneous materials has been demonstrated. By promoting ordered pathways between nucleating bubbles and replenishing liquid, engineered thermal gradients have been shown to be as effective as structured surfaces in boiling enhancement, yet

inherently resistant to foiling. These planar “bi-conductive” surfaces have been characterized and their geometries optimized based on analysis of the bubble departure phenomena and surface tension effects.

CHAPTER 1: INTRODUCTION

1.1 Background

In this Chapter, basic background information is provided on phase change heat transfer, pool boiling and different regimes of pool boiling. This information will provide a background to the motivations and objectives of the current proposed research.

1.1.1 *Pool Boiling Heat Transfer*

Phase-change heat transfer is ubiquitous in nearly all industries due to the advantages of harnessing the latent heat stored within fluids. Pool boiling is an efficient but very complex mode of phase change heat transfer, including hydrodynamic instabilities, heat and mass transfer, and surface sciences. Boiling heat transfer is used in a number of industries and plays a critical role in various large-scale applications including chemical processing, water purification, power generation, and HVAC [1-3]. As such, even modest increases in boiling heat transfer efficiency can translate directly to substantial energy and cost savings on a large scale.

1.1.2 *Pool Boiling Regimes*

Figure 1 shows a typical pool boiling curve with different regimes during boiling. A classical pool boiling curve is a plot of heat flux (q''), amount of heat transferred per unit area, as a function of wall superheat ($\Delta T = T_{surface} - T_{sat}$), the surface temperature above the fluid saturation temperature. As the surface temperature is independently controlled and increased above the saturation temperature, the fluid above the heated surface gets warmer and moves upward whereas the cold fluid from the

surrounding moves downward replacing the hot fluid. This creates a natural convection which is shown as Regime I. Eventually the surface temperature becomes hot enough to initiate the heterogeneous nucleation at the surface which is the onset of nucleate boiling, point A. This activation of nucleation sites depends on several properties such as surface roughness with available natural nucleation cavities, surface temperature, operating pressure, surface tension, thermal boundary layer thickness reported as Hsu's analysis [4].

Once the nucleate pool boiling is initiated by the heterogeneous nucleation, increase in wall superheat initiates more nucleation on the surface, and the heat flux eventually increases significantly as the heat transfer is driven by fluid latent energy. Regime II, from point A to point B in Fig.1, is the isolated bubble regime, where active nucleation sites are few and widely separated. With increasing the wall superheat, more nucleation sites become active with increased bubble frequency which further increases the heat flux and a sharp rise in heat flux is observed. Eventually the nucleation sites get closely packed where the bubbles merge and forms vapor slugs and columns. This is defined as Regime III in boiling curve (Point B to C). With further increase in surface wall superheat, vapor generation become so rapid and frequent that Helmholtz instability occurs at the upward vapor – downward liquid interface. This upward vapor motion finally inhibits the liquid return to the nucleation sites and surface reaches at the maximum heat transfer capability which is also called critical heat flux (CHF) point, defined as point C in Fig. 1.

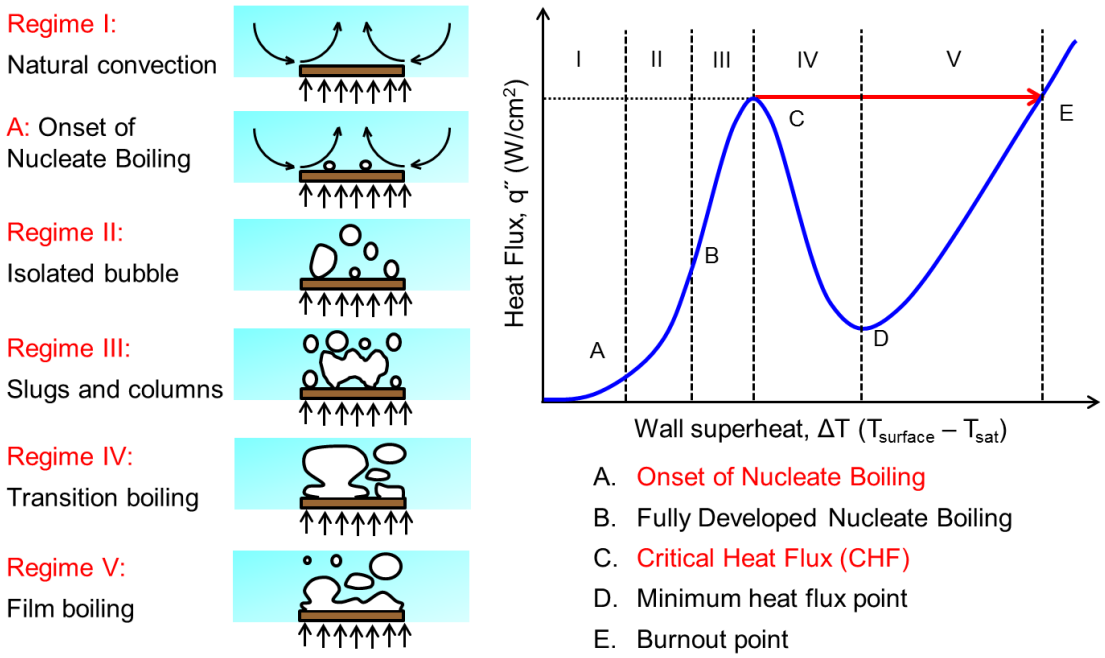

Figure 1.1: A representative pool boiling curve with different boiling regimes (adapted from [5])

For temperature controlled systems, increasing surface temperature beyond the critical heat flux point leads to overall decrease in heat transfer coefficient (ratio of heat flux to wall superheat). During this transition boiling (Regime IV, point C to D) wetted areas on the surface keep forming vapor films. This reduces the heat transfer from the surface due to low thermal conductivity of vapor regions. At one point the surface gets covered with a vapor film where the low density vapor blocks the high density liquid returning to the surface and initiates the Taylor instability. This minimum heat flux point (point D) is also referred as the Leidenfrost point and with this transition to film boiling triggers. Within the film boiling regime, the vapor film blanketing the heated surface becomes stable and a sustained film boiling can happen. During this heat flux is monotonically increases as the wall superheat increases due to increased conductivity of

vapor layer and radiative heat transfer at high surface temperatures. This increase in heat transfer can be observed until the failure of the system which is defined as the burn-out point (point E). For heat flux controlled systems, the transition from nucleate boiling to film boiling is not observed due to uncontrolled rise in surface temperature. Hence, for heat flux controlled systems, further increase in heat flux beyond the critical heat flux, no increase in heat flux is observed which leads to rapid increase in surface temperature at a constant heat flux until the burn-out point.

1.1.3 *Critical Heat Flux (CHF)*

During boiling, heat transfer is driven by the nucleation, growth, and departure of vapor from a surface, with large amounts of heat being removed via the latent heat associated with phase change [6, 7]. There is a finite rate at which heat can be dissipated from any surface. This maximum is the critical heat flux (CHF). CHF, also referred to as the boiling crisis, occurs when the production of vapor cannot be adequately balanced by the amount of liquid returning to the heated surface. When this occurs the surface undergoes dry-out, where an insulating layer of vapor blankets the solid surface. This leads to an immediate, uncontrollable, and drastic increase in surface temperature with dangerous and potentially catastrophic consequences, such as the destruction of electronic components or the meltdown of a nuclear reactor. This makes the design of heat flux controlled systems complicated. Hence, the systems are operated at a heat flux fairly below the critical heat flux point. Due to the importance of CHF on the design and operation of boiling systems, extensive research in this area has been conducted over the last fifty years and different CHF enhancement mechanisms are reported in the last one decade.

1.1.4 *Heat Transfer Coefficient (HTC)*

While safe operations of the phase change equipment are limited by the critical heat flux (CHF) [8, 9], heat transfer coefficient (HTC) sets the limit to conductance of the heat transfer processes [10-15]. The efficiency of boiling is quantified by the heat transfer coefficient (HTC), defined as the ratio of the surface heat flux to the superheat temperature, the temperature difference between the solid and the saturated fluid as given by Eq. (1.1). Here q″ is the heat flux and ΔT is the wall superheat, temperature above the saturation. Therefore along with CHF increase, enhancement in HTC in the nucleate boiling regime is desired for effective thermal management systems.

$$HTC = \frac{q''}{\Delta T} \tag{1.1}$$

1.2 Overview of Dissertation

The general goals of this dissertation are to demonstrate a scalable nanomanufacturing technique, analyze the factors affecting this boiling enhancement, and develop a heat transfer enhancement mechanism naturally insensitive to fouling and clogging during long time applications. Hence, the organization of this dissertation proposal is as follows. Chapter 1 introduces the background and importance of the proposed dissertation topic. Chapter 2 covers the motivations, objectives, and contributions to the field of the research. Chapter 3 provides a detailed literature review on pool boiling heat transfer. This covers an introduction on boiling of planner surfaces, classical pool boiling modeling of CHF, and HTC. Chapter 3 also presents different pool boiling heat transfer enhancement approaches including micro/nanostructured surfaces,

macro-machined surfaces, and mixed wettability surface boiling. In addition pool boiling models with enhanced surface designs are also presented in this Chapter.

Each of the following chapters is based on either published journal papers or manuscript in preparation and corresponds to a specific research objective. The pool boiling experimental procedure and experimental uncertainty used for all studies (Chapter 5 to 9) is described in detail in Chapter 4. It covers two boiling experimental setups. One was used for boiling with saturated water atmospheric conditions and the other for boiling with saturated FC 72 at atmospheric pressure. Chapter 5 presents the first focus of this dissertation proposal which is a scalable nanomanufacturing technique. A complete fabrication procedure is presented here. Also, pool boiling experimentation and boiling results are presented in detail in this Chapter. Chapter 6 follows the second aspect of this dissertation proposal. This chapter covers characterization and analysis of the effect of capillary wicking and roughness factor affecting the boiling enhancement on homogeneous structured surfaces which has one published journal and two manuscripts under preparation results. Chapter 7 covers the fundamental investigation of the effect of engineered nucleation sites and the effect of structure length scale on pool boiling heat transfer enhancement. Chapter 8 presents the final aspect of this proposal. The fabrication and characterization of a novel heat transfer enhancement mechanism is presented which is not sensitive to fouling and clogging as structured boiling. In Chapter 9, all the fundament understandings covered in Chapter 6, 7 and 8 are incorporated in one surface design to analyze the effect of combined mechanisms. Finally this dissertation wraps up with a summary and contributions of the research works accomplished in this work, and few recommendations for further advancement in Chapter 10.

CHAPTER 2: MOTIVATIONS AND OBJECTIVES

2.1 Motivations

A significant enhancement in heat transfer has been reported with the use of micro/nanostructures for the last one decade. Still the fundamental mechanisms are not well understood. As such, the present study has three main aspects with regard to general motivations and research contributions. The first aspect is the scalable nanomanufacturability for boiling applications, the second one is the characterizing and analyzing the factors affecting the boiling enhancement, and the third one is the heat transfer enhancement mechanism for robust and long-term reliability applications.

2.1.1 *Manufacturability*

While structured surfaces have been shown to greatly increase boiling heat transfer, the fabrication technology is limited by several factors such as the fabrication requires a specific base surface, through-mold electroplating, elevated temperature chemical oxidation, expensive small scale microfabrication technology. As such, a scalable manufacturing technique of surface-bound nanostructures for heat transfer devices is required to be developed.

2.1.2 *Physical Mechanism of Enhancement on Structured Surfaces*

While structured surfaces have been leveraged to substantially increase the pool boiling CHF and HTC, the fundamental understandings of various enhancement mechanisms are still limited till date due to a variety of factors. Boiling is a complex phenomenon due to the non-linear nature of three phase contact line motion. Also, limited visual observation at high heat fluxes till now makes it even harder to understand

the physics behind the variations in heat transfer performance of different boiling surfaces. Additionally, heat transfer enhancement through micro/nanostructures introduces further complexity in physical understanding of boiling fundamentals. Several different CHF and HTC mechanisms are proposed in the literature. These models are based on several assumptions and hypothesis and were subsequently refined and extended to more precise boiling conditions and geometries. Still all these models are limited to specific surface parameters and valid in a specific range of operation heat transfer limits. Hence, this complex boiling heat transfer phenomenon requires specific and individual treatment of factors affecting the CHF enhancement such as roughness factor, nucleation site density, capillary wicking, and controlled liquid and vapor flow field using the structured surfaces.

2.1.3 *Robustness and Long-term Reliability*

While the micro/nanostructured surfaces have been shown to significantly increase the pool boiling heat transfer, the reliability of these approaches for real-world applications is in question due to a variety of factors. All structured surfaces are inherently susceptible to mechanical failure (breaking of the micro/nanostructures), as well as fouling and clogging over time. During boiling, any and all contaminants within the fluid will inevitably be drawn into the structures. This will lead to clogging and filling of the small micro/nano-scale voids, and thus a loss of enhancement. Similarly, the robustness of extremely thin nanostructured coatings has not yet been demonstrated, leaving the potential for the coatings to be destroyed or altered over time via chemical reactions. Additionally, they are not effective with all working fluids, in particular highly

wetting fluids like FC-72. Hence, it is required to develop robust and reliable surfaces for high-efficiency and high heat flux boiling applications over long lifetimes.

2.2 Objectives and Contributions to the Field

The aim of this work is to develop scalable heat transfer surface fabrication methods and provide fundamental understanding of heat transfer enhancement mechanisms. Based on the overall goal, the specific objectives for the current work are stated below.

2.2.1 *Development of Scalable Nanomanufacturing Techniques*

The first objective of this dissertation is to develop a nanofabrication process that can be potentially scaled to large scale heat transfer surfaces. This requires the demonstration of a potential scalable nanomanufacturing technique that is compatible with different metallic and nonmetallic heat transfer surfaces. Additionally, the compatibility with in-situ depositions by which existing systems can be retrofitted with nanocoatings is very important for real world applications. Also, the first objective of this dissertation focuses on demonstrating the mitigation of nanocoatings due to fouling by stripping and re-coating which is not easily applicable to the nanofabrication techniques reported in the literature.

2.2.2 *Characterization of Individual Effects of Structured Surfaces on Boiling Heat Transfer*

The second objective of this dissertation is to decouple and understand the separate effects of enhanced structures on fundamental mechanisms of boiling heat transfer. This requires characterization and analysis of the role of surface wettability,

wickability, and surface roughness on pool boiling critical heat flux and heat transfer coefficient. In addition, the effect of substrate material, structure material, and morphology, the porosity of the structures with varied structure density, surface degradation due to fouling are important in understanding the physical mechanism of boiling performance. This dissertation also focuses on characterizing the effect of length scale of surface structures, and the effect of boiling fluid properties on pool boiling critical heat flux and heat transfer coefficient to investigate the fundamental physics behind heat transfer enhancement.

2.2.3 *Demonstration of Novel and Robust Enhancement Mechanisms*

To develop planar engineered heat transfer surfaces with no degradable structures or thin films, and naturally resistant to fouling, clogging is the third objective of this dissertation. As such, this section focuses on demonstrating a novel enhancement mechanism which relies on bubble dynamics and fluid properties rather than surface properties. Another objective of this section is to provide fundamental understanding of enhanced bubble dynamics during CHF and HTC enhancement.

2.2.4 *Design and Engineering of High Performance Surfaces*

The fourth focus of this dissertation is to engineer enhanced surfaces for increased boiling heat transfer. This section characterizes and analyzes the role of decoupled individual factors affecting pool boiling heat transfer enhancement such as structured coatings, variations in wettability, and spatial thermal gradient. Finally, this section focuses on incorporating all these decoupled factors and analyzes the effect of coupling during boiling enhancement.

CHAPTER 3: LITERATURE REVIEW

3.1 Boiling on Planar Surfaces

The classical boiling works involve boiling on planar surfaces, characterize and analyze the individual bubble nucleation, bubble dynamics during bubble coalescence, modeling nucleate boiling and critical heat flux for flat surfaces. This section provides a brief description on several classical boiling works.

3.1.1 *Nucleation*

As the surface temperature is increased above the saturation temperature during pool boiling, eventually the surface temperature becomes hot enough to initiate the heterogeneous nucleation at the surface which is the onset of nucleate boiling. After that by increasing the surface temperature keeps increasing and more nucleation sites get activated which increase the heat transfer during boiling. This activation of nucleation sites depends on several properties such as surface roughness with available natural nucleation cavities, surface temperature, operating pressure, surface tension, thermal boundary layer thickness as shown in the following reported as Hsu's analysis [4]. Here $r_{c,min}$ is the minimum cavity radius, $r_{c,max}$ is the maximum cavity radius, δ_t is the thermal boundary layer thickness, T_{sat} is the fluid saturation temperature, T_∞ is the ambient temperature, T_{wall} is the surface temperature, σ is the surface tension, ρ_v is the density of vapor, and h_{lv} is the latent heat of vaporization of boiling fluid.

$$\binom{r_{c,min}}{r_{c,max}} = \frac{\delta_t}{4}\left[1 - \frac{T_{sat}-T_\infty}{T_{wall}-T_{sat}}\binom{+}{-}\sqrt{\left(1 - \frac{T_{sat}-T_\infty}{T_{wall}-T_{sat}}\right)^2 - \frac{12.8\sigma T_{sat}}{\rho_v h_{lv}\delta_t(T_{wall}-T_{sat})}}\right] \tag{3.1}$$

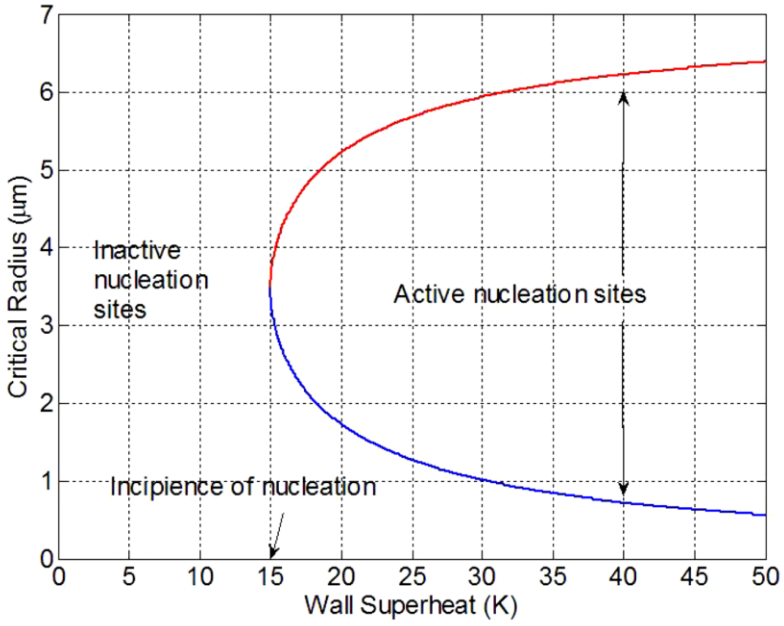

Figure 3.1: Prediction of active nucleation sites [5]

A representative prediction of active nucleation temperature and size has been presented in Fig. 3.1. The incipient wall superheat for flat silicon (15 K) was used to estimate the nucleation temperature and site size. The sizes of active nucleation cavities were estimated to be from 1 μm to 6 μm for wall superheat below 30 K, while for sub-micron cavities the wall superheat was found to be above 35 K.

3.1.2 *Heat Transfer Coefficient (HTC)*

A well-studied classical pool boiling phenomena is the characterization of bubble dynamics in the isolated bubble regimes during pool nucleate boiling. The *HTC* for surfaces in isolated bubble regime can be fairly estimated by a very popular Mikic and Rohsenow [16] micro-convection model presented in Eq. (3.2).

$$HTC = 2\left(\pi k_l \rho_l c_{pl}\right)^{1/2} f^{1/2} d_d^2\, n_a' \tag{3.2}$$

Here, the k_l is the thermal conductivity of liquid, ρ_l is the density of liquid, c_{pl} is the specific heat, f is the bubble departure frequency, d_d is the bubble departure diameter, and n_a' is the active nucleation site density. The first parameter bubble departure diameter can be predicted based on the surface contact angle as presented in Fig. 3.2 [10]

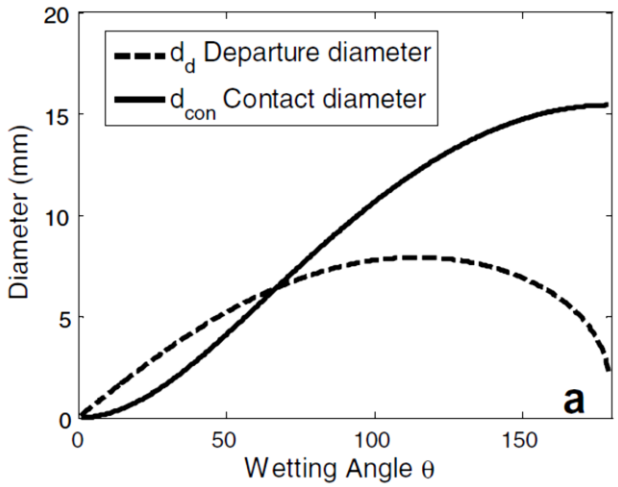

Figure 3.2: Prediction of bubble departure diameter [10]

The second parameter bubble departure frequency can be determined from the following correlation, Eq. (3.3), based on bubble departure diameter at saturated boiling conditions. Here σ is the surface tension, ρ_l is the liquid density, ρ_v is the vapor density and g is the gravitational acceleration. And the third parameter, active nucleation site density n_a' is best determined from the experimental visualization in the isolated boiling regime.

$$f\, d_d = 0.59 \left[\frac{\sigma(\rho_l - \rho_v)g}{\rho_l^2}\right]^{1/4} \tag{3.3}$$

3.1.3 *Critical Heat Flux (CHF)*

Through its use in a multitude of applications including power generation, chemical processing, water purification, and HVAC, boiling plays a crucial role in the lives of most people. During boiling, heat transfer is driven by the nucleation, growth, and departure of vapor from a heated surface, with large amounts of energy being transported via the latent heat associated with phase change [6, 7]. As the heat flux increases, a competition occurs between the vapor generated at the surface and the replenishing liquid, until the critical heat flux (CHF) is reached. CHF is the highest stable heat flux before the transition to film boiling occurs. If the heat flux applied to a surface exceeds the CHF, a drastic and uncontrollable increase in surface temperature is observed due to the rapid development of an insulating vapor layer blanketing the surface. Due to the importance of CHF on the design and operation of boiling systems, extensive research in this area has been conducted over the last fifty years. While the exact physical mechanisms of CHF are still not fully understood, a variety of correlations and models have been developed showing reasonable agreement with experimental measurements [17].

As CHF is approached, the high rate of vapor generation drastically impedes the ability to visualize the nature of the flow on and near the heated surface. This has been a significant hurdle in understanding the mechanism of CHF, and likely reason as to why no singularly accepted model exists to predict it. Kutateladze was the first to proposed that the hydrodynamic stability of two-phase flow was the key to triggering CHF [18, 19], and suggested the use of the nondimensional CHF parameter where q''_{CHF}

is the CHF value, and h_{fg}, σ, g, ρ_v, and ρ_l are the latent heat, surface tension, gravitational acceleration, and vapor and liquid densities, respectively.

$$K = \frac{q''_{CHF}}{\rho_v^{1/2} h_{fg} [\sigma g(\rho_l - \rho_v)]^{1/4}} \tag{3.4}$$

In the nucleate boiling regime, several heat transfer mechanisms such as transient conduction where bulk liquid replacing the departed bubble space conducts heat from surface to liquid [16, 20, 21], microconvection due to increased bubble-liquid interface velocity [21], and thin liquid film evaporation underneath the bubble have been identified to be contributing parameters affecting the overall boiling heat transfer performance [21].

Figure 3.3 presents some representative saturated pool boiling results for flat surfaces with water at atmospheric conditions. Here, Y-axis is the heat flux and X-axis is the wall superheat (surface temperature at the top of the surface above fluid saturation temperature). As can be seen, smooth flat silicon surfaces reach CHF as high as 84 W/cm^2 (red squares in Fig. 3.3) whereas bare copper can give CHF up to 125 W/cm^2 (red circles). Additionally, it can be seen that bare copper gives much higher HTC as opposed to flat silicon surface. This can be attributed to the availability of natural nucleation sites on metallic surfaces.

Researchers have also proposed several models and correlations to estimate the pool boiling critical heat flux (CHF) value. The precise critical heat flux (CHF) mechanism has been the issue of several investigations and arguments over the past few

decades due to the non-linear nature of three phase contact line motion [22]. Four different hydrodynamics CHF mechanisms are proposed in the literature, widely known Zuber [23] Helmholtz critical vapor packing CHF model, Kutateladze [18] critical vapor velocity CHF condition, Rohsenow and Griffith [24] increased nucleation site density CHF mechanism, and Haramura and Katto [25] liquid microlayer CHF model. These hydrodynamic models were subsequently refined and extended to more precise CHF conditions and geometries.

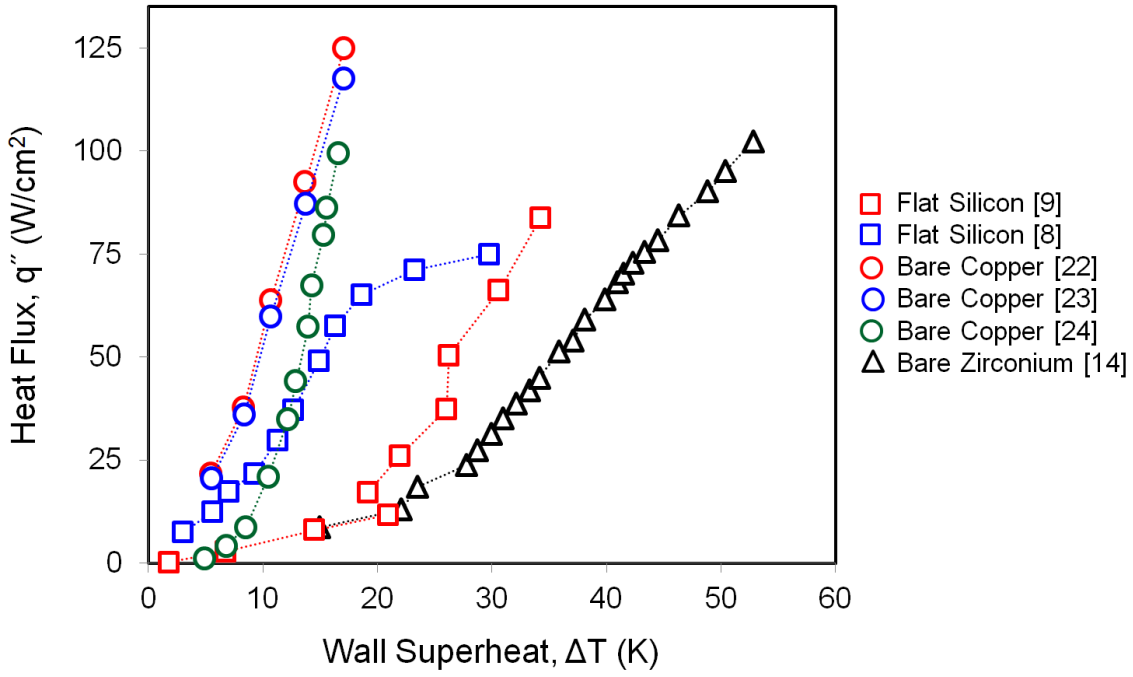

Figure 3.3: Representative pool boiling curves with saturated water at atmospheric conditions (collected from [8, 9, 14, 26-28]).

Dhir and Liaw developed a thermal model for theoretical prediction of CHF based on static contact angle [29]. They assumed that static vapor stems are implanted in the thermal layer. They demonstrated that CHF increases with decreasing contact angle.

Also, it is evident from their analysis that the CHF enhancement with reduced CA holds best for a contact angle range of 27º to 107º. Hence, CHF augmentation for surfaces with contact angle less than 27º is not explainable by bubble dynamics only [9].

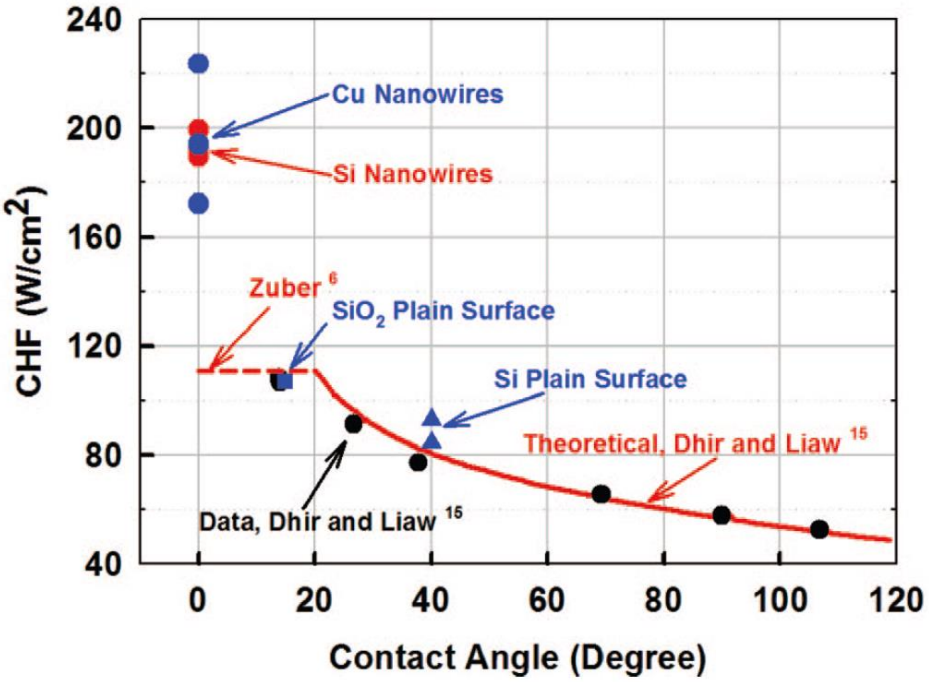

Figure 3.4: Effect of surface equilibrium contact angle on pool boiling critical heat flux with saturated water at atmospheric conditions [9].

A representative pool boiling results based on surface contact angle is shown in Fig. 3.4. Here pool boiling CHF as a function of equilibrium contact angle is presented for flat and structures surfaces. As the contact angle approaches zero degree using engineered surfaces, the contact angle approach of CHF enhancement fails to predict CHF for structured surfaces (more detailed will be discussed later). A more recent and widely known CHF model was proposed Kandlikar [30] which is based on the force balance analysis at the three phase contact line. Kandlikar included the effect of dynamic

receding contact angle on CHF and surface orientation and developed a theoretical model based on force balance parallel to the heater surface [30].

3.2 Boiling of Water on Engineered Surfaces

Boiling heat transfer is used in many applications, including the production of electricity, chemical processing, and high-heat flux thermal management. Due to its prevalence, and the important role it plays in numerous industries, the enhancement of boiling heat transfer has been studied for decades. During boiling, heat is transferred from a hot surface to a cooler fluid by (1) evaporation across liquid-vapor interfaces, (2) transient conduction, and (3) the micro-convection generated by the nucleation, growth, and departure of vapor bubbles [6, 27]. The efficiency of boiling is quantified by the heat transfer coefficient (HTC), defined as the ratio of the surface heat flux to the superheat temperature, the temperature difference between the solid and the saturated fluid. During boiling, there is a finite rate at which heat can be dissipated from any surface. This maximum is the critical heat flux (CHF). CHF, also referred to as the boiling crisis, occurs when the production of vapor cannot be adequately balanced by the amount of liquid returning to the heated surface. When this occurs the surface undergoes dry-out, where an insulating layer of vapor blankets the solid surface. This leads to an immediate, uncontrollable, and drastic increase in surface temperature with dangerous and potentially catastrophic consequences, such as the destruction of electronic components or the meltdown of a nuclear reactor.

Understanding and improving HTC and CHF in boiling systems has been extensively studied for decades, including the development of a variety of enhancement strategies [31, 32]. Traditionally, the use of enhanced surfaces has been primarily focused

on the creation of structures and complex geometries machined into, or attached onto, the boiling surface such as porous materials, sintered wires and meshes, as well as mechanically deformed structures [33-35]. With the development of increasingly precise fabrication tools, micro/nano-structured surface coatings have been explored in recent years, showing substantial increases in boiling performance. A variety of microscale and nanoscale wires, rods, posts, and other structures have been fabricated on silicon chips and shown to enhance HTC and CHF of water anywhere from 50% to 300%, depending on the working fluid [9, 11-13, 36-40]. Similarly, micro/nano-structures on copper and other metals have also been demonstrated [2, 14, 26, 27]. The role that surface structures play in boiling enhancement has been attributed to a variety of factors, including capillary wicking [9, 13, 14, 38, 39], increased nucleation site densities [9, 28], and increased contact line pinning [8]. Additionally, notable increases in HTC have been reported using embossed copper microstructures with specific contoured shapes [27]. These complex microscale shapes use evaporation momentum force to promote the separation of liquid and vapor flow paths and enhance micro-convection. This section focus on boiling enhancement using more recent advancement in fabrication technologies with much smaller sizes and more control of surface morphology.

3.2.1 *Nanostructured Surfaces*

Substantial enhancement in pool boiling heat transfer has been reported with the addition of nanostructures. CHF up to 200 W/cm^2 have been reported for nanostructured surfaces during pool boiling with water at atmospheric conditions. Chen et al. fabricated Si nanowires through electroless etching technique and Cu nanowires by electroplating of Cu through porous alumina membrane and demonstrated significant

CHF and HTC enhancement for water as the working fluid at atmospheric pool boiling conditions [9]. The representative images for the structured surfaces are presented in Fig. 3.5.

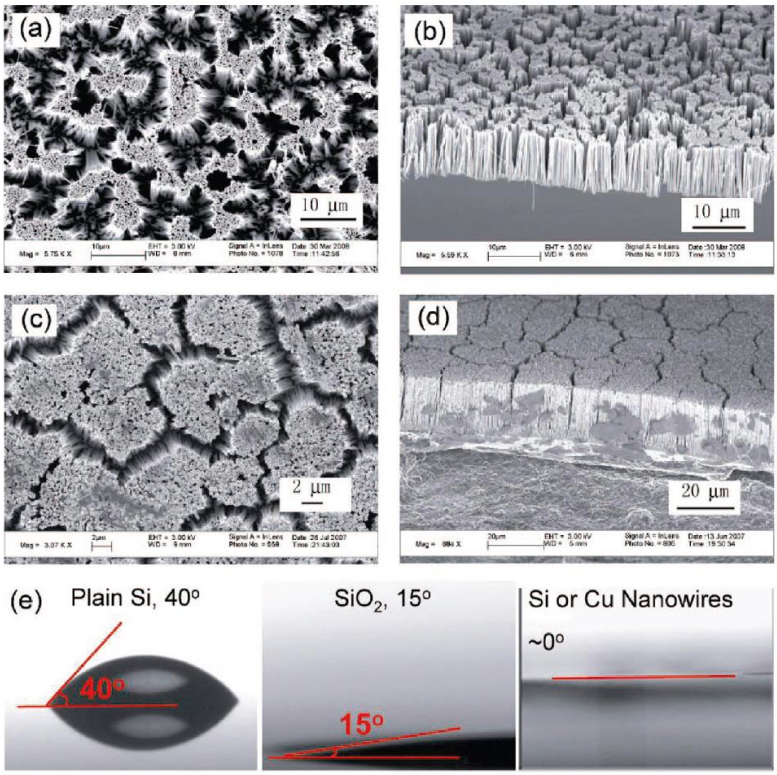

Figure 3.5: Scanning electron microscopy (SEM) images of nanowire surfaces (a) top view of Si Nanowires, (b) cross sectional view of Si Nanowires, (c) top view of Cu Nanowires, (d) cross sectional view of Cu nanowires, (e) equilibrium contact angles of a on Si, SiO2, and Si and Cu nanowire surfaces. [9]

By submerging the silicon surfaces into $AgNO_3$, and HF acid, 200-300 nm diameter, 40-50 µm height vertically aligned silicon nanowires were etched onto silicon. 200 nm diameter and 40-50 µm long copper nanowires were fabricated by electroplating copper through aluminum oxide nanoporous membrane. Figure 3.6 shows the pool

boiling results for silicon and copper nanowire surfaces and compared with nanosmooth flat silicon substrates. As can be seen, the nanostructures reach CHF up to 200 W/cm^2 whereas a flat silicon surface gives CHF of 84 W/cm^2.

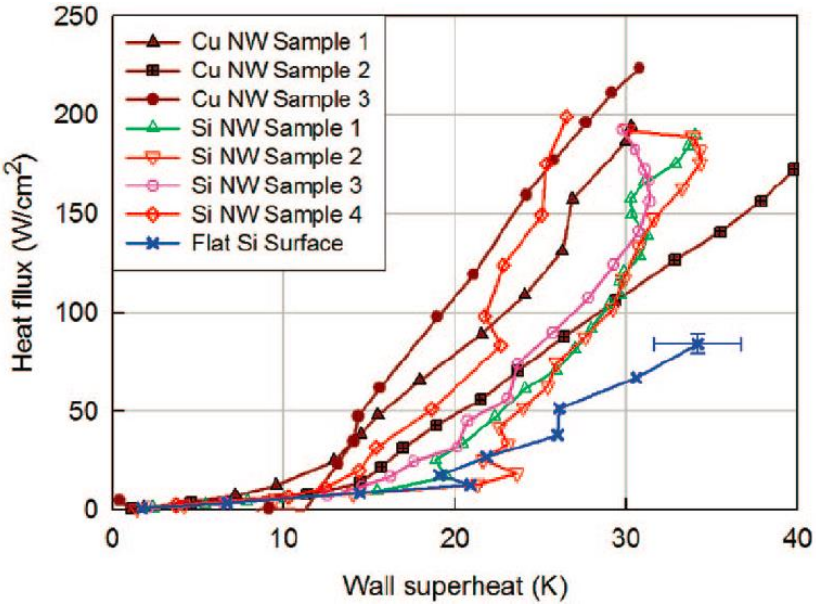

Figure 3.6: Pool boiling heat flux as a function of wall superheat for silicon and copper nanowire structures [9].

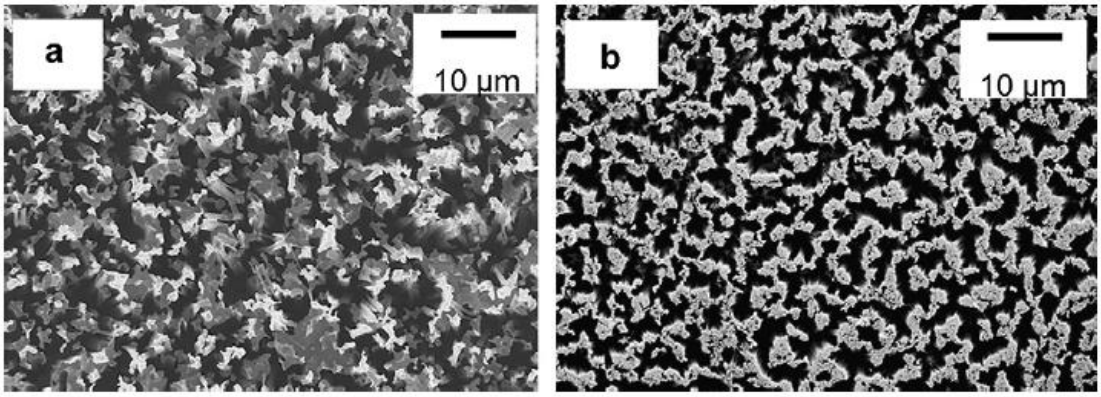

Figure 3.7: Scanning Electron Microscope images of Silicon Nanowires with average heights of (a) 35 mm and (b) 20 mm [12]

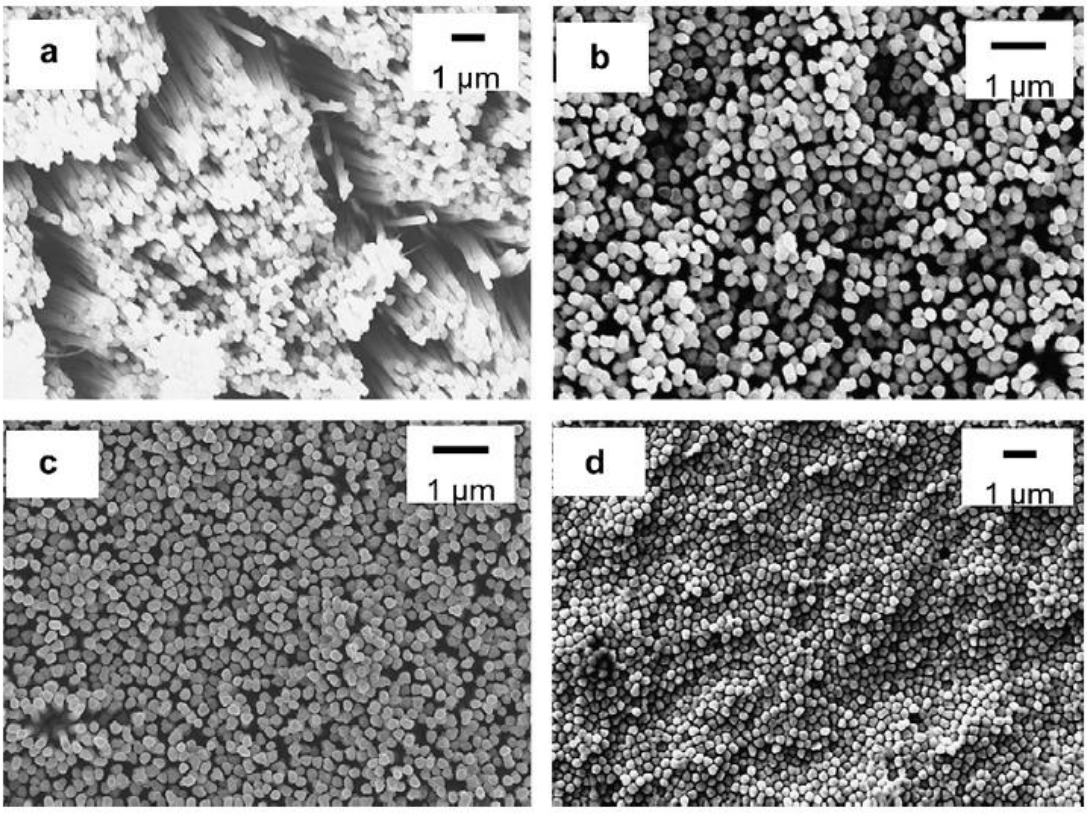

Figure 3.8: Scanning Electron Microscope images of Copper Nanowires with average heights of (a) 20 mm, (b) 10 mm, (c) 5 mm and (d) 2 mm [12].

Yao et al. fabricated metal particle assisted chemically etched silicon nanowires (SiNW), Fig. 3.7, and electrochemically deposited copper nanowires (CuNW), Fig. 3.8, of different heights to the study the effect of nanowire height during pool boiling heat transfer [12]. They observed that pool boiling CHF increases with increasing nanowire height regardless of the structure materials. They achieved a CHF of 134 W/cm^2 for the silicon nanowire height of 35 nm as shown in Fig. 3.9. They attributed this CHF enhancement to the formation of large cavities due to the increase in nanowire height for providing increased nucleation site densities which eventually increased the CHF.

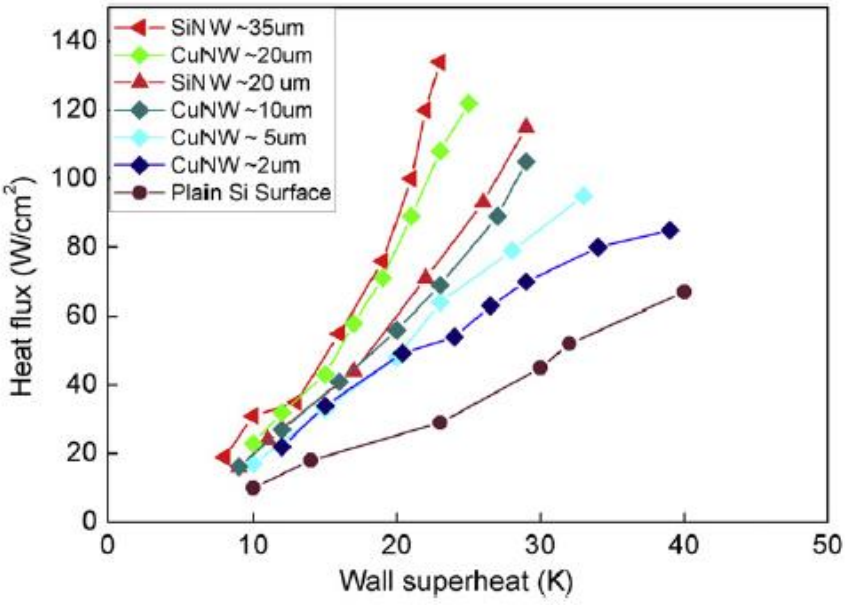

Figure 3.9: Pool boiling heat flux as a function of wall superheat for SiNW and CuNW surfaces with different heights [12].

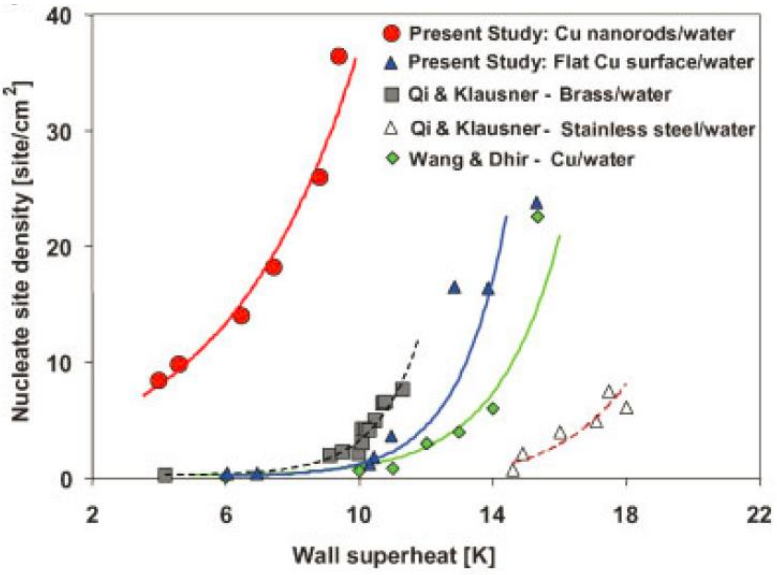

Figure 3.10: Visualization results of bubble dynamics during boiling. The surfaces with nanorods are shown to active 30 fold greater nucleate site densities in 5–10 K superheat range than that for bare surfaces [28].

Li et al. showed 30 fold increases in active nucleation site density as shown in Fig. 3.10 during pool boiling by adding Cu nanorods through oblique angle Cu atoms deposition technique [28]. They conducted bubble dynamic visualization within the heat flux range of 4 W/cm^2 to 25 W/cm^2. They observed that for nanostructured surfaces, nucleation site density is 30 fold higher than bare surface with in the range of 5 to 10 K wall superheat which results in CHF up to 160 W/cm^2. Hendricks et al. proposed a novel microreactor assisted solution based nanomaterial deposition technique to grow ZnO nanostructures on Al and Cu and showed around 4 times CHF and 10 times HTC enhancement compared to a flat surface [41].

3.2.2 *Microstructured Surfaces*

While the unique properties of nanostructures such as increased capillary wicking, wettability, submicron cavities, and high nucleation site density have been attributed to the CHF enhancement for nanostructured surfaces, increased surface roughness, and contact line pinning have been shown to increase CHF for microstructured surfaces. More than 190% CHF enhancement have been reported for deep reactive ion etching (DRIE) based silicon microstructured surfaces [8, 39] compared to flat silicon surface. Chu et al. fabricated different roughness scale deep reactive ion etched (DRIE) silicon microposts (Fig. 3.11) and achieved CHF of 208 W/cm^2 for a surface with roughness value of 6 [8]. Also Chu et al. [8] modified the Kandlikar model [30] by scaling the CHF with roughness factor and receding contact angle. Their proposed CHF model is shown in Fig. 3.12.

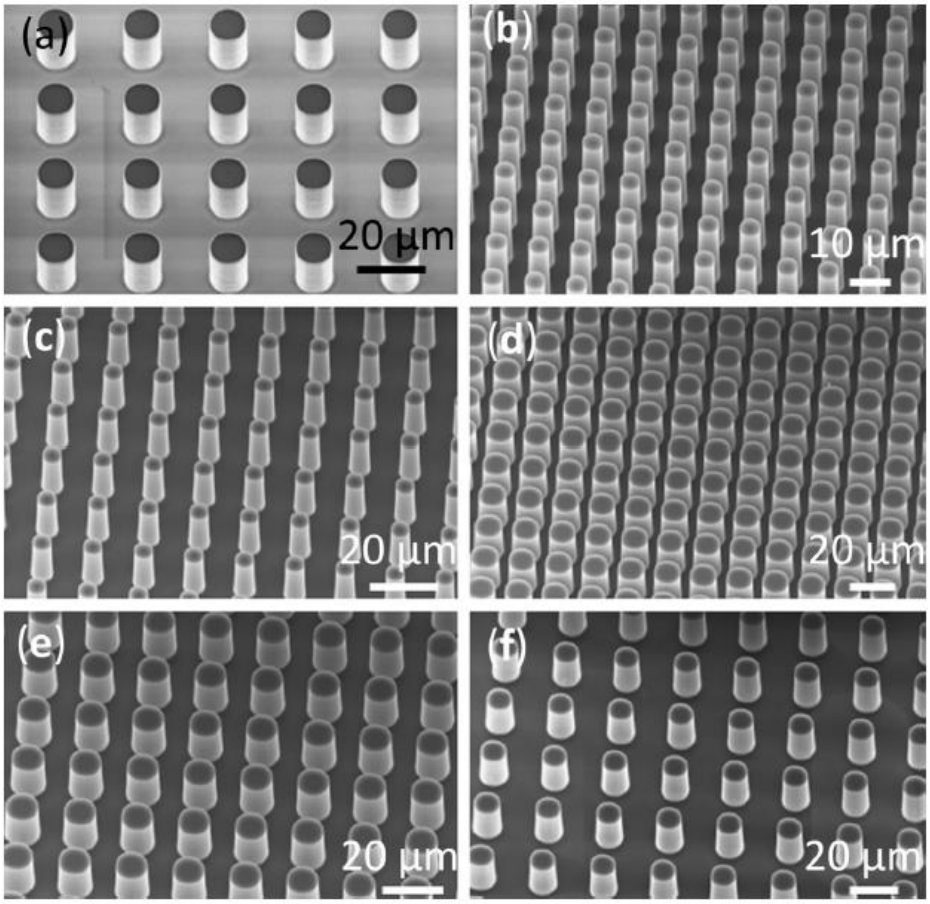

Figure 3.11: SEMs of the surfaces with silicon microstructures showing the geometries of pillars. The pillars heights are (a) 10 µm and (b)-(f) 20 µm, the center-to-center spacing of microposts (a) and (f) 15 µm, (b) and (d) 5 µm, and (c) and (e) 10 µm; and varied diameters of (a) and (d)-(f) 10 µm and (b) and (c) 5 µm [8].

On contrary to roughness augmented CHF model, O'Hanley et al. fabricated microstructure surfaces with varied roughness factors and analyzed the separate effects of surface wettability, porosity, along with roughness. They observed that surface wettability and roughness factor had negligible impact on CHF enhancement whereas maximum heat transfer enhancement was obtained for a surface with hydrophilic porous wicking structures [13].

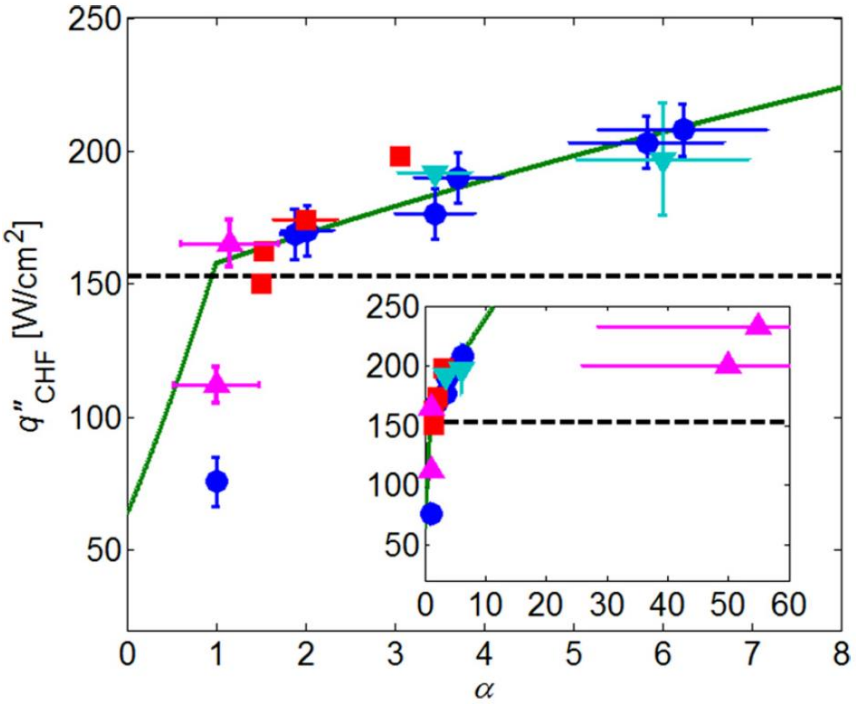

Figure 3.12: CHF as function of a surface roughness for microstructure surfaces [8]

3.2.3 *Hierarchical Surfaces*

While microstructured patterns provide increased hemiwicking through the micropost arrays, added nanostructures to these patterns attribute significant enhancement of capillary motion of the fluid to the nucleation sites for hierarchical surfaces. A CHF enhancement up to 230% with HTC enhancement up to 220% has been reported for micro/nano hierarchical surfaces [37], representative SEM images and boiling results are shown in Fig. 3.13 and Fig. 3.14 respectively, with compared to flat silicon surface. Kim et al. achieved significant CHF (~233 W/cm^2) enhancement using ZnO nanorod-Si micropost hierarchical surface[15]. They used tetramethyl ammonium hydroxide wet etching to fabricate Si microposts, and ammonia aqueous solution to grow ZnO nanorods. Ahn et al. fabricated Zirconium alloy based nano, micro and hierarchical surfaces to conduct pool boiling experiment [42]. They used hydrofluoric acid based anodization

technique on Zirconium alloy plates at constant electric potential (20 V) and solution temperature (10 °C). They achieved different surface morphologies by varying the exposure time of zirconium plates to the solution. They concluded that below 10° static contact angle the liquid spreading dynamics dominates on CHF enhancement. Chu et al. proposed a scalable high heat flux removing surface fabrication technique using alkaline based chemically oxidized CuO nanostructures on electroplated copper micropillars and achieved significant CHF (~250 W/cm^2) enhancement[37].

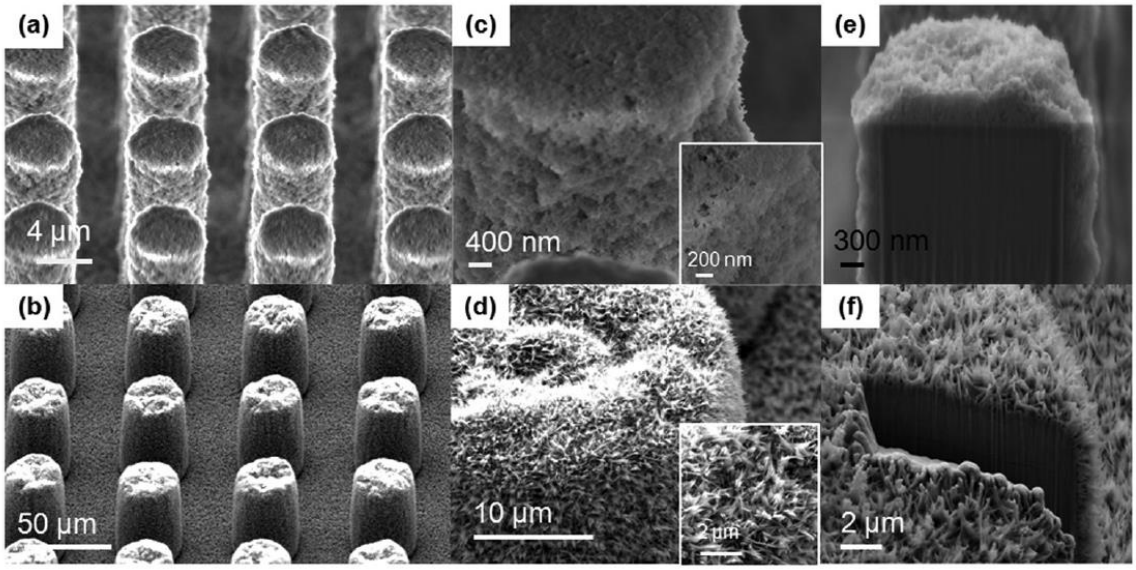

Figure 3.13: SEM images of the silica and CuO based hierarchical surfaces. (a) Microstructures coated with EPD (b) microstructures coated with CuO nanostructures (c) zoomed view of the silica-based micropillar and the inset is EPD-coated SiO_2 nanoparticles (d) Magnified view of the CuO hierarchical surfaces and the inset is CuO nanostructures (e) cross-sectional view of hierarchical silicon and (f) cross-sectional view hierarchical copper surface. [37]

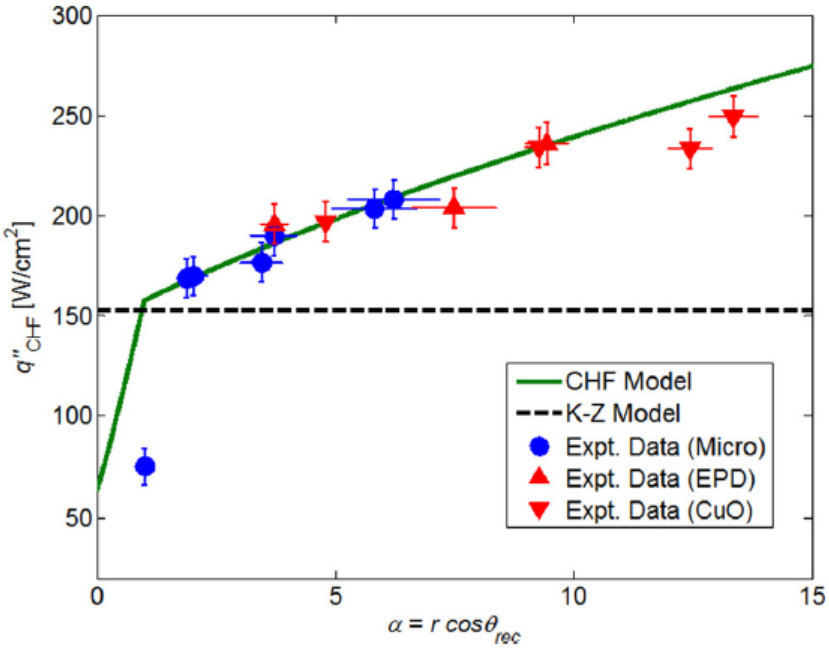

Figure 3.14: CHF as a function of surface roughness for hierarchical surfaces [37].

3.2.4 *Macro-machined Surfaces*

A significant enhancement in both critical heat flux and heat transfer coefficient has been reported for surfaces with macro-machined microchannel designs. Here the channels act as a heater from three sides. A bubble nucleating inside the channel grows and pushes the liquid from the channel to outside, and the bubble moves towards the top of the surface. Since the bubble moves outside, the channel brings more liquid to the channel and forms a micro-convection. A CNC milled channel surface was used to demonstrate a CHF increase in 90% and 280% increase in HTC compare to bare copper surface [26]. Hot embossed contoured microchannel surfaces as shown in Fig. 3.15 have been demonstrated to increase both CHF up to 150% and maximum HTC up to 740% compared to bare copper surface due to increased natural nucleation sites, controlled liquid-vapor motion [27].

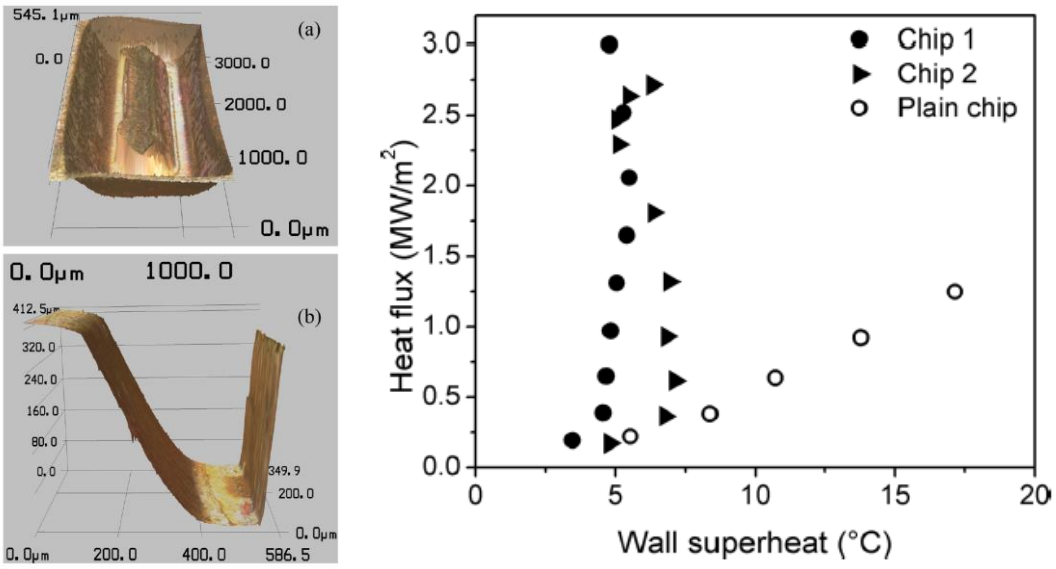

Figure 3.15: Enhanced surface details (a) single channel with rectangular geometry, and (b) cross-section of the channel, and (c) pool boiling heat transfer performance of enhanced surface designs compared to bare surfaces showing significant enhancement in both CHF and HTC. [27]

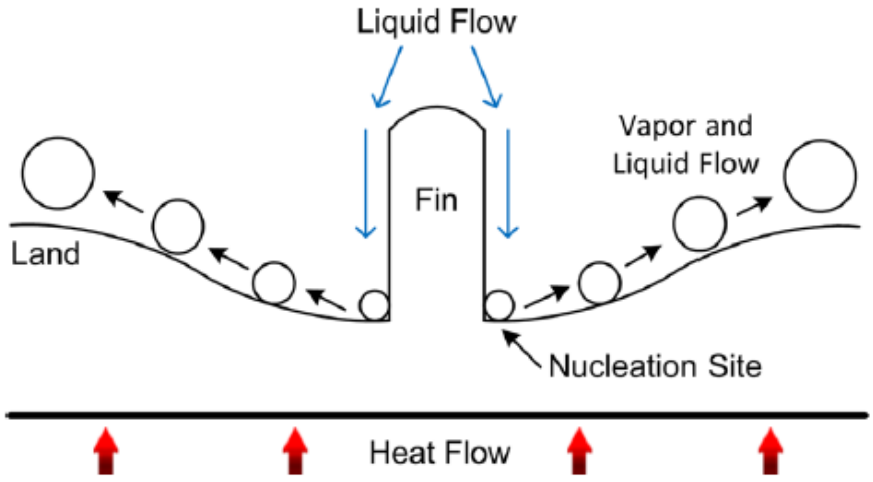

Figure 3.16: Schematic of enhanced surface design with controlled bubble dynamics showing separate liquid and vapor flow pathways during pool boiling. [27]

The heat transfer enhancement mechanism for these structures has been shown in Fig. 3.16. As can be seen, the surface contains complex contour geometries where the base of the fins act as the preferential nucleation sites and the bubbles move along the pathway given by inclined base at an angle of 14.1°. For this configuration, liquid travels along the sidewalls of the fins and maintains a controlled and preferential liquid and vapor flow pathways during boiling which becomes more pronounced at higher heat flux values.

3.2.5 *Heterogeneous Surfaces*

In addition to micro/nanostructured heat transfer enhancement mechanisms, another mechanism comprising mixed wettability on a surface has been shown to increase both CHF and HTC.

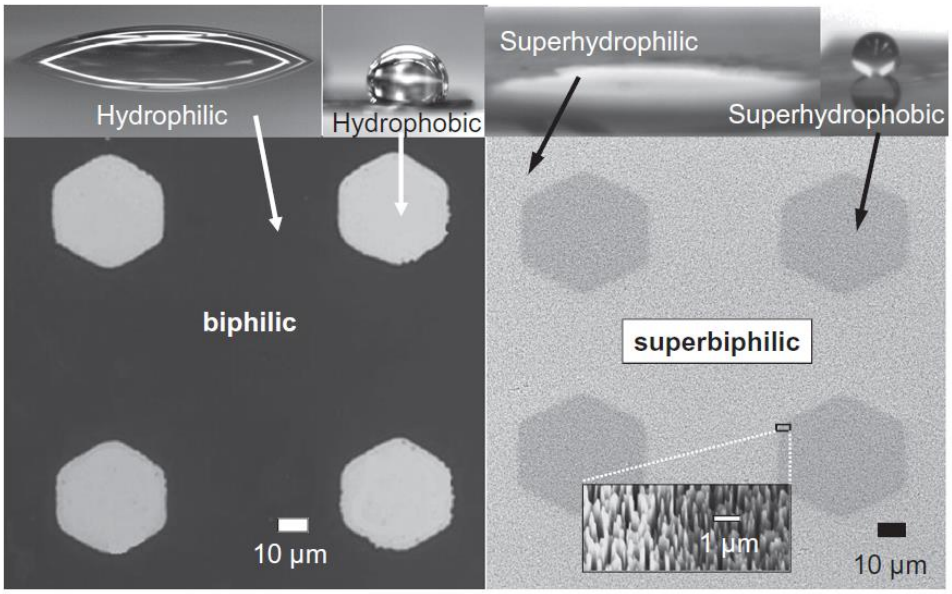

Figure 3.17: SEM images of bi-philic and super-bi-philic surfaces showing contact angle measures of hydrophilic, hydrophobic, superhydrophilic, and superhydrophobic surfaces. [10]

A CHF enhancement up to 150% and HTC up to 220% has been attributed to bi-philic surfaces [43], whereas, CHF increase up to 65% and HTC up to 540% have been achieved for super-bi-philic surfaces, compared to flat silicon surface [10]. Betz et al. demonstrated significant HTC (> 100 kW/m^2K) enhancement using superhydrophilic-superhydrophobic mixed wettability surface [10]. They used DRIE black silicon method to grow superhydrophilic nanostructures on SiO_2 coated silicon surface and traditional photolithography to pattern Teflon superhydrophobic dots. A representative mixed wettability surface design is shown in Figure 3.17.

3.3 Boiling of Dielectric Fluids on Engineered Surfaces

In addition to enhanced boiling with water as the heat transfer fluid, researchers have also used various refrigerant fluids to characterize the heat transfer performance of structured surfaces during pool boiling. This section provides a brief review of some pool boiling characterization of structured surfaces with commercial dielectric fluids.

Im et al. fabricated copper nanowire structures with varied wire height through electro-chemical depositing using AAO nanoporous membranes (Fig. 3.18) and characterized them with pool boiling using dielectric fluid (PF-5060) [44]. They observed increase in CHF and decrease in wall superheat for nanowire structures compared to bare surfaces due to increased capillary pressure, and nucleation sites through micro cavities. Maximum CHF enhancement was optimized at nanowire height of 2 μm (Fig. 3.19) which can be attributed to the balance between the capillary induced wettability and viscous drag.

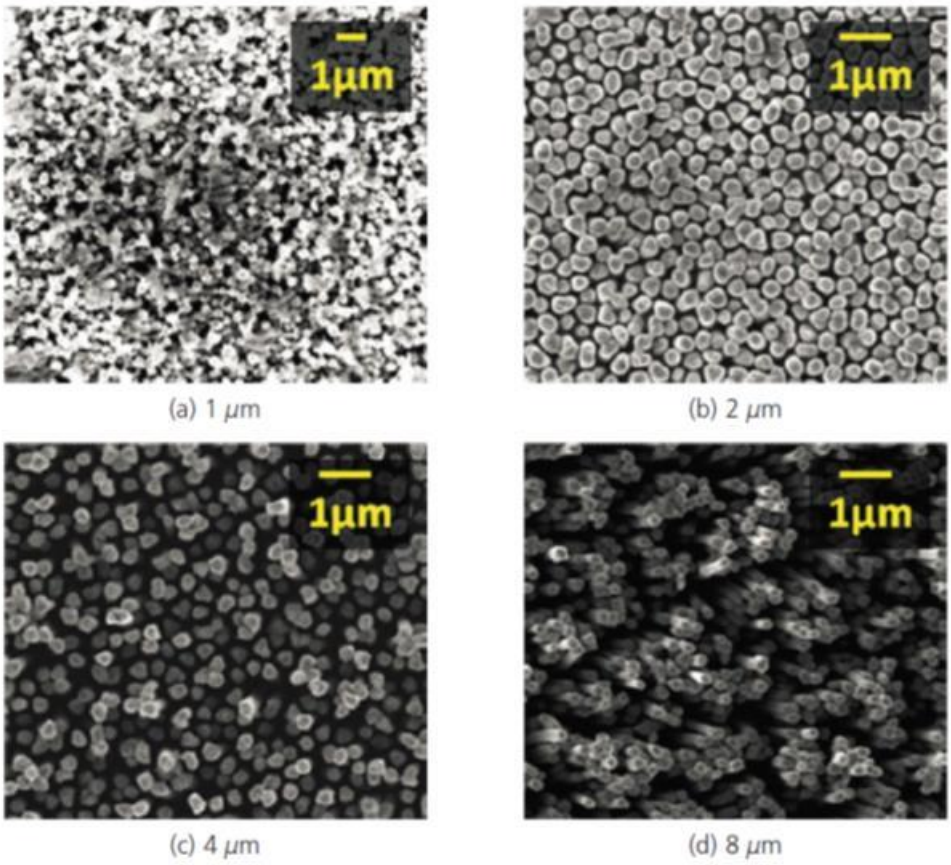

Figure 3.18: Scanning Electron Microscope images of CuNW at different heights. [44]

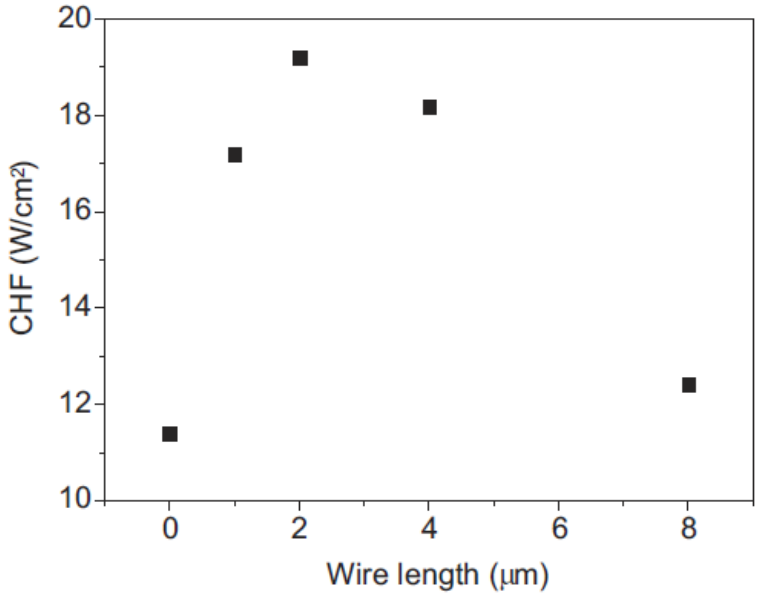

Figure 3.19: CHF as a function of nanowire height for pool boiling of PF-5060. [44]

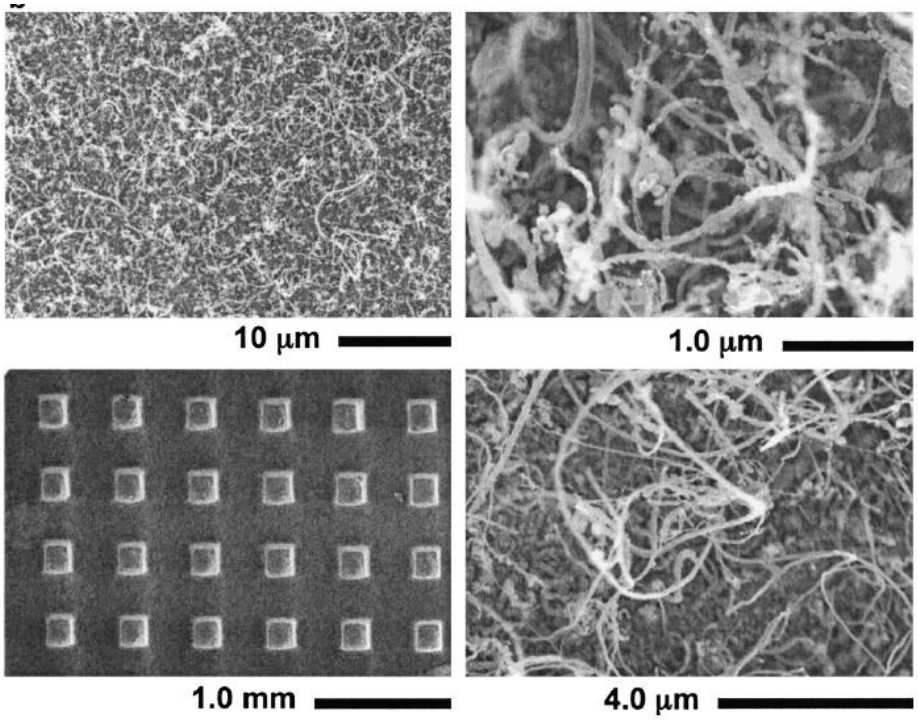

Figure 3.20: SEM images of fabricated copper microstud surfaces coated with CNT. [44]

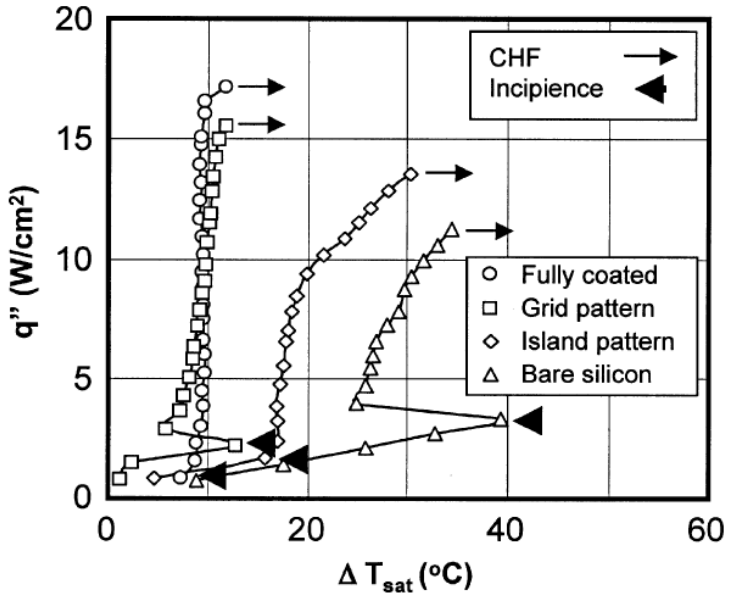

Figure 3.21: Heat flux as a function of wall superheat for fully CNT-coated, CNT-patterned, and bare silicon surfaces [44].

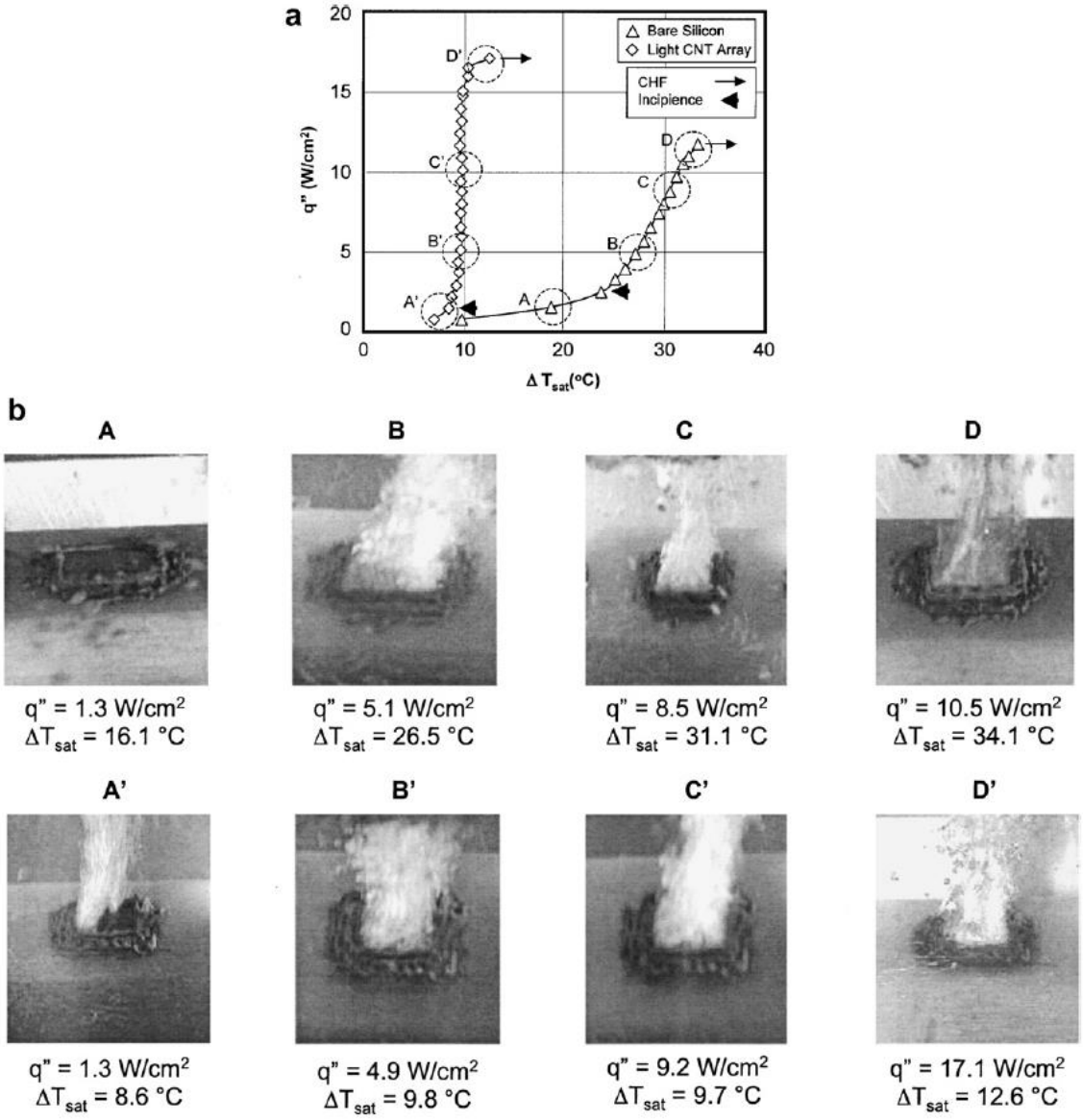

Figure 3.22: (a) Pool boiling heat transfer performance for silicon surfaces fully coated with CNT, and (b) corresponding images of during boiling photographs at various heat flux conditions [44].

Ujereh et al. synthesized CNT structures on to silicon and copper surfaces [44] and demonstrated that CHF and HTC enhancement for CNT coated silicon surfaces are monotonic enhancement, as shown in Fig. 3.21, 5% enhancement for island pattern, 60%

for grid pattern, and 100% for fully coated CNTs. Whereas, for copper and copper microstud surfaces coated with CNT, as shown in Fig. 3.22, this enhancement is less compared to that with silicon covered with CNT only surface. This was attributed to the reduction in CNT coverage at the circumference of microstruds, and effectiveness of CNTs at the top of microstuds due to the higher thermal conductivity of these copper microstuds.

CHAPTER 4: POOL BOILING EXPERIMENTAL APPARATUS

4.1 Experimental Apparatus for Boiling of Saturated Water

This section describes the pool boiling experimental setup and method used to characterize the heat transfer performance of engineered surfaces using water at atmospheric conditions.

4.1.1 *Experimental Apparatus*

The pool boiling experimental setup used for testing with saturated water is shown in Figure 4.1. It consists of an instrumented water bath attached to an insulated copper block with a 1 cm × 1 cm sample soldered to it. Two cartridge heaters were embedded into the copper block allowing for a maximum power of 1000 W. The heat input to these heaters was controlled with a variable autotransformer. Five 6 mm equally spaced T-type thermocouples were inserted into the insulated copper block along the centerline to measure the one-dimensional temperature gradient across and heat flux supplied to the test surfaces. A thermocouple 0.2 mm below the top copper surface was used to determine the surface temperature. The samples had ~1μm of thermally evaporated copper on their back sides to facilitate soldering to the copper block with 63/37 Tin/Lead solder with acid flux to provide good thermal contact. A Polycarbonate chamber holds the water bath for pool boiling where an auxiliary cartridge heater with a 300 W capacity (controlled with a second variac) was used to maintain the bath temperature at saturation conditions. The bath temperature was monitored using a T-type thermocouple placed within the 2 cm above the boiling surfaces. The temperature measurements were recorded using an NI DAQ system. All thermocouples were

calibrated using a fixed temperature chiller (Thermo Scientific HAAKE ARCTIC SC150 A25 refrigerated circulator bath chiller) and Omega thermometer calibrator (CL3512A).

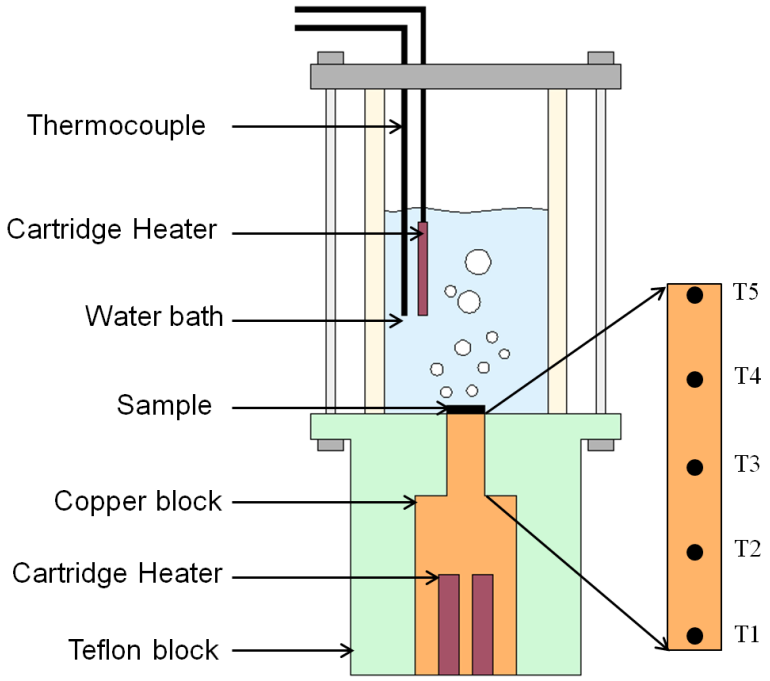

Figure 4.1: Schematic of pool boiling experimental setup for water

4.1.2 *Experimental Method*

All pool boiling experiments were conducted under atmospheric conditions with saturated water. Deionized water was degassed by boiling at 100 °C for 30 minutes, prior to being placed in the chamber. The heat flux is then slowly increased until a surface temperature at 100 °C is reached, and left there for another 30 minutes. To begin testing, the heat input to the sample was increased in small increments (5 W/cm^2 to 10 W/cm^2) and the system was left to reach thermal equilibrium. All measurements were recorded after the temperature variations for each thermocouple become less than 0.5 °C for 20 minutes. Each sample was tested up to CHF, which was taken as the largest stable

heat flux attainable. Beyond CHF a rapid increase in surface temperature was observed, resulting in the sample de-soldering from the copper block.

The heat flux was calculated from the average heat flux values determined from the middle three thermocouples (T_2 to T_4 in Fig. 4.1) as given by:

$$q'' = -k_{cu}\left(\frac{dT}{dx}\right)_{average} \tag{4.1}$$

$$q'' = -k_{cu}\ \frac{1}{2}\left[\left(\frac{\Delta T_{23}}{\Delta x_{23}}\right) + \left(\frac{\Delta T_{34}}{\Delta x_{34}}\right)\right] \tag{4.2}$$

where, k_{Cu} is the thermal conductivity of copper, ΔT is the temperature difference between adjacent thermocouples, and $\Delta x_{23} = \Delta x_{34} = \Delta x$ is the spacing between thermocouples.

Surface temperature was determined from the top thermocouple beneath the soldered sample (T_5 in Fig. 4.1) using Fourier's conduction law given in following equation.

$$T_s = T_5 - q''\left(\frac{L_{Cu}}{k_{Cu}} + \frac{L_{So}}{k_{So}} + \frac{L_{Su}}{k_{Su}}\right) \tag{4.3}$$

where T_s is the surface temperature, L_{Cu} is the distance from copper block top surface to the top thermocouple, L_{So} is the solder thickness, L_{Su} is the thickness of the substrate, and k_{cu}, k_{so}, and k_{su} are the thermal conductivity of copper, solder, and substrate respectively.

4.2 Experimental Apparatus for Boiling of Dielectric Fluids

The pool boiling experimental setup and method used to characterize the heat transfer performance of engineered surfaces using saturated FC 72 at atmospheric conditions are presented in this section. Although this dissertation presents the saturated

pool boiling results of FC 72 at atmospheric pressure, this experimental setup is designed to characterize the pool boiling heat transfer for other fluids. This experimental setup can be also be used for pool boiling at subcooled and high pressure conditions.

4.2.1 *Experimental Apparatus*

The schematic and the optical image of pool boiling experimental setup used for testing with saturated dielectric fluid are shown in Figure 4.2 and Figure 4.3 respectively. It consists of an instrumented dielectric fluid chamber attached to an insulated copper block with a 2 cm × 2cm sample soldered to it. Four cartridge heaters were embedded into the copper block allowing for a maximum power of 1600 W. The heat input to these heaters was controlled with a variable autotransformer. Three 1 cm equally spaced T-type thermocouples were inserted into the insulated copper block along the centerline to measure the one-dimensional temperature gradient across and heat flux supplied to the test surfaces. PEEK was used to provide the thermal insulation to the copper heater block. A T type thermocouple 0.3 mm below the top copper surface was used to determine the surface temperature. The heater block assembly was attached to the boiling chamber with a stainless steel plate and Viton O-ring. The samples were soldered to the copper block with 63/37 Tin/Lead solder with acid flux to provide good thermal contact.

A polycarbonate cylinder attached to the top of the 6-way cube with a custom-built gasket was used as the vapor condensing chamber during boiling. Aluminum coil connected to a fixed temperature chiller and flow controller valve was used to condense vapor and maintain atmospheric pressure. Another T-type thermocouple inserted in the condenser chamber and a differential pressure transducer was used to monitor the vapor

temperature and vapor pressure during boiling. An aluminum plate instrumented with condenser coils, pressure, temperature ports and bleed valve ports was assembled with a custom-built gasket at the top of the polycarbonate condenser chamber. All measurements were recorded using an NI DAQ system.

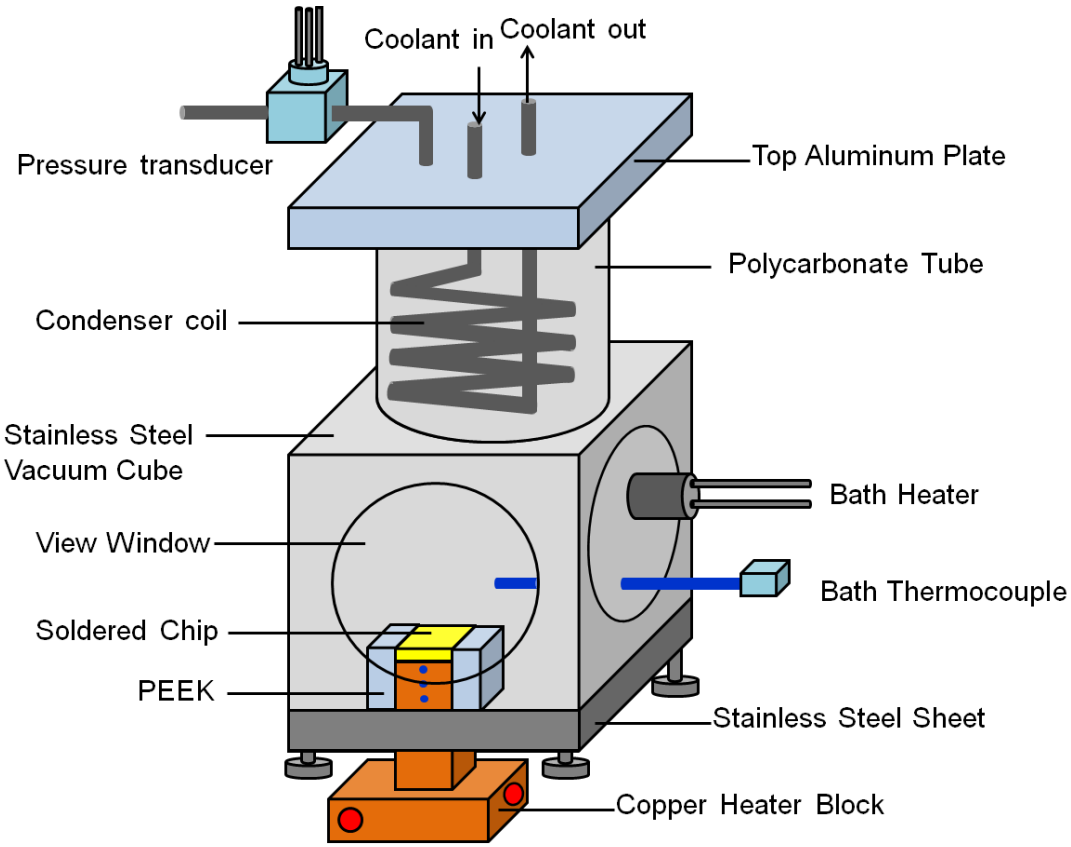

Figure 4.2: Schematic of pool boiling experimental setup for dielectric fluids

4.2.2 *Experimental Method*

All pool boiling experiments were conducted under atmospheric conditions with saturated FC 72. Prior to each test, the boiling fluid was placed inside the chamber and both the bath heater and test section heater were powered until the bulk fluid reaches beyond the saturated temperature and vigorous boiling occurs. Then the bleed port was

opened to purge the non-condensable gases from the chamber and condenser coil was turned on to maintain atmospheric pressure. Water at atmospheric temperature was pumped through the condenser coil using a constant temperature chiller.

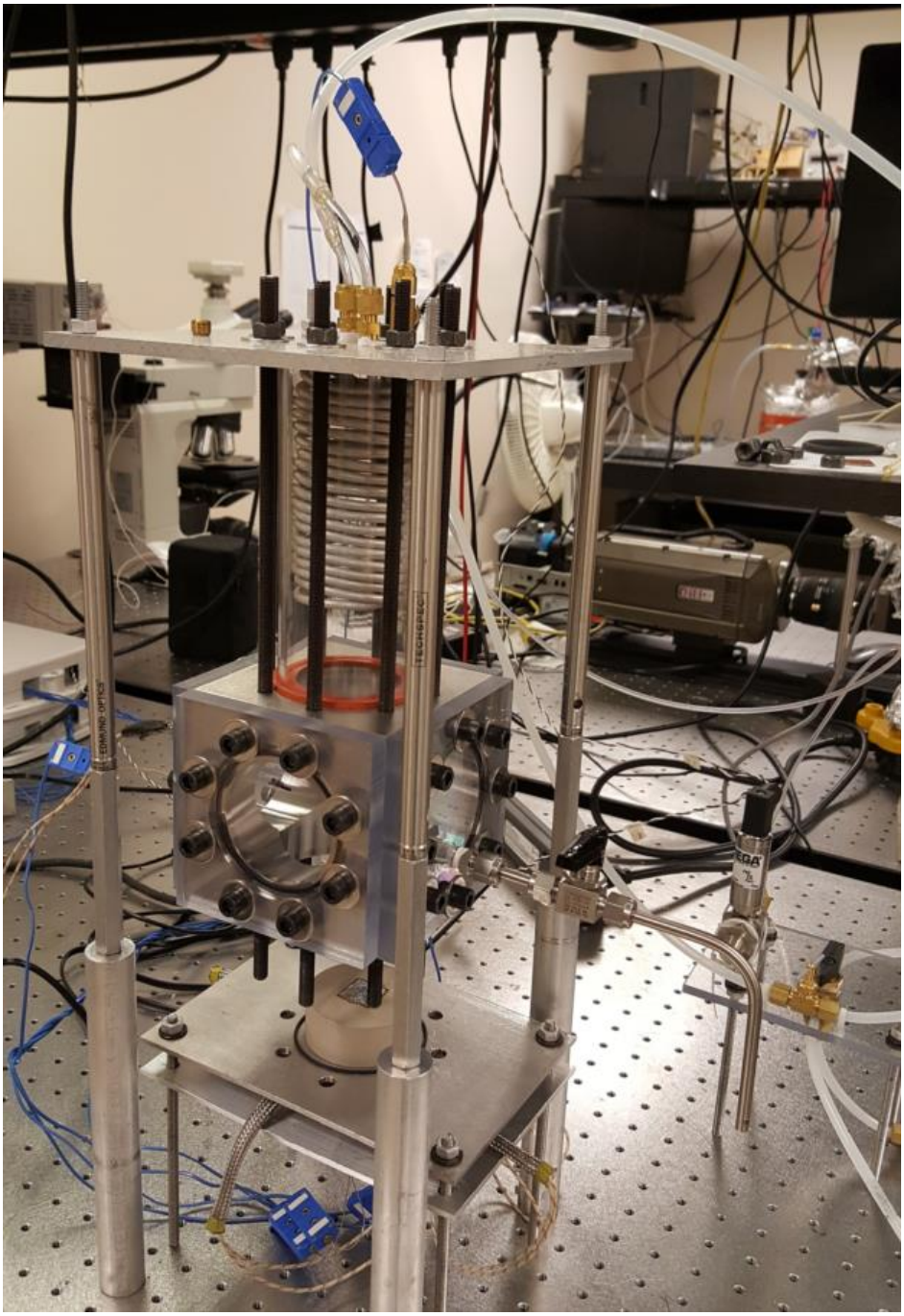

Figure 4.3: Optical image of pool boiling experimental setup for dielectric fluids

Then the test section heater power was dialed down to reach below the saturation temperature and allows complete rewetting of the surface. Finally the test section heater power was increased until the surface reaches saturation temperature. After the complete boiling system reached to equilibrium conditions, the heat flux to the test surfaces was slowly increased in increments of 1 W/cm^2. During boiling, the vapor pressure was maintained at atmospheric condition by changing the water flow rate through the condenser coil. Each sample was tested up to CHF, which was taken as the largest stable heat flux attainable.

4.3 Experimental Uncertainty

The experimental uncertainty associated with pool boiling heat transfer measurements, capillary wicking measurements and roughness factor measurements are presented in this section.

4.3.1 *Experimental Uncertainty during Pool Boiling*

The experimental uncertainties in the measured quantities were based on thermocouple accuracy, uncertainty in thermal conductivities, and the uncertainty in various physical dimensions. The propagation of these uncertainties, U, was evaluated for heat flux, q″, surface temperature, T_S, and heat transfer coefficient, HTC, based on the following equations.

$$\frac{U_{q''}}{q''} = \left[\left(\frac{U_{\Delta T}}{\Delta T}\right)^2 + \left(\frac{U_{k_{Cu}}}{k_{Cu}}\right)^2 + \left(\frac{U_{\Delta x}}{\Delta x}\right)^2\right]^{1/2} \tag{4.4}$$

$$\frac{U_{\Delta T}}{\Delta T} = \left[\left(\frac{U_{T_5}}{T_5}\right)^2 + \left(\frac{U_{T_{Sat}}}{T_{Sat}}\right)^2 + \left(\frac{U_{q''}}{q''}\right)^2 + \left(\frac{U_{R_{Cu}}}{R_{Cu}}\right)^2 + \left(\frac{U_{R_{So}}}{R_{So}}\right)^2 + \left(\frac{U_{R_{Su}}}{R_{Su}}\right)^2\right]^{1/2} \tag{4.5}$$

$$\left(\frac{U_{R_{Cu}}}{R_{Cu}}\right)^2 = \left[\left(\frac{U_{L_{Cu}}}{L_{Cu}}\right)^2 + \left(\frac{U_{k_{Cu}}}{k_{Cu}}\right)^2\right] \tag{4.6}$$

$$\left(\frac{U_{R_{So}}}{R_{So}}\right)^2 = \left[\left(\frac{U_{L_{So}}}{L_{So}}\right)^2 + \left(\frac{U_{k_{So}}}{k_{So}}\right)^2\right] \tag{4.7}$$

$$\left(\frac{U_{R_{Su}}}{R_{Su}}\right)^2 = \left[\left(\frac{U_{L_{Su}}}{L_{Su}}\right)^2 + \left(\frac{U_{k_{Su}}}{k_{Su}}\right)^2\right] \tag{4.8}$$

The uncertainty of the omega T-type thermocouple (TMQ-SS-020G-6) measurements was ±1 K. The uncertainties in the thermocouple locations and the solder thickness were approximated to be 250 μm and 20 μm, respectively. The thermal conductivity of copper at 373 K was estimated to be 395 ± 5 W/mK. Therefore, for the boiling setup utilized in this study, the maximum uncertainties in the heat flux, wall superheat, and heat transfer coefficient were calculated to be ± 5.95 W/cm^2, ± 1.75 K, and ± 3.58 kW/m^2-K, respectively.

4.3.2 *Experimental Uncertainty during Wicking*

Measurement accuracy associated with capillary wicking experiment is based on uncertainty associated with wicked volume flux. Hence, wicked volume flux uncertainty was estimated using Eq. 4.9, where D_C is the diameter of the capillary tube, dH is the change in liquid level height, and D_W is the diameter of wetted area. All measurements were conducted using high-speed imaging and the uncertainty of the measurement was based on pixel resolution (~2.79 μm per pixel) as well as the observed thickness and image distortion in the descending meniscus.

$$\frac{U_{\dot{V}_0''}}{\dot{V}_0''} = \left[\left(\frac{U_{D_C}}{D_C} \right)^2 + \left(\frac{U_{dH}}{dH} \right)^2 + \left(\frac{U_{D_W}}{D_W} \right)^2 \right]^{1/2} \tag{4.9}$$

4.3.3 *Experimental Uncertainty with Roughness Factor Estimation*

The uncertainty estimation for roughness factor is based on the accuracy associated with the number of nanostructures counted in a frame and the physical dimensions that were either measured from SEM images or reported directly from publications. Eqs 4.10 - 4.13 were used to calculate the uncertainties in roughness factor, using intentionally conservative values.

$$\frac{U_{r_A}}{r_A} = \left[\left(\frac{U_{D_A}}{D_A} \right)^2 + \left(\frac{U_{H_A}}{H_A} \right)^2 + \left(\frac{U_P}{P} \right)^2 \right]^{1/2} \tag{4.10}$$

$$\frac{U_{r_{TMV}}}{r_{TMV}} = \left[\left(\frac{U_N}{N} \right)^2 + \left(\frac{U_{D_N}}{D_N} \right)^2 + \left(\frac{U_{H_N}}{H_N} \right)^2 + \left(\frac{U_{A_{image}}}{A_{image}} \right)^2 \right]^{1/2} \tag{4.11}$$

$$\frac{U_{r_H}}{r_H} = \left[\left(\frac{U_{r_A}}{r_A} \right)^2 + \left(\frac{U_{r_{TMV}}}{r_{TMV}} \right)^2 + \left(\frac{U_{r_{agg}}}{r_{agg}} \right)^2 \right]^{1/2} \tag{4.12}$$

$$\frac{U_{r_{CN}}}{r_{CN}} = \left[\left(\frac{U_N}{N} \right)^2 + \left(\frac{U_b}{b} \right)^2 + \left(\frac{U_h}{h} \right)^2 + \left(\frac{U_{A_{image}}}{A_{image}} \right)^2 \right]^{1/2} \tag{4.13}$$

CHAPTER 5: SCALABLE NANOMANUFACTURING OF SURFACE COATINGS FOR BOILING APPLICATIONS

5.1 Introduction and Overview

The enhancement of phase-change heat transfer processes is of critical importance due to their impact on energy, the environment, and water resources, as well as their potential in high-power thermal management systems [1, 45, 46]. Recent studies have shown that micro/nano-structures can be used to substantially alter boiling [9], evaporation [47], freezing [48], and condensation [49] by influencing the nature and behavior of liquid, vapor, and solid interfaces. However, the fabrication methods used in these studies are not easily extended to practical applications, particularly over large-areas, complex geometries, and onto various surface materials. In this chapter, biological templates are used to demonstrate the scalable nanomanufacturing of high-surface-area coatings for enhanced boiling on various materials. Using self-assembly of the Tobacco mosaic virus, pool boiling critical heat flux and heat transfer coefficient have been increased by up to 200%. The solution-based room-temperature biotemplating process is simple and scalable; it requires no external power or special equipment. The coatings are robust with no physical degradation after 24 hours of nucleate boiling on gold, copper, aluminum, and stainless steel surfaces. Additionally, the process is compatible with in-situ depositions, allowing for the retrofitting of existing heat transfer equipment and a means to mitigate fouling via stripping and re-deposition, two issues critical to real-world implementation.

5.2 Biotemplated Nanofabrication

The *Tobacco mosaic virus* (TMV) based biotemplated nanofabrication technique has been incorporated to fabricate nanostructures on different metallic and non-metallic surfaces. This section presents a brief description on the TMV, its harvesting and replication, and biotemplating technique for nanostructured surfaces.

5.2.1 *The Tobacco mosaic virus (TMV) and its Genetic Modification*

The *Tobacco mosaic virus* (TMV) is the first virus ever discovered and completely harmless to humans. It is a well-studied biological structure, comprised of 2130 subunits of 17.5 kDa coat proteins arranged in a helical array around positive-sense single-stranded ribonucleic acid [50] (Figure 5.1a). It is a hollow cylindrical structure with 18 nm outer diameter, a 4 nm inner diameter, and a 300 nm length [50, 51] (Figure 5.1b). The TMV is stable up to 60 ºC over a wide pH range of 2 to 11, and compatible with several polar solvents and organic reactions [52].

In this work we used the TMV1cys, an engineered mutant of the wild-type virus. The TMV1cys contains a cysteine residue on the outer portion of each of its 2130 coat proteins. This modification is achieved through PCR-based site-directed mutagenesis, where a complementary DNA clone is produced from the wild-type viral RNA, and the specific cysteine codon is introduced in the third position of the coat protein open reading frame [53]. RNA transcripts are then used to infect the host plant for mass production of the virus. The TMV1cys is harvested 20 days after inoculation. The introduction of cysteine residues (amino acids with thiol groups) within the N-terminus of virus coat protein results in enhanced binding properties based on strong covalent

interactions [54]. This genetic modification allows for near vertical assembly and functionalized with various inorganic coatings, creating a highly textured three-dimensional scaffold for conformally coated inorganic nanostructures. Near vertical orientations are achieved due to the nature of the thiol binding sites introduced during genetic modification. As can be seen in Figure 5.1c,d, the cysteine residues are shielded from the protein surface by the protein C-terminus. Due to the helical arrangement of coat proteins, only the cysteine on the 3′ end is unexposed and available for surface attachment during self-assembly [55].

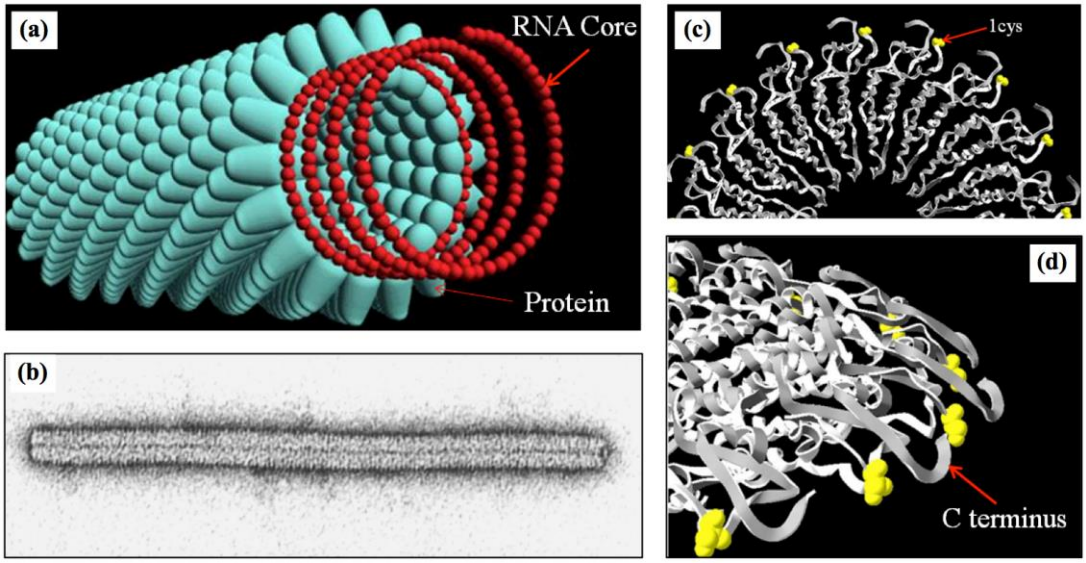

Figure 5.1: The *Tobacco mosaic virus* (TMV) and genetic modification. (a) Schematic representation of the TMV structure showing the RNA strand and coat proteins and (b) A TEM image of the wild-type virus. (c)-(d) Schematic representations of the cysteine residues introduced during genetic modification and the C-terminus shielding the cysteines. (a) Reprinted with permission from *The Encyclopedia Britannica* [56], Copyright 1996. (b) Reprinted with permission from *Elsevier* [51], Copyright 1999. (c-d) Reprinted witrh permission from *IOP* [55], Copyright 2008.

5.2.2 *Virus Harvesting and Replication*

Purified TMV solutions are prepared through the infection of the Tobacco plant (*Nicotiana tabacum cultivar Xanthi*). Seedlings are grown in the lab under repeating 12 hours of UV light followed by 12 hours of dark (Figure 5.2a-b). After 3-4 weeks, individual leaves are infected by spraying ~37 micron silicon carbide particles (Carborundum) onto the leaves and manually wiping previously purified virus solutions into the veins of the leaves with a cotton swab (Figure 5.2c). The abrasive SiC microparticles scratch the surface of the leaves and facilitate the infection process. The infected plants grow for another 2-3 weeks during which mosaic patterns appear on leaves. Leaves are then removed from the plants and stored in a freezer at -20 °C until the extraction process.

The extraction of the virus starts with blending of the infected tobacco leaves with buffer. After filtering the solution with cheese cloth (Figure 5.3a), chloroform is added at a ratio of 1:50. Then, the solution is centrifuged for 10 min at a fixed angle at 10000 rpm, and separates the solution from the bulk plant precipitations. An additional fixed angle centrifugation at 10000 rpm for 10 min is conducted with diluted TMV in sodium phosphate buffer (pH 7.0), Polyethylene glycol, and KCl, resulting in a pellet (Figure 5.3d), which is then diluted in 4 ml buffer.

A sugar solution is then prepared with 25 gm sucrose diluted in 100 mL phosphate buffer and stored them at -20 °C overnight. The virus is suspended at the top of sugar solution (Figure 5.3e) and centrifuged using a swinging bucket rotor at 22,500 rpm, 14 °C for 2 hours. After centrifuging, we collected a band of virus layer suspended inside the sugar layers (Figure 5.3f). Finally a two hour 30,000 rpm, 4 °C fixed angle

centrifuge step is performed, after which purified virus pellets precipitated at the side wall of the tube. The final purified TMV pellets are diluted with 4 ml sodium phosphate buffer and analyzed with a spectrophotometer to measure the concentration and purity of the virus solution.

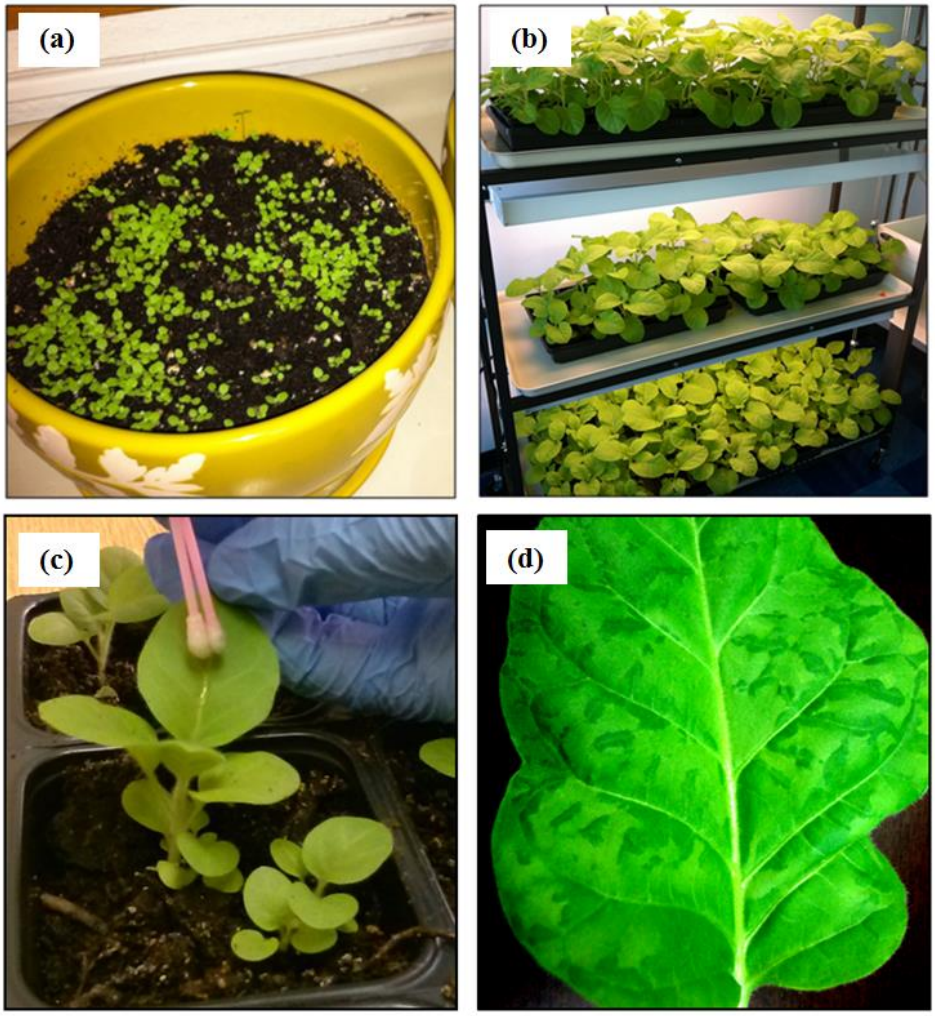

Figure 5.2. Replication of *Tobacco mosaic virus* (TMV). (a) Many seedlings initially grown in a single pot then (b) transplanted to individual trays where (c) they are manually infected. (d) Full grown infected leaf showing the mosaic pattern.

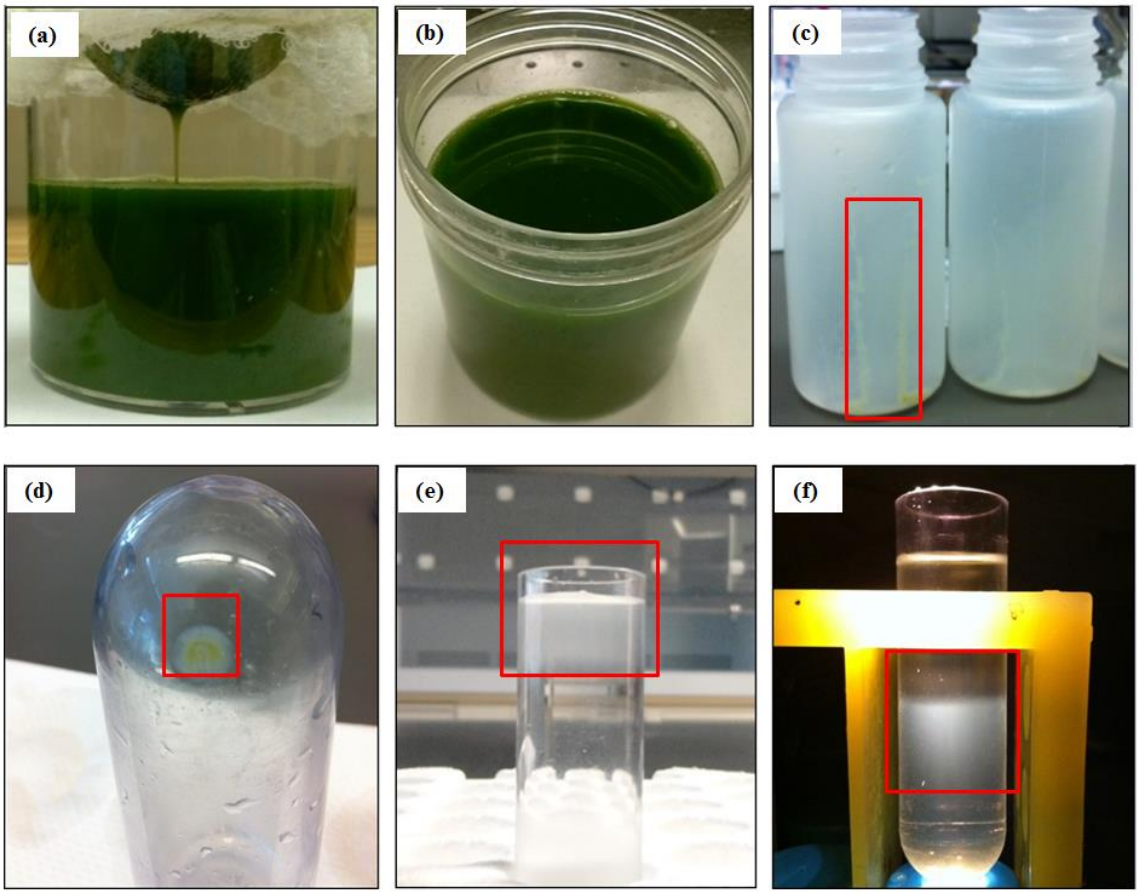

Figure 5.3: Extraction of *Tobacco mosaic virus* (TMV). (a)-(b) Preparation of blended leaf and extraction buffer solution for centrifugation. (c) Coarse separation of TMV after first centrifugation. (d) TMV pellet after second centrifugation. (e) Insertion of TMV solution into sugar solution. (f) Gradient layer formation of TMV after swinging angle centrifugation.

5.2.3 *Biotemplated Nanostructured Sample Preparation*

Figure 5.4 shows the agriculturally tractable process for replicating the TMV and the biotemplating process used in this work. Tobacco plants (*Nicotiana tabacum*) are grown in the lab for 3-4 weeks, and then infected with the TMV. The virus replicates

during the infection process for 2-3 more weeks, where the characteristic mosaic pattern can be seen on the infected leaf (Figure 5.4c). The leaves are then liquefied in a blender and the TMV is extracted using a series of chemical and centrifuging steps, where the final purified TMV is suspended in a phosphate buffer. Figure 5.4d shows the solution-based biotemplating process, where a metallic surface is first submerged in the virus solution for 24-48 hours and the TMV self-assembles in a near-vertical arrangement. The TMV are bound to the surface at one end and are repelled from each other due to their net negative outer surface charge. This orientation is preferential due to the fact that the thiol binding sites introduced during genetic modification are shielded from the surface of the virus due to the helical arrangement of coat proteins. The cysteine at the 3′ end, however, is fully exposed leaving a singular binding site available for surface attachment at one end [54]. After TMV assembly, the substrate is moved to a bath containing a palladium catalyst for 2-3 hours, and then an electroless nickel plating solution for 4-8 minutes. During these steps, palladium nanoclusters form on the surface and act as a catalyst during electroless nickel deposition. The electroless plating results in a uniform shell of nickel (~20-40 nm thick), fully encasing the TMV template (Figure 5.4e). This shell thickness was chosen to maximize the nanocoating porosity, while still resulting in nanostructures that were mechanically stable under pool boiling conditions, as well as ultrasonication during cleaning. Nanostructures with shell thickness notably less than 20 nm were easily removed during ultrasonication, and shell thickness notable thicker would unnecessarily reduce the coatings porosity.

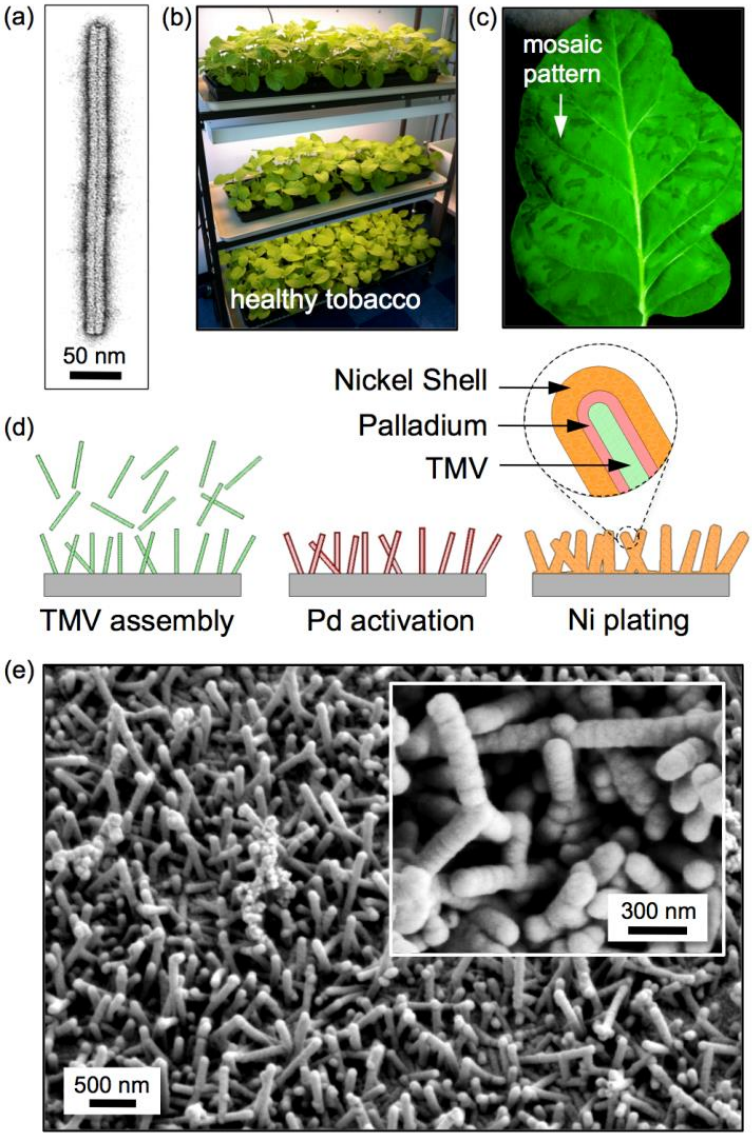

Figure 5.4: Scalable nanomanufacturing using self-assembled Tobacco mosaic virus (TMV). (a) TEM image of the wild-type TMV [51]. (b) Tobacco plants are grown in the lab and infected with the TMV, leading to (c) the characteristic mosaic pattern. (d) The three-step solution-based biotemplating process where the TMV assembles onto a metallic surface and is coated with palladium nanoclusters and then electrolessly plated to form a nickel shell. (e) SEM images of the surface-bound nickel nanostructured coating. (a) Reprinted with permission from *Elsevier*, Copyright 1999.

While the resulting nanostructure orientation is not perfectly vertical, the singular binding site at one end of the virus, and it's inherent surface charge, deters the TMV from laying flat or assembling into bundles. Because the surface is never dried during the procedure, liquid-vapor interfacial forces (which would make the TMV lay flat and/or bundle) do not play a role. The final electroless nickel deposition step provides rigidity to the surface-bound TMV, resulting in a highly porous and mechanically strong nanocoating. The virus acts solely as temporary scaffolding and plays no role in defining or maintaining the nanostructure thereafter.

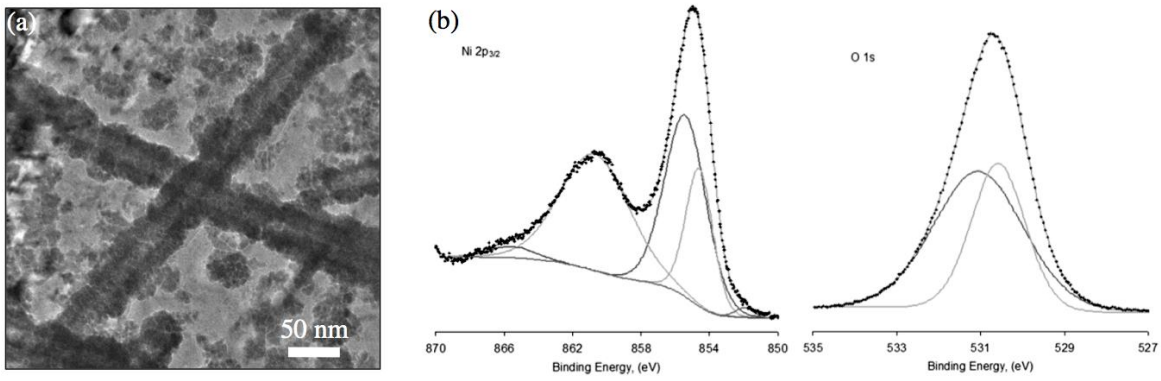

Figure 5.5: (a) TEM image of nickel coated TMV nanostructure and (b) XPS analysis results for the surface-bound nickel-coated TMV nanostructures [54] (b) Reprinted with permission from *ACS* [54], Copyright 2008.

Figure 5.5a shows a TEM image of the nickel-templated nanostructure, where the 18 nm diameter TMV can be seen inside of a nickel shell. The nanofabrication process used here was first reported by Royston *et al.* along with detailed XPS analysis of the resulting composition[54]. Figure 5.5b shows the high resolution Ni 2p3/2 and O 1s spectra of the TMV-templated nanostructures, as reported by Royston *et al.*[54]. The binding energy peaks indicate that the nickel shell is comprised primarily of nickel oxides

and hydroxides, with a small amount of crystalline nickel. They reported that ~59% of the nickel is in the form of NiO and ~38% is in the form of $Ni(OH)_2$.

5.2.4 *Scalability of TMV Biotemplating*

The biotemplated solution-based room-temperature process is compatible with various metallic surfaces, requires no power or equipment, and is scalable to large areas and complex geometries. This nanofabrication process as described in the earlier section has been carried out on various substrates including those most relevant for heat transfer equipment, namely copper, aluminum, and stainless steel. Figure 5.6 shows optical images of 1cm x 1cm samples before and after coating and SEM images of the structures at various magnifications. The copper, aluminum, and stainless steel surfaces were cut from larger sheets of metal with a thickness between 0.5 -1 mm. The surfaces were sanded for a few minutes using 200 grit sandpaper to remove contaminates and oxides, and left out in ambient conditions for 24 hours prior to deposition. The gold-coated silicon samples (Figure 5.6a) used a 0.1 mg/mL concentration of TMV for ~24 hours, while the other surfaces required 0.2 mg/mL for ~36-48 hours (Figure 5.6b-d). The need for increased concentration and assembly time is attributed to the reactive nature of the non-gold substrates. The buffer solution reacts with the surfaces, initially inhibiting the assembly of the TMV. This is most evident on copper where the TMV has assembled onto an underlying oxide structure produced during assembly. As such, it has the potential to enhance heat transfer in several large-scale applications, where traditional approaches are not practical or feasible.

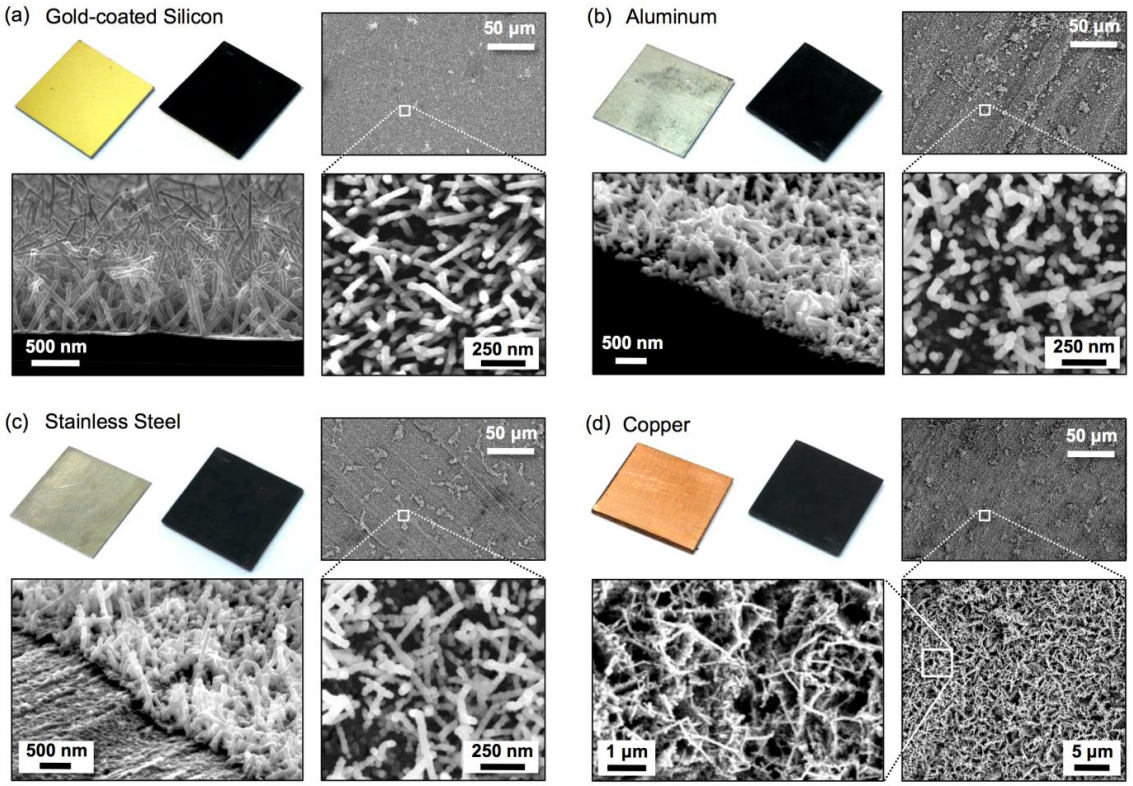

Figure 5.6: Biotemplated superhydrophilic nanostructured nickel coatings on various metallic surfaces. Fabrication results for virus-structured coatings on (a) gold, (b) aluminum, (c) stainless steel, (d) and copper showing 1cm x 1cm samples before and after deposition, as well as SEM images at various magnifications. Side-view and orthogonal SEM images were obtained by (a) cleaving a silicon sample or (b,c) masking and etching the nanostructures using photolithography.

5.3 Pool Boiling Characterization

Biotemplated nickel nanostructures, as described in section 5.2, were fabricated on several different surfaces and characterized during pool boiling. The coatings were characterized to measure heat transfer enhancement during pool boiling using a custom-built test set-up as discussed in section 4.1. Briefly, the 1 cm × 1cm

biotemplated nanostructured samples were soldered directly to a heater and submerged in a bath of saturated water open to atmospheric pressure, while heat flux, surface temperature, and water temperature were measured.

5.3.1 *Pool Boiling Results*

Heat flux as a function of wall superheat (surface to water temperature difference) is plotted in Figure 5.7a. The closed symbols represent bare surfaces, the open symbols represent those coated with nickel nanostructures, and the horizontal arrows show CHF. As a surface is heated to its CHF value, the rate at which vapor is produced at the surface cannot be balanced by replenishing liquid. A film of vapor blankets the surface, inhibiting heat transfer between the wall and liquid, leading to complete dry-out and an extreme increase in temperature. It can be seen that the CHF values for the bare and flat surfaces range from roughly 60-100 W/cm^2, which is consistent with the literature and Kandlikar's CHF model [8, 9, 30]. The superheat temperature at which CHF occurs varies notably between the bare surfaces due to variations in topography and nucleation sites, where the polished silicon substrates require higher temperatures. The nanostructured surfaces, however, all behave similar to one another. CHF values of up to 210 ± 6 W/cm^2 have been achieved, with an average value of 202 W/cm^2 and a standard deviation comparable to the experimental uncertainty. This performance is repeatable for all four substrate materials over a total of ten separate experiments. Figure 5.7b shows the heat transfer coefficient, HTC (heat flux divided by wall superheat), as a function of heat flux, showing similar enhancements. CHF has been nearly doubled for bare copper surfaces and nearly tripled for flat nickel surfaces. The TMV nanocoatings tested here exhibit extreme superhydrophilicity, where a droplet placed on the surface is immediately

drawn into the structures through capillary action resulting in no measureable contact angle. The enhancements in CHF are attributed to this ability, where the coatings delay global dry-out of the surface by efficiently wicking liquid through the nanostructures to locally dry regions. This replenishing liquid allows for higher rates of stable vapor production and therefore higher heat fluxes [36, 57].

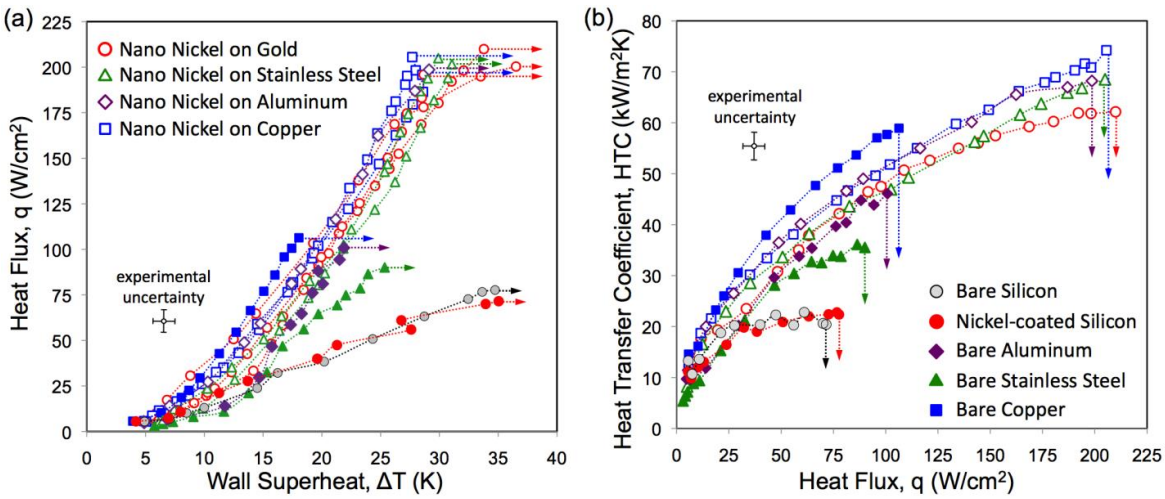

Figure 5.7: Pool boiling results for nanostructures on different substrate materials (a) CHF as a function of wall superheat, and (b) HTC as a function of heat flux.

5.3.2 *In-situ Deposition and Fouling Mitigation*

The coatings were repeatedly tested to evaluate their integrity and reliability during nucleate boiling. Figure 5.8a shows the results of repeated boiling tests for two nickel nanostructures on gold samples. The samples were continuously boiled for 5-10 hours up to CHF, and then left out in ambient air for 48 hours before being re-soldered and tested again. A shift in the boiling curve and a drop in CHF of about five percent is observed. This is attributed to fouling by particulates and organic materials from the ambient environment, the soldering steps, handling of surfaces between tests, and boiling

itself. During nanostructured boiling any contaminants present in the liquid will be drawn to the surface with the potential to clog or fill the nanostructures. To allow for instrumentation the boiling chamber used here was open to the environment and exposed to silicone sealants, thermal grease, plastic walls, and soldering flux, all of which could lead to premature fouling. To remove contaminants, the surfaces were cleaned using solvents in an ultrasonic bath followed by air plasma cleaning for one minute. As can be seen in Figure 5.8a, the performance improved with cleaning and returned back to the original boiling curve within the experimental uncertainty after repeated cycling. Figure 5.8c shows SEM images of one sample imaged in between various tests for up to 24 hours of boiling, including three CHF events. The nickel nanostructures are intact with no noticeable change in morphology. These images, combined with the experimental results, show that reversible fouling leads to the minimal degradation observed, and not the destruction of nanostructures.

The procedures and test set-up used in this work accelerated fouling due to the need for instrumentation and interchangeable samples, leading to measureable (but minimal) degradation. Fouling, however, remains an important hurdle for real-world implementation where continuous operation over months and even years is required. While all nanostructured coatings are inherently vulnerable to fouling, the room-temperature solution-based biotemplating process provides a means to mitigate its impact by stripping and re-coating surfaces using *in-situ* depositions. After a nanostructured coating has degraded substantially, it can be easily removed using a dilute acidic solution and then a new coating can be re-deposited. This provides the ability to retrofit exiting systems comprised of large areas and complex geometries (inside heat exchangers,

boilers, and HVAC equipment) by simply passing the solutions through them. It also provides a means to periodically rejuvenate the coatings after they degrade. This unique capability will allow for low-cost and large-scale implementation.

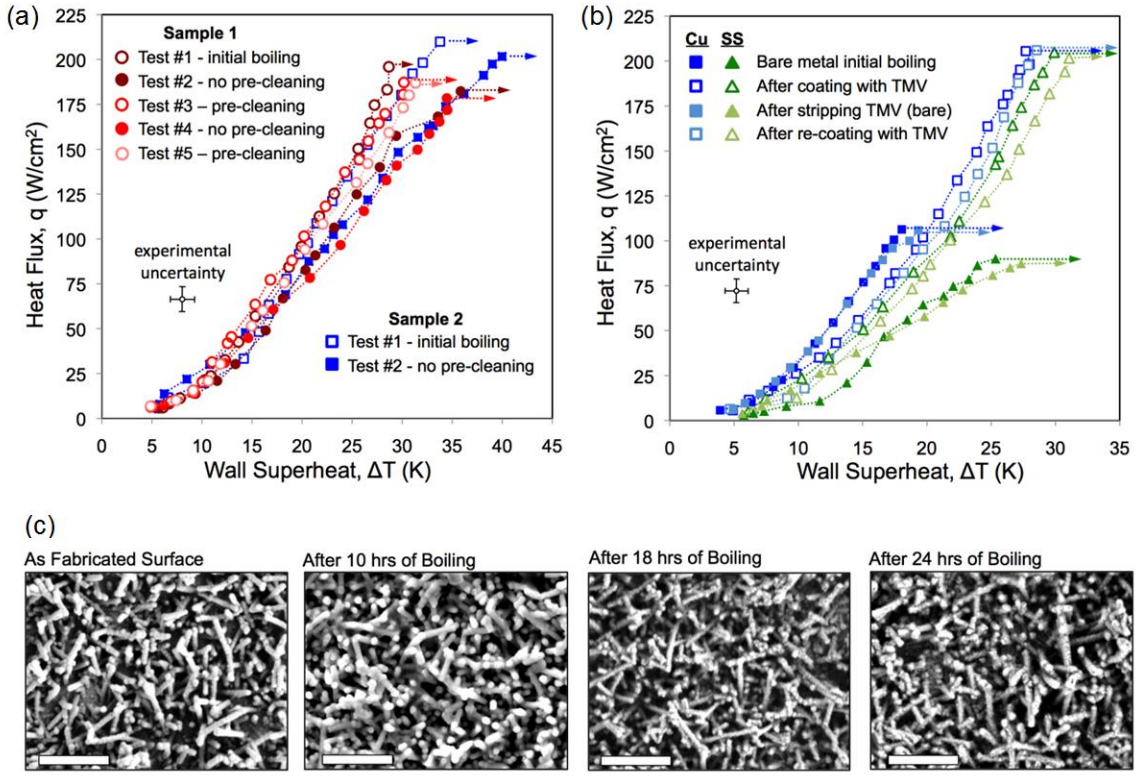

Figure 5.8: (a) Pool boiling curves showing repeatable performance and the effects of reversible fouling and pre-cleaning. (b) Results for copper and stainless steel samples after stripping and re-deposition of TMV nanocoatings, showing repeatable performance and a means to retrofit existing equipment as well as mitigate the effects of fouling. (c) SEM images showing that the TMV nanostructures remain intact with no mechanical failure after 24 hours of sustained nucleate boiling (scale bars are 1 μm).

.

Figure 5.8b demonstrates the boiling performance of copper and stainless steel samples after repeated stripping and re-deposition, where the coatings are stripped by immersion in a 2 M HCl solution. Boiling performance is characterized after each stripping and each deposition. The sequential boiling curves show repeatable performance in both the bare and nanostructured states. These tests demonstrate the efficacy of the removal and re-deposition of TMV-structured coatings using *in situ* solution-based techniques.

5.3.3 *Surface Wettability and Comparison with CHF Predictions*

Static, advancing, and receding contact angle measurements were performed using a 2mm diameter distilled water droplet deposited onto the surfaces from a microsyringe pump. Videos were captured with a Phantom V210 high-speed camera at 800 pixel × 800 pixel resolutions. The images were then analyzed using ImageJ software. The flat Ni, bare SS, bare Al, and bare Cu samples have intrinsic contact angles of 80°, 75°, 68°, and 60°. The addition of TMV nanostructures reduced the static contact angles of all the surfaces to ~ 0^0. Receding contact angle measurements were used to validate the experimental apparatus and CHF values using Kandlikar's CHF model [30]. Figure 5.9 shows good agreement between the measured CHF values for flat surfaces as compared to the model, with the superhydrophilic surfaces exceeding the predictions due to the capillary wicking effect, as seen in the literature.

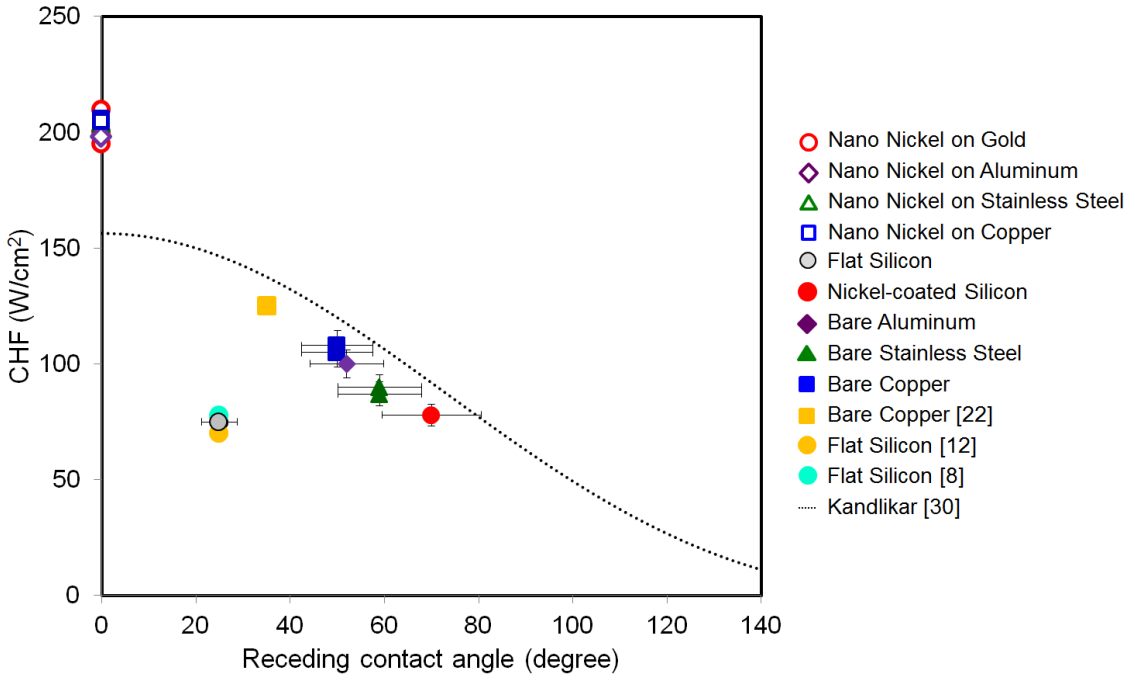

Figure 5.9. Comparison with CHF Predictions. Experimental pool boiling results showing good agreement for non-structured surfaces as compared to other work [8, 12, 26] and Kandlikar's CHF model [30].

5.4 Conclusions

A biotemplated nanofabrication technique to fabricated nanostructures has been reported in this chapter. Using the self-assembly and metalization of the *Tobacco mosaic virus*, superhydrophilic coatings were fabricated using an inexpensive solution-based process on several different metallic and non-metallic surfaces. Pool boiling heat transfer performance were characterized for the structures and compared with bare surfaces. Nearly 200% enhancement in both CHF and HTC has been demonstrated for these structured surfaces as compared to flat surfaces.

1. This work shows for the first time, the scalable manufacturing of nanostructured coatings for enhanced boiling on a variety of surfaces relevant to thermal and fluidic applications.

2. Superhydrophilic coatings were fabricated on copper, aluminum, stainless steel, and gold coated silicon surfaces.

3. Although, the pool boiling CHF and HTC have been shown to vary for all different bare surfaces, it has been demonstrated in this chapter that the heat transfer for this biotemplated nanostructures are independent of substrate materials.

4. These coating have been demonstrated to be reliable and robust for over 24 hours of sustained nucleate boiling.

5. Additionally, this simple solution-based process is demonstrated to be compatible with *in situ* depositions, by which existing systems can be retrofitted with nanocoatings and the effects of fouling can be mitigated by stripping and re-coating.

Publications:

1. M.M. Rahman, E. Ölçeroğlu, and M. McCarthy, "Scalable Nanomanufacturing of Virus-templated Coatings for Enhanced Boiling", *Advanced Materials Interfaces*, vol. 1, no. 2, 1300107, 2014.
2. E. Ölçeroğlu, C.Y. Hsieh, M.M. Rahman, K.K.S Lau, and M. McCarthy, "Full-Field Dynamic Characterization of Superhydrophobic Condensation on Biotemplated Nanostructured Surfaces", *Langmuir*, 30 (25), pp 7556–7566, 2014.

CHAPTER 6: WICKABILITY AND CHF ON STRUCTURED SUPERHYDROPHILIC SURFACES

6.1 Introduction and Overview

The enhancement of boiling heat transfer has the potential to impact a variety of industries, the consumption of energy and water resources, as well as the development of high-heat-flux thermal management applications. Accordingly, numerous researchers have developed novel fabrication strategies to create superhydrophilic coatings with enhanced wetting properties. These coatings have led to increases in boiling efficiency as well as critical heat flux (CHF), the maximum stable heat transfer rate achievable during boiling. While a variety of models and experiments have been reported, the mechanisms triggering CHF and the role of surface structures on its enhancement are still a matter of debate. In this chapter, biological templates have been used to demonstrate that wickability is the single key factor in dictating CHF on structured superhydrophilic surfaces. The flexibility and simplicity of biotemplating using the Tobacco mosaic virus has been leveraged to create a range of surfaces with varying scales, morphologies, and roughness factors. Their wickabilities have been quantified via the wicked volume flux (a phenomenological parameter analogous to contact angle), and its role on CHF enhancement has been clearly demonstrated using data from over three dozen individual surfaces. These results are repeatable and independent of the substrate material; degradation due to fouling; structure material, morphology, and intrinsic contact angle; as well as structure scale (including micro, nano, hierarchical designs), and heat transfer fluids. Using these results, an experimentally validated correlation for CHF has been reported based on the dimensionless wickability. Additionally, the rigidity of virus-

structured surfaces have been optimized based on structure shell thickness and demonstrated to achieve a CHF of 257 W/cm^2 for water, representing the highest reported value to date for a superhydrophilic coating. While the role of wickability on CHF has often been cited anecdotally, this chapter provides a quantitative and definitive measure of the phenomena. It provides insight into the nature of CHF, as well as a framework to design and optimize coatings for further enhancement.

6.2 CHF Correlation and Surface Wickability

The exact mechanisms triggering critical heat flux (CHF) have been the focus of numerous investigations and arguments for over five decades due to the complex, highly dynamic, and difficult to observe nature of the liquid-vapor interfaces and three phase contact line during nucleate pool boiling. Table 6.1 lists a small number of existing models and correlations including the seminal work by Kutateladze [18], Zuber [23], and Lienhard and Dhir [58] considering hydrodynamic instabilities. Borishanskii's model [59] includes the effect of viscosity in is based on co-axial two-phase flow stability. Haramura and Katto's macrolayer dry-out model [25], and the macrolayer lift-off model of Guan *et al.* [60] are based on the destruction of a liquid macrolayer underneath large mushroom bubbles feed by small vapor stems. The table includes work considering the effects of contact angle from Liao *et al.* [61], as well as the often-cited model by Kandlikar [30] based on vapor momentum flux and the associated model by Chu *et al.* [8] augmented to include roughness factor. The models are presented in terms of the nondimensionl CHF, K, as well the value predicted for K for water at atmospheric conditions, showing values of $K \sim 0.12\text{-}0.18$. This by no means an exhaustive list, but provides a general outline.

Table 6.1: Summary of selected pool boiling CHF models

Author	**Modeling Approach**	$\frac{q''_{CHF}}{\rho_v^{1/2} h_{lv}\left[\sigma(\rho_l-\rho_v)g\right]^{1/4}} = K$	**K 1 atm. Pr. Sat. water**
Kutateladze [18]	Dimensional analysis, destruction of stability of two phase flow near the heater surface	0.16	0.16
Zuber [23]	Array of large vapor columns become Helmholtz unstable	0.131	0.131
Lienhard and Dhir [58]	Helmholtz unstable wavelength is equal to Taylor wavelength	0.149	0.149
Borishanskii [59]	Instability in two phase boundary where liquid flows coaxially in countercurrent manner	$0.13 + 4\left[\rho_l\sigma^{3/2}/\left\{\mu^2 g^{1/2}\left(\rho_l-\rho_v\right)^{1/2}\right\}\right]^{-0.4}$	0.142
Haramura and Katto [25]	Small vapor jets form in the macrolayer under the bubble, and Kelvin-Rayleigh instability results in lateral coalescence of vapor stems.	$0.122\left[1+\rho_v/\rho_l\right]^{1/4}\left[1-0.0584\left(\rho_v/\rho_l\right)^{0.2}\right]^{5/16} \times\left[\rho_v/\rho_l\right]^{1/8}\left[\left(\rho_v/\rho_l+1\right)/\left(11\rho_v/16\rho_l+1\right)^{3/5}\right]^{5/16}$	0.048
Kandlikar [30]	Force balance parallel to the heater surface at the liquid-vapor interface of a bubble	$\left[\frac{1+\cos\beta}{16}\right]\left[\frac{2}{\pi}+\frac{\pi}{4}(1+\cos\beta)\cos\phi\right]^{1/2}$	0.186
Liao et al. [61]	Nonlinear curve fitting	$0.131\left[1+\rho_v/\rho_l\right]^{1/4}\left[1+(0.0056)(55-\theta)\right]$	0.171
Guan et al. [60]	Liquid macrolayer lift-off mechanism	$0.241\left[1+\rho_v/\rho_l\right]^{1/2}\left[\rho_v/\rho_l\right]^{1/10}$	0.115
Chu et al. [8]	Force balance model modified by longer effective contact line length based on amplified roughness	$\left[\frac{1+\cos\beta}{16}\right]\left[\frac{2(1+\alpha)}{\pi(1+\cos\beta)}+\frac{\pi}{4}(1+\cos\beta)\cos\phi\right]^{1/2}$	--

As CHF is approached, the high rate of vapor generation drastically impedes the ability to visualize flow on and near the heated surface. This has been a significant hurdle in understanding the mechanism of CHF, and a likely reason as to why no singularly accepted model exists to predict it. Kutateladze was the first to proposed that

the hydrodynamic stability was the key to triggering CHF [18, 19], and suggested the use of a nondimensional grouping for CHF of

$$K = \frac{q''_{CHF}}{\rho_v^{1/2} h_{fg} [\sigma g (\rho_l - \rho_v)]^{1/4}} \tag{6.1}$$

where q''_{CHF} is the CHF value, and h_{fg}, σ, g, ρ_v, and ρ_l are the latent heat, surface tension, gravitational acceleration, and vapor and liquid densities, respectively.

Using hydrodynamic analysis to determine the critical vapor velocity at CHF, Zuber suggested a value of K = 0.131 based on the Helmholtz instability of vapor columns [23]. Lienhard and Dhir claimed that the critical wavelength of instability should be given by the most dangerous Taylor wavelength [58], resulting in K = 0.149. Kutateladze, however, found a value of K = 0.16 from the fitting of experimental data [18, 19]. In the following decades, numerous more models have been developed, using the nondimensional CHF parameter given by Eq. 1. Most notably, these include the macrolayer dryout model developed by Haramura and Katto [25], as well as the associated macrolayer lift-off model developed by Guan *et al.* [60], which consider vapor stems feeding large mushroom bubbles with a liquid macrolayer underneath (as opposed to the vapor columns suggested by Zuber). These approaches have gained attention in recent years due to their consistency with visual observations and increased accuracy at a wider range of operating conditions [62, 63]. For water at atmospheric conditions, the macrolayer dry-out and lift-off models predict values of K = 0.13 and K = 0.115, respectively [25, 60].

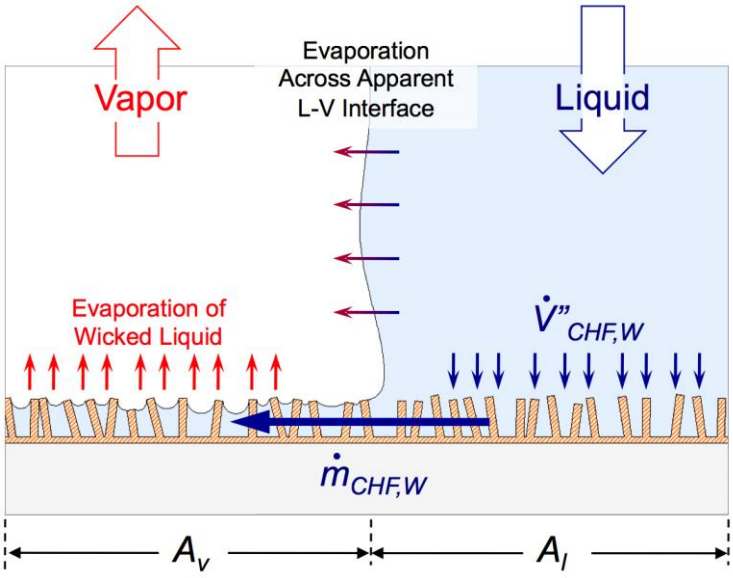

Figure 6.1: Schematic representation of the role of wickability in enhancing the critical heat flux. The wicked liquid is drawn into the nanostructures in the wetted areas, transported underneath the apparent liquid−vapor interface, and evaporated.

None of these approaches, however, take into account the effects of surface structures, wettability, or wickability, and greatly under predict CHF for superhydrophilic structured surfaces. While Kandlikar's model [30] incorporates the effects of contact angle, experimental results of CHF consistently exceed its predictions for contact angles approaching zero. This suggests another mechanism of enhancement is at play in addition to wettability. Chu et al. showed substantial increases in CHF for structured surfaces and presented a model based on Kandlikar's vapor momentum flux incorporating the roughness factor, *r*, and suggested the increase in the contact line length delays CHF [8]. The above discussion of CHF models is by no means an exhaustive review. For a more detailed treatment of the proposed mechanisms triggering CHF, and the various predictive models (including the impact of wettability and structures) the authors point to

the work of Bergles [17], Carey [22][41], Kandlikar [30], Lu *et al.* [64], Kim [6], and Guan *et al.*[60].

The effect of wickability on CHF can be analyzed through a simple examination of the apparent liquid-vapor-solid contact line on a heated surface. Figure 6.1 illustrates this, where some fraction of the surface is covered with liquid and another with vapor (e.i. a vapor column, bubble, or stem). While some portion of the liquid is evaporated across the apparent liquid-vapor interface, additional liquid is transported underneath the apparent contact line and evaporated across the complex liquid-vapor interface supported by the surface structures. The increase in CHF for a wicking surface (as compared to the corresponding non-wicking surface) can therefore be related to the latent heat associated with the wicked liquid flow rate, and given by

$$\Delta q''_{CHF} = q''_{CHF,W} - q''_{CHF,NW} = \frac{\dot{m}_{CHF,W} h_{fg}}{A_t} = \dot{V}''_{CHF,W} \rho_l h_{fg} \left(\frac{A_l}{A_t} \right) \tag{6.2}$$

where the subscripts W and NW indicate wicking and non-wicking, $\dot{m}_{CHF,W}$ is the liquid mass flow wicked under the apparent contact line at CHF, $\dot{V}''_{CHF,W}$ is the volumetric flux of liquid wicked into the surface at CHF, and A_t is the total heated surface area. Nondimensionalizing Eq. 6.2 in the form of Eq. 6.1 yields

$$K_W - K_{NW} = \frac{A_l}{A_t} \left(\frac{\dot{V}''_{CHF,W} \rho_l}{\rho_v^{1/2} [\sigma g (\rho_l - \rho_v)]^{1/4}} \right) \tag{6.3}$$

where the difference in K for wicking and non-wicking surfaces is proportional to the wetted area fraction as well as the wicked volume flux at CHF. Wetted area fraction has been observed to monotonically decline with increasing heat flux and drastically decrease as CHF is reached [65-68]. The minimum stable wetted area fraction at CHF has been

measured to be anywhere from 50% to 90%, including recent work by Jung *et al.* using a novel infrared thermometry technique to measure the local wetting state and heat flux during the transition through CHF for FC-72 [66].

6.3 Wickability Characterization

Eq. 6.3 suggests that surfaces capable of wicking liquid at high rates will delay the unstable drop in wetted fraction associated with CHF. While measuring the wicked volume flux across a surface during an actual CHF event is extremely difficult, Ahn *et al.* reported a novel method of characterizing the rate of liquid flow drawn into a surface due to capillarity [57]. Using a modified version of this approach, the maximum wicked volume flux of each of the surfaces has been measured in this chapter. This section presents the wickability characterization for both water and highly wetting fluid FC 72.

6.3.1 *Wickability of Water*

Figure 6.2a shows the experimental technique used to measure wickability (wicked volume flux, $\dot{V}_0''$) for structured surfaces. This is done using high-speed imaging and motion tracking of the volume of water being drawn from a capillary tube and into surface structures. Some representative high speed images of capillary wicking is shown in Fig. 6.2b. A PFA tube of 500 μm inner diameter is filled with ~1.5 μL of DI water using a micro-syringe pump. The tube is mounted vertically with a pendant droplet forming at the lower end. A structured sample to be tested is slowly raised up from below the tube with a translational stage with micron-level precision. When the pendant droplet touches the sample the liquid is wicked into the surface structures and propagates radially outward from the point of contact. After the very initial contact, two phenomena occur

sequentially as shown in Figure 6.3a for the structured surfaces considered here. First, the pendant droplet deforms to wet the surface and spreads out to a constant wetted area, A_W, as shown in stage 1 to 2 in Fig. 6.3a. After this initial spreading phase ends, the liquid is then wicked through the surface structures and the liquid flow rate is measured by monitoring the change in height of the liquid meniscus within the tube, as shown in stage 2 to stage 3 in Fig. 6.3a. As seen, this technique successfully segregates these two phases to allow for the direct measurement of wicking after all spreading has ceased. This is critical to the accuracy of the method.

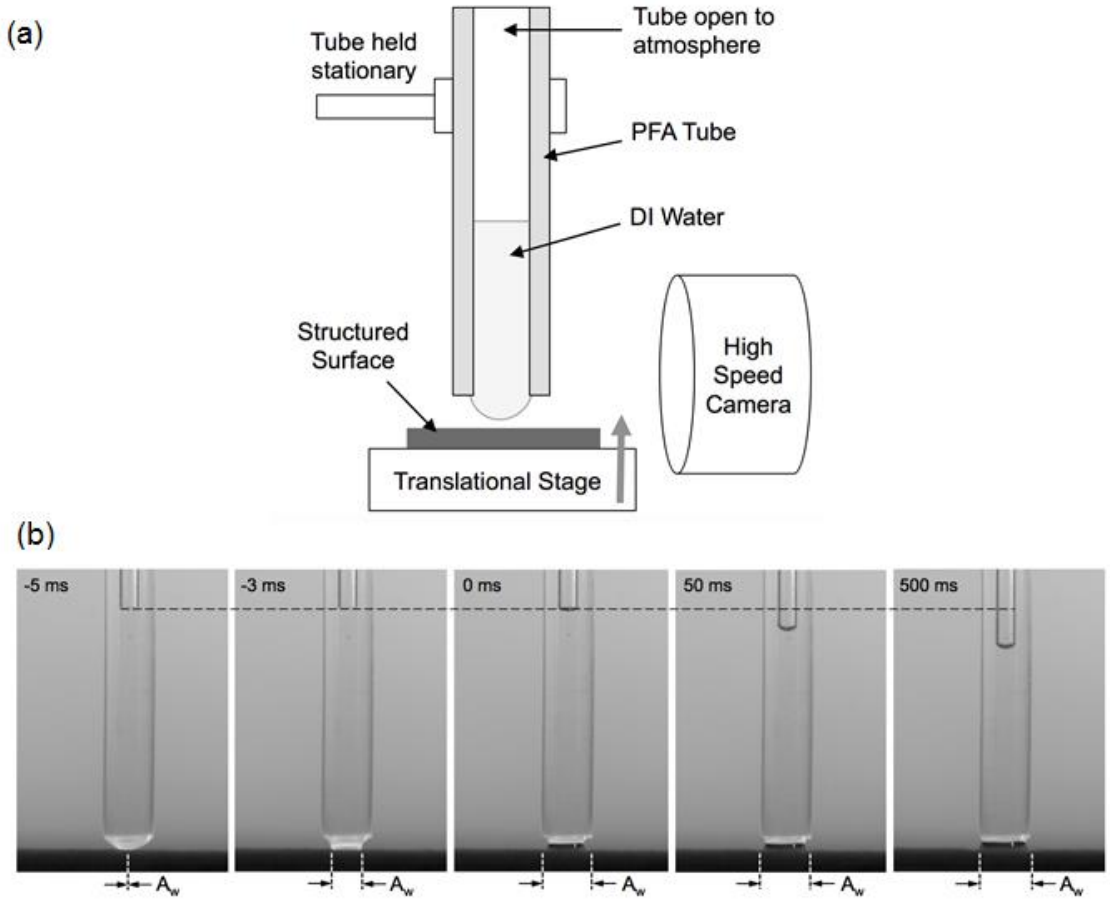

Figure 6.2: The characterization of surface wickability. Schematic of capillary wicking experimental setup to measure initial wicked volume flux for structured surfaces using water.

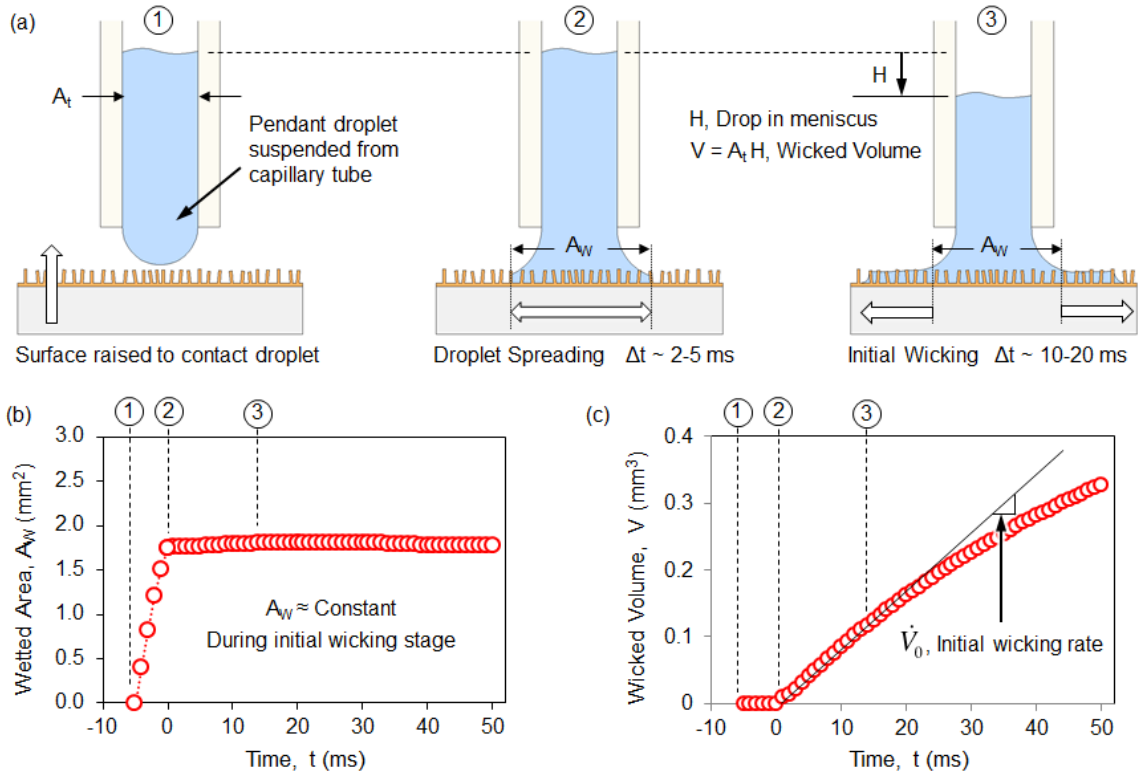

Figure 6.3: The characterization of surface wickability. (a) Schematic of the wicking measurement technique, where a structured surface is raised to touch a pendant droplet attached to a capillary tube. The droplet first quickly deforms to a constant wetted area, AW, and then liquid is wicked through the surface structures. (b) The apparent wetted area as a function of time, where the droplet spreading phase (-5 ms < t < 0) occurs entirely before the liquid wicking phase (t > 0). (c) Wicked volume as a function of time, calculated by tracking the high-speed images of the displaced meniscus in the tube.

Figure 6.3b shows the measured wetted area, A_W, as a function of time. As can be seen, the wetted are is initially increasing until it reaches the equilibrium wetted area due to spreading. Figure 6.3c shows results from image tracking of the meniscus height, where the dynamic wicked volume is calculated as $V = A_T h$, where A_T is the cross-sectional area of the tube's inner passageway and h is the distance the meniscus has

dropped. As can been seen, spreading occurs prior to wicking ($t < 0$) extremely fast (~5 ms), and the resulting maximum volumetric flow rate and wetted area can be determined at $t = 0$. The uncertainty in wetted radius and meniscus height is estimated using image pixel size to be ±0.014 mm, resulting in an uncertainty in wicked volume flux (based on propagation of measurement error) of ±0.16 mm/s.

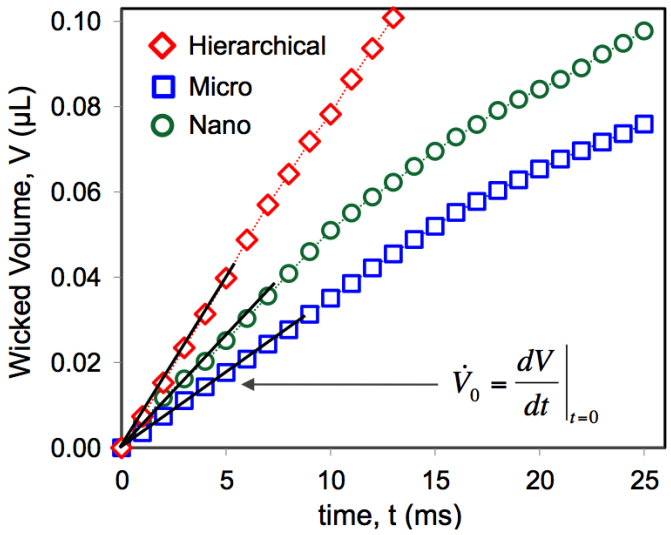

Figure 6.4. Experimental measurement of wickability. (a) High-speed imaging of water being drawn from a 500 μm inner diameter capillary tube after a structured surface is raised into contact with a pendant droplet resulting in wicking across the surface. (b) Experimental results of wicked volume as a function of time (for three select surfaces), calculated by tracking the displacement of the water level in the tube, showing the initial (maximum) volumetric flow rate.

Figure 6.4 shows wicked volume with respect to time for three representative silicon surfaces (nano, micro and hierarchical) considered here. The maximum wicked volume flux is calculated as

$$\dot{V}_0''=\frac{1}{A_W}\left(dV/dt\right)_{t=0} \tag{6.4}$$

where $(dV/dt)_{t=0}$ is the initial (maximum) volume flow rate, and A_W is apparent wetted area of the surface. As such, $\dot{V}_0''$ is a measurable phenomenological parameter that characterizes the inherent wickability of a structured surface. This is analogous to characterizing wettability using contact angle. Using this approach, the wicked volume flux captures the effects of micro/nano-structure size, shape, morphology, permeability, intrinsic contact angle, and porosity all into one phenomenological parameter. This technique yields a direct measurement of the actual mass flow rate, as opposed to the speed of a wicking front, and therefore does not rely on assumptions regarding the permeability or geometry of the structures. This fact allows for a direct (and accurate) correlation with CHF, via the additional latent heat associated with the wicked liquid mass flow.

6.3.2 *Wickability of FC 72*

Since capillary wicking provides a means to estimate the rewetting capability of active nucleation sites during boiling as presented in section 6.2, surface wickability has been quantified via capillary wicked volume flux in section 6.3.1 for water as the working fluid. Since, FC 72 is a highly wetting fluid with low surface tension as compared to water, the quantification of capillary wicking volume flux also becomes complicated. The high liquid density of FC 72 requires extra vacuum pressure to keep the fluid inside the capillary tube up to the desired height. In addition, the volatile feature of FC 72 makes it harder to create a liquid pendent droplet at one end of the capillary tube

as opposed to water. Hence, this section presents a method to estimate the wicked volume flux using a capillary tube incorporating a micro syringe system.

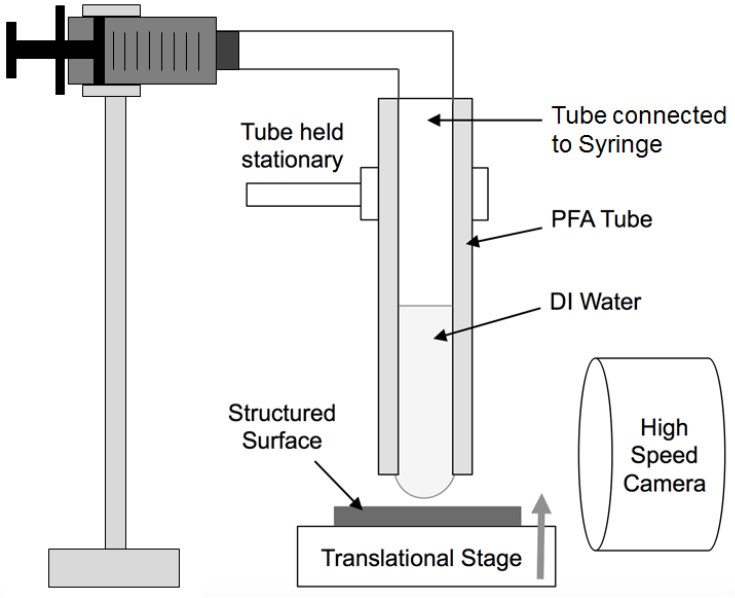

Figure 6.5: Schematic of capillary wicking experimental setup to measure initial wicked volume flux for structured surfaces using low surface tension fluids.

Briefly, for water wicking described in section 6.3.1, the tube end opposite to the liquid pendant side was open to the atmosphere. Here, a new syringe wicking method, as shown in Fig.6.5, is introduced to measure the capillary wicked volume flux for fluids other than water. A syringe with micro-syringe pump is attached to the capillary tube to insert the fluid inside the tube up to the desired height during infusion. Then using the pump withdrawal, a liquid pendant is formed at the end of the capillary tube. The surface is then raised using the micro-meter translational stage until it touches the pendant droplet.

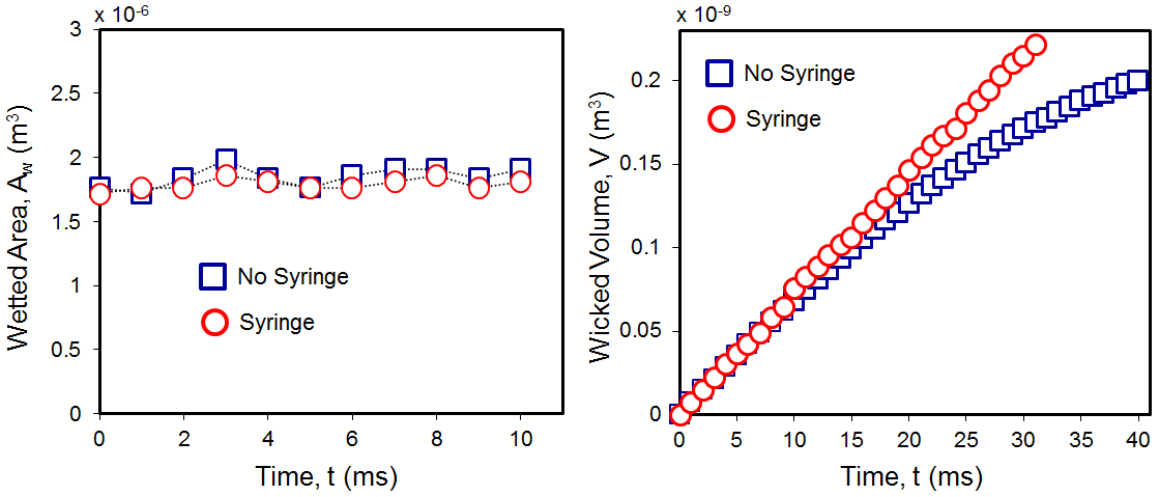

Figure 6.6: Comparison of capillary wicking results using water for both with and without syringe (a) wetted area as a function of time, and (b) wicked volume as a function of time demonstrating that the added syringe backpressure has negligible effect on the initial wicked volume flux measurements.

Now, since liquid back pressure is added due to attaching the syringe at the open side of the tube for FC 72, it is required to verify the reproducibility of the new wicking technique with the previous wicking method as described in section 6.2. Figure 6.6 shows the capillary wicking results using syringe with water and compared with the wicking results without syringe (prior technique). From the wetted area as a function of time plot (Fig. 6.6a), it can be seen that the average wetted area for both with and without the syringe methods are similar. While some variations in wicked volumetric flow rates are observed in wicked volume as a function of time plot (Fig. 6.6b), the initial wicked volumetric flow rate is also similar for both cases. This demonstrates that the syringe back pressure to hold the liquid inside the capillary tube

and form liquid pendant at the end of the tube in new capillary wicking experimental technique does not affect the initial wicked volume flux results.

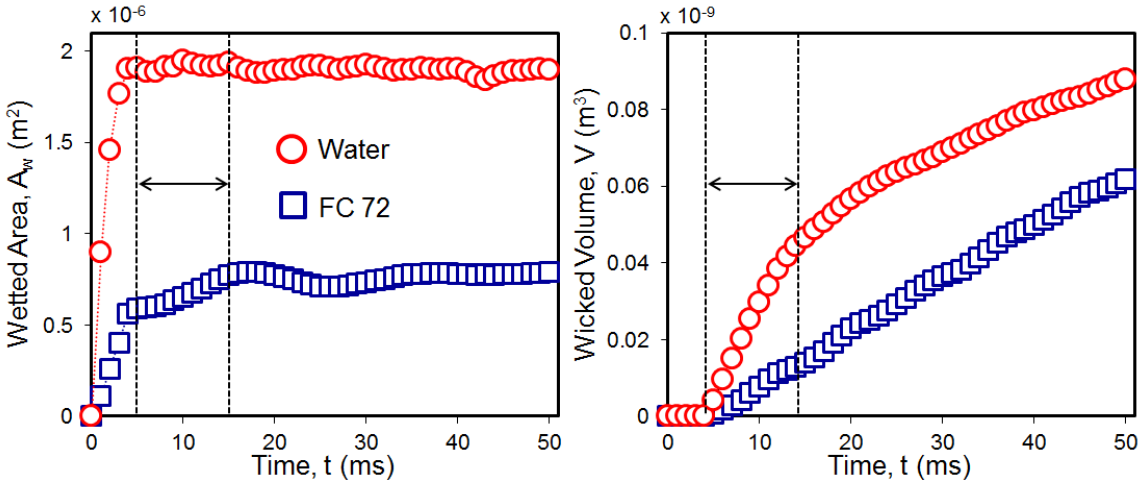

Figure 6.7: Capillary wicking results of FC 72 compared with water using syringe wicking method (a) wetted area as a function of time and (b) wicked volume as a function of time.

Now a representative surface wickability using FC 72 and the syringe wicking technique is presented in Fig. 6.7. To compare, both the capillary wicking results for FC 72 and water using syringe wicking technique are reported here. As can be seen from wetted area as a function of time in Fig. 6.7a, the wetted area initially increases due to liquid spreading, and as the liquid pendant reaches equilibrium, the wetted area for water becomes approximately constant, whereas, the wetted area for FC 72 keeps changing in all different stages of wicking test. Figure 6.7b shows the wicked volume as a function of time for both water and FC 72. To estimate the wicked volume flux for FC 72, initial wicked volumetric flowrate was taken as the linear ingredient of the wicked volume curve in Fig. 6.7b, and then the average wetted area was taken in that initial maximum

wicking region (Fig. 6.7a). Since, the wetted area is continuously changing unlike constant wetted area for water; this average wetted area for FC 72 incorporates additional measurement uncertainty in the wickability measurements which was included in the representation of wicked volume flux.

The actual wicked volume flux experienced at CHF is a complicated function of the flow field including highly dynamic variations in wetted area fraction, contact line speed, and contact line density during nucleate boiling [65]. It is assumed here, however, to scale linearly with the measured wicked volume flux, $\dot{V}''_{CHF,W} \propto \dot{V}''_0$, which is characterized using a quasi-static wetting state as shown in Figure 6.1. Eq. 6.3 can therefore be re-written as

$$K_W - K_{NW} \propto \left(\frac{\dot{V}''_0 \rho_l}{\rho_v^{1/2} [\sigma g (\rho_l - \rho_v)]^{1/4}} \right) \tag{6.5}$$

where the proportionality is used due to the unknown wetted area fraction at CHF, as well as the unknown proportionality between the actual wicked volume flux at CHF, $\dot{V}''_{CHF,W}$, and the measured wicked volume flux, $\dot{V}''_0$. This results in the nondimensional CHF for a wicking surface, K_W, given by

$$K_W = K_{NW} + CWi \tag{6.6}$$

where K_{NW} is the nondimensioanl CHF for the corresponding non-wicking surface, C is an unknown constant of proportionality, and Wi is defined here as the dimensionless wicking number given by

$$Wi \equiv \frac{\dot{V}''_0 \rho_l}{\rho_v^{1/2} [\sigma g (\rho_l - \rho_v)]^{1/4}} \tag{6.7}$$

Wi is the nondimensional form of the wicked volume flux, and represents the ratio of the liquid mass flux wicked into the surface structures relative to the critical mass flux of vapor leaving the surface as calculated using classical hydrodynamic instability analysis [69]. Hence, by knowing the wicked volume flux ($\dot{V}_0''$) as presented in this section, the non-dimensional wicking number can be estimated for structured surfaces, and eventually CHF during pool boiling can be predicted for structured surfaces.

6.4 Structured Surfaces

To characterize the effect of wickability on CHF, more than three dozens of different surfaces have been fabricated. This section provides a detailed overview of the fabricated surfaces and the fabrication techniques.

6.4.1 *TMV on Silicon Substrates*

Using a simple solution-based room-temperature process as described in Chapter 5, core-shell nickel nanostructures can be confomally deposited onto numerous materials without the need for any external power, heat, or special equipment. Briefly, the TMV assembles onto the surface from solution, followed by the successive reduction of palladium and nickel onto the outer surface of the assembled virus. The TMV acts as a temporary scaffold and plays no part in defining or maintaining the nanostructures after nickel deposition. The coatings are mechanically robust and show no physical degradation or mechanical failure after continuous nucleate boiling, including the repeated occurrence of CHF and burnout [2], with temperatures exceeding 200 °C.

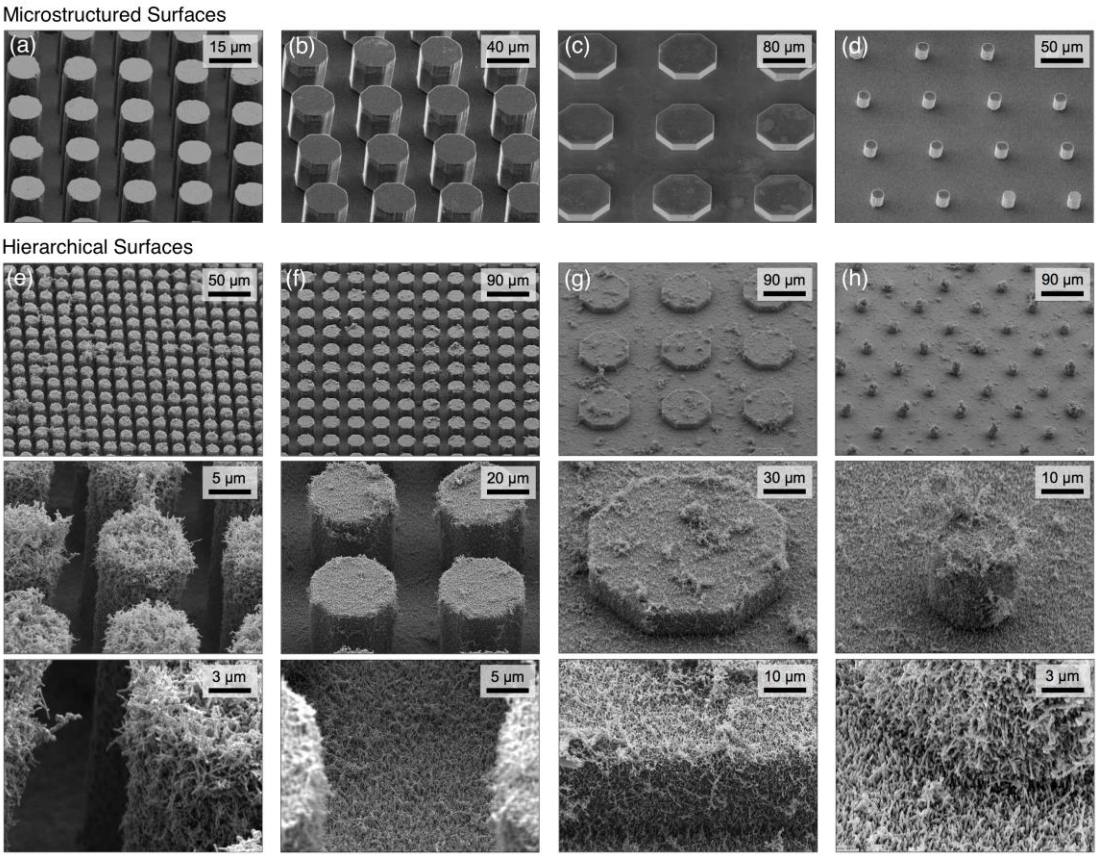

Figure 6.8: Micro, nano, and hierarchically structured silicon surfaces fabricated to characterize the effect of wickability on pool boiling CHF. (a-d) SEM images of four representative microstructure geometries fabricated using deep reactive ion etching. (e-f) Hierarchical surfaces at three different magnifications composed of the microstructures shown in (a-d) conformally coated with TMV-templated nickel nanostructures.

TMV biotemplating has been used here to create a multitude of structured surfaces with large variations in roughness factor as well as wickability. Figure 6.8 shows representative SEM images of eight of the twenty silicon samples fabricated for this work including four microstructured surfaces (Figure 6.8a-d), as well as four hierarchically structured surfaces (Figure 6.8e-h) composed of nickel-coated TMV conformally

assembled on to the corresponding microstructure geometries. Figure 6.8e-h shows SEM images of the hierarchical surfaces at increasing magnifications, demonstrating the conformal nature of the nickel-coated TMV nanostrutures.

The microstructured surfaces were fabricated using deep reactive ion etching of the underlying silicon substrate and are coated with a thin (20-40 nm) layer of nickel, to maintain a consistent intrinsic contact angle for all twenty samples. A total of nine different microstructure designs and their corresponding nine hierarchal designs were created, along with two nanostructured samples fabricated on flat silicon substrates. The micropost geometries (diameter × pitch × height) were varied for each design, and combining them with the conformal TMV nanostructures resulted in roughness factors (defined as the actual surface area relative to the footprint area) of r = 1.03 – 57.24. All of the surfaces fabricated in this work demonstrated superhydrophilic behaviors and exhibited no measurable contact angle.

6.4.2 *Copper Oxide Nanostructures (CuO)*

To compare the results for TMV-structured surfaces with alternative materials and structures, a series of copper oxide nanostructured surfaces have also been fabricated and characterized. CuO nanostructures are ideal for this comparison due to the ability to easily tune their morphologies. Figure 6.9 shows the five distinct CuO nanostructures fabricated and tested in this work, along with the chemical composition, bath temperature, and growth times used to create each. Surface CN1 (Figure 6.9a) was produced using the recipe reported by Chu *et al.* [37], while surfaces CN2 and CN3 use the same alkaline bath but vary the temperature and/or growth time. CN4 (Figure 6.9d)

was produced using the method reported by Love *et al.* [70], and CN5 (Figure 6.9e) was produced by immersing a copper sample into a simple bath of phosphate buffer at room temperature.

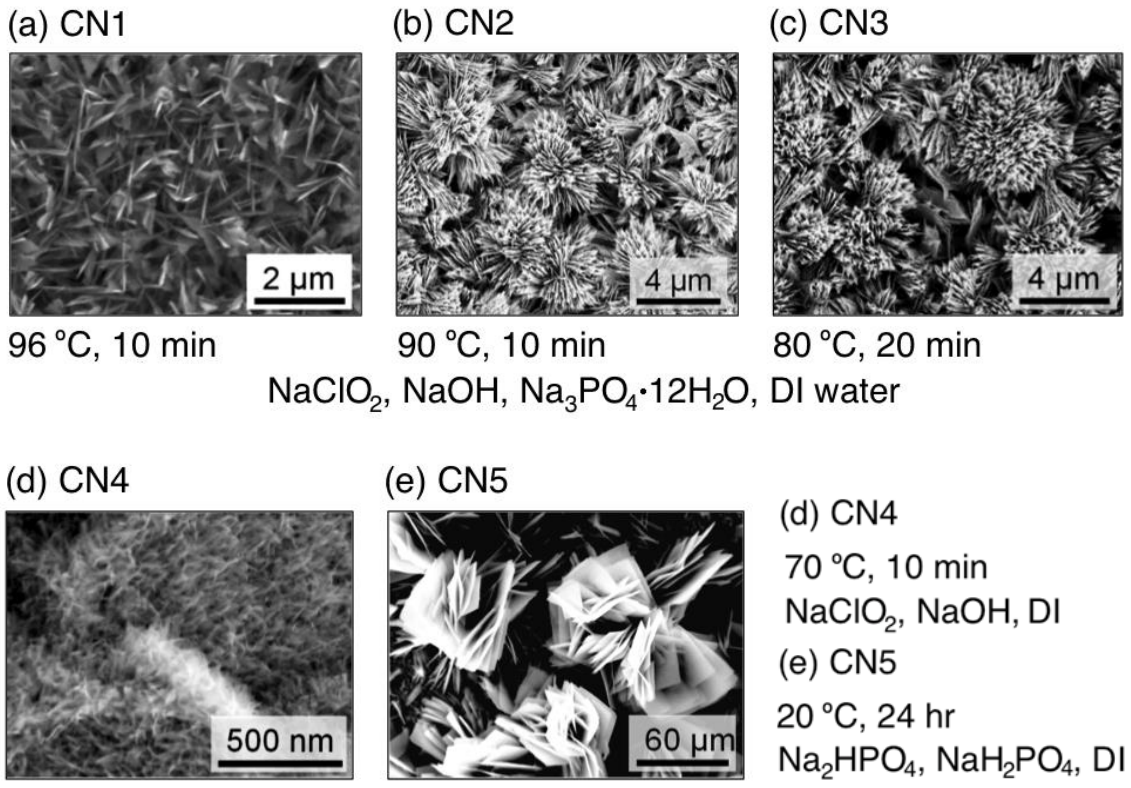

Figure 6.9: Copper oxide nanostructured coatings. (a-e) SEM images of five different CuO nanostructured coatings and the corresponding fabrication conditions, including solution temperature, time, and composition.

6.4.3 Estimation of Roughness Factor

To characterize the effect of roughness factor on CHF enhancement as demonstrated by Chu et al. [8], the roughness factor for all different structured surfaces fabricated in section 6.4.2 are estimated using image analysis and presented in this section.

The roughness factors for ordered cylindrical structures including micropost arrays, nanowires, and nanorods were estimated using Eq. 6.8 using the structure diameter (D_A), height (H_A), and center-to-center pitch (P). In Eq. 6.8, C is a constant set equal to $C = \pi/2$ for deep-etched silicon microposts to account for scalloped features [8], and C = 1 for smooth nanowires and nanorods. Roughness factor for nanowires and nanorods reported in the literature were estimated using Eq. 6.8, where the diameter and height were given by their reported values, and the pitches were estimated based on the provided SEM images [9, 12, 28]. For other ordered array structures, roughness factors were calculated directly from their reported values [8, 15, 37].

$$r_A = 1 + \left(\frac{\pi D_A H_A}{P^2} \right) \times C \tag{6.8}$$

The roughness factors for TMV nanostructured surfaces were estimated using Eq. 6.9 and by examining SEM images at various magnifications. At high magnifications, the number of cylindrical nickel-coated TMV structures in the frame (N) is counted, and the average diameter (D_N) and length (H_N) is measured, resulting in

$$r_{TMV} = 1 + \left[\frac{N\left(\pi D_N H_N\right)}{A_{image}} \right] \tag{6.9}$$

where A_{image} is the area of the selected frame.

The density of TMV on the surfaces depends on the concentration of virus solution, deposition time, and substrate material. Figure 6.10 shows SEM images of two surfaces with subtly different TMV densities. The roughness factor estimation for a given

surface was therefore based on an average value for multiple images across the sample. Based on SEM images, the average nanostructure diameter (D_N) was typically between 100 - 150 nm, and the average height (H_N) taken to be 500 nm. Since the roughness factors are estimated based on the number of nanostructures observed in a single frame, there is the likelihood of missing underlying nanostructures in top-down SEMs, hence, these roughness factors are by definition under-predictions.

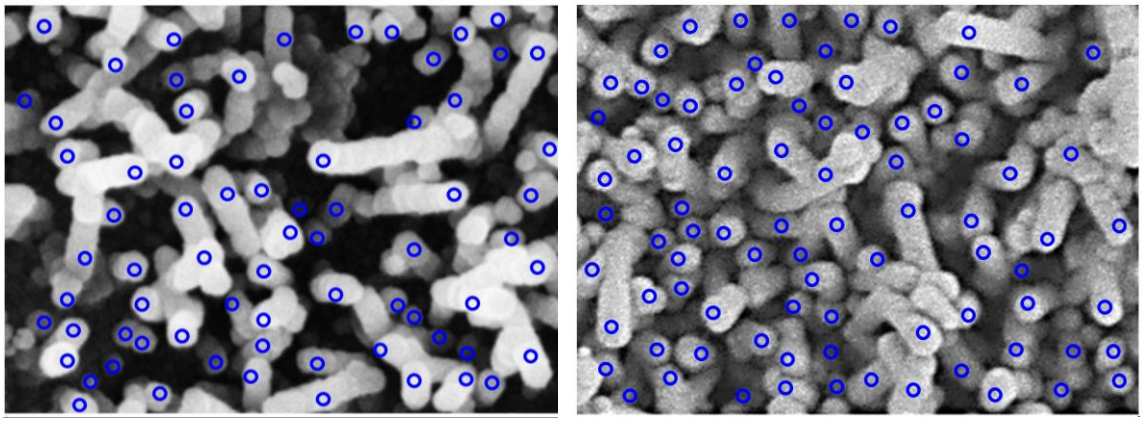

(a) (b)

Figure 6.10: SEM images used for roughness estimation of TMV-structured surfaces including (a) less densely packed, and (b) more densely packed cylindrical nanostructures.

Figure 6.8 shows SEM images of TMV structured surfaces, where TMV aggregates can be seen on the surface, thus increasing roughness factor. This phenomenon was typically minimal for nanostructured surfaces, but was pronounced for some hierarchical designs. The additional roughness factor associated with aggregates (r_{agg}) was estimated by examining the average number, size, and density of aggregates on a surface using SEM images at various magnifications. The roughness factor associated with TMV aggregates varied from surface to surface, with values from less than one to up

to 15 (accounting for up to 35% of the total roughness in extreme cases). The uncertainty in measuring aggregate roughness was conservatively estimated to be ±50%. This estimation is also an under-prediction due to the lack of visibility of underlying TMV nanostructures in a top-down SEM image.

The roughness factors for hierarchical surfaces (r_H) were estimated using Eq. 6.7 where r_{TMV} is the roughness factor for TMV nanostructures, r_A is the roughness factor for silicon microposts, and r_{agg} is the roughness factor due to aggregation of nanostructures.

$$r_H = (r_{TMV} \times r_A) + r_{agg} \tag{6.10}$$

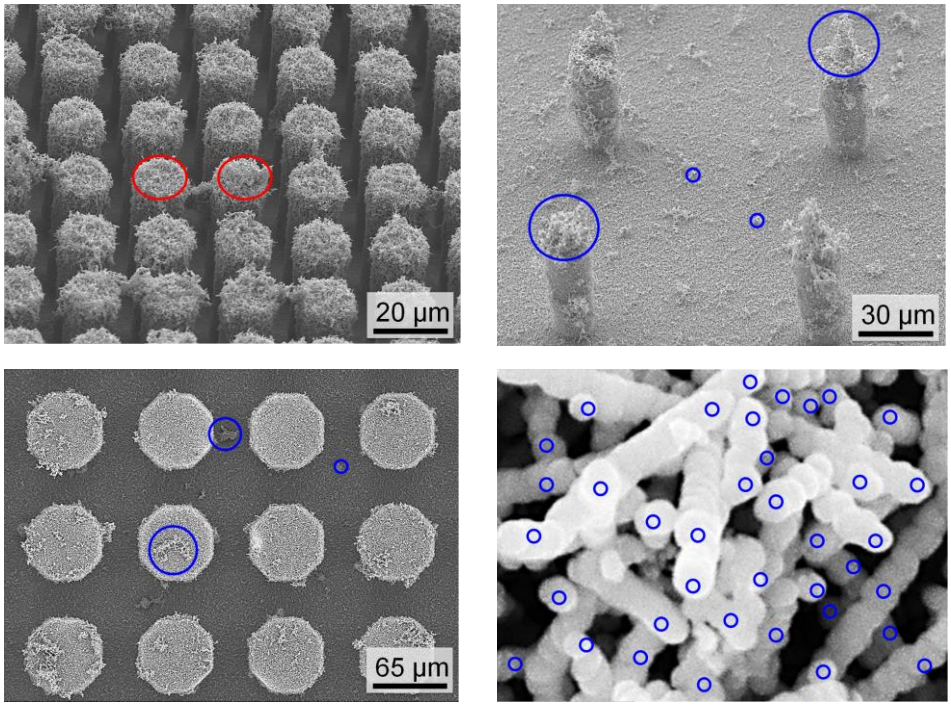

Figure 6.11: TMV aggregation on hierarchical surfaces.

Roughness factors for the copper oxide nanostructured surfaces fabricated in this work were measured using one of two equations based on nanostructure shape. For rectangular pedal-like structures (Figure 6.12a), Eq. 6.11 was used to estimate the roughness factor ($r_{CN\text{-}R}$) where N is the number of CuO nanostructures in a frame, and b and h are the base and height of the nearly rectangular prismatic nanostructures. Assuming a negligible thickness, 2(b x h) is the total surface area of both sides. For needle-like triangular nanostructures (Figure 6.12b) Eq. 6.12 was used, where b is the length of the triangular base and h is the height of the triangular prism, assuming negligible thicknesses. Typical values for b and h ranged from 100 – 900 nm.

$$r_{CN-R} = 1 + \left[\frac{N}{A_{image}} 2(b \times h) \right] \tag{6.11}$$

$$r_{CN-T} = 1 + \left[\frac{N}{A_{image}} (b \times h) \right] \tag{6.12}$$

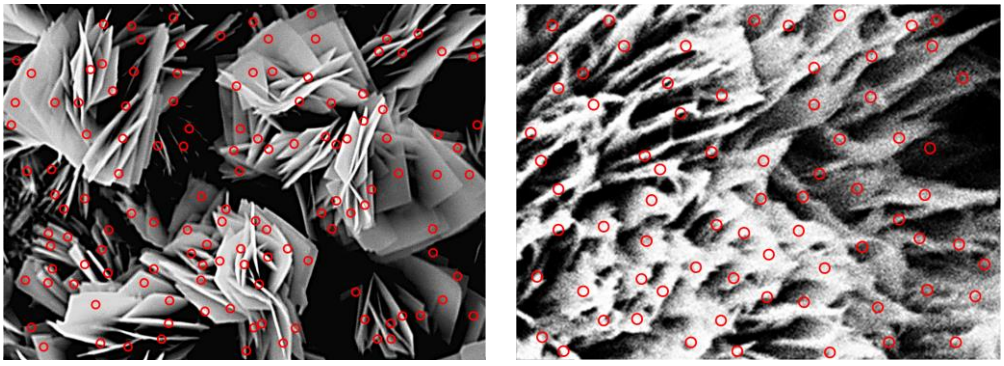

(a) (b)

Figure 6.12: Roughness estimation of CuO nanostructures on (a) rectangular and (b) triangular shaped structures.

6.5 Results: Boiling of Saturated Water

To characterize the effects of wickability on CHF, the micro, nano, and hierarchically structured silicon surfaces shown in Fig. 6.8, copper oxide nanostructures shown in Fig. 6.9, and biotemplated nickel nanostructures on different metallic and non-metallic surfaces presented in Chapter 5 were tested in this section during nucleate pool boiling of water at atmospheric conditions using the experimental setup reported in section 4.1.

6.5.1 *Silicon Substrates*

Figure 6.13a shows selected boiling curves for several of the designs where CHF is signified with a horizontal arrow. Figure 6.13b shows CHF as a function of the experimentally measured wicked volume flux, $\dot{V}_0''$, as described in section 6.3 for all twenty structured silicon samples, shown in Fig. 6.14, as well as a single flat silicon sample. Figure 6.13c shows the compete legend for all the tests including sample names, micropost array geometries, estimated roughness factors as described in section 6.4.3, wickabilities as measured from the capillary wick tests, and CHF values. Here M stands for silicon microstructure surfaces, N stands for nanostructured surfaces, and H stands for biotemplated hierarchical surfaces. As can be seen from Figure 6.13b, a clear and distinct linear relationship between CHF and wicked volume flux exists, as predicted from the closed form model. Using a hierarchical design, a maximum CHF of 257 W/cm^2 has been achieved at a wicked volume flux of over 5 mm/s. This represents the highest reported CHF for water on a silicon substrate, as well as the highest reported CHF for a superhydrophilic surface (contact angle ~ 0°) on any substrate. This result is comparable

with the work of Chu *et al.* [37] using hierarchical surfaces to show a CHF of 250 W/cm^2.

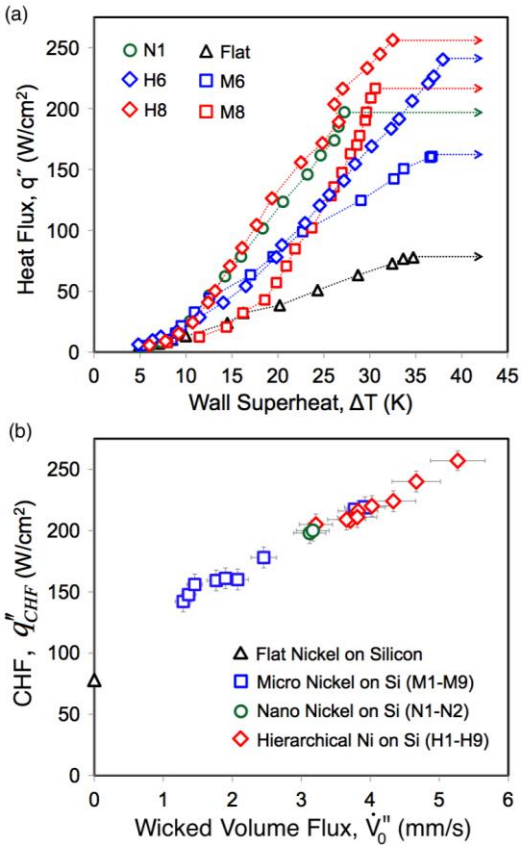

(c)

	Micro Geometry (D×P×H μm)	r	$\dot{V}_0''$ (mm/s)	CHF (W/cm²)
M1	4×70×8	1.03	1.29	142
M2	15×90×16	1.15	1.37	148
M3	120×205×16	1.23	1.46	156
M4	15×90×32	1.29	2.08	160
M5	120×205×32	1.45	1.77	159
M6	40×65×32	2.50	1.90	161
M7	15×21×16	3.69	2.46	178
M8	15×21×32	6.37	3.78	217
M9	4×7×16	7.45	3.92	219
N1	-	6.42	3.12	198
N2	- 8.67	6.63	3.17	200
H1	4×70×8	6.84	3.71	208
H2	15×90×16	8.67	3.66	209
H3	120×205×16	10.24	3.82	216
H4	15×90×32	11.87	3.81	211
H5	120×205×32	9.87	4.33	224
H6	40×65×32	19.30	4.67	240
H7	15×21×16	25.84	4.02	220
H8	15×21×32	57.24	5.27	257
H9	4×7×16	49.36	3.21	205

Figure 6.13: Experimental characterization of the CHF and wickability of structured silicon surfaces. (a) Boiling curves for six selected samples, where CHF is signified with an arrow. (b) Experimental results of CHF plotted against the wicked volume flux for all twenty silicon surfaces, showing a linear trend. (c) Details of the twenty micro, nano, and hierarchical silicon surfaces including sample name, microstructure geometry (diameter x pitch x height), roughness factor, *r*, wicked volume flux, $\dot{V}_0''$, and *CHF*.

Additionally, it is seen that microstructured designs can also exhibit high wickability and CHF, with values of nearly 4 mm/s and 220 W/cm^2, respectively. The

nanostructured surfaces provide a CHF of around 200 W/cm^2, consistent with prior results [2]. Figure 6.15 shows the complete boiling curves for all twenty silicon surfaces tested in this work, including heat flux as a function of wall superheat (Figure 6.15a), as well as heat transfer coefficient as a function of heat flux (Figure 6.15b).

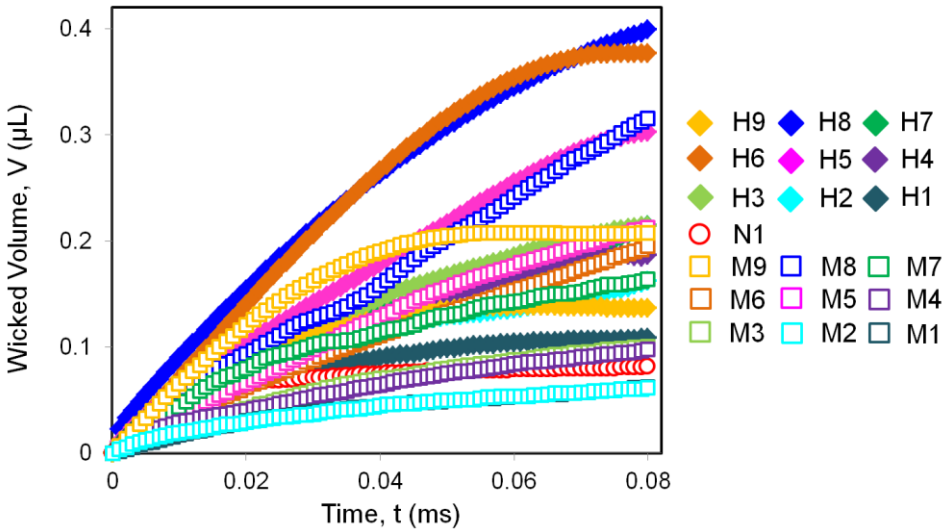

Figure 6.14: Wicked volume as a function of time for all twenty micro, nano, and hierarchical silicon surfaces.

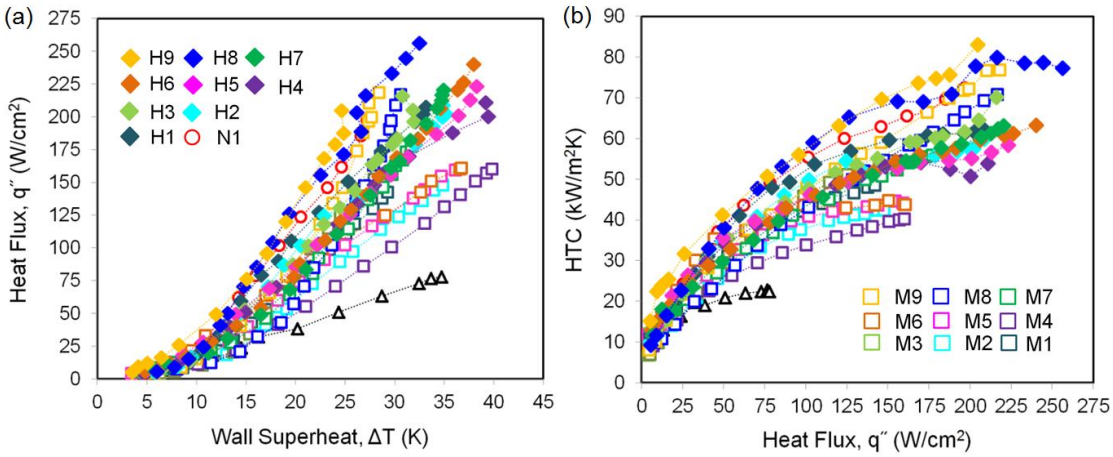

Figure 6.15: Pool boiling results for structured surfaces (a) CHF as a function of wall superheat and (b) HTC as a function of heat flux.

6.5.2 *Effect of Substrate, Nanostructure Density, and Fouling*

Depending on variations in the substrate material as well as the micro/nano-structures themselves, wickability can vary from sample to sample, spatially across a surface, as well as over time. This includes the effects of surface defects and variations in structure density, as well as degradation due to fouling. To investigate these effects, various TMV-templated nanostructured surfaces have been fabricated and tested on non-silicon substrates, as first demonstrated in prior Chapter 5. In that work, the TMV biotemplating technique was optimized for deposition onto aluminum, copper, and stainless steel. During the optimization process, a variety of non-ideal surface coatings were created with lower-quality surface coverages. Figure 6.16a shows SEM images of the results of an optimized deposition, with a high concentration of nickel nanostructures, as compared to an un-optimized deposition with a low concentration. Additionally, Rahman *et al.* showed that a slight decrease in CHF (~5%) is observed after repeated testing of the surfaces including repeated CHF and burnout events [2]. This decrease was attributed to reversible fouling, and after cleaning the surfaces returned to their initial values.

The performance TMV coatings with varying nanostructure densities, as well as coatings degraded by fouling were measured to characterize the impact on wickability and CHF. Figure 6.16b shows the CHF versus wickability data for silicon, aluminum, copper, and stainless steel surfaces with both high and low density coatings, as well as samples degraded by fouling after repeated testing. As can be seen, the variation in TMV density and surface fouling leads to variations in the measured CHF. However, these variations are accompanied by corresponding variations in the measured wickability, with

the data closely following the linear trend seen for micro, nano, and hierarchical silicon surfaces. This is strong evidence pointing to wickability as not only the key factor in CHF enhancement, but also a convenient phenomenological parameter that is easily measured and accurately accounts for the complex effects of variations in morphology, surface defects, and degradation due to fouling.

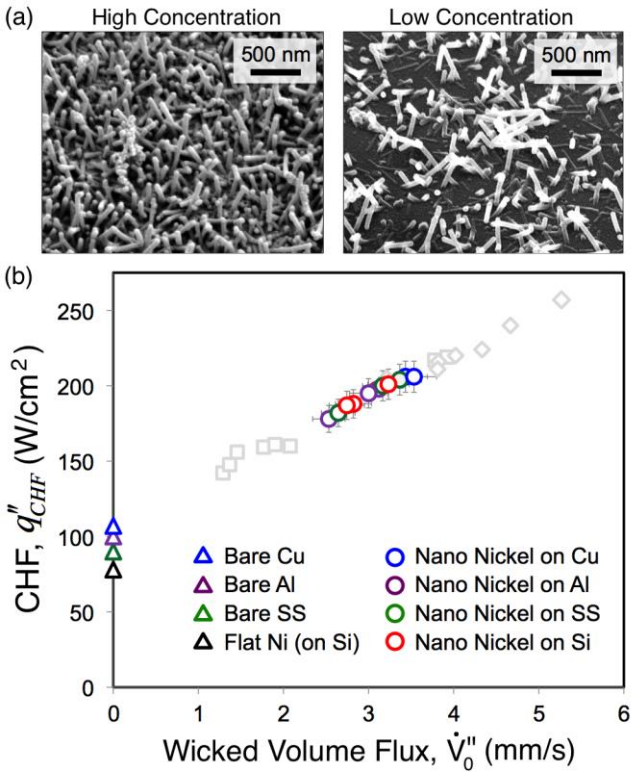

Figure 6.16: Effect of substrate material, TMV morphology, and fouling on wicking-enhanced CHF. (a) SEM images showing high-concentration and low-concentration TMV coatings. (b) CHF as a function of wicked volume flux for TMV nanostructures on multiple metallic substrates, showing variations in performance due to differences in morphology as well as fouling after repeated testing. The results are compared to the corresponding bare surfaces as well as the micro, nano, and hierarchal silicon surfaces (light grey symbols).

6.5.3 *Effect of Nanostructure Material and Morphology*

To compare the results for TMV-structured surfaces with alternative materials and structures, a series of copper oxide nanostructured surfaces have also been fabricated and characterized during pool boiling (Fig. 6.17a). While it is difficult to quantify the variations in surface morphology and roughness factor for the five CuO nanostructures shown in Figure 6.9a-e, the wickability of each sample is easily measured. Additionally, it can be seen that a small change in bath conditions between CN1 and CN2 (90°C to 96°C), leads to noticeable variations in CHF (56% increase). Nevertheless, Figure 6.17b shows that the enhancement of CHF is due to wickability and is consistent with the results from the nickel-coated TMV-structured surfaces.

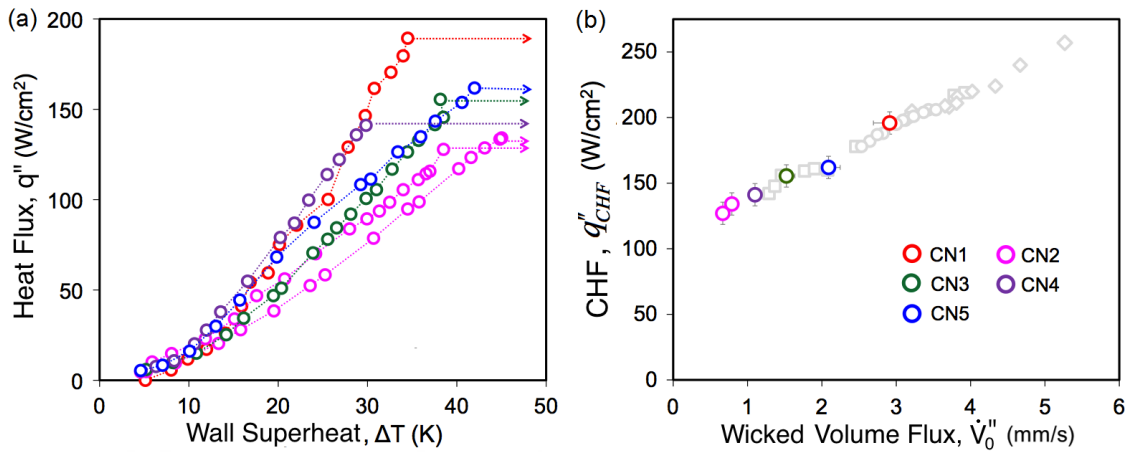

Figure 6.17: Results for copper oxide nanostructured coatings. (a) Boiling curves and (b) CHF as a function wicked volume flux, showing consistency with TMV-structured micro, nano, and hierarchical coatings on silicon and metallic substrates (light grey symbols).

6.5.4 Effect of Wickability on CHF

Figure 6.14a-b shows the entirety of the CHF data collected for all of the surfaces fabricated and tested in this work, including non-structured hydrophilic and structured superhydrophilic surfaces, plotted against the surface wickability (Figure 6.14a) and surface wettability (Figure 6.14b).

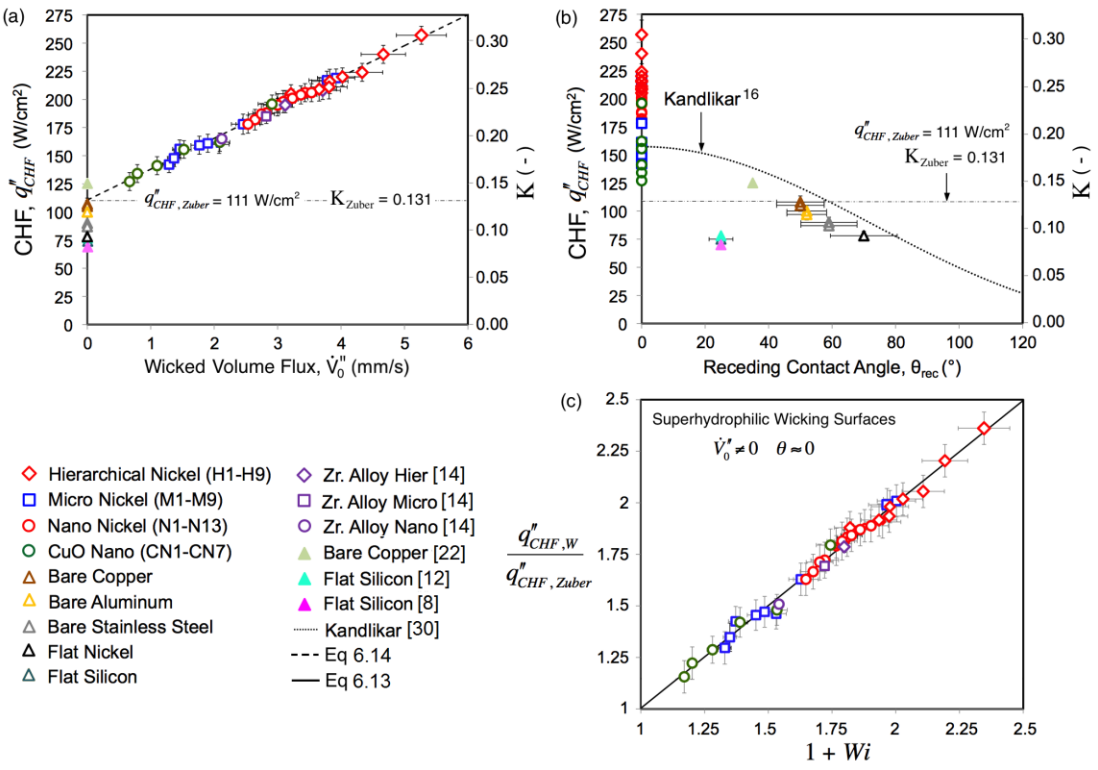

Figure 6.18: Effect of wickability on CHF. Experimentally measured CHF as a function of (a) wicked volume flux and (b) receding contact angle for over forty individual surfaces, showing the importance of wickability for structured superhydrophilic surfaces. The data includes variations in scale (micro, nano, hierarchical), morphology, fouling, structure material, and substrate material, as well as data from other researchers [14]. (c) CHF enhancement as a function of wicking number, *Wi*, for superhydrophilic surfaces showing excellent agreement with the developed correlation given by Eq. 6.13.

The non-structured surfaces exhibit measurable contact angles and no measurable wickability, while the structured samples exhibit varying wickability but no measurable contact angle. For non-wicking surfaces, CHF is consistent with existing literature and established models from Zuber [23] and Kandlikar [30]. The CHF of structured superhydrophilic surfaces, however, cannot be predicted using traditional modeling approaches. This trend is commonly shown in the open literature, including the large spread in data at contact angles of zero degrees.

Fitting the data shown in Figure 6.18a with the linear relationship predicted by Eq. 6.6 yields a value of $K_{NW} = K_{Zuber} = 0.131$. This is consistent with numerous experimental results validating Zuber's limit for flat surfaces not capable of capillary wicking. Interestingly, this fit also yields a value of $C = K_{Zuber} = 0.131$, suggesting a nondimensional correlation for CHF on structured superhydrophilic surfaces of the form

$$K_W = K_{Zuber}(1 + Wi) \tag{6.13}$$

where the dimensionless wicking number, Wi, is given by Eq. 6.12. Rearranging terms, this results in a CHF enhancement factor relative to Zuber's limit of

$$\frac{q''_{CHF,W}}{q''_{CHF,Zuber}} = 1+Wi \tag{6.14}$$

Figure 6.18c shows the experimental data for each of the superhydrophilic surfaces fabricated here, matching the CHF enhancement factor given by Eq. 6.14 to well within the measured experimental uncertainty (<10%). In addition to the 36 individual samples fabricated and tested in this work, Figure 6.18 includes results from Ahn *et al.* using micro, nano, and hierarchically structured zirconium alloy [57]. This data was

extracted from the reported CHF, adsorbed volume measurements, and optical images of capillary wicking experiments. These results show that wickabililty (quantified here by the wicked volume flux and dimensionless wicking number, *Wi*) is the critical parameter dictating CHF on structured superhydrophilic surfaces. A definitive and consistent linear relationship for CHF with respect to wickability is seen, as predicted by the simple analytic model. These results are independent of variations in structure length scale (micro, nano, and hierarchical); substrate material (silicon, aluminum, stainless steel, copper, and zirconium); nanostructure density; roughness factor; degradation due to fouling; as well as surface structure material and morphology (etched silicon micropost arrays, virus-templated nickel nanosturtures, copper oxide nanostructures, and anodized zirconium).

The techniques explained in Section 6.4.3, were used to evaluate surface roughness factor for all of the micro, nano, and hierarchical silicon surfaces fabricated and tested in this work. Additionally, roughness factors of numerous structured surfaces in the open literature were also estimated using Eq. 6.8- Eq. 6.12. This was done using the reported values for micro/nano-structure dimensions (height, diameter, pitch, etc.) as well as values extracted from SEM images, as necessary. Figure 6.19 shows the reported CHF values as a function of estimated roughness factors for this work, as well as five other publications [9, 12, 15, 28, 37]. As can be seen, for moderate-to-low roughness factors ($r < 10$) CHF is generally well predicted by the proposed model from Chu *et al.* [8], especially for ordered arrays of silicon microposts. For large roughness factors ($r > 10$), no discernable trend is observed and the model greatly over-predicts CHF.

The roughness factors estimated here include large error bars associated with

the conservative measurement uncertainties assumed. This is particularly evident for large values of roughness factor. Nevertheless, these estimates by definition under-predict roughness factor and even accounting for this uncertainty, these results suggest that a mechanisms other than increased contact line length due to surface roughness is playing a role in CHF enhancement.

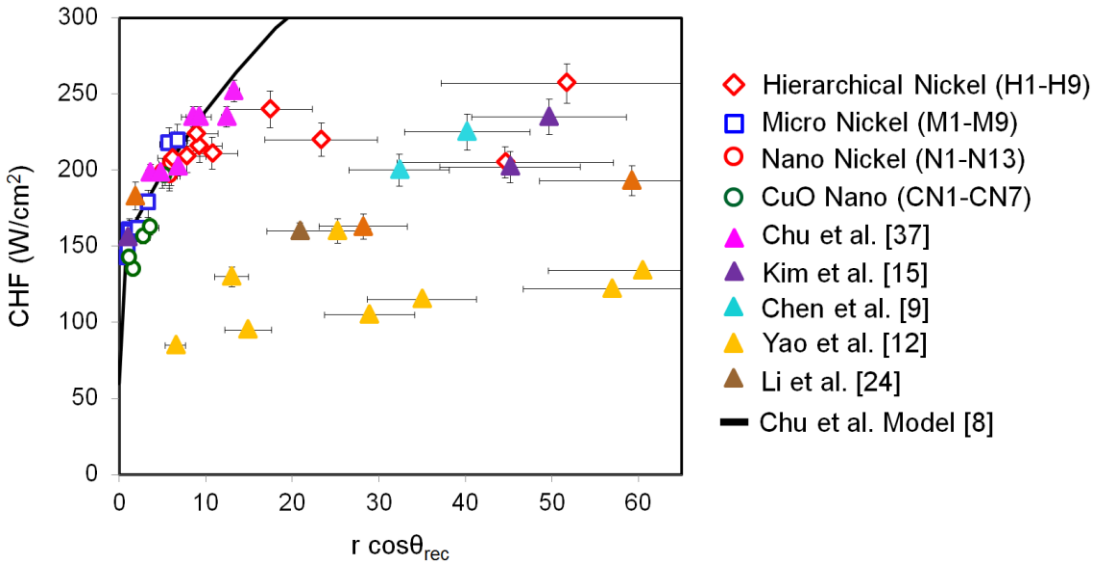

Figure 6.19: CHF as a function of surface roughness factor and receding contact angle.

6.5.5 Optimization of Biotemplated Nanofabrication for Boiling Applications

To test the mechanical strength of the TMV-structures and optimize the fabrication process, a series of samples were fabricated with varying nanostructure thicknesses and tested during pool boiling. This variability was achieved by changing the electroless nickel plating time during fabrication, as seen in Figure 6.20a.

The nickel nanostructures were fabricated using *Tobacco mosaic virus* (TMV) based biotemplating process as described in Chapter 5. TMV is cylindrical shaped biological material which measures 18 nm outside diameter and 300 nm length.

Electroplated nickel solution puts thin nickel shell outside the nanorods where the thickness is a function of plating time. Hence, by varying the shell thickness, the structure size changes which results in variations of structure porosity. In this work, total 11 nanostructured surfaces were prepared starting from nickel deposition time 2 min to 60 min. Figure 6.20b shows the measured structure diameter as a function of nickel deposition time where the structure size linearly increases with solution time. The structure diameters were measured by analyzing SEM images using ImageJ.

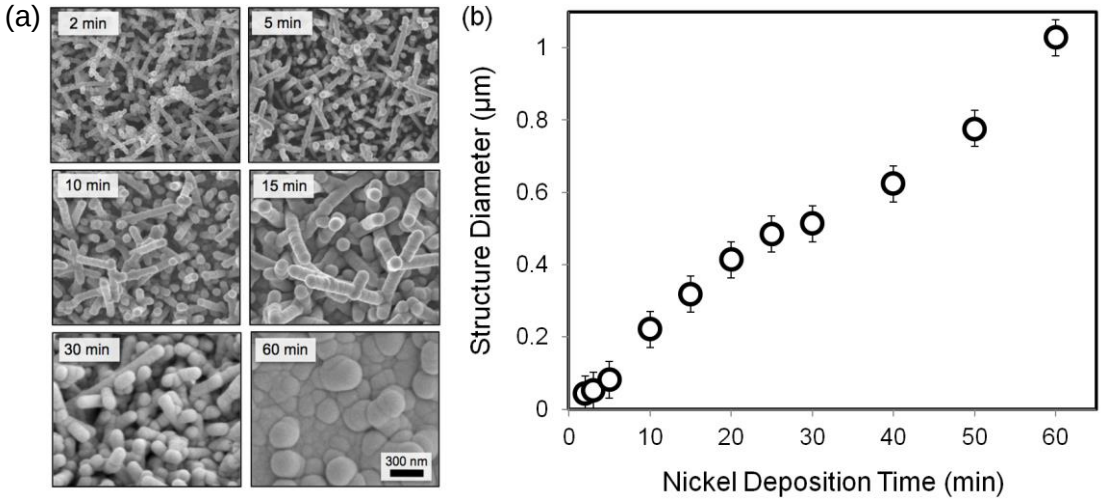

Figure 6.20: Effect of nickel deposition time on nanostructure size. (a) SEM images of various samples fabricated with different nanostructure thicknesses. (b) Diameter of biotemplated nanorods as a function of nickel coating deposition time.

The performance of nanostructures was analyzed during wickability test using the capillary wicking method reported in section 6.3 which is analogous to structure porosity and wettability. Wicked volume as a function of time for some representative structures is shown in Figure 6.21a. It can be seen that the initial wicked volumetric flow rate decreases as the nickel deposition time increases except the nickel deposition times

of 2 min (green circles) and 3 min (not shown here). Nanostructured surfaces with nickel deposition time 5 min (blue circles in Fig. 6.21a) exhibits the maximum wicked volumetric flow rate, and nanostructured surface with 60 min nickel deposition (red squares in Fig. 6.21a) time exhibits minimum wicked volumetric flowrate. This nickel deposition time depended wicking performance is also observed in pool boiling CHF results. Figure 6.21b presents the pool boiling heat flux as a function of wall superheat for some nanostructures showing the variation in boiling performance based on nickel deposition time or in other words structure porosity.

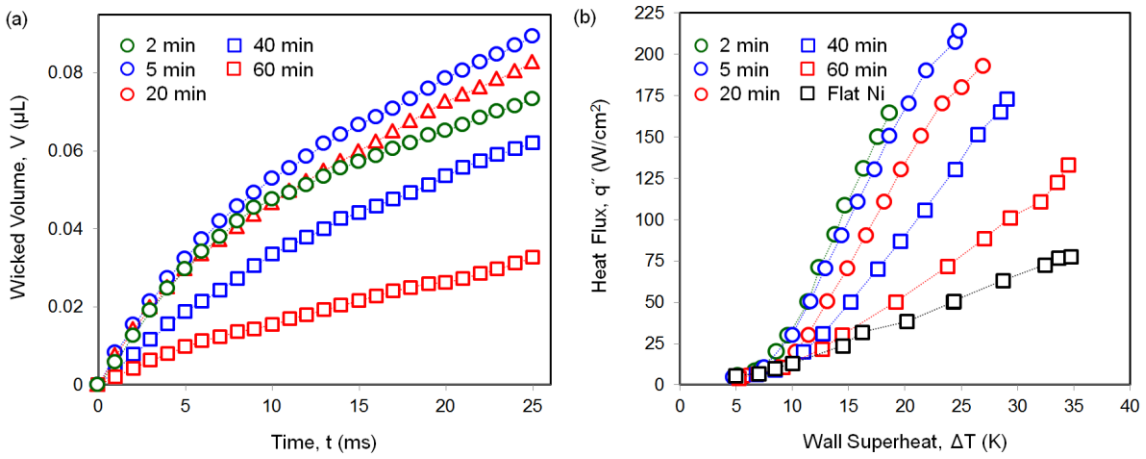

Figure 6.21: Experimental results (a) wicked volume as a function of time and (b) pool boiling heat flux as a function of wall superheat for nickel nanostructures showing the effect of nickel deposition time.

Figure 6.22 presents the CHF value as a function of nickel deposition time as compared to the CHF value predicted from wickability testing and Eqn. 6.14. As can be seen, excellent agreement is seen between the predicted and measured values for deposition times greater than five minutes. For deposition times of less than five minutes,

the nanostructures were too thin to withstand the mechanical loading and failed during boiling, resulting in a difference between predicted and measured CHF.

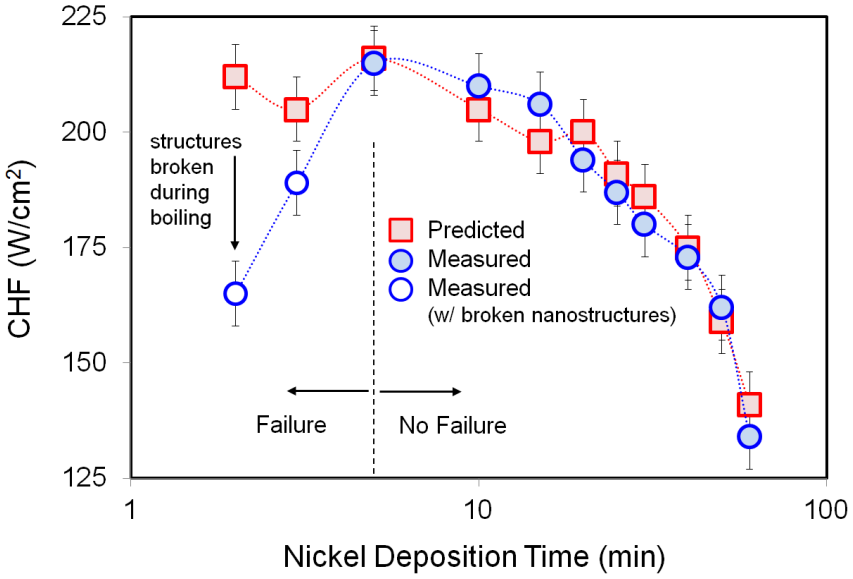

Figure 6.22: Comparison of measured and predicted CHF values showing the effect of nickel deposition time on pool boiling performance and mechanical failure of TMV coatings for deposition times of less than five minutes.

6.6 Results: Boiling of Saturated FC 72

To characterize the effects of wickability on CHF, in addition to varying the structures, the effect of working fluid was also tested. All the wickability results and pool boiling results presented earlier to develop the wickability depended CHF correlation in Eq. 6.14 was with water as the working fluid. This chapter presents the capillary wicking and pool boiling results for microstructure, nanostructured and hierarchical surfaces for FC 72 using the capillary wicking technique reported in section 6.3, and pool boiling experimental setup reported in section 4.2.

Since capillary wicking provides a means to estimate the rewetting capability of active nucleation sites during boiling, an experimental CHF correlation on the basis of non-dimensional wickability has been demonstrated in section 6.5. Surface wickability has been quantified via capillary wicked volume flux for over three dozen individual surfaces. The structured surfaces include several substrate materials, different nanostructures, microstructures, and hierarchical structures, different structure materials, various nanostructure densities and surface fouling properties. However, this CHF model along with most of the literature models has showed a good agreement for boiling CHF where water is used as the working fluid.

In this section, several structured surfaces have been fabricated and characterized during pool boiling heat transfer using dielectric FC-72 as the working fluid. Since, FC 72 is a highly wetting fluid with low surface tension as compared to water, the quantification of capillary wicking volume flux also becomes complicated. The high liquid density of FC 72 requires extra vacuum pressure to keep the fluid inside the capillary tube up to the desired height. In addition, the volatile feature of FC 72 makes it harder to create a liquid pendent droplet at one end of the capillary tube as opposed to water. Hence, this section presents a method to estimate the wicked volume flux using a capillary tube incorporating a micro syringe system. Finally, the experimental results with FC 72 are compared with the experimentally derived correlation relating CHF and surface wickability for water.

To analyze the effect of capillary wicking on CHF and validate the non-dimensional grouping of wicking number and CHF for structured surfaces, four different

structures have been fabricated (Figure 6.23) in this work. A *Tobacco mosaic virus* (TMV) based biotemplated nickel nanostructured surface (Fig. 6.23a) was fabricated as described in Chapter 5. Figure 6.23b shows SEM image of chemically oxidized copper oxide nanostructured surface prepared following the recipe described in section 6.3 (CN1). Microstructure surfaces of 15 µm diameter, 21 µm center-to-center pitch and 32 µm height (Fig. 6.23c) were fabricated using traditional photolithography and deep reactive ion etching process. Finally biotemplated nickel nanostructures were incorporated on the silicon microstructures to fabricate hierarchical nickel surfaces as shown in Fig. 6.23d. Here the micropost design used in hierarchical surface was 40 µm diameter, 65 µm center-to-center pitches and 32 µm height.

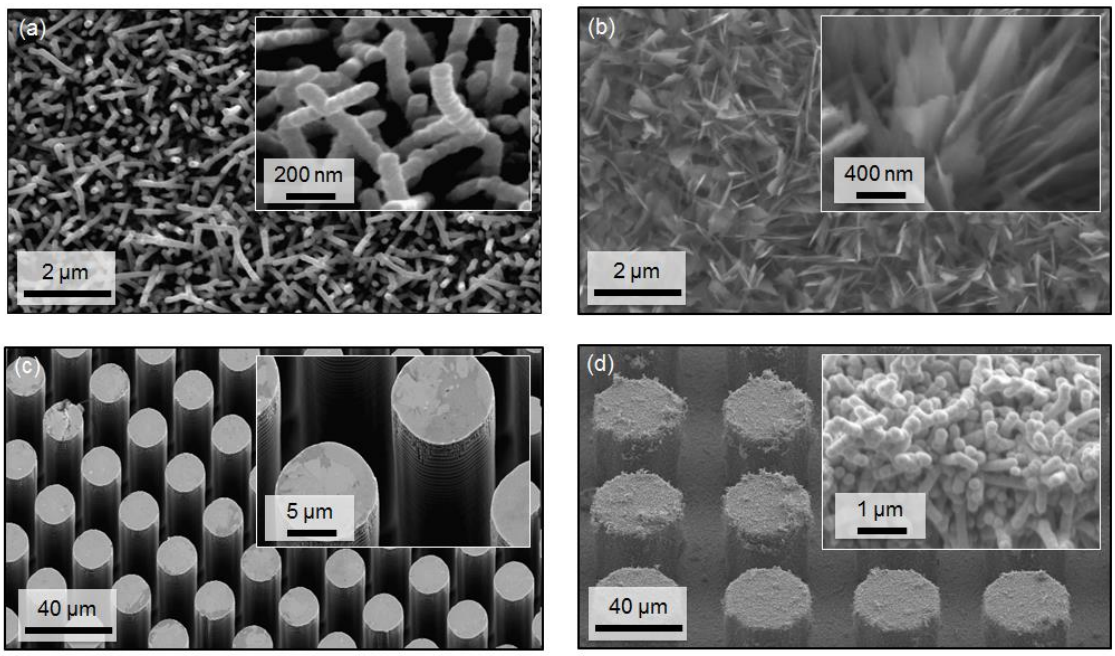

Figure 6.23: SEM image of structured surfaces fabricated to analyze the effect of capillary wicking on pool boiling CHF using dielectric fluid.

6.6.1 *Wicking Results for FC 72*

The effect of fluid wettability on capillary wicking measurements is presented in Fig. 6.24. The capillary wicking results for both FC 72 and water using syringe wicking technique are reported here. As can be seen from wetted area as a function of time in Fig. 6.24a, the wetted area initially increases due to liquid spreading, and as the liquid pendant reaches equilibrium, the wetted area for water becomes approximately constant, whereas, the wetted area for FC 72 keeps changing in all different stages of wicking test.

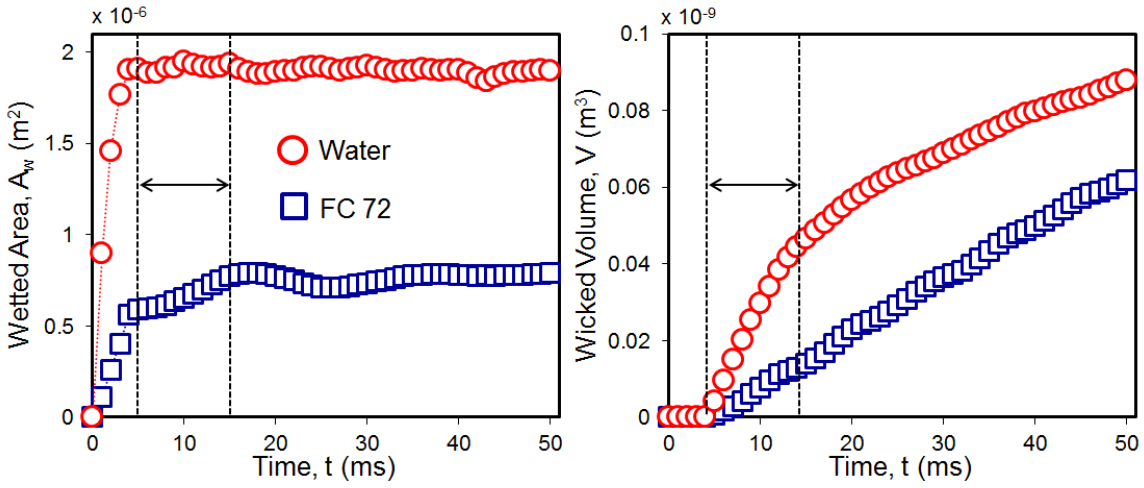

Figure 6.24: Capillary wicking results of FC 72 compared with water using syringe wicking method (a) wetted area as a function of time and (b) wicked volume as a function of time.

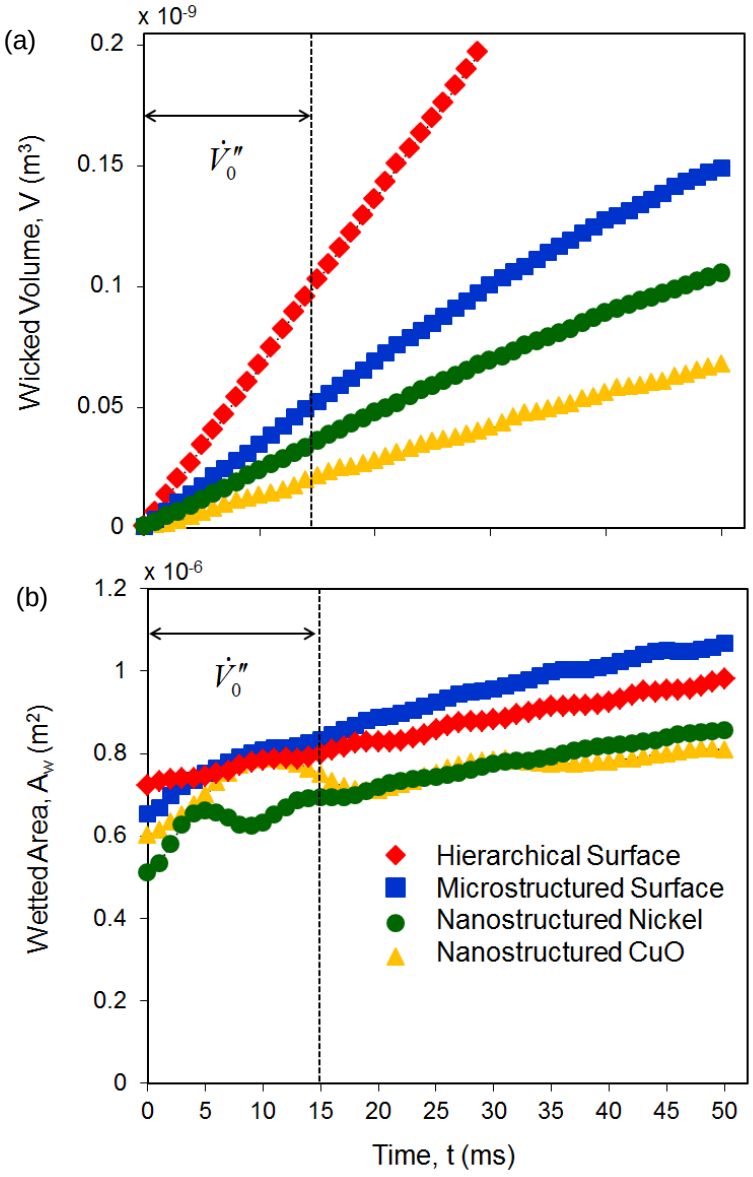

Figure 6.25: Capillary wicking results for the micro, nano and hierarchical structured surfaces using FC 72. (a) Wicked volume as a function of time and (b) Wetted area as a function of time.

Figure 6.24b shows the wicked volume as a function of time for both water and FC 72. To estimate the wicked volume flux for FC 72, initial wicked volumetric flowrate was taken as the linear ingredient of the wicked volume curve in Fig. 6.24b, and then the

average wetted area was taken in that initial maximum wicking region (Fig. 6.24a). Since, the wetted area is continuously changing unlike constant wetted area for water; this average wetted area for FC 72 incorporates additional measurement uncertainty in the wickability measurements which was included in the representation of non-dimensional wicking number. Figure 6.25a shows the wicked volume as a function of time and Fig. 6.25b presents the wetted area as a function of time for all the structured surfaces fabricated for this work. Here time t = 0 ms is the time when the liquid level inside the capillary tube starts changing. The initial wicked volumetric flowrate is taken as the linear ingredient at time t = 0 ms in the time t = 0 ms to t = 15 ms region. And the wetted area is taken as the average wetted area in the same time frame.

6.6.2 *Boiling Results for FC 72*

To characterize the pool boiling performance of structured surfaces, saturated FC 72 pool boiling experiments were performed using the experimental apparatus and methods described in section 4.2. Figure 6.26 shows the pool boiling heat flux as a function of wall superheat for micro, nano and hierarchical surfaces and compared with bare copper and bare silicon surfaces. Black square represents bare silicon surface and black triangle represents bare copper surface. It can be seen that bare silicon and bare copper surfaces reach CHF up to 11.4 W/cm^2 and 17 W/cm^2 respectively. By adding copper oxide nanostructures onto bare copper, CHF can be increased up to 19.4 W/cm^2 shown in yellow triangles, whereas, biotemplated nickel nanostructures onto bare silicon can give CHF as high as 21.9 W/cm^2 (green circle in Fig. 6.26). Additionally, microstructure surface (blue square in Fig. 6.26) gives both high CHF (23.4 W/cm^2) and HTC at CHF (19.2 kW/m^{2}K) compared to nanostructured surfaces. Finally, the

biotemplated hierarchical surface shown in red diamonds in Fig. 6.26 demonstrates significant enhancement in CHF up to 34.4 which is 200% enhancement in CHF as opposed to bare silicon surface.

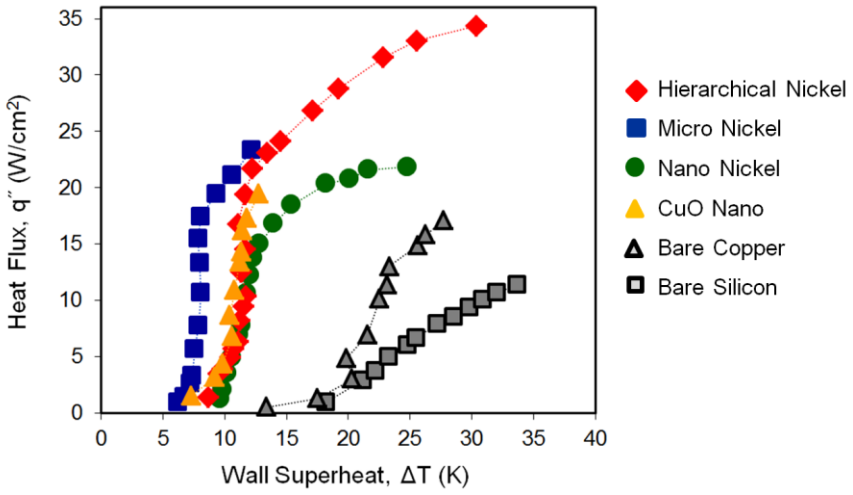

Figure 6.26: Pool boiling heat flux as a function of time for micro, nano and hierarchical surfaces compared with bare silicon and bare copper surfaces.

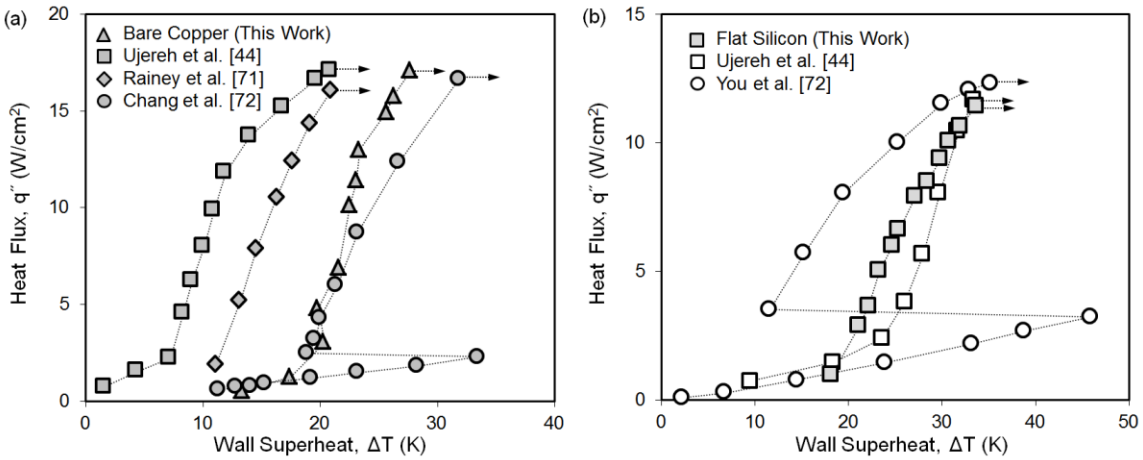

Figure 6.27: Pool boiling heat flux as a function of time for (a) bare copper and (b) bare silicon surfaces compared with literature [44, 71, 72].

Figure 6.27 shows the comparative pool FC 72 boiling heat flux as a function of wall superheat curves for bare copper (Fig. 6.27a) and bare silicon (Fig. 6.27b)

surfaces with the boiling curves in the literature. Although boiling is a complex phenomenon which generates different boiling curves and varies among researchers' results depending on surface finish, and experimental methods, and nucleation, it can be seen that the reference boiling results presented here are in good agreement in terms of both CHF and HTC at CHF.

6.6.3 *Effect of Wickability on CHF*

The effect of wickability on pool boiling CHF for structured surfaces is presented in Fig. 6.28 in non-dimensional form.

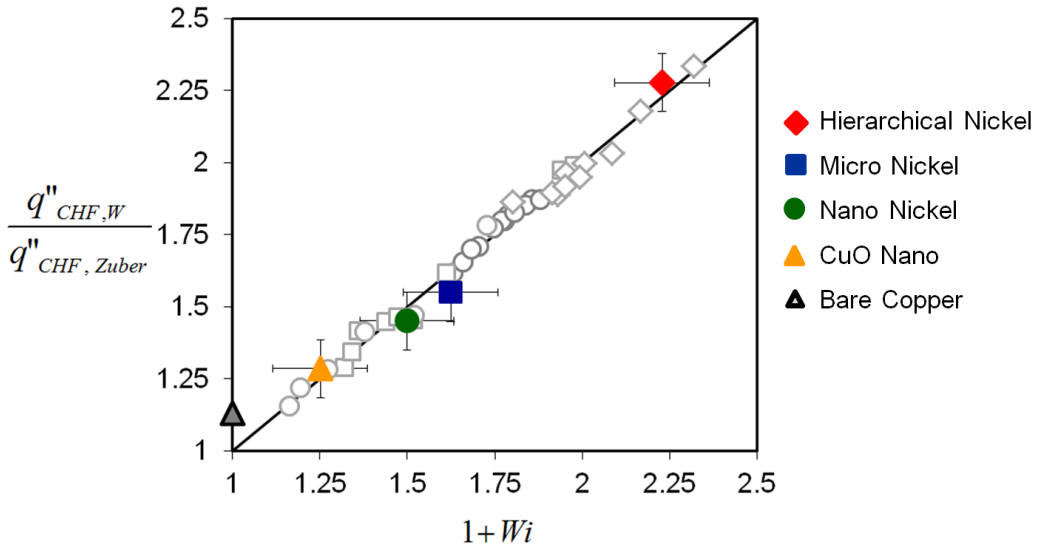

Figure 6.28: Effect of wickability on CHF using water (gray data) and FC 72 (color data) as the working fluid. Experimentally measured CHF enhancement as a function of wicking number, *Wi*, for structured surfaces showing excellent agreement with the developed correlation.

Here, the Y-axis is the CHF for wicking structures non-dimensionalized with Zuber's [23] hydrodynamic CHF limit, and X-axis is the non-dimensional wicking

number which contains the experimentally measured wicked volume flux. The solid black line represents the experimentally validated CHF correlation based on wickability, developed for water in section 6.7, and the gray dots are the data for structured surfaces with water as presented in section 6.7. It can be seen from Fig. 6.28 that the CHF correlation based on wickability can still accurately capture the CHF enhancement for structured surfaces during boiling. This demonstrates the validity of experimentally developed CHF correlation for structured surfaces based on capillary wicking using highly wetting fluid FC 72, and the validity of non-dimensional grouping of both CHF and wicked volume flux.

6.7 Conclusions

A biotemplated nanofabrication technique based on the self-assembly and metallization of the *Tobacco mosaic virus* (TMV) has been used to fabricate numerous superhydrophilic surfaces with large variations in wickability, surface morphology, and roughness factor. More than 700% HTC enhancement has been reported by adding engineered nucleation sites on superhydrophilic nanostructured surfaces. The wickability of each surface has been experimentally measured along with its CHF, and a distinct dependency between the two is seen. The results are consistent with predictions using a simple wicking model, as well as data from the open literature. This work shows that the wickability of a surface can be quantified and accurately characterized as the maximum wicked volume flux capable of being drawn into the structures and transported past the apparent liquid-vapor-solid contact line on a surface. The experimentally verified correlation relating CHF and wicked volume flux shows excellent agreement for three dozen independent samples fabricated for this work including those with variations in

scale (micro, nano, and hierarchical), substrate material (silicon, aluminum, stainless steel, and copper), nanostructure density, roughness factor, degradation due to fouling, as well as structure material and morphology (etched silicon microposts, virus-templated nickel nanostructures, and copper oxide nanostructures). Biotemplated nanofabrication technique has been optimized based on nickel deposition time for fabrication of robust nickel nanostructures. Finally, the wickability enhanced CHF correlation is validated using alternate fluid other that water, here highly wetting fluid FC 72.

1. Wickability is demonstrated to be the single key factor in dictating critical heat flux on structured superhydrophilic surfaces with negligible contact angles.
2. An experimentally validated non-dimensional correlation for CHF enhancement, including the definition of the dimensionless wicking number, *Wi* has been developed.
3. Nickel deposition time has been optimized for biotemplating nanofabrication process based on surface wickability and pool boiling CHF.
4. Wickability enhanced CHF correlation has been validated using FC 72 in addition to water which suggest that this empirical correlation is valid for alternate fluids as well.

Publications:

M.M. Rahman, E. Ölçeroğlu, and M. McCarthy, "The Role of Wickability on the Critical Heat Flux of Structured Superhydrophilic Surfaces", *Langmuir*, 2014, 30 (37), pp 11225–11234

CHAPTER 7: BOILING ENHANCEMENT ON MULTISCALE AND HETEROGENEOUS STRUCTURED SURFACES

7.1 Introduction and Overview

This chapter investigates the role of engineered nucleation sites and the effect of structure length scale on CHF and HTC enhancement during pool boiling. Significant enhancement in both CHF and HTC has been reported for single length scale nanostructures [2, 9, 28, 41, 42, 64, 73-76], microstructures [8, 12, 13, 26, 27, 36, 39, 77], and multiple length scale hierarchical structures [11, 14, 37, 39, 57, 78-80], and surfaces with mixed wettability [10, 43] during pool boiling. This substantial enhancement in heat transfer has been attributed to increased wickability, wettability, nucleation site density, surface roughness, controlled liquid vapor flow field.

While the enhancement in pool boiling heat transfer has been achieved through several different techniques by fabricating various enhanced surfaces, this dissertation focuses on separating these individual effects and characterizes them. The Chapter 6 of this dissertation investigates the role of wickability, and roughness factor on CHF for homogeneous structures with characteristic lengths much smaller than the inherent flow structures (~ 1mm), and identifies that capillary wicking through surface structures is the single factor determining the critical heat flux (CHF).

This chapter focuses on heterogeneous surfaces which are demonstrated to increase both CHF and HTC during pool boiling. Heterogeneous structures such as mixed wettability surfaces with structure characteristic lengths much smaller than the inherent flow structures (~ 1mm), are shown to substantially increase the pool boiling HTC [10,

43]. Hence, the first part of this chapter investigates the role of these engineered nucleations site on both CHF and HTC.

Separately, it has been shown that structured surfaces such microchannel geometries with length scales comparable to the flow yield significant enhancement in both CHF and HTC [11, 26, 27]. By adding structures much smaller than the flow with structures comparable to flow, the enhancement mechanism becomes more complicated enhancement mechanisms with each length scale contributing differently. Hence, the combination of the two has been incorporated in the second part of this chapter and demonstrated the effect of each length scale structures during pool boiling enhancement. Nanoscale structures are identified to enhance CHF, while micro-to-milli scale structures have been found to enhance nucleation and therefore heat transfer coefficient (HTC) of these heterogeneous hierarchical surfaces.

7.2 Effect of Engineered Nucleation Sites

This section investigates the role of engineered nucleation sites on pool boiling heat transfer enhancement. A series of mixed wettability surfaces have been fabricated on silicon substrates, and reentrant cavities have been incorporated on the metallic nanostructured surfaces and characterized during pool boiling with water. The experimental test setup and procedure are explained in section 4.1.

7.2.1 *Super-bi-philic Surfaces*

To promote nucleation at low wall superheats, engineered nucleation sites have been added to the superhydrophilic surfaces. *Tobacco mosaic virus* (TMV) based

biotemplated nanofabrication discussed in the Chapter 5 is utilized to fabricate superhydrophilic nickel nanostructures on gold coated silicon surfaces.

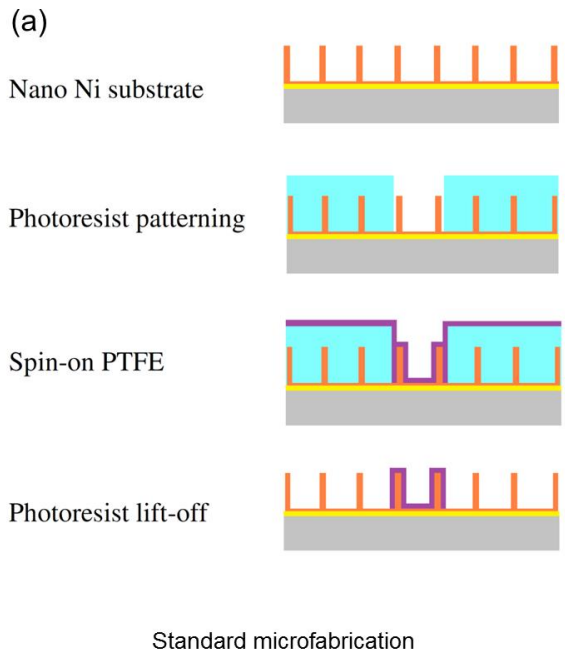

(b) Super-bi-philic TMV-structured Surfaces

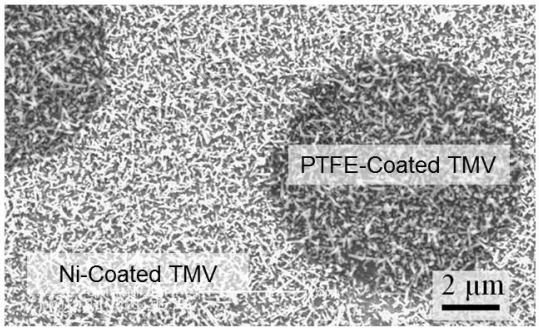

(c) Different super-bi-philic designs

Diam. (µm)	***Pitch*** (µm)	***Area Ratio***
5	10	20 %
5	30	2 %
5	50	1 %
15	30	20 %
45	90	20 %

Figure 7.1: Fabrication and designs of super-bi-philic nickel nanostructured surfaces. (a) Steps of standard microfabrication, (b) SEM image of a super-bi-philic design where dark regions are superhydrophobic nickel nanostructures and lighter regions are superhydrophilic nickel nanostructures, and (c) different super-bi-philic designs with varied hydrophobic dot size and center-to-center spacing.

Traditional photolithography, as shown in Fig. 7.1a, is conducted using Shipley 1813 spun at 3000 rpm, exposed at 18 mW/cm^2 for 10 seconds, and developed in MF351 solution diluted at a ratio of 1:3 for 30 seconds. This creates open dots onto nanostructures covered with photoresist everywhere else. Spin-on Teflon is then applied onto the photoresist patterned surfaces. After the lift-off step of positive photoresist, the

surfaces are baked at 155 °C for 5 minutes to form ~ 10 nm Teflon coating onto the structures. Figure 7.1b presents the SEM image of a super-bi-philic design where dark regions are superhydrophobic PTFE coated nickel nanostructures and lighter regions are superhydrophilic nickel nanostructures. Total five different super-bi-philic designs with varied superhydrophobic dot size and center-to-center spacing are fabricated as shown in Fig. 7.1c.

7.2.2 *Nanostructured Surfaces with Engineered Nucleation Sites*

Traditional CNC milling is used to fabricate engineered nucleation sites on copper and aluminum surfaces. For copper surface, 65 mL NH_4OH aqueous solution diluted with 200 mL DI water based nanofabrication technique is used to fabricate CuO micro/nanostructures on copper, as shown in Fig. 7.2a. Then CNC milling is used to create deep holes onto the nanostructured copper surfaces (Fig. 7.2b). Two different engineered nucleation site designs with fixed cavity size and varied center-to-center spacing are incorporated in this work. The details of different engineered copper surfaces are shown in Fig. 7.2c. TMV based biotemplated nanofabrication is utilized to fabricated nickel nanostructures on aluminum (Fig. 7.3a). Finally CNC milling is used to create cavities on the nanostructured aluminum surfaces (Fig. 7.3b). Figure 7.3c presents four different engineered surface designs with varied cavity size, center-to-center pitch, and cavity depth.

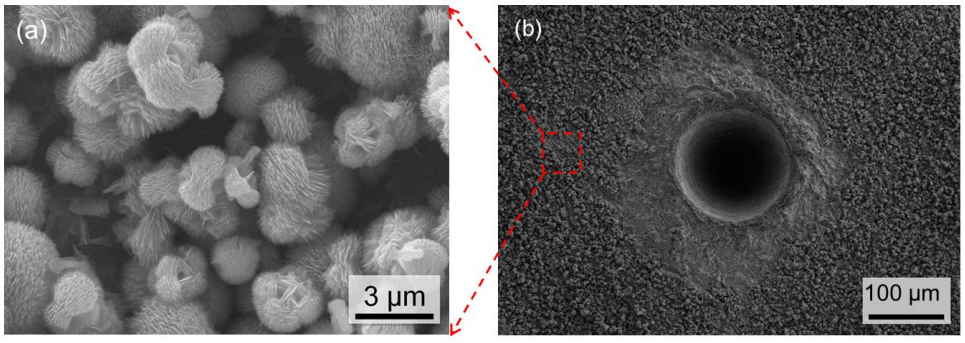

(c)

Diam. (µm)	***Pitch*** (µm)	***Depth*** (µm)	***Area Ratio***
120	300	150	13 %
120	600	150	3 %

Figure 7.2: Fabrication and designs of engineered nucleation sites on copper nanostructured surfaces. (a) SEM images of CuO micro/nanostructured surfaces (b) machined cavities onto the structured surface, and (c) different engineered nucleation site designs.

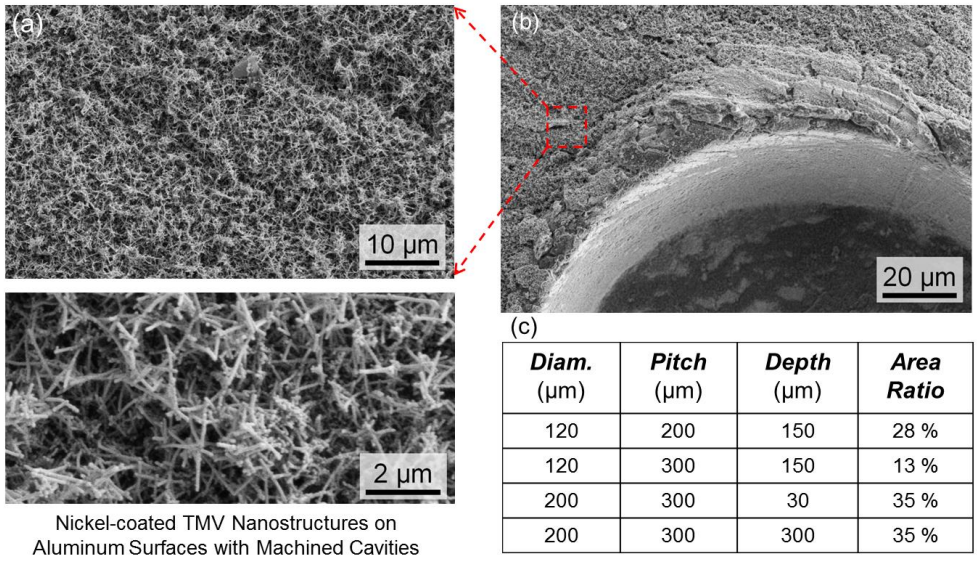

(c)

Diam. (µm)	***Pitch*** (µm)	***Depth*** (µm)	***Area Ratio***
120	200	150	28 %
120	300	150	13 %
200	300	30	35 %
200	300	300	35 %

Figure 7.3: Fabrication and designs of engineered nucleation sites on nanostructured aluminum surfaces. (a) SEM images of nickel nanostructures (b) machined cavities onto the structured surface, and (c) different engineered nucleation site designs.

7.2.3 *Pool Boiling Results*

Figure 7.4 shows the pool boiling curves for fabricated super-bi-philic surfaces and compared with the heat dissipation performance of nanostructured and flat surfaces. It can be seen from Fig. 7.4a that flat silicon surface reaches a CHF of 78 W/cm^2 whereas nickel nanostructured surface gives CHF of 196 W/cm^2 due to increased wickability as demonstrated in Chapter 6. When the superhydrophobic dots are incorporated on the superhydrophilic surfaces, maximum HTC as shown in Fig. 7.4b is significantly increased. Interestingly, although HTC increases substantially, CHF for all super-bi-philic designs are seen to be decreasing compared to nanostructured superhydrophilic surfaces. While the enhancement in HTC can be attributed to onset of nucleation at low wall superheat temperatures and increased nucleation site density, the reduction in CHF can be attributed to reduction in active wicking areas on the surfaces.

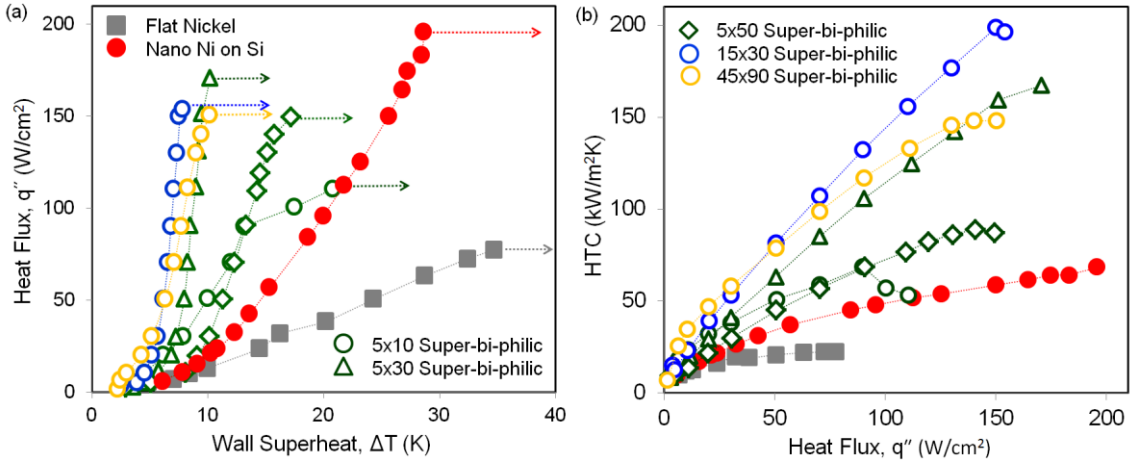

Figure 7.4: Pool boiling heat transfer performance of super-bi-philic surfaces. (a) Heat flux as a function of wall superheat. (b) HTC as a function of heat flux.

Figure 7.5 presents the HTC as a function of heat flux for surfaces with engineered nucleation sites on copper (Fig. 7.5a), and surfaces with engineered nucleation sites on aluminum (Fig. 7.5b). As can be seen from Fig. 7.5a, CuO micro/nanostructures increases both CHF and HTC compared to bare copper surface, and the maximum enhancement in both CHF and HTC for surfaces with engineered nucleation sites was obtained for the reentrant cavity design of 120 micron diameter, 300 micron pitch and 150 micron depth.

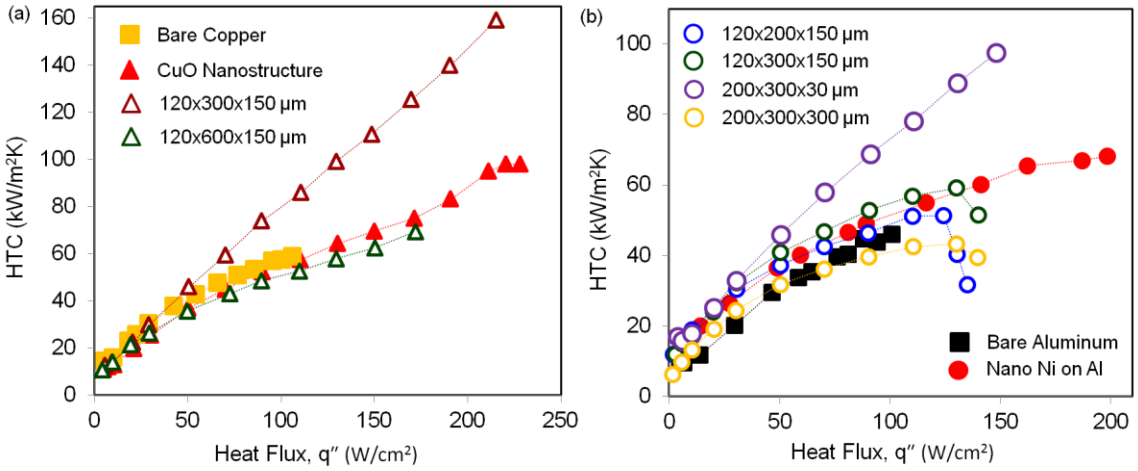

Figure 7.5: Pool boiling heat transfer performance of super-bi-philic surfaces. (a) Heat flux as a function of wall superheat. (b) HTC as a function of heat flux.

HTC as a function of heat flux for surfaces with engineered nucleation sites on biotemplated nickel nanostructures are shown in Fig. 7.5b. The maximum enhancement in HTC is attained for the surfaces with 200 µm diameter, 300 µm center-to-center spacing, and 30 µm deep re-entrant cavity designs. Also, HTC enhancement is observed for surfaces with small spacing and shallow cavity designs. The reduction in CHF compared to nanostructured superhydrophilic surfaces due to added nucleation sites is

also observed for surfaces with engineered nucleation sites on both copper and aluminum.

7.2.4 *Effect of Engineered Nucleation Sites on HTC*

Figure 7.6 presents the maximum HTC as a function of CHF for all engineered surfaces compared to boiling results for mixed wettability surfaces available in the literature [10]. It can be seen that by adding superhydrophobic dots on superhydrophilic surface, HTC can be significantly increased up to HTC~ 210 kW/m^{2}K. Engineered nucleation boiling results show that by adding these sites, even though HTC increases significantly, this enhancement occurs with the penalty of reduction in overall CHF compared to a superhydrophilic nanostructured surface. The optimized HTC enhancement with less reduction in CHF can be achieved for a macro-machined copper oxide nanostructured surface with a design of 120 µm cavity diameter, 300 µm cavity center-to-center spacing and 150 µm cavity depth.

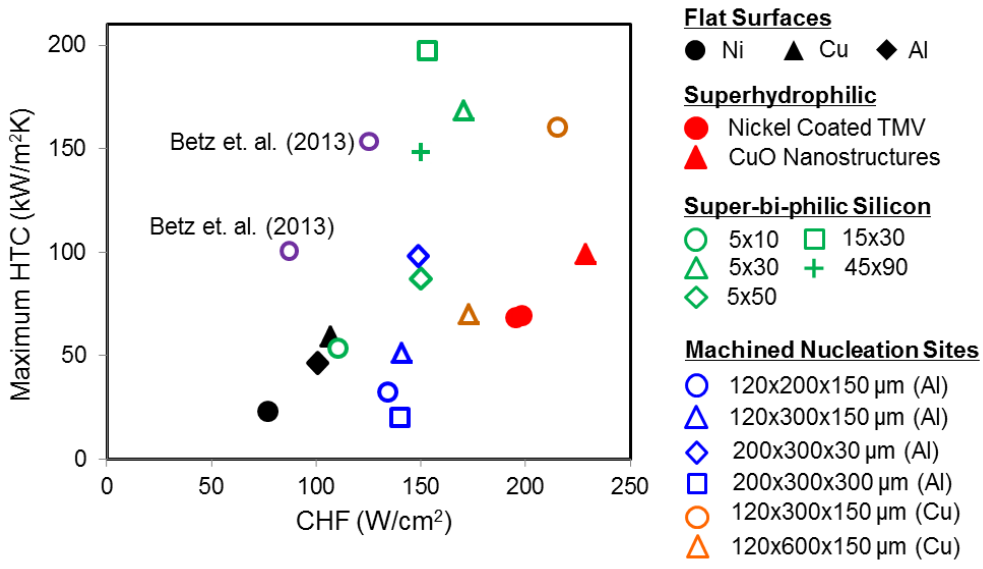

Figure 7.6: Maximum HTC as a function of CHF for all engineered nucleation surfaces.

7.2.5 *Effect of Engineered Nucleation Sites on Wickability and CHF*

The effect of wickability on pool boiling CHF for heterogeneous structured surfaces with engineered nucleation sites is presented in Fig. 7.7 in non-dimensional form. Here, the Y-axis is the CHF for wicking structures non-dimensionalized with Zuber's [23] hydrodynamic CHF limit, and X-axis is the non-dimensional wicking number which contains the experimentally measured wicked volume flux. The solid black line represents the experimentally validated CHF correlation based on wickability, developed for water in section 6.7, and the gray dots are the data for structured surfaces with water as presented in section 6.7.

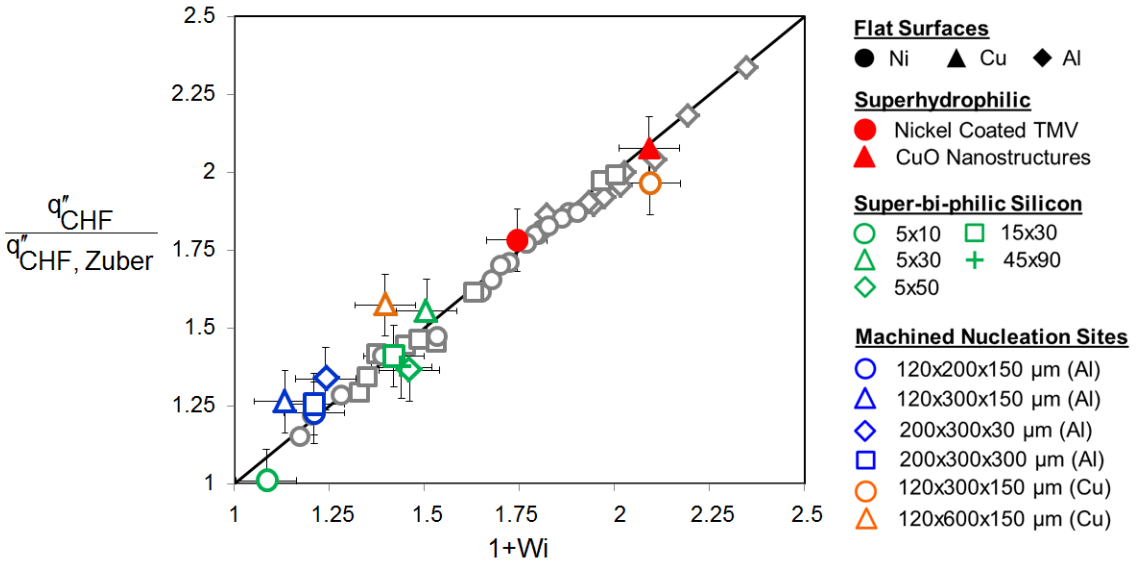

Figure 7.7: Effect of wickability on CHF enhancement for surfaces with engineered nucleation sites. Previously reported data is shown with light grey symbols.

The capillary wicking tests were conducted for these structured surfaces with water using the capillary wick test described in section 6.3. Although by adding engineered nucleation sites onto structured surfaces, HTC increases significantly, this

enhancement occurs with the penalty of CHF due to reduced wicking areas. Still, as can be seen from Fig. 7.7, the CHF correlation based on wickability can still accurately capture the CHF enhancement for structured surfaces during boiling. This demonstrates the validity of experimentally developed CHF correlation for structured surfaces based on capillary wicking for heterogeneous structures, and the validity of non-dimensional grouping of both CHF and wicked volume flux.

7.3 Multiscale Surfaces

While the nanostructures are shown to increase CHF through increased capillary wicking and microchannel geometries are used to increase both CHF and HTC, this section has incorporated both length scale structures. The heat performances of individual nanostructures, microchannel geometries, and the combined hierarchical surfaces have been analyzed during pool boiling. The enhancement mechanism for these substantially different structures with characteristic length scale much smaller and comparable to flow length scale are identified and reported in this section.

7.3.1 *Microchannel Surfaces*

To study the effect of structure length scale, five different microchannel designs, structure scale comparable to flow scale (~ 1mm), as shown in Fig. 7.8 were patterned on bare copper using Wire EDM (Electrical Discharge Machining). A 70 mm × 70 mm × 4 mm copper block was patterned with 0.254 mm thick wire at a minimum spark gap of 0.381 mm ± 0.127 mm and diced into 20 mm × 20 mm × 1 mm chips using wire EDM. Finally the chips were diced into 10 mm × 10 mm using shearing metal cutter. Fig. 7.8a shows surfaces with four and ten microchannel embedded in copper. M

represents microchannel only surface and the number after that represent the number of channels patterned. The microchannel width and maximum depths are defined in Fig. 7.8b and dimensions of various designs fabricated are presented in Fig. 7.8c.

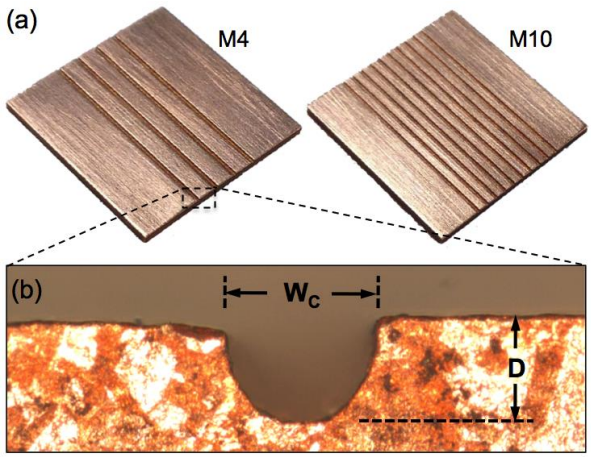

(c) Name	M2	M4	M6	M8	M10
# Channels	2	4	6	8	10
W_C (mm)	0.42	0.43	0.42	0.42	0.42
D (mm)	0.29	0.25	0.29	0.31	0.30
W_F (mm)	3.28	1.90	1.38	0.97	0.78
Area Ratio	1.14	1.25	1.43	1.52	1.65

Figure 7.8: Channels patterned using Wire EDM. (a) Digital camera image of 4-channels and 10-channels designs (b) optical microscope image of a channel showing channel width and channel maximum depth, and (c) the dimensions of all five channel surface designs.

7.3.2 *Nanostructured CuO Surfaces*

Four different copper oxide (CuO) nanostructures were fabricated for this work. Elevated temperature (70 °C) alkaline solution based needle like copper oxide (CuO-1) nanostructured surfaces were fabricated as described by Love et al. [70]. For this, bare Cu surfaces cleaned with 2% HCl for 10 minutes and DI water were submersed

in a solution bath of $NaClO_2$, NaOH, DI water (16:1:100 wt %) for 10 minutes to fabricate CuO-1 nanostructured surfaces. Flowerlike CuO nanostructures (CuO-2) were fabricated using a room temperature alkaline solution. Pre-cleaned surfaces with HCl and DI water were submerged in the sodium phosphate buffer consisting Na_2HPO_4, NaH_2PO_4, DI water (0.91:0.56:100 wt %) for 24 hours.

Sharp blade like (1-1.5 μm height) nanostructures (CuO-3) were fabricated at an elevated temperature (96 °C) as described by Chu et al. [37]. A chemical bath composed of $NaClO_2$, NaOH, $Na_3P0_4.12H_20$, DI water (3.75:5:10:100 wt %) mixture was used for oxide reaction on copper surfaces for 10 minutes. 3D hierarchical patterned copper oxide nanostructures (CuO-4) were synthesized using a single step 60 °C ammonia solution bath [81]. The chemical bath was composed of 65 mM NH_4OH diluted in DI water and the chemical reaction was conducted for 20 hours to fabricate the CuO-4 nanostructures. Detailed fabrication processes and SEM images of fabricated surfaces are summarized in Fig. 7.9.

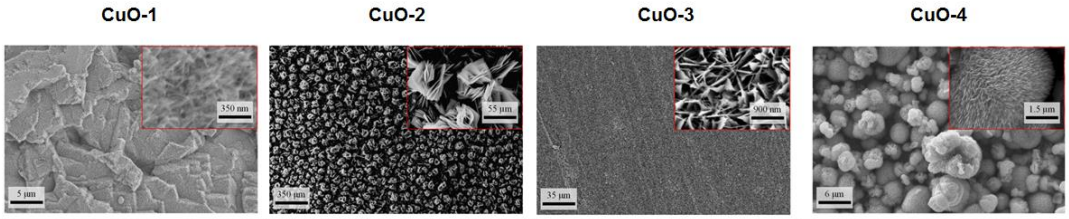

	CuO-1	CuO-2	CuO-3	CuO-4
Bath	$NaClO_2$, NaOH, DI water (16:1:100 wt %)	Na_2HPO_4, NaH_2PO_4, DI water (.91:.56:100 wt%)	$NaClO_2$, NaOH, $Na_3P0_4.12H_20$, DI water (3.75:5:10:100 wt %)	65 mM NH_4OH diluted in DI water
Temp	70 °C	Room Temperature	96 °C	60 °C
Time	10 min	24 h	10 min	20 h

Figure 7.9: SEM images and chemical bath composition, reaction temperature and time for different CuO nanostructures (CuO-1 to CuO-4).

7.3.3 *Multiscale Surface*

Five different microchannel surfaces were cleaned with 2% HCl for 10 minutes, triple rinsed with DI water, dried with dry N_2 and submerged in four different CuO chemical baths (as discussed in section 7.3.2) to fabricate twenty different hierarchical channel surfaces. Figure 7.10 presents SEM images of four different nanostructures and two different hierarchical surfaces at different views to demonstrate conformal coating of the nanostructures inside the channels and on copper fins.

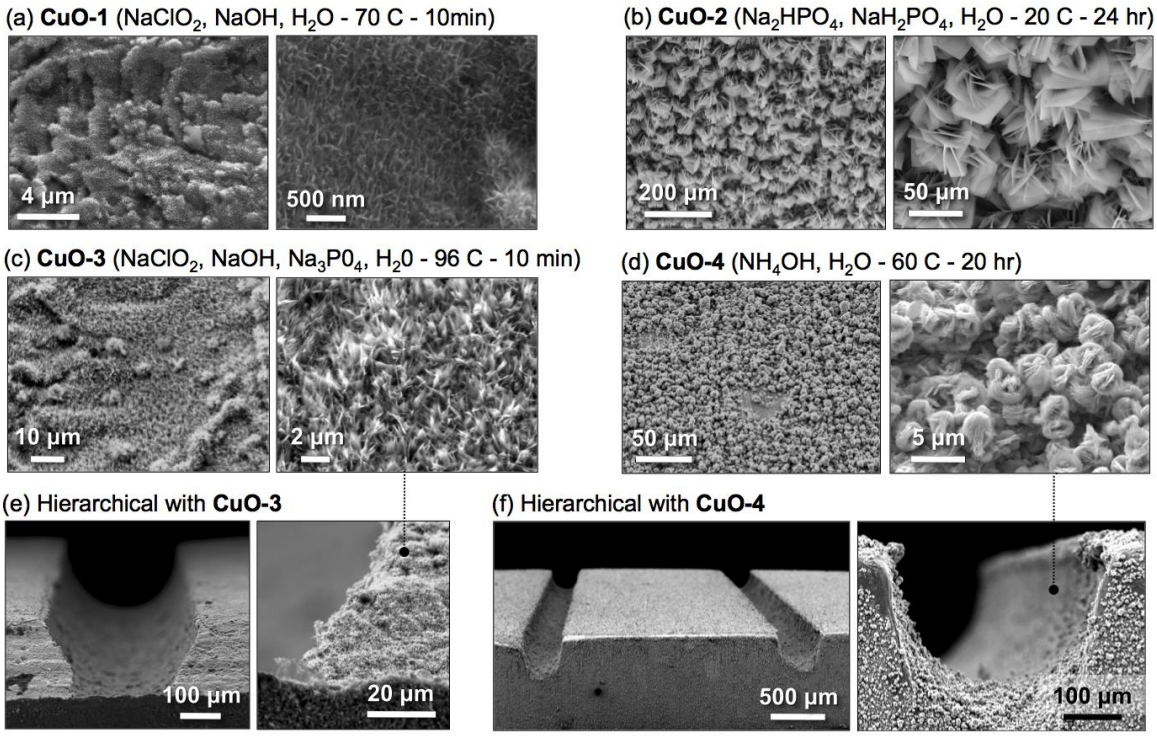

Figure 7.10: Different CuO superhydrophilic nanocoatings on various channel surfaces. Fabrication results for different CuO nano coatings on bare copper (a) CuO-1, (b) CuO-2, (c) CuO-3, (d) and CuO-4 at various magnifications. Side-view SEM images of (e) CuO-3 nanocoated channel and side wall, and (f) CuO-4 nanocoated channel surface.

7.3.4 *Boiling Results on Single Length Scale Surfaces*

In this section, heat transfer performance for all single length scale surfaces has been characterized during pool boiling. Heat flux as a function of wall superheat, and heat transfer coefficient (HTC) as a function of heat flux for bare Cu, five different microchannel and four different nanostructured surfaces are plotted in Figure 3a and 3b respectively. The CHF value for the bare Cu is roughly 117 W/cm^2, which is consistent with the literature bare Cu boiling [2, 26-28]. As can be seen, the microchannel increases both CHF (~ 200 W/cm^2) and HTC (~ 186 kW/m^{2}K for M8). This enhancement of heat transfer through microchannel is also observed in the literature where they attributed to the increased evaporation momentum through increased nucleation sites, microconvection and ordered liquid and vapor flow field for this enhancement [26, 27].

It can be seen that by adding nanostructures, CHF can be significantly increased ranging from 141 W/cm^2 to 228 W/cm^2 while HTC is decreasing compared to bare Cu surface. The enhancement in CHF for nanostructured surfaces can be attributed to the enhancement in capillary wicking as shown in Fig. 7.12. All different nanostructured surfaces (CuO-1 to CuO-4) were characterized based on capillary wicking performance as reported in an earlier publication [39], and Chapter 6. As can be seen, the nanostructures are widely different in terms of both capillary wicking and CHF which were used to investigate of effect of length scale on boiling heat transfer performance. The decrease in HTC for CuO-1 to CuO-3 surfaces in Fig. 7.11 attributes to suppression of nucleation sites from naturally rough bare Cu by adding these nanostructures. The best performing nanostructure CuO-4 (CHF~ 228 W/cm^2) shows a better performance in HTC

(~98 kW/m^{2}K) at the CHF value due to its addition nucleation features at the micro/nanoscale of this copper nanostructure surface.

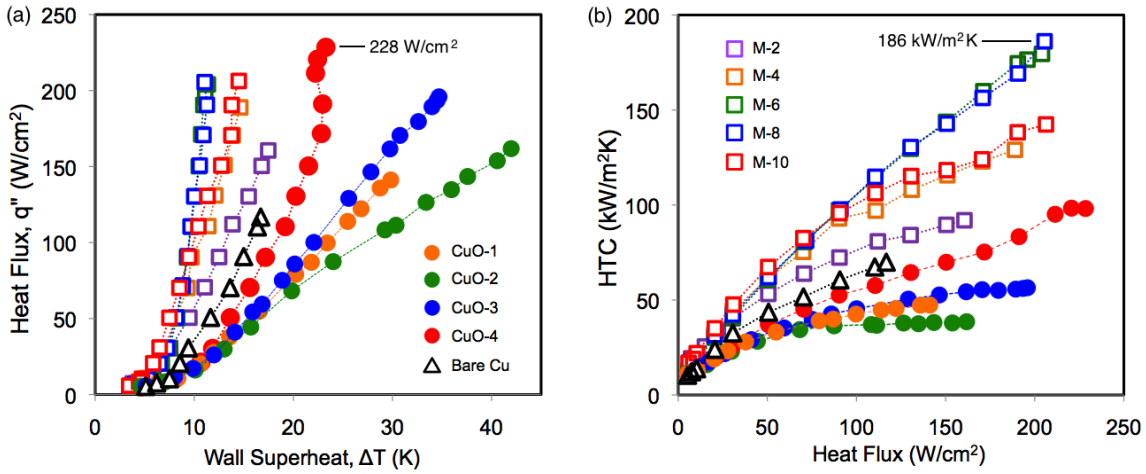

Figure 7.11: Enhanced heat transfer during pool boiling using all CuO nanocoatings and channel surfaces. Experimental results of (a) heat flux as a function of superheat, and (b) heat transfer coefficient as a function of heat flux.

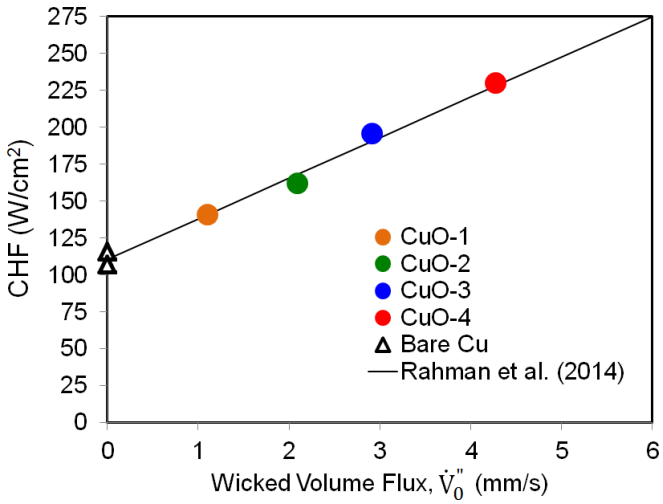

Figure 7.12: CHF as a function of liquid initial volume flux for CuO nanostructured surfaces.

Interestingly, as can be seen from Fig. 7.11a, pool boiling curves are shifted to the right of bare copper boiling curve, and curves for microchannel designs are shifter to the left. This suggests that nanostructures increase heat transfer through capillary wicking and microchannel increase heat transfer through nucleation and enhanced bubble dynamics.

7.3.5 *Boiling Results on Multiscale Surfaces*

Pool boiling results for all hierarchical copper microchannel surfaces are presented in this section. Figure 7.13 to Figure 7.16 shows the heat flux as a function of wall superheat, and heat transfer coefficient as a function of heat flux for respectively nano CuO-1, CuO-2, CuO-3, and CuO-4 based hierarchical surfaces.

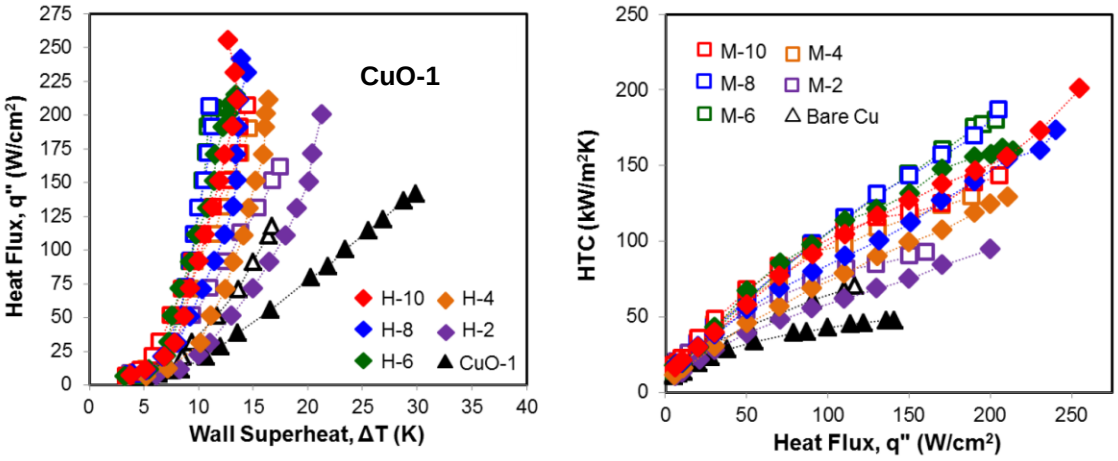

Figure 7.13: Pool boiling curves for CuO-1 based surfaces (a) heat flux as a function of wall superheat, and (b) HTC as a function of heat flux.

As can be seen from Fig. 7.13 and Fig. 7.14, although the CHF and HTC for all multiscale surfaces have increased for both copper nanostructures, this enhancement is independent of the nanostructure performance. The capillary wicking for both CuO-1 and CuO-2 nanostructured surfaces are different as shown in Fig. 7.12. Although the addition

of nanostructures increases CHF by increasing wicking, the pool boiling curves for multiscale surfaces based on CuO-1 and CuO-2 nanostructures are dominated by microchannel boiling. This suggests the indifferent heat transfer enhancement for these two different nanostructure coated multiscale surfaces.

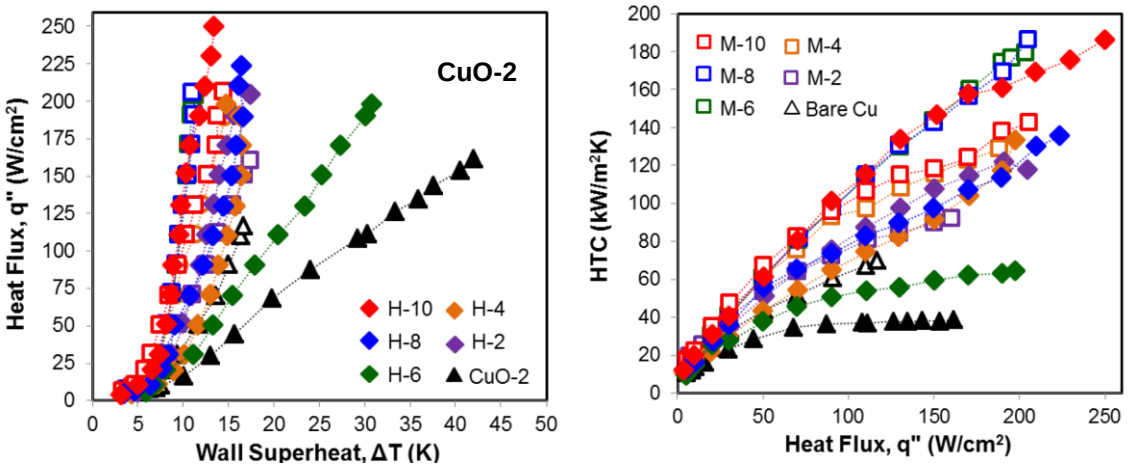

Figure 7.14: Pool boiling curves for CuO-2 based surfaces (a) heat flux as a function of wall superheat, and (b) HTC as a function of heat flux.

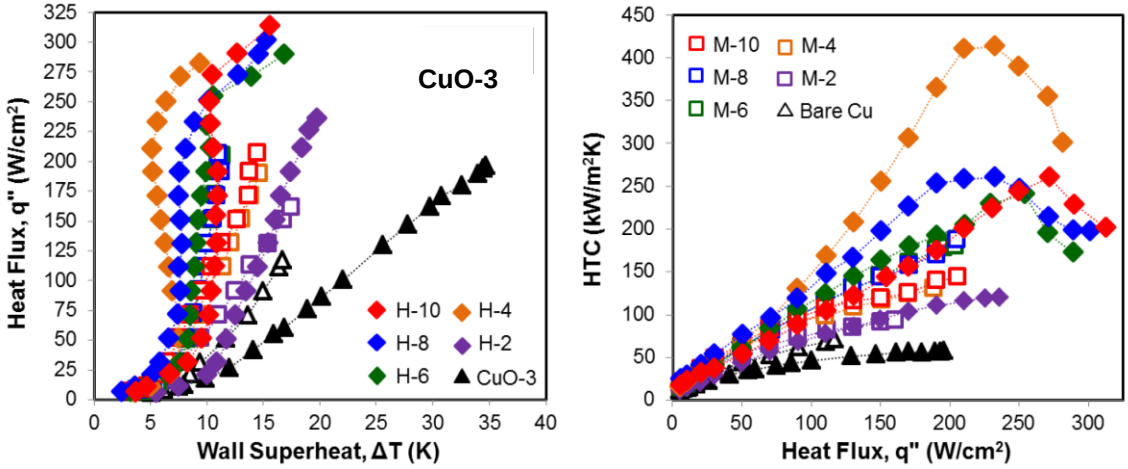

Figure 7.15: Pool boiling curves for CuO-3 based surfaces (a) heat flux as a function of wall superheat, and (b) HTC as a function of heat flux.

Figure 7.15 shows the heat transfer performance of CuO-3 nanostructure based hierarchical surfaces. Heat flux as a function of wall superheat for is presented in Figure 7.15a and HTC as a function of heat flux is presented in Fig. 7.15b. It can be seen that by adding a higher wicking nanostructures (CHF~ 196 W/cm^2) onto copper microchannel surfaces, CHF is significantly increased to 236 W/cm^2 for only 2 channels hierarchical surface while 4, 6, 8, and 10 channel hierarchical surfaces shows CHF values ranging from 280 W/cm^2 to 313 W/cm^2. A maximum CHF of ~ 313 W/cm^2 was achieved for 10 channel CuO-3 hierarchical surface. More than 5.9 fold HTC (~ 413 kW/m^2 K) enhancement compared to bare Cu surface was achieved for a 4 channel CuO-3 based hierarchical surface while other designs provides HTC varying from 120 kW/m^{2}K to 260 kW/m^{2}K. It can also be seen that all the multiscale surfaces based on CuO-3 nanostructures, pool boiling curves follow similar trend. A rapid increase in heat transfer is observed initially, and then HTC is decreasing at the later stages of boiling.

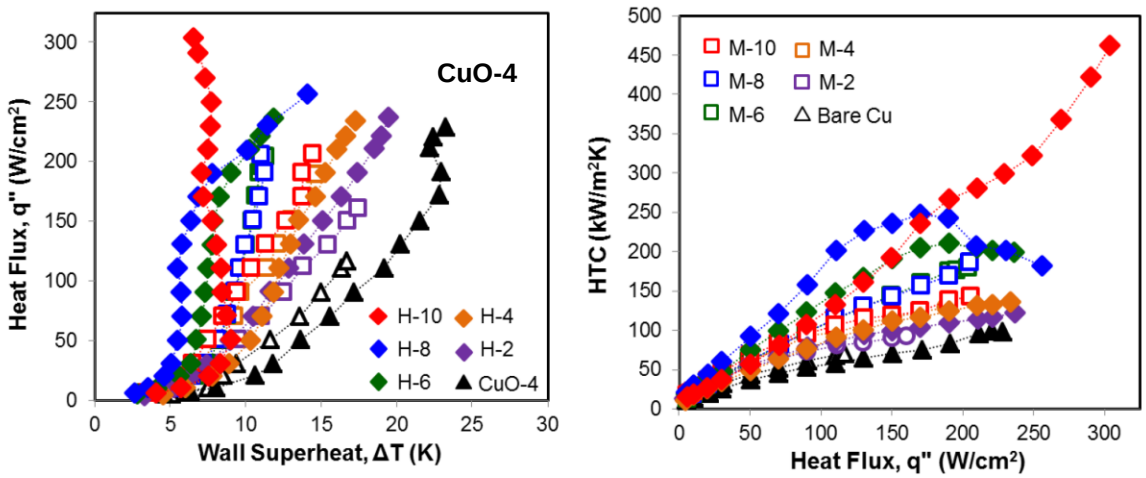

Figure 7.16: Pool boiling curves for CuO-4 based surfaces (a) heat flux as a function of wall superheat, and (b) HTC as a function of heat flux.

CuO-4 based hierarchical microchannel surface boiling results are presented in Fig. 7.16. A maximum CHF value of 304 W/cm^2 with a maximum HTC value of 462 kW/m^{2}K was achieved for the 10 channel CuO-4 hierarchical surface. It can be seen that by increasing the number of channels along with this hierarchical nanostructures, CHF and HTC both increases due to increased surface wickability, microconvection, nucleation site density, and controlled liquid and vapor flow field [26, 27, 82, 83]. The pool boiling curves for all multiscale surfaces based on CuO-4 nanostructures are also similar as the surfaces with CuO-3 based multiscale surfaces except four channel hierarchical surface. As explained for CuO-3 based surfaces, this initial enhancement in heat transfer is dominated by the microchannel boiling whereas the later stage of boiling enhancement is mostly due to the nanostructure wicking.

Figure 7.17 presents heat flux as a function of wall superheat for a bare Cu, CuO-3 nanostructured, CuO-4 nanostructured, 10 channels microstructured (M-10), and 10 channels hierarchical (H-10) surfaces depicting the heat transfer enhancement mechanisms and repeatability for multiscale surface boiling. Figure 7.17a is based on CuO-3 nanostructures and Fig. 7.17b is based on CuO-4 nanostructures. It can be seen that for the hierarchical surface at heat flux over 50 W/cm^2, there is a near vertical behavior in heat transfer which is consistent with the microchannel only surface due to rapid generation of nucleation sites and enhanced bubble dynamics. This happens until around 200 - 250 W/cm^2 after which the boiling curve shares similar heat transfer gradient as of nanostructured surfaces. This implies that after this heat flux, apparently further bubble nucleation halts and enhanced wicking by the nanostructures delays dry-out by providing more fluid to the nucleated regimes which further increases the CHF.

This boiling phenomenon is very well consistent with all CuO-3 based hierarchical surface boiling exceeding heat flux of 250 W/cm^2. The rapid bubble formation and hemi-wicking based heat transfer enhancement mechanism can also be observed for CuO-4 based hierarchical surfaces (H2 to H8) where the transition occurs after 200 W/cm^2. This can be attributed to the rapid bubble explosion of the nanostructures which is also seen from the CuO-4 nanostructure boiling after heat flux of 200 W/cm^2. On contrary, CuO-4 based 10 channels multiscale surface (H-10) shows continuous bubble nucleation until CHF which is also consistent with the literature and might be due to the addition nucleation sites and enhanced bubble dynamics promoted by hierarchical shaped CuO-4 nanostructures [11, 26, 27].

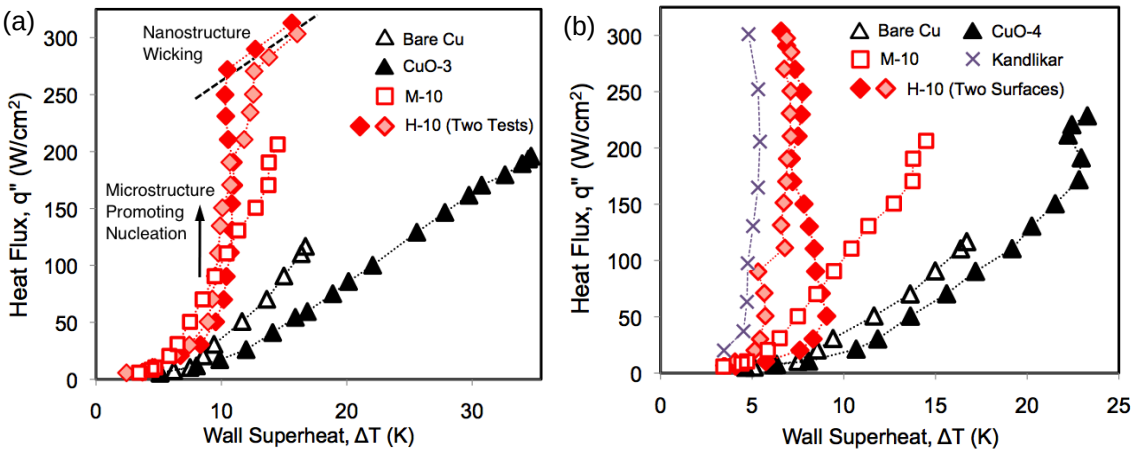

Figure 7.17: Heat transfer mechanism for (a) CuO-3 and (b) CuO-4 based hierarchical channel surfaces showing rapid bubble explosion in the channel dominated boiling regimes and nanostructure wicking dominated delayed dry-out regimes.

7.3.6 *Effect of Channel on CHF and HTC*

Figure 7.18 presents the summary of pool boiling results for all micro, nano and hierarchical surfaces. CHF as a function of number of channels and maximum HTC

as a function of number of channels are shown in Figure 7.18a and 7.18b respectively. Open symbols represent bare and microchannel surfaces and closed symbols represent hierarchical microchannel surfaces. It can be seen that by increasing the number of channels, CHF increases up to 6 channels compared to bare copper surface after which CHF levels off for 8 and 10 channel surfaces at the CHF of 6 channel surfaces. This implies that for a fixed channel width and channel depth, the effect of fin width has lower effect on heat transfer enhancement after a certain fin width (1.38 mm for 6 channel surface) which is also consistent with the boiling results reported by Cooke et al. [26]. HTC results as shown in Fig. 7.18b also shows that HTC increases until 6 channel surfaces after which HTC levels off for 8 channel surface and for 10 channel surface, HTC becomes lower due to significant decrease in fin width for constant channel width and depth which is similar with the argument presented by Cooke et al. [26].

It can also be seen that by adding nanostructures on bare Cu surface, CHF increases with increasing surface wickability whereas HTC is higher only for CuO-4 surface due to additional nucleation sites added by CuO micro/nanostructures. Hierarchical channel surfaces with lower wicking CuO nanostructured (CuO-1 and CuO-2) surfaces show moderate or nearly no enhancement in both CHF and HTC. By adding higher wicking nanostructures (CuO-3 and CuO-4), both CHF and HTC increases by increasing the number of channels demonstrating a maximum CHF of 313 W/cm^2 for 10 channel CuO-3 surface and maximum HTC of 462 kW/m^2K for 10 channel CuO-4 surface.

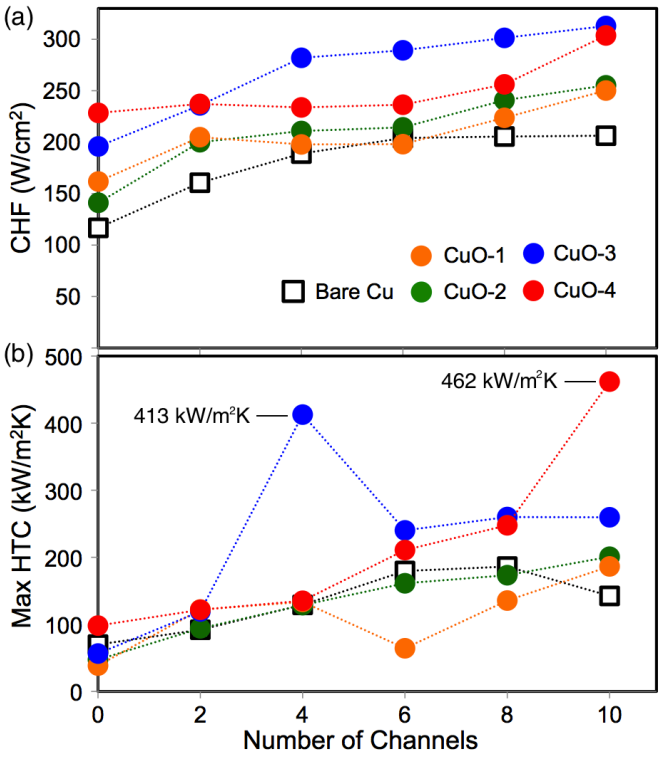

Figure 7.18: Heat transfer enhancement for hierarchical channel surfaces (a) CHF as a function of number of channels, and (b) maximum HTC as a function of number of channels.

7.4 Conclusions

This chapter investigates the effect of engineered nucleation sites and structure length scale on pool boiling heat transfer enhancement. In the first part, biotemplated nanostructured and copper oxide micro/nano superhydrophilic surfaces have been synthesized using solution based nanofabrication techniques. Engineered nucleation sites have been fabricated using traditional photolithography and CNC macromilling. Heat transfer enhancement capabilities are assessed through pool boiling. Significant enhancement in heat transfer coefficient (800%) and critical heat flux (95%) has been achieved with the engineered nanostructured surfaces. Wickability dictates the CHF

enhancement for superhydrophilic surfaces whereas engineered nucleation sites promote heat transfer coefficient through early nucleation.

In the second part of this chapter, solution based nanostructures were incorporated onto the macromachined microchannel structures. Four different nanostructures were deposited on five different microchannel surfaces forming twenty different multiscale structures. Pool boiling enhancement on surface structures from ~100 nm to ~1mm has been investigated. A CHF of 313 W/cm^2 and HTC of 462 kW/m^2K were obtained for multiscale surface.

1. Significant enhancement in HTC has been demonstrated for nanostructured engineered nucleation surfaces.

2. The enhancement in HTC for engineered nucleation surfaces has been achieved with the penalty of reducing the CHF compared to nanostructured surfaces.

3. The reduction in CHF for engineered nucleation surfaces has been attributed to the reduction in wicking areas.

4. Wickability enhanced CHF correlation has been demonstrated to accurately predict CHF for heterogeneous structured surfaces.

5. While the nanostructures with characteristic length much smaller that flow length scale (~ 1 mm) have been shown to increase the CHF by increasing capillary wicking, the microchannel structures with characteristic length comparable to flow length scale increase both CHF and HTC by increasing the nucleation site density, and enhanced bubble dynamics.

6. A Significant increase in CHF and HTC of 170% and 570%, respectively, has been achieved by combining the increasing nucleation site density and increasing capillary wicking through multiscale surfaces.

7. The enhancement of multiscale surfaces suggest that microchannels dominates the initial heat transfer enhancement through rapid nucleation and nanostructures increases heat transfer at the later stages through capillary wicking.

CHAPTER 8: BOILING ENHANCEMENT USING ENGINEERED THERMAL GRADIENTS

8.1 Introduction and Overview

While structured surfaces have been shown to greatly increase boiling heat transfer, the reliability of these approaches for real-world applications is in question do to a variety of factors. All structured surfaces are inherently susceptible to mechanical failure (breaking of the micro/nano-structures), as well as fouling and clogging over time. During boiling, any and all contaminants within the fluid will inevitably be drawn into the structures. This will lead to clogging and filling of the small micro/nano-scale voids, and thus a loss of enhancement [2]. Similarly, the robustness of extremely thin nanostructured coatings ($\leq 1\mu m$) has not yet been demonstrated, leaving the potential for the coatings to be destroyed or altered over time via chemical reactions[84]. The use of low-surface-energy materials to promote nucleation at small superheats has been successfully demonstrated as well [10, 43, 85, 86], however these "bi-philic" surfaces are prone to degradation of the thin non-wetting films. Additionally, they are not effective with all working fluids, in particular highly wetting fluids like FC-72.

These previously demonstrated enhancement techniques rely on surface properties and interfacial phenomena, which are inherently susceptible to degradation. Here we report the enhancement of CHF and HTC using surfaces with in-plane variations in substrate thermal conductivity. These "bi-conductive" surfaces are comprised of rows of low-conductivity epoxy embedded into high-conductivity copper substrates, and therefore rely on bulk properties rather than surface properties to enhance boiling. They

create spatial variations in the surface temperature during boiling, and by tuning the wavelength of these variations to coincide with the capillary length, have shown increases in HTC and CHF of greater than a factor 5x and 2x, respectively. These counterintuitive results are explained by an examination of the resulting liquid and vapor flow fields, as well as enhanced bubble dynamics. This novel enhancement mechanism has not yet been observed or studied, and holds the potential for creating robust and reliable surfaces for high-efficiency and high heat flux boiling applications over long lifetimes.

8.2 Bi-Conductive Surfaces for Tailoring Bubble Dynamics during Boiling

Figure 8.1a-d shows the bi-conductive surfaces fabricated and tested for the current work. Grooves were first machined into copper substrates and subsequently filled with a two-part high-temperature epoxy. After curing the entire part was sanded by hand to remove excess epoxy, resulting in flat surfaces with lines of epoxy dividing the copper into parallel strips. Bi-conductive surfaces were fabricated with a varying number of epoxy divisions per centimeter, N. Figure 1a shows optical images of the $N = 2$ cm^{-1} and $N = 12$ cm^{-1} designs. In total, seven distinct surfaces have been fabricated and tested including a bare copper surface and bi-conductive surfaces with $N = 2$, 4, 6, 8, 10, and 12 cm^{-1}. Figure 8.1b-d shows scanning electron microscope (SEM) images of the embedded epoxy divisions which have a measured width of 420 ± 5 μm, depth of 290 ± 23 μm, and center-to-center pitches of P = 0.96 – 3.7 mm.

The bi-conductive surfaces have a periodic arrangement of low-conductivity material embedded within a high-conductivity substrate. The thermal conductivity of the epoxy (<1 W/mK) is several orders of magnitude less than that of copper (~400 W/mK).

When submerged in a fluid and heated from the underside, this creates an in-plane variation in surface temperature.

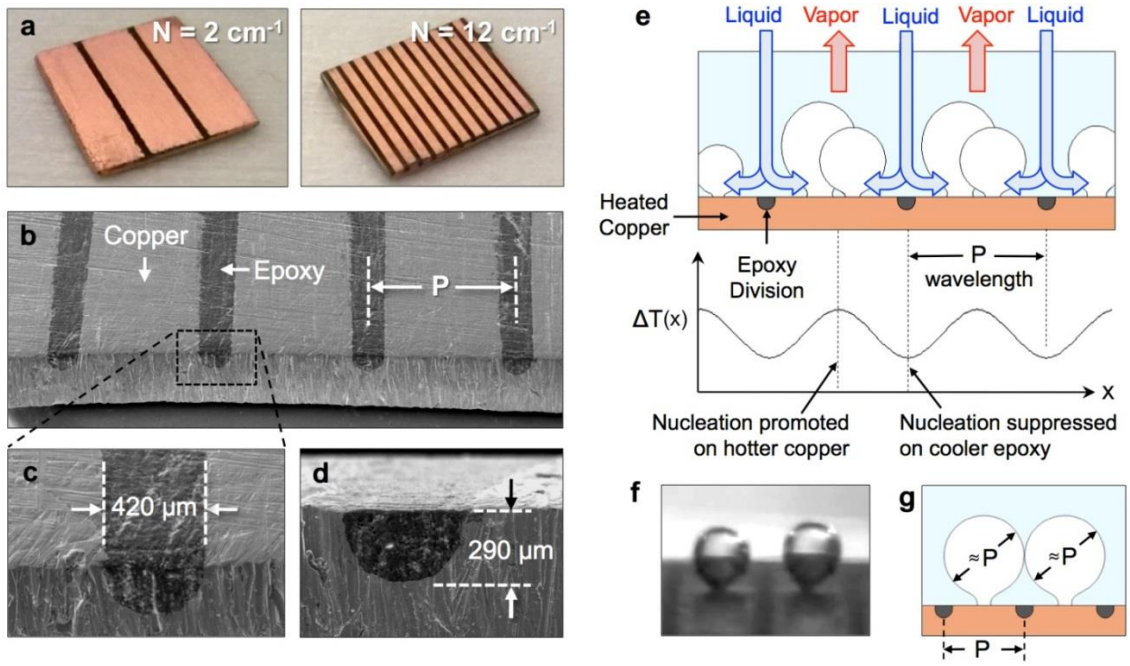

Figure 8.1: The fabricated surfaces showing (a) samples with two and twelve divisions per centimeter, and (b–d) scanning electron microscope (SEM) images of the low-conductivity epoxy divisions embedded in high-conductivity copper. (e) Schematic of the resulting flow field where spatial variations in wall superheat temperature, $\Delta T(x)$, promotes spatial ordering. Nucleation sites, as well as the liquid and vapor flow paths, are tailored to coincide with the wavelength of the in-plane temperature variations given by the pitch, P. (f) Image of the onset of nucleate boiling ($\Delta T \sim 5$ K), where bubbles preferentially nucleate in the center of the copper segments resulting in (g) control over the nominal bubble diameter during lateral coalescence.

Due to the extreme conductivity difference, there is essentially no heat conducted through the epoxy. The top surface of the epoxy will therefore (to first order)

track the temperature of the fluid directly above it. The copper surface, however, will exceed the temperature of the fluid and convectively heat it. In the case of saturated pool boiling studied here, the liquid water is at $T_{Sat} \sim 100°C$ and the hot copper surface is superheated relative to this saturation temperature. At low wall superheats (prior to bubble nucleation) the in-plane temperature variations will promote the formation of Rayleigh-Bérnard convection rolls aligned with the epoxy divisions. It has been shown that this instability is triggered immediately for any finite superheating of a surface with a spatially varying temperature, such as those considered here [87]. The resulting flow-field draws cooler liquid down toward the surface from above the epoxy divisions, while warmer fluid rises from above the hot copper. The counter-rotating convection rolls will produce a stagnation point in the center of the copper, resulting in a local minimum in convective heat transfer and therefore a local maximum in surface temperature [88]. As the wall superheat is increased this local maximum temperature promotes bubble nucleation along the center of the copper regions, resulting in the ordered flow-field shown schematically in Fig. 8.1e. The in-plane variations in wall superheat take a periodic form with a wavelength equal to the pitch between epoxy divisions, P. This superheat wavelength dictates the nature and location of the ordered pathways of escaping vapor and replenishing liquid returning to the surface during nucleate boiling. Figure 1f shows an image of the onset of nucleate boiling, where the first few nucleation sites are activated on a bi-conductive surface ($N = 4$ cm^{-1}) at a wall superheat of ~ 5 K. As can be seen, the vapor bubbles preferentially nucleate near the center of the copper due to the local maximum in surface temperature. This is consistently seen for all of the surfaces tested, and demonstrates that the wettability of the epoxy is not promoting

nucleation due to a lower surface energy (see supplemental movies). Additionally, Fig. 1g shows how the superheat wavelength, *P*, imparts a level of control over the bubble diameter during lateral coalescence. By ordering nucleation sites and liquid return pathways, the size of bubbles undergoing lateral coalescence across an epoxy division is tuned to nominally coincide with the superheat wavelength, *P*.

These bi-conductive surfaces have been shown here to promote HTC and CHF by ordering the vapor and liquid flow-fields during pool boiling, resulting in enhanced bubble dynamics and departure, as well as a delay of the boiling crisis. These enhancements are explicitly derived from bulk material properties (thermal conductivity), as opposed to surface properties or surface structures. Unlike surface coatings, this fundamental mechanism is not susceptible to material degradation and log-term reliability issues. Nor is it reliant on specific fluids or fluid properties to promote boiling, as is required for surfaces incorporating low surface energy materials. Similarly, these flat bi-conductive surfaces do not rely on surface wicking nor are they susceptible to mechanical failure or clogging, which will occur on structured surfaces. Additionally, they can be easily fabricated on a variety of materials using traditional machining techniques and do not rely on complex manufacturing, or precise geometric shapes, to impart boiling enhancement.

8.3 High Speed Imaging

Visualization of the boiling process is conducted using a Phantom V210 high-speed camera (Vision Research) recorded at over 3,000 fps. High-speed imaging is used to visualize bubble dynamics during nucleate boiling at low heat fluxes. At higher fluxes the large production of vapor makes visualization difficult, resulting in no useful

information regarding the impact of bi-conductive surface on the boiling process. Figure 8.2 shows representative images extracted from high-speed imaging, showing nucleate boiling on bi-conductive surfaces with various values of *N*.

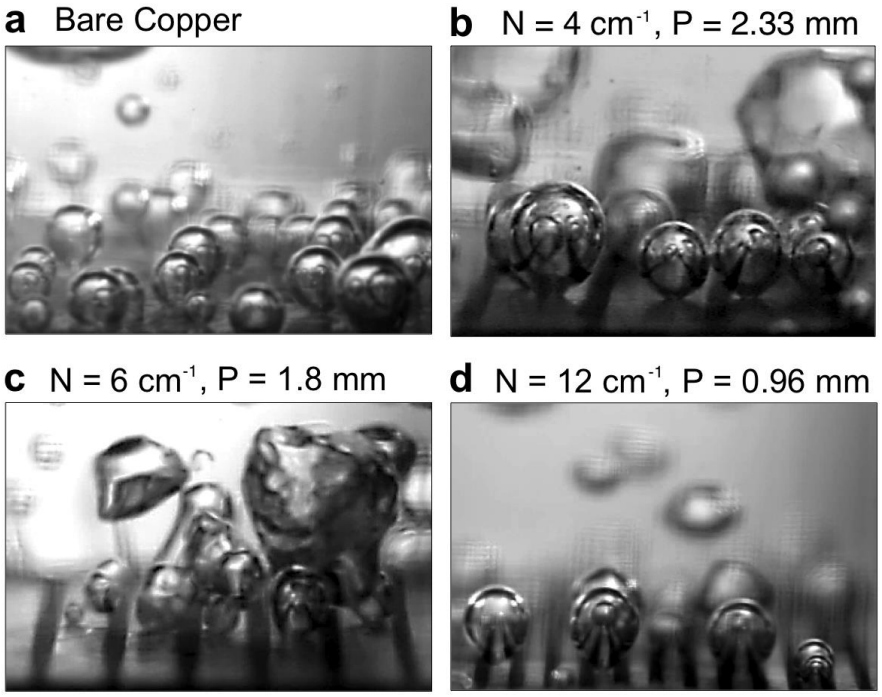

Figure 8.2: Nucleate boiling on bi-conductive surfaces**.** High-speed imaging of nucleate boiling at ~10-15 W/cm^2 on (a) a bare copper surface and bi-conductive surfaces with (b) $N = 4$ cm^{-1}, (c) $N = 6$ cm $^{-1}$, and (d) $N = 12$ cm^{-1} designs. For each bi-conductive surface, nucleation is seen in the center of the high-temperature copper and no lateral motion of the three-phase contact lines beneath vapor bubbles is observed. The low-temperature epoxy divisions remain wetted at all times providing ordered pathways near the surface for replenishing liquid to feed the bubble ebullition cycles.

All of the surfaces tested exhibited similar incipience temperatures, with the onset of nucleate boiling occurring around $\Delta T \sim$ 5-7 K. It can be seen that bubbles form

exclusively on the copper regions, with the low-temperature epoxy divisions suppressing the nucleation process as expected. More importantly, the epoxy divisions remain wetted at all times and resist the lateral motion of bubbles across them. This allows for the formation of order pathways for liquid return above the cold epoxy divisions.

8.4 Pool Boiling Results

Figure 8.3 shows the measured boiling curves, and heat transfer coefficient as a function of superheat for each surface tested. The bare copper surface reached a CHF of ~116 W/cm^2 with a maximum HTC of ~70 kW/m^{2}K. This closely matches the results from various other researchers, demonstrating the accuracy of the experimental apparatus [11, 27, 28]. Substantial increases in boiling performance can be seen for nearly all of the bi-conductive surfaces as compared to bare copper. At moderate superheats (ΔT = 10-11 K), an increase in heat flux and heat transfer coefficient of greater than 5x has been demonstrated using bi-conductive surfaces with a pitch of P = 2.33 mm (N = 4 cm^{-1}). While the incipience temperature does not vary substantially for any of the surfaces tested, heat transfer is increased due to enhanced bubble dynamics on the bi-conductive surfaces. This demonstrates that the addition of epoxy does not enhance HTC by promoting nucleation at lower superheats, as shown for structured surfaces and surfaces with mixed wettability [9-11, 27, 28, 43, 86].

By creating in-plane variations in the superheat temperature, the nucleation, growth, and departure of vapor has been substantially affected. Spatial ordering of the flow field allows for the efficient removal of vapor and return of liquid, accelerating the ebullition cycle and promoting the departure of bubbles. The efficient return of

replenishing liquid has been seen to delay dry-out and enhance CHF up to a factor of 2x using bi-conductive surfaces.

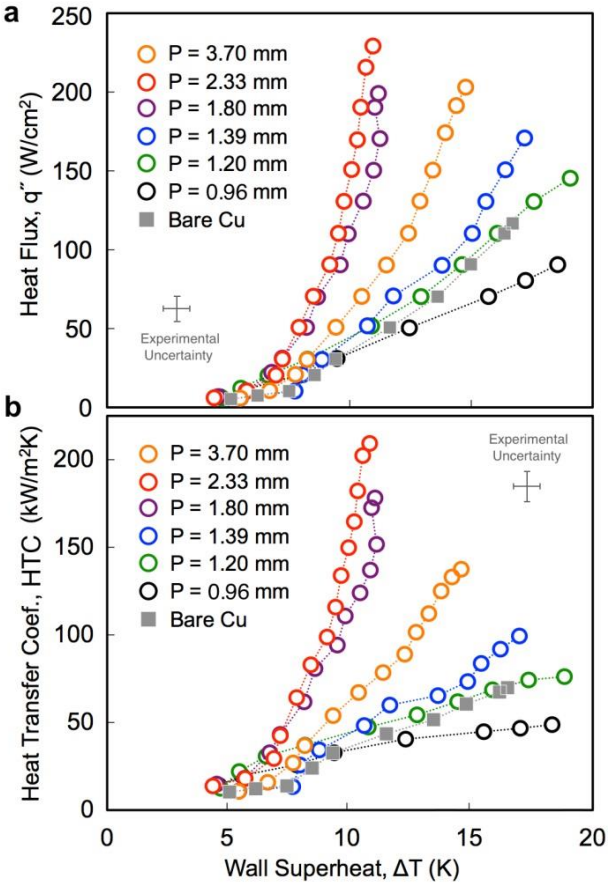

Figure 8.3: Experimental results for (a) heat flux and (b) heat transfer coefficient as a function of wall superheat temperature. Increased performance is seen for five of the six bi-conductive surfaces, corresponding to those with wavelengths of P = 1.2–3.7 mm. A decrease in performance is seen for the P = 0.96 mm design.

8.5 Enhancement Mechanism

8.5.1 *Preferential Nucleation*

To understand the variations in surface temperature and the relative rates of heat transfer through the epoxy and copper sections of the bi-conductive surfaces, a first

order thermal circuit analysis has been conducted. Figure 8.4 shows a segment of a bi-conductive surface with an embedded epoxy division approximated with a rectangular cross section. The epoxy dimensions are W_E = 0.42 mm and D = 0.29 mm, as measured in SEM imaging (Figure 8.1). The width of the copper section is given by $W_C = P - W_E$ where the pitch P varies for each surface from 0.96 to 3.7 mm. This results in copper widths of W_C = 0.54 – 3.28 mm for the six bi-conductive surfaces fabricated and tested. Equations 8.1 and 8.2 give the convective thermal resistances in the water above the epoxy and copper sections, while Equations 8.3 and 8.4 give the conductive resistances through the epoxy and copper.

$$R_{conv}^{E} = \frac{1}{hA_E} = \frac{1}{hW_E L} \tag{8.1}$$

$$R_{conv}^{C} = \frac{1}{hA_C} = \frac{1}{hW_C L} \tag{8.2}$$

$$R_{cond}^{E} = \frac{D}{k_E A_E} = \frac{D}{k_E W_E L} \tag{8.3}$$

$$R_{cond}^{C} = \frac{D}{k_C A_C} = \frac{D}{k_C W_C L} \tag{8.4}$$

In Equations 8.1-8.4, k is the thermal conductivity, L is the length of the epoxy division (also the edge length of the sample), and the subscripts E and C are used to denote the epoxy and copper, respectively. It is assumed in this analysis that k_C = 400 W/mK and k_E = 1 W/mK. The heat transfer coefficient in the fluid is given by h, and assumed to be constant across the whole surface. The total heat transfer rate passing through this segment of the bi-conductive surface is given by q_T, with some portion of that passing through the epoxy (q_E) and some passing through the copper (q_C), such that

$$q_T = q_E + q_C \tag{8.5}$$

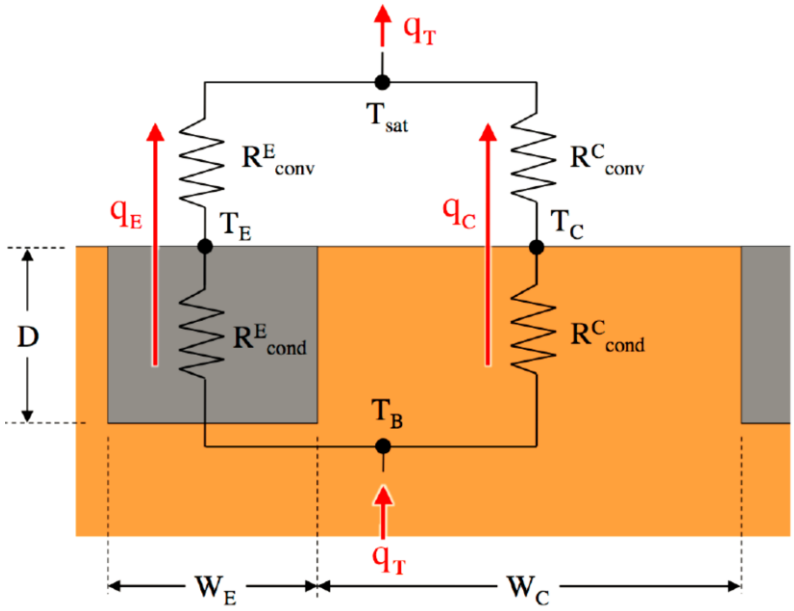

Figure 8.4: Thermal circuit diagram for a segment of a bi-conductive surface showing the relevant conductive and convective resistances between the base copper and the saturated fluid.

Using this thermal circuit model, the fraction of the heat transfer passing through the epoxy divisions can be calculated as

$$\frac{q_E}{q_T} = \frac{q_E}{q_E + q_C} = \frac{1}{1 + \left(q_C / q_E\right)} \tag{8.6}$$

where q_C / q_E is evaluated as

$$\frac{q_C}{q_E} = \frac{\left(T_B - T_{sat}\right) / \left(R^C_{cond} + R^C_{conv}\right)}{\left(T_B - T_{sat}\right) / \left(R^E_{cond} + R^E_{conv}\right)} = \frac{R^E_{cond} + R^E_{conv}}{R^C_{cond} + R^C_{conv}} \tag{8.7}$$

Combining equations 8.5 and 8.7 yields

$$\frac{q_E}{q_T} = \left[1 + \frac{W_C}{W_E}\left(\frac{1 + hD/k_E}{1 + hD/k_C}\right)\right]^{-1} \tag{8.8}$$

Additionally, the ratio of the wall superheat above the epoxy to the superheat above the copper can also be solved for as

$$\frac{\Delta T_{sat,E}}{\Delta T_{sat,C}} = \frac{T_E - T_{sat}}{T_C - T_{sat}} = \frac{q_E R_{conv}^E}{q_C R_{conv}^C} \tag{8.9}$$

which reduces to

$$\frac{\Delta T_{sat,E}}{\Delta T_{sat,C}} = \frac{1 + hD/k_C}{1 + hD/k_E} \tag{8.10}$$

Evaluation of equations 8.8 and 8.10 provides a first order estimate of the magnitude of the heat transfer rate through the epoxy divisions, as well as the ability of the bi-conductive surfaces to suppress the wall superheat above the epoxy divisions. It can be shown that during the nucleate boiling process, the percentage of heat transferred across the epoxy division is extremely small. Evaluating equation 8.8 using the experimentally measured heat transfer coefficients during nucleate boiling, h = 50–210 kW/m^{2}K (Figure 8.3), results in q_E / q_T = 0.2% - 2% for the highest performing surfaces (P = 3.7-1.8 mm). For the lower performing surfaces (P = 1.39-0.69 mm) this increases to q_E / q_T = 0.8% - 5%. Similarly, by evaluating equation 8.10, it can be shown that the ratio of the superheats between the epoxy and fluid to the copper and fluid is $\Delta T_{sat,E}$ / $\Delta T_{sat,C}$ = 1.9% - 6.7%, over the same range of h.

Prior to the onset of nucleate boiling, the measured heat transfer coefficients reach values of $h \sim 5$ kW/m^{2}K. During this convection-dominated region, the lower heat transfer coefficients result in higher convective resistances that become comparable to the conductive resistances in the epoxy. Because of this, the percentage of heat transfer over the epoxy increases to q_E / q_T = 5% - 11% for the highest performing surfaces (P = 3.7-

1.8 mm), and q_E / q_T = 15% - 24% for the lower performing surfaces (P = 1.39-0.69 mm), with $\Delta T_{sat,E} / \Delta T_{sat,C}$ = 41%. As discussed in the manuscript, this ~ 60% reduction in wall superheat over the epoxy divisions is sufficient to produce unstable convective flows and promote the preferential nucleation of vapor bubbles near the center of the copper segments.

8.5.2 *Resonance-like Enhancement*

The enhancements shown here have been attributed to the ability of in-plane variations in wall superheat to impart order to the resulting liquid and vapor flows, leading to high HTC and a delay in CHF. By reducing the superheat temperature in the vicinity of the low-conductivity materials, the epoxy divisions suppress nucleation and remain wetted during boiling. While this reduces the local heat transfer rate near the epoxy, it increases the global heat transfer rate over the entire surface by imparting spatial ordering and enhanced bubble dynamics. For this order to be maintained the cold epoxy divisions must remain wetted at all times. Figure 8.5 shows time-lapse imaging of vapor bubbles undergoing lateral coalescence, and demonstrates the ability of the epoxy divisions to remain wetted during boiling.

In all of the imaging of bare copper surfaces carried out in this work, the three-phase contact line beneath a bubble undergoes visible in-plane motion during lateral coalescence, as is typically seen [89, 90]. This behavior, however, is not seen on the bi-conductive surfaces where the epoxy divisions remain wetted at all times and effectively create boundaries that the three-phase contact lines do not move over. This behavior is essential for creating and maintaining ordered pathways of escaping vapor and replenishing liquid and is seen as the key contributor to boiling enhancement. Several

researchers have observed and characterized the complex motion of contact lines during nucleate boiling and boiling crisis. These include the work by Kim *et al*. [67] and Jung *et al*. [66] using IR thermometry to visualize the liquid-solid interface and measure contact line length, density, and speed.

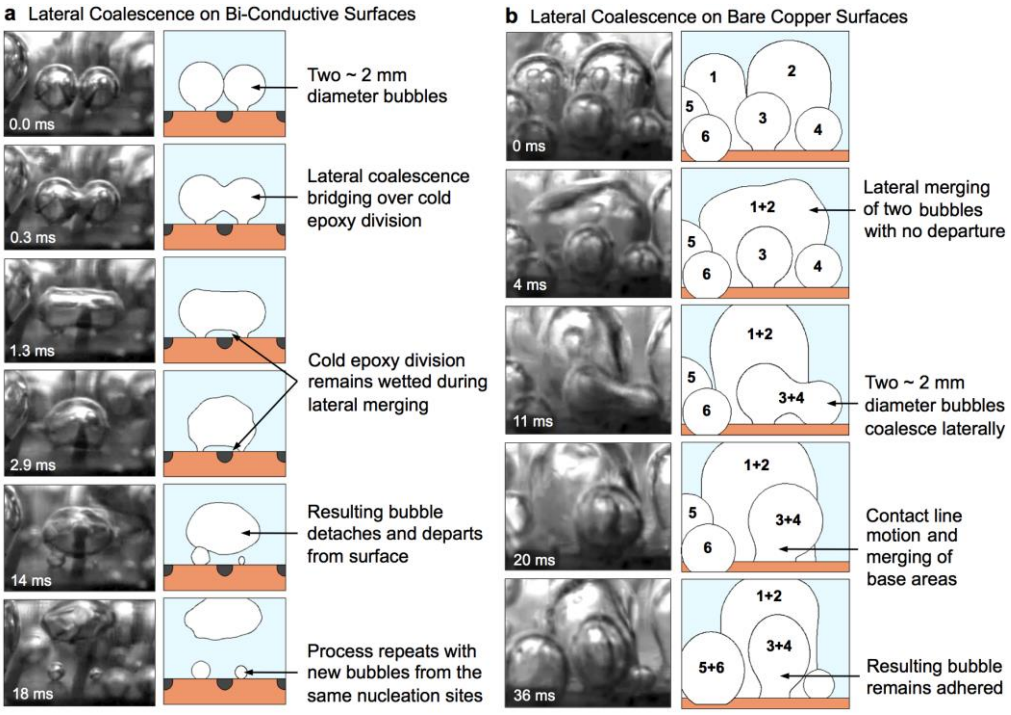

Figure 8.5: Lateral coalescence, contact line motion, and bubble departure. High-speed time lapse imaging of the lateral coalescence of attached vapor bubbles on (a) bi-conductive surfaces, and (b) bare copper surfaces at ~10-15 W/cm^2. (a) When two bubbles laterally coalesce over an epoxy division, the cold epoxy remains wetted and no contact line motion is observed. By remaining wetted at all times, the epoxy divisions promote departure at small diameters and maintain ordered flow paths for replenishing liquid. (b) Conversely, lateral coalescence on bare copper surfaces typically includes the lateral motion of contact lines, and merging of non-wetted base areas beneath the vapor bubbles.

In addition to spatially ordering the escaping vapor and returning liquid flows, the epoxy divisions promote the coalescence-induced departure of laterally merging bubbles. Figure 8.5a shows the coalescence of two ~2mm bubbles bridging over an epoxy division. As the two bubbles merge the underlying epoxy division between them remains wetted at all times. A thin liquid layer remains on the cold epoxy surface and the non-wetted base areas below each bubble do not merge, collapse, or otherwise move during the entire process. The resulting bubble deforms due to surface tension and is quickly ejected from the surface. The low temperature epoxy inhibits the inward lateral merging of the non-wetted bases, and helps draw replenishing liquid underneath the bubble thus promoting departure. Conversely, Figure 8.5b shows time lapse imaging during pool boiling on bare copper surfaces at a comparable heat flux, where three distinct lateral coalescence events are visible. During the 36 ms movie several bubbles are seen coalescing laterally, and in each event the non-wetted base areas merge inward and the resulting bubbles do not depart. The result is a new non-wetted base area beneath the larger coalesced bubble that is still attached to the surface. While this high-speed imaging is conducted at relatively low heat fluxes, it does provide insight into the mechanism driving boiling enhancement on bi-conductive surfaces. The behaviors visualized at low fluxes, along with the pool boiling results shown in Figure 8.3, can be used to draw conclusions regarding the nature of enhancement across all boiling regimes up to CHF.

The enhancement mechanisms proposed here are inherently linked to the wavelength of the spatial variations in surface superheat, P, as illustrated in Figure 8.1. To probe the effect of this wavelength on boiling performance, the pitch between epoxy

divisions has been systematically varied. The percent increase in CHF and HTC of the bi-conductive surfaces relative to bare copper is plotted in Figure 8.6 against the superheat wavelength, P, normalized by the capillary length, λ_C. The capillary length is the characteristic length scale of an interface subject to both surface tension and gravitational forces, and for a bubble is given by

$$\lambda_C = \sqrt{\frac{\sigma}{g(\rho_l - \rho_v)}} \tag{8.11}$$

where σ is the surface tension at the interface, g is the acceleration of gravity, and ρ_l and ρ_v are the densities of the liquid and vapor phases, respectively. The relative importance of surface tension and buoyancy (gravitational) forces on a bubble is captured through the nondimensional Bond number, Bo, given by

$$Bo = \frac{{L_C}^2 g(\rho_l - \rho_v)}{\sigma} \tag{8.12}$$

where L_c is the characteristic length. Defining the Bond number using the wavelength of the superheat variations, P, as the characteristic length of the surface results in

$$Bo_P^{1/2} = P\sqrt{\frac{g(\rho_l - \rho_v)}{\sigma}} = \frac{P}{\lambda_C} \tag{8.13}$$

Figure 8.6 shows the importance of Bond number and capillary length on the boiling enhancement of bi-conductive surfaces, where all fluid properties are evaluated at the saturation temperature and the edge length of the sample is used as the characteristic length for bare copper. A clear maximum in performance is seen when the superheat wavelength (and pitch between epoxy divisions, P) coincides with the capillary length of

the fluid, and the Bond number approaches unity. This optimal wavelength can be explained by examining the nominal bubble departure diameter during boiling. This is traditionally characterized by defining the Bond number using the bubble departure diameter, D, as the characteristic length. Numerous correlations exist to predict bubble departure using the nondimensional departure diameter given by $Bo_D^{1/2}$ [91-95]. These include the classical works of Fritz [94] and Cole and Rohsenow [92], which have shown good agreement with experimental results for decades. Fritz's empirical correlation relates the departure diameter to the contact angle of the surface, θ, and is given by

$$Bo_D^{1/2} = 0.0208\,\theta \tag{8.14}$$

Cole and Rohsenow's correlation for water is given by

$$Bo_D^{1/2} = 1.5x10^{-4}\,Ja^{*5/4} \tag{8.15}$$

The effects of sensible and latent heat are incorporated in this correlation through the use of the modified Jakob number defined as

$$Ja^* = \frac{\rho_l C_{pl} T_{Sat}}{\rho_v h_{fg}} \tag{8.16}$$

where C_{pl} is the heat capacity of the liquid and h_{fg} is the latent heat of vaporization [89]. Evaluating equations (8.14) and (8.15) for saturated water on copper results in values of $Bo_D^{1/2}$ = 1.04 ±0.1 and $Bo_D^{1/2}$ = 0.98 ±0.1, respectively, considering the uncertainties in contact angle and material properties. The bubble departure diameters predicted by both

models closely match the optimal pitch between epoxy divisions found experimentally to be $Bo_P^{1/2} \approx 1$.

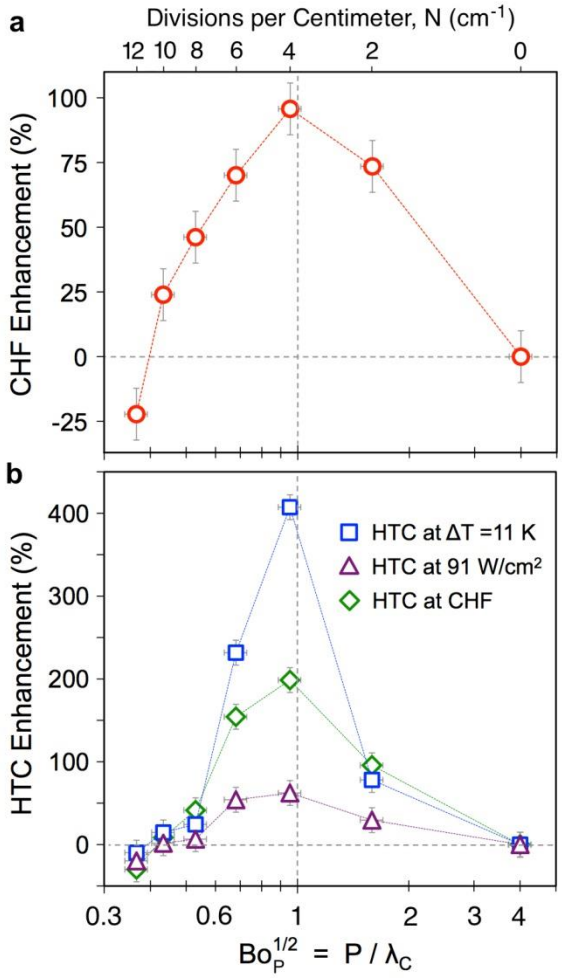

Figure 8.6: Experimental results showing the percent increase in (a) critical heat flux (CHF), and (b) heat transfer coefficient (HTC) for bi-conductive surfaces as compared to bare copper surfaces. Optimal performance is seen at Bond numbers of unity with a 2x increase in CHF and a 5x increase in HTC. These results highlights the importance of tuning the wavelength of spatial temperature variations, P, with the capillary length of the working fluid, λ_C, resulting in enhanced boiling performance over all stages of boiling.

These predictions show that as the wavelength of the variations in superheat, P, approaches the departure diameter of the bubbles, a resonance-like effect is seen leading to substantial increases in both HTC and CHF. Interestingly, Figure 8.6b shows that this resonance-like enhancement in heat transfer is seen at the same wavelength for all phases of boiling. At a common wall superheat of ΔT = 11 K, the heat transfer rates of the various surfaces range from 40-230 W/cm^{-2} (Fig. 8.3a). This corresponds to a greater than 5x difference in vapor production rates between the highest and lowest performing surfaces. At a common heat flux of 91 W/cm^{-2}, the required wall superheat more than doubles across the surfaces tested, varying from 9 K to 19 K. At CHF, each surface is operating at distinctly different heat fluxes (from 91 to 230 W/cm^{-2}) and wall superheats (from 11 to 19 K). Yet in all three cases, the maximum HTC is observed for bi-conductive surfaces where the pitch between epoxy divisions, P, is equal to the capillary length, λ_C.

Adding epoxy divisions and therefore reducing the area available for heat transfer by ~18%, results in up to a 5x increase in heat transfer rate at a given superheat. This result is explained by examining the nature of the bubble nucleation, growth, and departure process. The addition of non-conductive epoxy imparts order to the resulting vapor and liquid flows, which helps draw cool liquid to the surface and promotes departure of nucleating bubbles. While less of the surface area is available to transfer heat, this spatial order enhances the ebullition cycle and also delays dry-out. Figure 8.6b shows with the addition of two and four epoxy divisions per centimeter (N = 2 cm^{-1} and N = 4 cm^{-1} designs), the heat transfer rates steadily increase as compared to the bare surface. The performance enhancement reaches a maximum at a Bond number of unity,

$Bo_P^{1/2}$ = 1, and then decreases for smaller Bond numbers ($N \geq 6$ cm^{-1}). As the Bond number decreases, two factors affecting performance arise. First, the pitch between the epoxy divisions becomes smaller than the nominal bubble departure diameter, and secondly, the effect of surface tension becomes more pronounced. For $N \geq 6$ cm^{-1} bubbles grow to diameters wider than the pitch between epoxy divisions before they can depart. This impedes the counter flow of cooler liquid returning to the surface and disrupts the desired spatial ordering of flow fields. Additionally, for $Bo_P < 1$ the effects of surface tension on the bubble departure process is evident, where the non-wetted base area beneath a bubble can grow to the entire width of the copper section. This is particularly evident for the $N = 12$ cm^{-1} design, which has a Bond number of $Bo_P = 0.13$, and shows performance worse than bare copper. In this case, the reduction of area available to conduct heat and the adverse effects of surface tension has outweighed any potential improvements associated with ordered flows. A decrease in HTC and CHF of approximately 25% as compared to a bare copper surface is seen.

8.6 Conclusions

By imparting in-plane variations in surface temperature onto flat surfaces using low-conductivity materials, extreme increases in pool boiling heat transfer is achieved in this chapter. Bi-conductive surfaces were characterized using high-speed imaging to identify the relevant bubbles dynamics driving enhancement. By using temperature gradients to order the location of nucleation sites, as well as promote the formation of distinct pathways for liquid and vapor flows, HTC has been increased from 41 kW/m^{2}K to 210 kW/m^{2}K (at $\Delta T = 11$ K) and CHF has been increased from

116 W/cm^2 to 230 W/cm^2. The bi-conductive geometry was analyzed and optimized for boiling water at atmospheric pressures, showing optimal performance when the wavelength of surface temperature variations matches the capillary length of the fluid. The principle of tailoring flow fields through variations in local surface temperature represents a novel and potentially transformative tool for the enhancement of boiling heat transfer in next-generation high heat flux applications. Bi-conductive surfaces not only produce substantial increases in performance (>5x increase in HTC shown here), but are also cheaply manufactured using traditional methods, scalable to large areas and various material, and do not contain fragile surface structures or thin coatings. They are easily implementable and naturally insensitive to the degradation, mechanical failure, and fouling associated with other boiling enhancement approaches.

1. Invented the "Bi-Conductive" surface design for boiling enhancement using engineered thermal gradients to promote spatial ordering of liquid and vapor flow fields.
2. By tuning the wavelength of these variations to coincide with the capillary length of the fluid, a resonance-like enhancement effect is seen leading to a greater than 5x improvement in heat transfer rate at moderate superheats.
3. The counterintuitive result by which heat transfer is increased with the addition of non-conductive materials is shown to be a product of the resulting flow field near the surface.
4. Preferential nucleation and spatial ordering have shown to increase the pool boiling heat transfer for bi-conductive surfaces.

5. A significant enhancement in heat transfer has been demonstrated for a planar surface that does not rely on thin films or three-dimensional structures to impart enhancement, due to the inherent susceptibility of these approaches to fouling and degradation.

Publications:

M.M. Rahman, J. Pollack, and M. McCarthy, "Increasing Boiling Heat Transfer using Low Conductivity Materials", *Scientific Reports*, 5, 13145 (2015)

CHAPTER 9: BOILING ENHANCEMENT ON NANOSTRUCTURED SURFACES WITH ENGINEERED VARIATIONS IN WETTABILITY AND THERMAL CONDUCTIVITY

9.1 Introduction and Overview

While engineered surfaces can be used to increase boiling performance [8, 9, 12, 13, 26, 36-40, 43, 96-98], increasing CHF as well as HTC requires an understanding of the impact of various surface designs on each specific boiling phenomenon. Chapter 5 of this dissertation has demonstrated that manipulating the liquid-vapor interface using micro/nano-scale coatings can substantially increase CHF through wicking. A variety of nano and micro scale features have been added to the flat surfaces to enhance CHF up to 300%. These surfaces were shown to increase the surface capillary wicking to delay burn-out. Additionally, engineered nucleation sites on to nanostructured surfaces have been shown to increase HTC by increasing nucleation site density in Chapter 7. It has also been shown that while the HTC for these surfaces with engineered nucleation sites increase, there is a penalty in CHF compared to nanostructured surfaces due to reduction in wickability. These surfaces with mixed wettability were shown to nucleate at low wall superheats. By decreasing the temperature required for the onset of nucleate boiling (ONB) and increasing nucleation sites, the maximum HTC was increased by up to 650%.

Additionally, by imparting spatial order to the liquid-vapor flow fields away from the surface, increases in both HTC and CHF for bi-conductive surfaces have been shown in Chapter 8. The use of flat surfaces with embedded non-conductive materials to create in-plane variations in surface temperature [99] is shown. These “bi-conductive” surfaces demonstrated an increase in HTC of 400% by imparting spatial order to the

nucleation process, and the resulting liquid and vapor flows, as well as through enhanced bubble dynamics.

This work isolates and investigates three of the enhancement mechanisms discussed here (nanostructures, mixed wettability, and bi-conductive surfaces) to study their individual effects on both CHF and HTC. Based on these results, two heterogeneous surfaces combining multiple enhancement techniques are fabricated and characterized during pool boiling of water at atmospheric pressure.

9.2 Nanostructured Surfaces and Wickability

Nanostructured coatings for boiling enhancement have been studied extensively starting with Chen et al, who used silicon and copper nanowires on silicon surfaces to increase CHF [9]. Numerous other researchers have investigated the impact of nanostructures on boiling and have offered a variety of explanations. Most notable the role of surface wicking has been cited as a critical factor for CHF enhancement [9, 12, 38, 41, 57, 64]. Nanostructured hydrophilic coatings produce superhydrophilic surfaces with contact angles approaching zero degrees. These structures can also wick liquids laterally across a surface during boiling, which is seen as a viable mechanistic explanation of the delayed dry-out and increased CHF observed for nanostructured surfaces. Specifically, the role of wickability on CHF for a variety of structured surfaces, using a wicking measurement technique first described by Ahn et al [57] was experimentally demonstrated in Chapter 6.

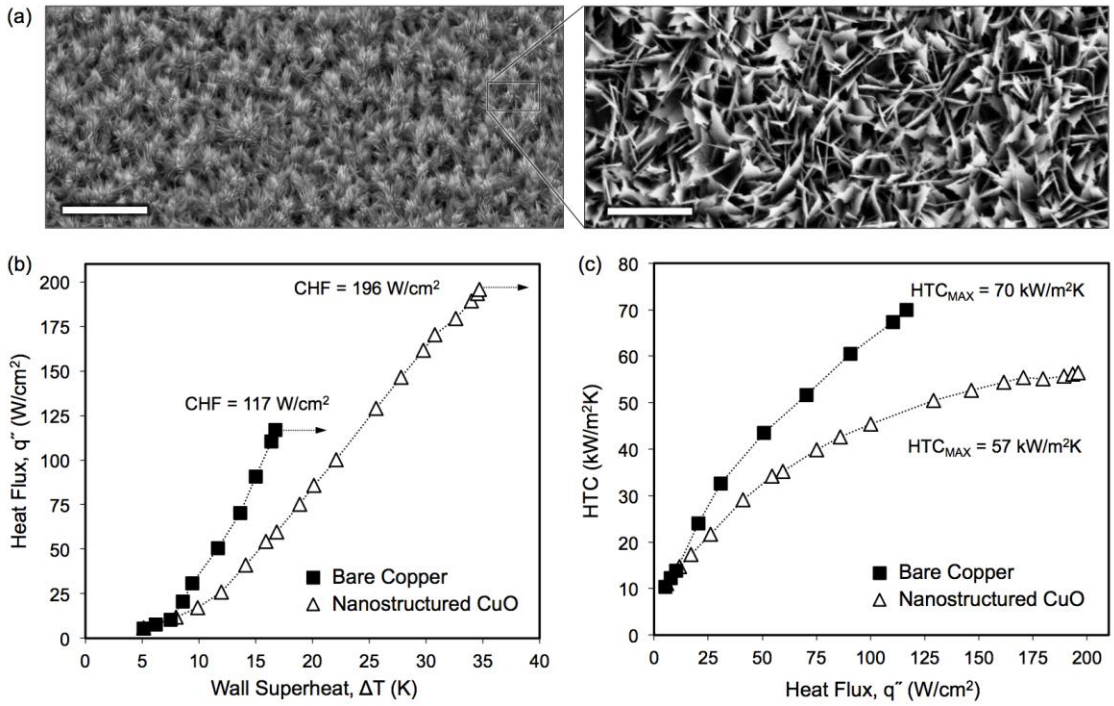

Figure 9.1: The effects of nanostructured coatings on pool boiling. (a) SEM images showing nanostructured CuO surfaces at two different magnifications, as well as (b) heat flux and (c) heat transfer coefficient results, as compared to bare copper surfaces.

To demonstrate the effects of nanoscale coatings on boiling heat transfer, copper substrates have been oxidized to create high-surface-area copper oxide (CuO) nanostructures. The sharp blade-like CuO nanostructures are fabricated using the method described by Chu et al., where a copper substrate is immersed in a mixture of $NaClO_2$, NaOH, $Na_3P0_4.12H_20$, and DI water (3.75:5:10:100 wt%) at 96 °C for 10 minutes [37]. Figure 9.1a shows scanning electron microscope (SEM) images of the fabricated CuO nanostructured surfaces at two different magnifications. Figure 9.1b and 9.1c shows heat flux as a function of wall superheat, and heat transfer coefficient as a function of heat flux for the nanostructured surface as compared to bare copper. The horizontal arrows

indicate CHF for each surface, which corresponds to largest stable heat flux before dry-out. It can be seen that the bare Cu reaches CHF value of roughly 117 W/cm^2 with a maximum HTC of 70 kW/m^{2}K, which is consistent with the open literature [26, 27]. A CHF value of 196 W/cm^2 has been measured for the nanostructured CuO surface at a wall superheat of 34.5 K. The experimental uncertainties for CHF and maximum HTC are ±3.0% and ±6.3%, respectively. This performance is repeatable and closely matches the results of several researchers for nanostructured boiling, in particular the work of Chu et al. using the same fabrication process [37].

As can be seen, the addition of nanostructures results in a notable increase in CHF, but also a simultaneous decrease in HTC over the entire boiling curve. CHF has been increased by 68%, and the maximum HTC has been reduced by 19%. This decrease in HTC is attributed to the suppression of active nucleation sites due to the nanostructured coating. The CuO nanostructures reduce the effect cavity size of a range of potential nucleation sites on the machined copper surface to much less than 1 μm, thus requiring larger superheats to activate them [4]. Conversely, several researchers with boiling on silicon substrates have shown increases in HTC with the addition of nanostructures [2, 9, 12]. This is due to the fact that the sizes of potential nucleation sites on a polished silicon surface are much smaller than the size of the cavities created by typical nanostructured coatings.

The increase in CHF seen can be explained by evaluating the ability of the nanostructured coating to laterally wick liquids across its surface as discussed in Chapter 6. Using the wicking experimental values measured in Chapter 6 for the CuO

nanostructured surfaces, the wicked volume flux is $\dot{V}_0'' = 2.78$ mm/s with an experimental uncertainty of ±5.8%, resulting in a dimensionless wicking number of Wi = 0.73. Rahman's CHF correlation therefore predicts a CHF value of q''_{CHF} = 192 W/cm^2, as compared to the measured value of q''_{CHF} = 196 W/cm^2. This represents a discrepancy between prediction and measurement of ~2%, which is less than the estimated accuracy of the experimental apparatus, demonstrating the efficacy of this model.

9.3 Mixed Wettability and Nucleation

The addition of nanostructured coatings onto copper surfaces is shown to increase CHF and delay dry-out via wicking, but also decrease HTC by supressing nucleation. This highlights the complexities of boiling and the difficulty in engineering surfaces for its enhancement. CHF represents the maximum heat transfer rate and essentially limits the operating range of a boiling surface. Most systems, however, do not operate near CHF for obvious safety reasons. HTC is arguably a more important measure of boiling enhancement and, as was shown, nanostructured coatings degrade HTC on copper.

HTC is a measure of the efficiency of boiling and strongly depends on the nucleation process, the nucleation site density, and the bubble ebullition cycle as shown by Mikic and Rohsenow [16]. One reported method of increasing HTC during boiling is by increasing the activation of nucleation sites at low wall superheats using surfaces low-surface-energy materials [10, 43, 85, 86]. The inclusion of hydrophobic spots onto an otherwise hydrophilic surface was shown by Betz et al. [43]. By reducing the wall superheat required to activate the engineered nucleation sites using hydrophobic dots, an

HTC enhancement of 100% was reported for these patterned biphilic surfaces. By further decreasing the wettability of the nucleation sites Betz et al. increased this HTC enhancement up to 650% using nanostructured superbiphilic surfaces [10].

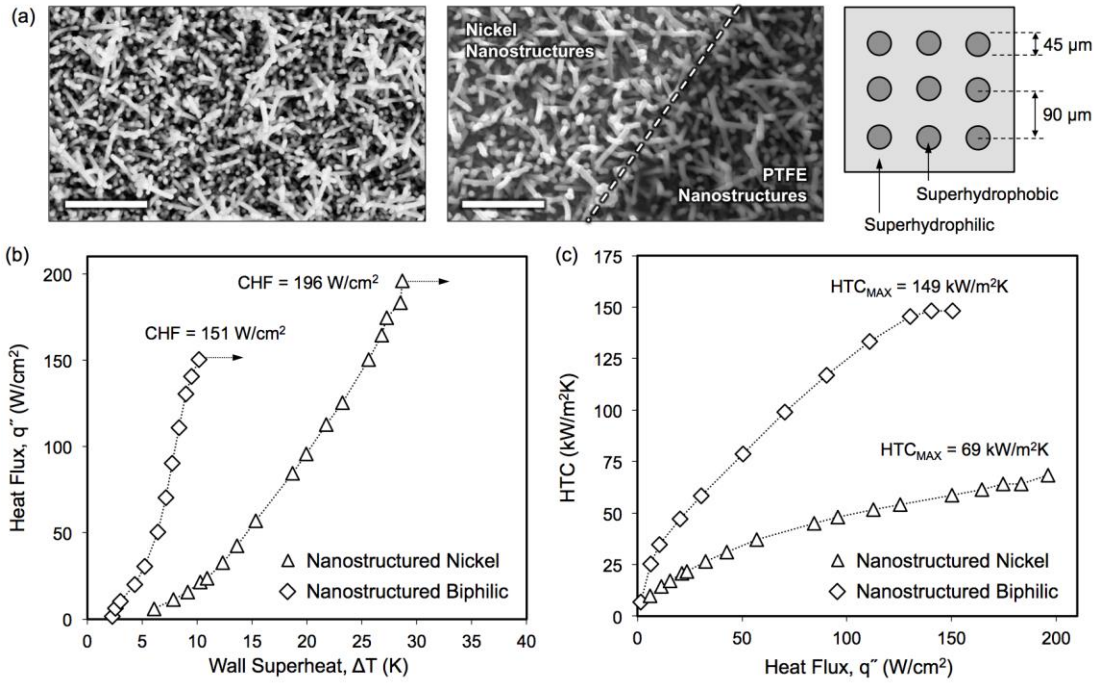

Figure 9.2: The effects of nanostructured surfaces with mixed wettability on pool boiling. (a) SEM images of nanostructured nickel coatings, fabricated using biotemplating, as well as patterned conformal PTFE films (~ 10-20 nm thick) creating an array of superhydrophobic dots on an otherwise superhydrophilic surface. Boiling results for (b) heat flux and (c) heat transfer coefficient, as compared to the performance of superhydrophilic nanostructured surfaces.

The effects mixed-wettability on nanostructured surfaces during pool boiling is demonstrated here using nanostructured nickel coatings on silicon substrates. Figure 9.2a shows SEM images of the nickel nanostructures, both with and without a thin conformal PTFE coating, as well as a schematic representation of the mixed-wettability pattern

tested. Biotemplated nickel nanostructures are fabricated through the self-assembly and metallization of the *Tobacco mosaic virus* (TMV) using a simple room-temperature solution-based nanofabrication technique as reported in Chapter 5. Briefly, gold-coated silicon substrates are immersed in a phosphate buffer solution containing purified TMV for 24 hours during which the viruses assemble onto the surface. The viral nano-rods are then metallized using a palladium-activated autocatalytic nickel solution. This results in a rough superhydrophilic nanostructured nickel surface with average nanostructure heights of 1-1.5 μm and diameters of ~100 nm. The nanostructured surfaces are then patterned using traditional photolithography to create a photoresist layer with 45 μm diameter openings spaced 90 μm apart. A thin coating of PTFE (AF1600 Teflon) is then spin-coated, cured, and lifted off of the nanostructures, resulting in superhydrophobic islands on an otherwise superhydrophilic nanostructured surface (Fig. 9.2a).

Figure 9.2b shows the boiling curves for the nanostructured biphilic surface as compared to a TMV-templated nickel nanostructured surface with no PTFE islands. The nanostructured surface again reaches a CHF of 196 W/cm^2 with an experimental uncertainty of ±3.0%, with the onset of nucleate boiling (ONB) occurring at a wall superheat of 6 K. The nanostructured biphilic surface has an ONB at a wall superheat of less than 3 K, and reaches a CHF value of 151 W/cm^2 with an experimental uncertainty of ±3.9%. The maximum HTC for the nanostructured biphilic surfaces is 149 kW/m^{2}K with an experimental uncertainty of ±2.4%, representing a 116% increase over the superhydrophilic nanostructured surfaces without mixed wettability. While HTC has been enhanced by promoting the activation of nucleation sites at lower superheats, the CHF for nanostructured biphilic surfaces has been reduced by ~25% as compared to

nanostructured surfaces. This reduction in CHF is attributed to an effective reduction in capillary wicking. The addition of superhydrophobic islands in the arrangement shown in Fig. 4a will reduce the ability of liquid to be wicked laterally across the surface by creating barriers that liquid cannot pass through. This again demonstrates the complex and coupled nature of boiling phenomena and engineered surface designs to simultaneously increase CHF and HTC.

9.4 Bi-Conductive Surfaces

The enhancement mechanisms characterized in the prior two sections occur primarily at the "beginning" of the boiling curve (ONB), and the "end" of the boiling curve (CHF). By enhancing bubble dynamics and the ebullition cycle, boiling performance can be increased in a more general way and across the entire boiling curve. The enhancements in CHF and HTC using nanostructures and mixed-wettability rely on surface and interfacial phenomena, namely surface capillary wicking and the nucleation process. A novel enhancement mechanism derived from bulk material properties with no surface structures was reported in Chapter 8.

Figure 9.3 shows the pool boiling performance of the optimal bi-conductive design, with a pitch between epoxy divisions of P = 2.33 mm compared against a bare copper surface. Heat flux as a function of wall superheat is plotted in Fig. 9.3a and heat transfer coefficient as a function of heat flux is plotted in Fig. 9.3b. The heat flux and HTC across the bi-conductive surface are calculated using the total surface area in contact with the fluid, including both the copper and epoxy regions. The bi-conductive surface reaches a CHF of 230 W/cm^2, representing roughly a two-fold increase in CHF and a three-fold increase in maximum HTC. The experimental uncertainties for CHF and

maximum HTC for the bi-conductive surface are estimated to be ±2.6% and ±1.7%, respectively. More interestingly, at a moderate wall superheat of ~10 K, the bi-conductive surfaces show a five-fold increase in heat flux as compared to bare copper. These enhancements are derived directly from enhanced bubble dynamics and an increase in the ebullition cycle. CHF is increased without the use of surface structures or capillary wicking, and HTC is increased without using low-surface-energy materials and no change in ONB.

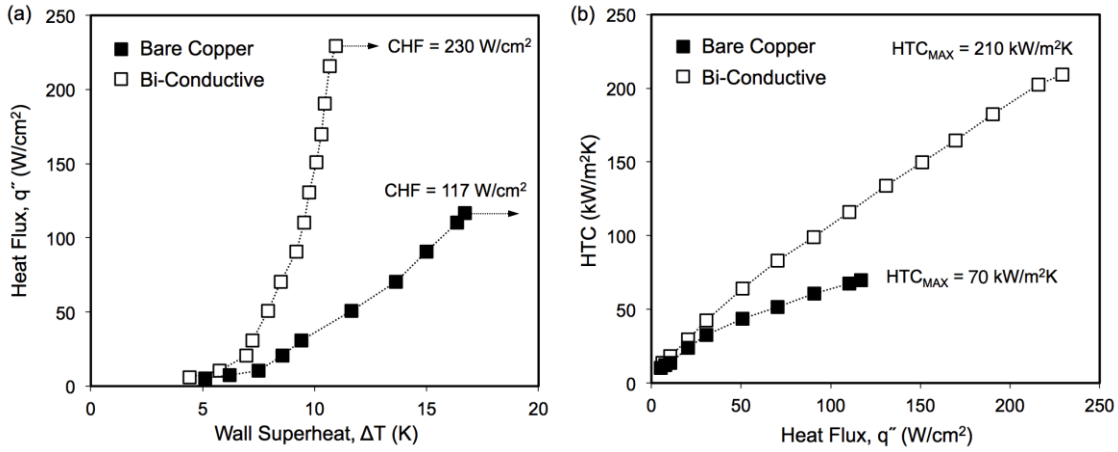

Figure 9.3: The effects of bi-conductivity on pool boiling. (a) Heat flux and (b) heat transfer coefficient, as compared to bare copper surfaces with no epoxy divisions.

9.5 Nanostructured Surfaces with Engineered Variations in Wettability and Thermal Conductivity

Nanostructures have been shown to increase CHF through capillary wicking, but degrade HTC. Mixed wettability has been shown to increase HTC by increasing nucleation sites and triggering ONB at lower superheats, but degrade CHF. The bi-conductive surfaces, however, have been shown to simultaneously increase CHF as well as HTC across the entire boiling curve. They have higher CHF than nanostructured

coatings, and higher HTC as compared to biphilic surfaces. Most importantly, the mechanisms of enhancement for the bi-conductive surfaces (bubble dynamics and spatial order) are independent to those for nanostructured coatings (capillary wicking) and surfaces with mixed wettability (nucleation). This suggests that these different enhancement approaches can be superimposed onto one another for further increases in performance.

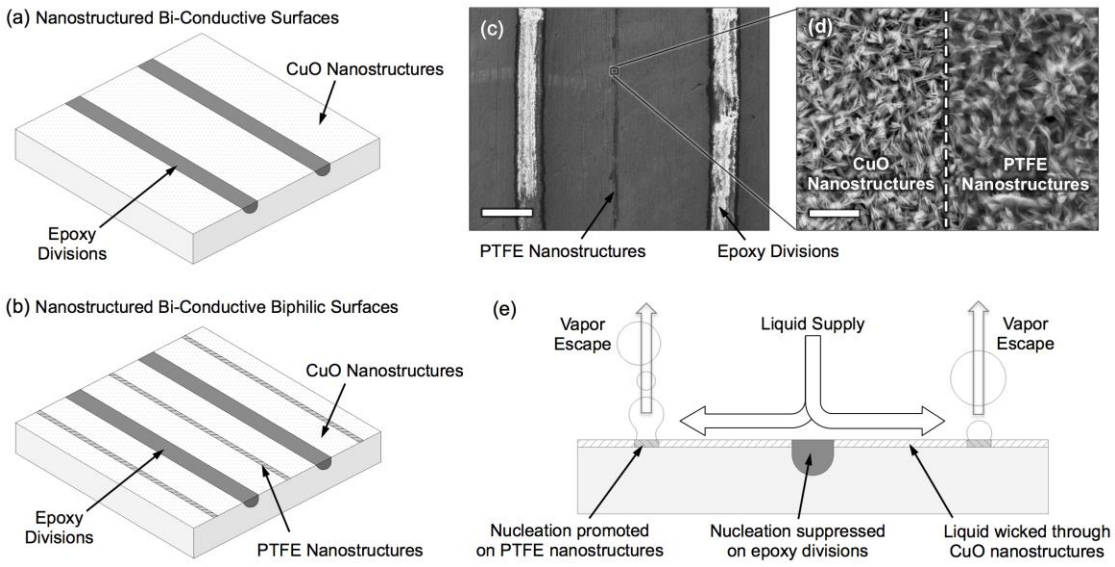

Figure 9.4: Heterogeneous surface designs combining nanostructures, mixed-wettability, and bi-conductivity. Schematic representations of (a) the nanostructured bi-conductive surfaces, and (b) the nanostructured bi-conductive biphilic surfaces. (c) SEM image of a nanostructured bi-conductive biphilic surface showing the CuO nanostructures, two embedded epoxy divisions separated by 2.33 mm, and a 50-60 μm wide line of superhydrophobic nanostructures in between them. (d) Magnification of the interface separating the superhydrophilic CuO nanostructures, and the superhydrophobic PTFE-coated nanostructures. (e) Schematic representation of the desired flow field.

Figure 9.4 shows the two heterogeneous surface designs fabricated and characterized here. Nanostructured bi-conductive copper surfaces (Fig. 9.4a) were fabricated by using the previously described CuO nanostructure growth technique applied directly to an optimized bi-conductive surface (P = 2.33 mm). Nanostructured bi-conductive biphilic surfaces (Fig. 9.4b) were also fabricated by using the previously describe technique to create mixed wettability on nanostructured surfaces. Nanostructured bi-conductive surfaces were patterned using photolithography, after which PTFE was spun on, cured, and finally lifted-off to yield the pattern shown in Fig. 9.4b. Figure 9.4c shows SEM images of a nanostructured bi-conductive biphilic surface, where a ~50 μm thick line of PTFE-coated nanostructures is patterned at the center of the nanostructured CuO region.

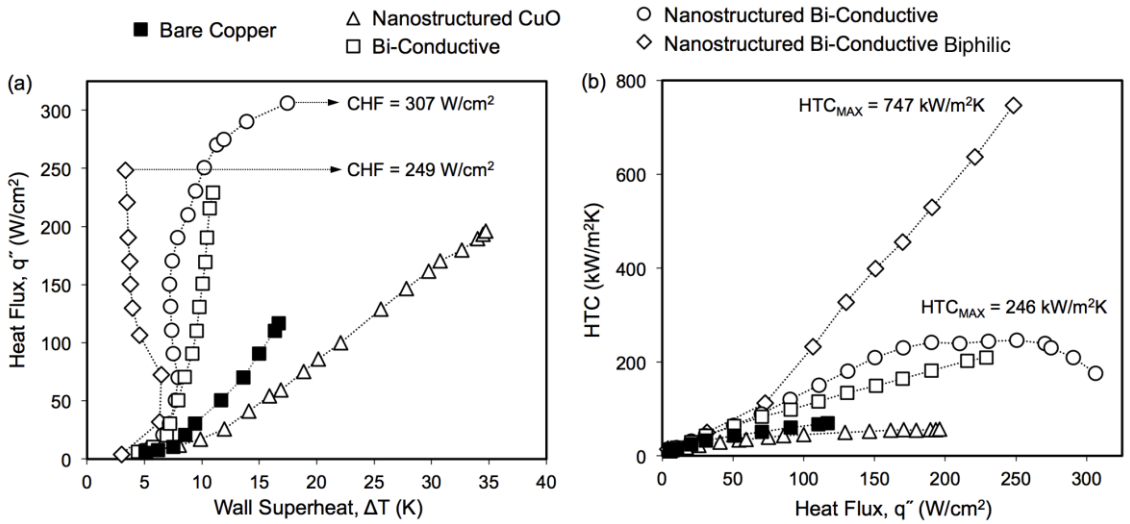

Figure 9.5: Pool boiling performance of the heterogeneous surface designs, showing (a) heat flux and (b) heat transfer coefficient, as compared against the performance of bare copper, surface with nanostructured CuO only, and surfaces with bi-conductivity only.

Figure 9.4d shows a magnified image of the boundary between superhydrophilic CuO nanostructures and the superhydrophobic PTFE nanostructures. Figure 9.4e shows a schematic representation of the desired flow field during nucleate boiling on the nanostructured bi-conductive biphilic surfaces. Nucleation is promoted at low superheats on the superhydrophobic PTFE nanostructures, and suppressed on the epoxy divisions due to a locally low surface temperature. By selectively promoting and suppressing nucleation, spatial order of the resulting liquid and vapor flow paths is created which enhances the ebullition cycle increasing both CHF and HTC. The nanostructures on the copper surface provide a pathway to wicked liquid from the epoxy divisions to the superhydrophobic nucleation sites, thus further delaying dry-out.

The performance of both heterogeneous designs (Fig. 9.4a and 9.4b) is shown in Fig. 9.5 compared against bare copper, nanostructured surfaces, and bi-conductive surfaces, where the total projected footprint area is used to calculate heat flux and HTC for all surfaces. As can been seen, the bi-conductive surfaces notably outperform the nanostructured surfaces in both CHF (17% higher) and HTC (270% higher). Over the majority of the boiling curve, the nanostructured bi-conductive surfaces, denoted by open circles in Fig. 9.5, show comparable performance to the bi-conductive surfaces with no nanostructures (open squares). The two curves generally follow one another with the nanostructure bi-conductive surface showing only a modest enhancement in HTC. However, the addition of nanostructures to a bi-conductive surface has delayed dry-out and lead to an increase in CHF up to 307 W/cm^2 with an experimental uncertainty of ±1.9%. This increase in CHF due to capillary wicking through the nanostructures (~77 W/cm^2) is consistent with the increase in CHF by adding nanostructures to a bare copper

surface (~79 W/cm^2), as seen in Fig. 9.1. Comparing the nanostructured bi-conductive surfaces (open circles) to the nanostructured surfaces (open triangles) highlights the impact of the simple addition of epoxy divisions. The two curves show drastically different behaviors, with the addition of bi-conductivity leading to larger CHF, as well as substantially increased HTC (> 330%). The nanostructured bi-conductive biphilic surfaces (open diamonds) were made by adding mixed-wettability to the nanostructured bi-conductive surfaces (open circles). These PTFE coatings are shown to lower the superheat required for ONB and enhance nucleation, leading to a maximum HTC of 747 kW/m^{2}K which represents a > 200% increase as compared to the nanostructured bi-conductive surfaces with no PTFE. As seen before, however, the introduction of superhydrophobic nanostructures limits capillary wicking, resulting in a slight decrease in CHF (19%). The observed increase in HTC is achieved by reducing the wall superheat at high heat fluxes. As seen in Fig. 9.5a, soon after ONB the required wall superheat decreases from ~7 K to ~3 K as heat flux is increased to CHF. This counterintuitive behavior is attributed to the continued and rapid activation of additional nucleation sites at higher heat fluxes, as well as favorable bubble dynamics associated with spatial ordering of liquid vapor and flow fields. Similar behaviors have been observed and reported previously by Kandlikar [27] and Jaikumar and Kandlikar [100, 101] using engineered surfaces with preferential nucleation sites and designed to promote spatial ordering of liquid and vapor flow fields.

9.6 Conclusions

This chapter has individually investigated the effects of nanostructured coatings, mixed-wettability and bi-conductivity using nanostructured surfaces with

engineered variations in wettability and thermal conductivity during saturated pool boiling of water at atmospheric conditions. Two heterogeneous surface designs combining the elements of nanostructures, mixed wettability, and bi-conductivity were fabricated. The superposition of these various enhancement techniques has been shown to produces increases in CHF and HTC of over a factor of 2.5x and 10x, respectively, as compared to bare copper surfaces. Specific conclusions of this chapter are as follows:

1. Nanostructures are shown to delay dry-out and increase CHF due to capillary wicking through the nanoscale surface structures.
2. The nanostructured coatings resulted in a decrease in HTC across the entire boiling curve as compared to bare copper surfaces due to the suppression of nucleation due to nanoscale features.
3. The HTC of nanostructured surfaces was shown to increase with the addition of patterned low-surface-energy films, creating surface with mixed-wettability due to increased nucleation sites and a decrease in the superheat required for ONB.
4. Nanostructured surfaces with mixed-wettability, however, have shown to reduce CHF due to the suppression of capillary wicking.
5. Bi-conductive surfaces were shown to increase both HTC and CHF by promoting ordered liquid and vapor pathways with enhanced bubble dynamics.
6. The heterogeneous surface with nanostructures and engineered variations in thermal conductivity has been shown to increase CHF by 3 fold due to preferential nucleation, spatial ordering and nanostructure wickability whereas the HTC enhancement is moderate.

7. The heterogeneous surface with nanostructures, engineered thermal gradient and mixed wettability has been shown to increase HTC by 10 fold due to further enhancement in bubble dynamics through superhydrophobic lines on bi-conductive surfaces. Whereas CHF has been shown to decrease compared to Nanostructured Bi-Conductive surface due to suppression of wicking areas.

Publications:

M. M. Rahman, and M. McCarthy, "Boiling Enhancement on Nanostructured Surfaces with Engineered Variations in Wettability and Thermal Conductivity", *Heat Transfer Engineering* (in press).

CHAPTER 10: SUMMARY AND CONTRIBUTIONS

10.1 Overall Summary

The objectives of this dissertation were identified and categorized into three major focus areas: (1) a detailed characterization of the effects of structured surfaces on boiling performance, including the role of capillary wicking, as well as the effects of surface morphology, material, and length scales; (2) scalable nanomanufacturing of structured coatings using nanoscale biological templates, and (3) the realization of novel surfaces for boiling enhancement that are resistant to degradation. To achieve these objectives, this dissertation has been organized in total 10 chapters. While Chapter 1 to Chapter 3 provides introduction, motivation and objectives, and brief summary of literature review respectively, Chapter 4 to Chapter 9 have been organized to achieve all the objectives mentioned here. The experimental apparatus and methods to attain the above mentioned goals are presented in Chapter 4.

Chapter 5 focuses on scalable nanomanufacturing of structured surfaces for pool boiling heat transfer enhancement which is the focus area 2. A simple room temperature solution based nanofabrication process has been demonstrated to fabricate nanostructures on to various metallic and non-metallic substrates. Using the self-assembly and metallization of the *Tobacco mosaic virus* (TMV) in a three step process, nickel nanostructures were deposited on gold coated silicon, aluminum, copper and stainless steel surfaces. The heat transfer performance of these nanostructures was characterized during pool boiling. A substantial increase in CHF and HTC, nearly 200% enhancement compared to flat silicon reference, has been achieved for biotemplated

nickel nanostructures. To identify the effect of fouling, repeated pool boiling tests were performed on selected surfaces, and showed that the heat transfer performance of these nanostructures are depended on the liquid quality. Depending on the cleaning technique, the structures can be returned to its original performance. Also, the process of retrofitting and fouling mitigation has been demonstrated for selected nanostructured surfaces. For retrofitting the existing devices, and mitigating the devices due to fouling over repeated application, it has been demonstrated in Chapter 5 that the nanostructures can be stripped from the devices using chemical solutions, and then the devices can be recoated with nanostructures without overhauling the heat transfer systems.

Chapter 6 and Chapter 7 focus on separating the effect of enhancement parameters and characterizing them during pool boiling. Boiling is a complex phenomenon, and it is very hard to see what is happening during high heat fluxes. To predict and model this high heat flux boiling, researchers have made several assumptions to quantify and predict the pool boiling critical heat flux (CHF) and heat transfer coefficient (HTC). Several pool boiling models were developed and validated in a limited range of experimental results over the past few decades; still the fundamentals are not fully understood. To overcome this issue, Chapter 6 and Chapter 7 have carefully separated contributing factors affecting the pool boiling heat transfer which are widely cited in the literature. Then using custom built experimentations, these factors were systematically varied and characterized during pool boiling.

Recalling the most cited parameters those affect the pool boiling heat transfer are increased capillary wicking, roughness factor, nucleation site density, and controlled liquid and vapor flow field. In Chapter 6, homogenous micro/nanostructures with

characteristic length scale much smaller than the flow scale (~ 1 mm), were fabricated and characterized the effect of surface wickability and roughness factor on boiling enhancement. Over twenty different nanostructures on silicon including biotemplated nickel nanostructures, micropost geometries with varied dimensions, and hierarchical surfaces with varied microstructures coated with biotemplated nickel, were fabricated for this chapter. Additionally, to address the variability in nanostructure materials, different copper oxide nanostructures were fabricated and to address the variability in structure morphology, substrate materials, biotemplated nanostructures on different metallic and non –metallic surfaces were fabricated and nanostructures with varied density and porosity were fabricated as well. The wickability of the structures was characterized using a custom-built capillary wick test technique. Pool boiling heat transfer performance was characterized for all the fabricated structures using saturated water and saturated FC 72 at atmospheric conditions. It has been demonstrated in Chapter 6 that wickability is the single factor dictating CHF for structured superhydrophilic surfaces during pool boiling. Then, the pool boiling CHF for structured superhydrophilic surfaces has been modeled with experimentally developed correlation based on non-dimensional wickability. It has been demonstrated that the experimentally verified correlation relating CHF and wicked volume flux shows excellent agreement for three dozen independent samples fabricated for this work including those with variations in scale (micro, nano, and hierarchical), substrate material (silicon, aluminum, stainless steel, and copper), nanostructure density, roughness factor, degradation due to fouling, as well as structure material and morphology (etched silicon microposts, virus-templated nickel nanostructures, and copper oxide nanostructures). This correlation has also been shown to

accurately predict the CHF for structured surfaces using alternate fluid (here FC 72). Finally, this chapter leverages the surface wickability and heat transfer performance to optimize shell thickness of the biotemplated nickel nanostructures for rigid and robust coatings. The experimental findings from Chapter 6 suggests that although the roughness augmented CHF can be found to be valid until certain enhancement ranges, the wickability is the single factor which delays dry-out through enhanced liquid transport through the structures to the nucleation areas.

While Chapter 6 focuses on separating the effect of surface wickability and roughness using homogeneous micro/nanostructured surfaces, Chapter 7 investigates the role of engineered nucleation sites and structure length scale using heterogeneous structures. By adding nucleation sites on to homogenous wicking structures and combining the structures with two incomparable length scales, the boiling enhancement mechanism becomes more complicated. Chapter 7 investigates and characterizes these effects during pool boiling. In the first part of Chapter 7, engineered nucleation sites have been incorporated on to superhydrophilic nanostructured surfaces. It has been demonstrated that although these nucleation sites increase HTC substantially, this HTC enhancement occurs with the penalty of CHF compared to nanostructures surfaces. This reduction in CHF has been shown to be the effect of decrease in wicking areas which has been demonstrated by measuring the wickability of these surfaces. Additionally, the CHF correlation relating the wickability has been shown to accurately predict the CHF for these heterogeneous structures.

In the second part of Chapter 7, the role of structure length scale on boiling heat transfer enhancement is characterized. To achieve that, four different nanostructures

with structure length scale much smaller than flow length scale (~ 1 mm) with widely varying wickability and CHF, and five different microchannel surfaces with characteristic length scale comparable to flow length scale were fabricated and characterized during pool boiling. A CHF value of 313 W/cm^2 with HTC of 462 kW/m^2K was achieved for the multiscale hierarchical surfaces. It has been demonstrated that for surfaces with multiscale structures, the heat transfer enhancement is initially dominated by large length scale structures (microchannel here), and at the later stages, nanostructures delay dry-out by increasing the liquid transport through capillary.

Chapter 8 focuses on the third objective of this dissertation which is fabrication and characterization of enhanced heat transfer surfaces that are resistant to degradation. A novel heat transfer enhancement mechanism through engineered planar surfaces has been demonstrated in this chapter. By promoting ordered pathways between nucleating bubbles and replenishing liquid, engineered thermal gradients have been shown to be as effective as structured surfaces in boiling enhancement, yet inherently resistant to foiling. These planar "bi-conductive" surfaces have been characterized and their geometries optimized based on analysis of the bubble departure phenomena and surface tension effects.

Finally the fundamentals of Chapter 6, Chapter 7 and Chapter 8 are all combined into one heterogeneous surface in Chapter 9 which systematically investigates the effect of all the individual factors. As Chapter 8 demonstrates a novel heat transfer enhancement surface where heat transfer is increased by the spatial temperature gradient which promotes preferential nucleation and spatial ordering of bubbles on the conductive areas only, hence, this chapter takes the optimized bi-conductive design (pitch is 2.33

mm) as the base for heterogeneous surface. Copper oxide nanostructures were chemically oxidized on the copper areas as Chapter 6 identifies that capillary wicking is the single factor affecting CHF enhancement during pool boiling. Also, hydrophobic PTFE lines were deposited at the center of the nanostructured copper areas since these superhydrophobic regions promote nucleation at low wall superheat and thus increase HTC as shown in Chapter 7. The idea of combining all three factors, engineered thermal conductivity, wicking nanostructures, and nucleating superhydrophobic PTFE lines, have shown to provide significant enhancement in heat transfer. CHF of 307 W/cm^2 was achieved for bi-conductive surfaces with nanostructures on the copper areas, and a HTC of 747 kW/m^2K was achieved for nanostructured surfaces with engineered wettability and thermal gradient surfaces. The conclusions of this chapter further amplifies the fundamental understanding of this dissertation which are: (1) homogenous structures with characteristic length much smaller that the flow length scale increase CHF (2) surfaces with engineered nucleation sites increase HTC with the penalty of CHF compared to nanostructured surface where the CHF is dictated by capillary wicking, (3) for surfaces with structures both much smaller and comparable to flow length scale, initial heat transfer mechanism is determined by the large length scale structures which promotes nucleation and enhanced bubble dynamics, where the small length scale structures provide wicking to delay burn-out, and (4) variations in engineered thermal conductivity promotes nucleation and spatial ordering.

10.2 Specific Contributions to the Field

The specific contributions of this dissertation are presented in this section and organized based on the chapters and focus of this dissertation.

10.2.1 *Scalable Nanomanufacturing of Surface Coatings for Boiling Applications*

1. Demonstrated, for the first time, the scalable nanomanufacturing of structured coatings independent of substrate material, geometry, or size.
2. Using TMV biotemplating, engineered coatings were deposited and characterized on silicon, aluminum, copper, and stainless steel, showing repeatable increases in CHF and a route to retro-fit existing systems and fouling mitigation.

10.2.2 *Wickability and CHF on Structured Superhydrophilic Surfaces*

1. Demonstrated, for the first time, a quantitative and predictive model for CHF based on capillary wicking through surface structures. This has shown that capillary wicking is the single factor dictating CHF on structured superhydrophilic surfaces (contact angle ~ 0°) with structures less than 100 μm in size, notably less than the fluid length scales of ~ 1mm for water.
2. Characterized the effects of fouling on CHF for enhanced surfaces as a reduction of wickability.
3. Optimized the biotemplated nickel nanostructure fabrication process for high heat transfer applications.
4. Validated the predictive CHF model for wickability-enhanced boiling using alternate fluids and working conditions.

10.2.3 *Boiling Enhancement on Multiscale and Heterogeneous Structured Surfaces*

1. Characterized the effect of engineered nucleation sites on increasing HTC but decreasing CHF on superhydrophilic surface, showing consistent predictions form the developed model.

2. Identified and characterized the effect of ‘large’ scale surface structures (> 100 μm) on boiling enhancement and showed extreme increases in HTC and CHF of 220% and 238%, respectively, for hierarchical surfaces.

10.2.4 *Boiling Enhancement using Engineered Thermal Gradients*

1. Invented the “Bi-Conductive” surface design for boiling enhancement using engineered thermal gradients to promote spatial ordering of liquid and vapor flow fields.
2. Characterized bi-conductive surfaces using high-speed imaging to identify the relevant bubbles dynamics driving enhancement.
3. Analyzed and optimized the bi-conductive geometry (for boiling water at atmospheric pressures), showing optimal performance when the wavelength of surface temperature variations matches the capillary length of the fluid.

10.2.5 *Boiling Enhancement on Nanostructured Surfaces with Engineered Variations in Wettability and Thermal Conductivity*

1. Characterized the effect of engineered nucleation sites, and engineered variations in thermal conductivity on nanostructured surfaces during pool boiling heat transfer.
2. Identified that for nanostructured surfaces with engineered variations in wettability and thermal gradient, bi-conductive surfaces promote preferential nucleation and spatial ordering on enhanced bubble dynamics, engineered nucleation sites facilitate bubble dynamics of bi-conductive mechanism, and nanostructures provide wicking to delay dry-out.

10.3 Recommendations for Future Research

Significant progress was made in the area of enhanced pool boiling heat transfer with the research reported in this dissertation. Still, boiling is a complex phenomenon, and non-linear hydrodynamic problem. Enhanced structures have added more complexity to this problem. Although, this dissertation addresses three major issues currently involved in the literature, and demonstrates potential solutions to these issues, still for the further advancement in the surface technology, few recommendations for future research are given in this section.

10.3.1 *Scalable Nanomanufacturing of Surface Coatings for Boiling Applications*

This dissertation aims to provide potential solution to the scalable nanomanufacturing of surface coatings using a biotemplated solution based nanofabrication technique. This three step room temperature solution based process has been shown to be feasible for fabricating nanostructures on various metallic and non-metallic substrates. All the surfaces used in this work are flat surfaces whereas real world application of nanofabrication requires nanostructures deposited on non-flat geometries as well. Also, the overarching issues such as the repeatability, rigidity, long-term performance, mechanical properties and thermal aging effects are required to be tested for developing robust and reliable micro/nanocoatings for efficient heat and fluid transport.

10.3.2 *Wickability and CHF on Structured Superhydrophilic Surfaces*

This dissertation demonstrated significant enhancement in CHF for structured surfaces based on enhanced capillary wicking. It has also been demonstrated that

wickability is the single factor which affect the pool boiling heat transfer enhancement for structured superhydrophilic surfaces and an experimentally validated CHF correlation is reported. This model was also validated with a highly wetting fluid FC 72. For further verification and advancement of this work, the effect of capillary tube diameter, effect of base surface size, effect of boiling pressure, effect of sub-cooling can be tested.

10.3.3 *Boiling Enhancement using Engineered Thermal Gradients*

This dissertation presents a novel planar surface design for which the pool boiling heat transfer enhancement does not require any structures or films. The enhancement mechanism relies on bulk fluid properties rather than the surface properties. The design was optimized with bi-conductive pitch, *P*, as shown in Fig. 8.1 (center-to-center distance between two epoxy divisions) equal to the fluid capillary length. Still, the depth, width, and length, of non-conductive epoxy divisions are not optimized for best heat transfer performance. A detailed thermal circuit analysis might be conducted to design test surfaces and verified during pool boiling. Additionally, for this dissertation, nonconductive lines were embedded onto conductive surfaces. The orientation of bi-conductive designs can be varied such as conductive circles onto nonconductive area, nonconductive cross lines onto conductive surfaces and tested during pool boiling heat transfer.

BIBLIOGRAPHY

[1] Beér, J. M., 2007, "High Efficiency Electric Power Generation: The Environmental Role," Prog. Energy Combust. Sci., **33**(2), pp. 107-134.

[2] Rahman, M. M., Ölçeroğlu, E., and McCarthy, M., 2014, "Scalable Nanomanufacturing of Virus-templated Coatings for Enhanced Boiling," Advanced Materials Interfaces, **1**(2), pp. 1300107-5.

[3] King, S. M., Rahman, M. M., Krick, A., Branco, L., McCarthy, M., 2012, "Biotemplated Nanostructured Surfaces for Enhanced Phase Change Heat Transfer," *Proceedings of the ASME 2012 10th International Conference on Nanochannels, Microchannels, and Minichannels*, ASME, Puerto Rico, USA.

[4] Hsu, Y. Y., 1962, "On the Size Range of Active Nucleation Cavities on a Heating Surface," J. Heat Transfer, **84**(3), pp. 207-213.

[5] Carey, V. P., 1992, Liquid-Vapor Phase-change Phenomena, *Hemisphere Publishing Corporation*, New York, NY.

[6] Kim, J., 2009, "Review of Nucleate Pool Boiling Bubble Heat Transfer Mechanisms," Int. J. Multiphase Flow, **35**(12), pp. 1067-1076.

[7] Lu, Y.-W., and Kandlikar, S. G., 2011, "Nanoscale Surface Modification Techniques for Pool Boiling Enhancement—A Critical Review and Future Directions," Heat Transfer Eng., **32**(10), pp. 827-842.

[8] Chu, K.-H., Enright, R., and Wang, E. N., 2012, "Structured Surfaces for Enhanced Pool Boiling Heat Transfer," Appl. Phys. Lett., **100**(24), pp. 241603-241604.

[9] Chen, R., Lu, M.-C., Srinivasan, V., Wang, Z., Cho, H. H., and Majumdar, A., 2009, "Nanowires for Enhanced Boiling Heat Transfer," Nano Lett., **9**(2), pp. 548-553.

[10] Betz, A. R., Jenkins, J., Kim, C.-J. C., and Attinger, D., 2013, "Boiling Heat Transfer on Superhydrophilic, Superhydrophobic, and Superbiphilic Surfaces," Int. J. Heat Mass Transfer, **57**(2), pp. 733-741.

[11] Cooke, D., and Kandlikar, S. G., 2011, "Pool Boiling Heat Transfer and Bubble Dynamics Over Plain and Enhanced Microchannels," J. Heat Transfer, **133**(5), pp. 052902-052902.

[12] Yao, Z., Lu, Y. W., and Kandlikar, S. G., 2011, "Effects of Nanowire Height on Pool Boiling Performance of Water on Silicon Chips," Int. J. Therm. Sci., **50**(11), pp. 2084-2090.

[13] O'Hanley, H., Coyle, C., Buongiorno, J., McKrell, T., Hu, L.-W., Rubner, M., and Cohen, R., 2013, "Separate Effects of Surface Roughness, Wettability, and Porosity on the Boiling Critical Heat Flux," Appl. Phys. Lett., **103**(2), pp. 024102-024105.

[14] Ahn, H. S., Lee, C., Kim, H., Jo, H., Kang, S., Kim, J., Shin, J., and Kim, M. H., 2010, "Pool Boiling CHF Enhancement by Micro/Nanoscale Modification of Zircaloy-4 Surface," Nucl. Eng. Des., **240**(10), pp. 3350-3360.

[15] Kim, S., Kim, H. D., Kim, H., Ahn, H. S., Jo, H., Kim, J., and Kim, M. H., 2010, "Effects of Nano-Fluid and Surfaces with Nano Structure on the Increase of CHF," Exp. Therm Fluid Sci., **34**(4), pp. 487-495.

[16] Mikic, B. B., and Rohsenow, W. M., 1969, "A New Correlation of Pool-Boiling Data Including the Effect of Heating Surface Characteristics," J. Heat Transfer, **91**(2), pp. 245-250.

[17] Bergles, A. E., 1992, "What is the Real Mechanism of CHF in Pool Boiling?," *Proceedings of the Engineering Foundation Conference on Pool and External Flow Boiling*, ASME, pp. 165–170.

[18] Kutateladze, S. S., 1948, "On the Transition to Film Boiling under Natural Convection," Kotloturbostroenie, **3**(0), pp. 10–12.

[19] Kutateladze, S. S., 1951, "A Hydrodynamic Theory of Changes in a Boiling Process Under Free Convection," Izvestia Akademia Nauk, S.S.S.R., Otdelenie Tekhnicheski Nauk, **4**(0), p. 529.

[20] Chi-Yeh, H., and Griffith, P., 1965, "The Mechanism of Heat Transfer in Nucleate Pool Boiling—Part I: Bubble Initiaton, Growth and Departure," Int. J. Heat Mass Transfer, **8**(6), pp. 887-904.

[21] Moghaddam, S., and Kiger, K., 2009, "Physical Mechanisms of Heat Transfer During Single Bubble Nucleate Boiling of FC-72 Under Saturation Conditions-I. Experimental Investigation," Int. J. Heat Mass Transfer, **52**(5–6), pp. 1284-1294.

[22] Carey, V. P., 2008, Liquid-Vapor Phase-Change Phenomena: An Introduction to the Thermophysics of Vaporization and Condensation Processes in Heat Transfer Equipment, *Taylor and Francis*, New York.

[23] Zuber, N., 1959, "Hydrodynamic Aspects of Boiling Heat Transfer," University of California: Los Angeles, Cailfornia, 1959.

[24] Rohsenow, W. M., Griffith, P., 1955, "Correlation of Maximum Heat Flux Data for Boiling of Saturated Liquids," Chem. Eng. Prog., **52**.

[25] Haramura, Y., and Katto, Y., 1983, "A New Hydrodynamic Model of Critical Heat Flux, Applicable Widely to Both Pool and Forced Convection Boiling On Submerged Bodies In Saturated Liquids," Int. J. Heat Mass Transfer, **26**(3), pp. 389-399.

[26] Cooke, D., and Kandlikar, S. G., 2012, "Effect of Open Microchannel Geometry on Pool Boiling Enhancement," Int. J. Heat Mass Transfer, **55**(4), pp. 1004-1013.

[27] Kandlikar, S. G., 2013, "Controlling Bubble Motion over Heated Surface Through Evaporation Momentum Force to Enhance Pool Boiling Heat Transfer," Appl. Phys. Lett., **102**(5), pp. 051611-051615.

[28] Li, C., Wang, Z., Wang, P.-I., Peles, Y., Koratkar, N., and Peterson, G. P., 2008, "Nanostructured Copper Interfaces for Enhanced Boiling," Small, **4**(8), pp. 1084-1088.

[29] Dhir, V. K., and Liaw, S. P., 1989, "Framework for a Unified Model for Nucleate and Transition Pool Boiling," J. Heat Transfer, **111**(3), pp. 739-746.

[30] Kandlikar, S. G., 2001, "A Theoretical Model to Predict Pool Boiling CHF Incorporating Effects of Contact Angle and Orientation," J. Heat Transfer, **123**(6), pp. 1071-1079.

[31] Bergles, A. E., 1997, "Special Issue: New Developments in Pool BoilingEnhancement of pool boiling," Int. J. Refrig., **20**(8), pp. 545-551.

[32] Bergles, A. E., and Manglik, R. M., 2013, "Current Progress and New Developments in Enhanced Heat and Mass Transfer," Journal of Enhanced Heat Transfer, **20**(1), pp. 1-15.

[33] Ayub, Z. H., and Bergles, A. E., 1987, "Pool Boiling from GEWA Surfaces in Water and R-113," Wärme- und Stoffübertragung, **21**(4), pp. 209-219.

[34] Li, C., and Peterson, G. P., 2007, "Parametric Study of Pool Boiling on Horizontal Highly Conductive Microporous Coated Surfaces," J. Heat Transfer, **129**(11), pp. 1465-1475.

[35] Marto, P. J., and Lepere, V. J., 1982, "Pool Boiling Heat Transfer From Enhanced Surfaces to Dielectric Fluids," J. Heat Transfer, **104**(2), pp. 292-299.

[36] Bon, B., Klausner, J. F., and McKenna, E., 2013, "The Hoodoo: A New Surface Structure for Enhanced Boiling Heat Transfer," J. Therm. Sci. Eng. Appl., **5**(1), pp. 011003-011003.

[37] Chu, K.-H., Joung, Y. S., Enright, R., Buie, C. R., and Wang, E. N., 2013, "Hierarchically Structured Surfaces for Boiling Critical Heat Flux Enhancement," Appl. Phys. Lett., **102**(15), pp. 151602-151604.

[38] Im, Y., Dietz, C., Lee, S. S., and Joshi, Y., 2012, "Flower-Like CuO Nanostructures for Enhanced Boiling," Nanosc. Microsc. Therm., **16**(3), pp. 145-153.

[39] Rahman, M. M., Ölçeroğlu, E., and McCarthy, M., 2014, "Role of Wickability on the Critical Heat Flux of Structured Superhydrophilic Surfaces," Langmuir, **30**(37), pp. 11225-11234.

[40] Zou, A., and Maroo, S. C., **2013**, "Critical Height of Micro/Nano Structures for Pool Boiling Heat Transfer Enhancement," Appl. Phys. Lett., **103**(22), pp. 221602-5.

[41] Hendricks, T. J., Krishnan, S., Choi, C., Chang, C.-H., and Paul, B., 2010, "Enhancement of Pool-Boiling Heat Transfer using Nanostructured Surfaces on Aluminum and Copper," Int. J. Heat Mass Transfer, **53**(15–16), pp. 3357-3365.

[42] Ahn, H. S., Jo, H. J., Kang, S. H., and Kim, M. H., 2011, "Effect of Liquid Spreading Due to Nano/Microstructures on The Critical Heat Flux During Pool Boiling," Appl. Phys. Lett., **98**(7), pp. 071908-071903.

[43] Betz, A. R., Xu, J., Qiu, H., and Attinger, D., 2010, "Do Surfaces with Mixed Hydrophilic and Hydrophobic Areas Enhance Pool Boiling?," Appl. Phys. Lett., **97**(14), pp. 141909-141903.

[44] Ujereh, S., Fisher, T., and Mudawar, I., 2007, "Effects of Carbon Nanotube Arrays on Nucleate Pool Boiling," Int. J. Heat Mass Transfer, **50**(19–20), pp. 4023-4038.

[45] Masanet, E., and Walker, M. E., 2013, "Energy-Water Efficiency and U.S. Industrial Steam," AIChE Journal, **59**(7), pp. 2268-2274.

[46] Garimella, S. V., Joshi, Y. K., Bar-Cohen, A., Mahajan, R., Toh, K. C., Carey, V. P., Baelmans, M., Lohan, J., Sammakia, B., and Andros, F., 2002, "Thermal Challenges in Next Generation Electronic Systems - Summary of Panel Presentations and Discussions," IEEE T. Compon. Pack. T., **25**(4), pp. 569-575.

[47] Xiao, R., Maroo, S. C., and Wang, E. N., 2013, "Negative Pressures in Nanoporous Membranes for Thin Film Evaporation," Appl. Phys. Lett., **102**(12), p. 123103.

[48] Mishchenko, L., Hatton, B., Bahadur, V., Taylor, J. A., Krupenkin, T., and Aizenberg, J., 2010, "Design of Ice-free Nanostructured Surfaces Based on Repulsion of Impacting Water Droplets," ACS Nano, **4**(12), pp. 7699-7707.

[49] Boreyko, J. B., and Chen, C.-H., 2009, "Self-Propelled Dropwise Condensate on Superhydrophobic Surfaces," Phys. Rev. Lett., **103**(18), p. 184501.

[50] Fraenkel-Conrat, H., and Williams, R. C., 1955, "Reconstitution of Active Tobacco Mosaic Virus from Its Inactive Protein and Nucleic Acid Components," *Proceedings of the National Academy of Sciences*, **41**(10), pp. 690-698.

[51] Leapman, R. D., and Rizzo, N. W., 1999, "Towards Single Atom Analysis of Biological Structures," Ultramicroscopy, **78**(1-4), pp. 251-268.

[52] Shenton, W., Douglas, T., Young, M., Stubbs, G., and Mann, S., 1999, "Inorganic–Organic Nanotube Composites from Template Mineralization of Tobacco Mosaic Virus," Adv. Mater., **11**(3), pp. 253-256.

[53] Lee, S.-Y., Choi, J., Royston, E., Janes, D. B., Culver, J. N., and Harris, M. T., 2006, "Deposition of Platinum Clusters on Surface-Modified Tobacco Mosaic Virus," J. Nanosci. Nanotechnol., **6**(4), pp. 974-981.

[54] Royston, E., Ghosh, A., Kofinas, P., Harris, M. T., and Culver, J. N., 2008, "Self-Assembly of Virus-Structured High Surface Area Nanomaterials and Their Application as Battery Electrodes," Langmuir, **24**(3), pp. 906-912.

[55] Gerasopoulos, K., McCarthy, Royston, E., Culver, J. N., Ghodssi, R., , 2008, "Nanostructured Nickel Electrodes using the Tobacco Mosaic Virus for Microbattery Applications," J. Micromech. Microeng., **18**(104003).

[56] 1996, "Tobacco mosaic virus: Schematic Structure. Art. Encyclopedia Britannica Online ".

[57] Ahn, H. S., Park, G., Kim, J. M., Kim, J., and Kim, M. H., 2012, "The Effect of Water Absorption on Critical Heat Flux Enhancement During Pool Boiling," Exp. Therm Fluid Sci., **42**(0), pp. 187-195.

[58] Lienhard, J. H., and Dhir, V. K., 1973, "Hydrodynamic Prediction of Peak Pool-boiling Heat Fluxes from Finite Bodies," J. Heat Transfer, **95**(2), pp. 152-158.

[59] Borishanskii, V. M., 1955, "On the Problem of Generalizing Experimental Data on the Cessation of Bubble Boiling in Large Volume of Liquids," T. K.I.T., ed.Moscow.

[60] Guan, C.-K., Klausner, J. F., and Mei, R., 2011, "A New Mechanistic Model for Pool Boiling CHF on Horizontal Surfaces," Int. J. Heat Mass Transfer, **54**(17–18), pp. 3960-3969.

[61] Liao, L., Bao, R., and Liu, Z., 2008, "Compositive Effects of Orientation and Contact Angle on Critical Heat Flux in Pool Boiling of Water," Heat Mass Transfer, **44**(12), pp. 1447-1453.

[62] Rajvanshi, A. K., Saini, J. S., and Prakash, R., 1992, "Investigation of Macrolayer Thickness in Nucleate Pool Boiling at High Heat-Flux," Int. J. Heat Mass Transfer, **35**(2), pp. 343-350.

[63] Sakashita, H., and Ono, A., 2009, "Boiling Behaviors and Critical Heat Flux on a Horizontal Plate in Saturated Pool Boiling of Water at High Pressures," Int. J. Heat Mass Transfer, **52**(3–4), pp. 744-750.

[64] Lu, M.-C., Chen, R., Srinivasan, V., Carey, V. P., and Majumdar, A., 2011, "Critical Heat Flux of Pool Boiling on Si Nanowire Array-Coated Surfaces," Int. J. Heat Mass Transfer, **54**(25–26), pp. 5359-5367.

[65] Chu, I. C., No, H. C., and Song, C. H., 2013, "Visualization of Boiling Structure and Critical Heat Flux Phenomenon for a Narrow Heating Surface in a Horizontal Pool of Saturated Water," Int. J. Heat Mass Transfer, **62**(0), pp. 142-152.

[66] Jung, J., Kim, S. J., and Kim, J., 2014, "Observations of the Critical Heat Flux Process During Pool Boiling of FC-72," J. Heat Transfer, **136**(4), p. 041501.

[67] Kim, H., Park, Y., and Buongiorno, J., 2013, "Measurement of Wetted Area Fraction in Subcooled Pool Boiling of Water Using Infrared Thermography," Nucl. Eng. Des., **264**(0), pp. 103-110.

[68] Theofanous, T. G., Dinh, T. N., Tu, J. P., and Dinh, A. T., 2002, "The Boiling Crisis Phenomenon - Part II: Dryout Dynamics and Burnout," Exp. Therm Fluid Sci., **26**(6-7), pp. 793-810.

[69] Guan, C.-K., Bon, B., Klausner, J., and Mei, R., 2014, "Comparison of CHF Enhancement on Microstructured Surfaces With a Predictive Model," Heat Transfer Eng., **35**(5), pp. 452-460.

[70] Love, B. J., and Packman, P. F., 1993, "Effects of Surface Modifications on the Peel Strength of Copper Based Polymer/Metal Interfaces with Characteristic Morphologies," J. Adhesion, **40**(2-4), pp. 139-150.

[71] Rainey, K. N., and You, S. M., 2001, "Effects of Heater Size and Orientation on Pool Boiling Heat Transfer from Microporous Coated Surfaces," Int. J. Heat Mass Transfer, **44**(14), pp. 2589-2599.

[72] Chang, J. Y., and You, S. M., 1996, "Heater Orientation Effects on Pool Boiling of Micro-Porous-Enhanced Surfaces in Saturated FC-72," J. Heat Transfer, **118**(4), pp. 937-943.

[73] Zhang, M., Banerjee, D., Fang, S., Ahn, H. S., Sinha, N., and Baughman, R. H., 2006, "Pool Boiling Experiments on Multiwalled Carbon Nanotube (MWCNT) Forests," J. Heat Transfer, **128**(12), pp. 1335-1342.

[74] Im, Y., Joshi, Y., Dietz, C., and Lee, S., 2010, "Enhanced Boiling of a Dielectric Liquid on Copper Nanowire Surfaces," Int. J. Micronano Scale Transp., **1**(1), pp. 79-96.

[75] Li, S., Furberg, R., Toprak, M. S., Palm, B., and Muhammed, M., 2008, "Nature-Inspired Boiling Enhancement by Novel Nanostructured Macroporous Surfaces," Adv. Funct. Mater., **18**(15), pp. 2215-2220.

[76] Phan, H. T., Caney, N., Marty, P., Colasson, S., and Gavillet, J., 2009, "Surface Wettability Control by Nanocoating: The Effects on Pool Boiling Heat Transfer and Nucleation Mechanism," Int. J. Heat Mass Transfer, **52**(23–24), pp. 5459-5471.

[77] Mitrovic, J., and Hartmann, F., 2004, "A New Microstructure for Pool Boiling," Superlattices Microstruct., **35**(3–6), pp. 617-628.

[78] Launay, S., Fedorov, A. G., Joshi, Y., Cao, A., and Ajayan, P. M., 2006, "Hybrid Micro-Nano Structured Thermal Interfaces for Pool Boiling Heat Transfer Enhancement," Microelectron. J., **37**(11), pp. 1158-1164.

[79] Minseok, H., and Graham, S., "Pool Boiling Enhancement Through Hierarchical Texturing of Surfaces," *Proc. 2016 15th IEEE Intersociety Conference on Thermal and Thermomechanical Phenomena in Electronic Systems (ITherm)*, pp. 388-394.

[80] Moon, H. W., Yoon, Y. J., Park, J. H., Myung, B.-S., and Kim, D. E., 2016, "Dynamic Wetting and Boiling Characteristics on Micro-Structured and Micro/Nano Hierarchically Structured Surfaces," Exp. Therm Fluid Sci., **74**(0), pp. 19-26.

[81] Liu, J., Huang, X., Li, Y., Sulieman, K. M., He, X., and Sun, F., 2006, "Hierarchical Nanostructures of Cupric Oxide on a Copper Substrate: Controllable Morphology and Wettability," J. Mater. Chem., **16**(45), pp. 4427-4434.

[82] Jaikumar, A., and Kandlikar, S. G., 2015, "Enhanced Pool Boiling for Electronics Cooling using Porous Fin Tops on Open Microchannels with FC-87," Appl. Therm. Eng., **91**(0), pp. 426-433.

[83] Ahn, H. S., Lee, C., Kim, J., and Kim, M. H., 2012, "The Effect of Capillary Wicking Action of Micro/Nano Structures on Pool Boiling Critical Heat Flux," Int. J. Heat Mass Transfer, **55**(1–3), pp. 89-92.

[84] Lee, C. Y., Zhang, B. J., and Kim, K. J., 2012, "Morphological Change of Plain and Nano-Porous Surfaces During Boiling and Its Effect on Nucleate Pool Boiling Heat Transfer," Exp. Therm Fluid Sci., **40**(0), pp. 150-158.

[85] Henley, J. J., and Hummel, R. L., 1967, "A Third Factor in Boiling Nucleation," Ind. Eng. Chem. Fund, **6**(4), pp. 603-606.

[86] Jo, H., Ahn, H. S., Kang, S., and Kim, M. H., 2011, "A Study of Nucleate Boiling Heat Transfer on Hydrophilic, Hydrophobic and Heterogeneous Wetting Surfaces," Int. J. Heat Mass Transfer, **54**(25–26), pp. 5643-5652.

[87] Freund, G., Pesch, W., and Zimmermann, W., 2011, "Rayleigh-Benard Convection in the Presence of Spatial Temperature Modulations," J. Fluid Mech., **673**(0), pp. 318-348.

[88] Sparrow, E. M., and Carlson, C. K., 1986, "Local and Average Natural Convection Nusselt Numbers for a Uniformly Heated, Shrouded or Unshrouded Horizontal Plate," Int. J. Heat Mass Transfer, **29**(3), pp. 369-379.

[89] Dhir, V. K., Abarajith, H. S., and Li, D., 2007, "Bubble Dynamics and Heat Transfer during Pool and Flow Boiling," Heat Transfer Eng., **28**(7), pp. 608-624.

[90] Mukherjee, A., and Dhir, V. K., 2005, "Study of Lateral Merger of Vapor Bubbles During Nucleate Pool Boiling," J. Heat Transfer, **126**(6), pp. 1023-1039.

[91] Cole, R., 1967, "Bubble Frequencies and Departure Volumes at Subatmospheric Pressures," AIChE Journal, **13**(4), pp. 779-783.

[92] Cole, R., Rohsenow, W.M., 1968, "Correlation of Bubble Departure Diameters for Boiling of Saturated Liquids," Chem. Eng. Prog. Symp. Ser., **65**(0), pp. 211-213.

[93] Cole, R., and Shulman, H. L., 1966, "Bubble Departure Diameters at Subatmospheric Pressures." Chem. Eng. Prog. Symp. Ser., **62**(0), 6–16.

[94] Fritz, W., 1935, "Berechnung des Maximalvolume von Dampfblasen," Phys. Z., **36**(0), pp. 379-388.

[95] Kim, J., and Kim, M. H., 2006, "On The Departure Behaviors of Bubble at Nucleate Pool Boiling," Int. J. Multiphase Flow, **32**(10–11), pp. 1269-1286.

[96] Mori, S., Mt Aznam, S., and Okuyama, K., 2015, "Enhancement of The Critical Heat Flux in Saturated Pool Boiling of Water by Nanoparticle-coating and a Honeycomb Porous Plate," Int. J. Heat Mass Transfer, **80**(0), pp. 1-6.

[97] Kruse, C. M., Anderson, T., Wilson, C., Zuhlke, C., Alexander, D., Gogos, G., and Ndao, S., 2015, "Enhanced Pool-boiling Heat Transfer and Critical Heat Flux on Femtosecond Laser Processed Stainless Steel Surfaces," Int. J. Heat Mass Transfer, **82**(0), pp. 109-116.

[98] Feng, B., Weaver, K., and Peterson, G. P., 2012, "Enhancement of Critical Heat Flux in Pool Boiling using Atomic Layer Deposition of Alumina," Appl. Phys. Lett., **100**(5), p. 053120.

[99] Rahman, M. M., Pollack, J., and McCarthy, M., 2015, "Increasing Boiling Heat Transfer using Low Conductivity Materials," Sci. Rep., **5**(0), p. 13145.

[100] Jaikumar, A., and Kandlikar, S. G., 2016, "Pool Boiling Enhancement Through Bubble Induced Convective Liquid Flow in Feeder Microchannels," Appl. Phys. Lett., **108**(4), p. 041604.

[101] Jaikumar, A., and Kandlikar, S. G., 2016, "Ultra-high Pool Boiling Performance and Effect of Channel Width with Selectively Coated Open Microchannels," Int. J. Heat Mass Transfer, **95**(0), pp. 795-805.

VITA

Md Mahamudur Rahman was born on October 17, 1985 in Dhaka, Bangladesh. He completed his high school from Notre Dame College and Bachelor of Science in Mechanical Engineering degree from Bangladesh University of Engineering and Technology (BUET), Bangladesh. He joined The University of Texas at El Paso (UTEP) in January 2010 and earned his Master of Science in Mechanical Engineering degree in July 2011. During this he worked in the Center for Space Exploration and Technology Research (cSETR) as a Graduate Research Assistant. Then he started his Doctor of Philosophy in Mechanical Engineering at Drexel University from August 2011. At Drexel, he has worked in Multiscale Thermofluidics Laboratory as a Graduate Research Assistant under the guidance of Prof. Matthew McCarthy. As a PhD student, his research is focused on thermofluidic systems and scalable manufacturing of micro/nano-structured surfaces for the enhancement of phase change heat transfer performance during boiling. In addition to research experience, he has also worked as a Graduate Teaching Assistant for different undergraduate courses. Md Mahamudur has received the George Hill, Jr. Endowed Fellowship from the College of Engineering at Drexel University for demonstrating excellence in graduate career. He has also received poster awards in ASME IMECE 2014, and ASME IMECE 2012 conferences. Additionally, his research has been highlighted in Live Science's news, and as a frontispiece in Advanced Materials Interfaces. His research interests are in the areas of micro/nanofabrication, microfluidic devices, fundamental fluid mechanics, and heat transfer, and combustion.

EDUCATION

Doctor of Philosophy in Mechanical Engineering 2016

Drexel University (DU)
Philadelphia, Pennsylvania, USA
Dissertation Title: Boiling Enhancement on Engineered Surfaces
Advisor: Matthew McCarthy

Master of Science in Mechanical Engineering 2011

The University of Texas at El Paso (UTEP)
El Paso, Texas, USA
Thesis Title: An Experimental Study on The Effect of Particle Geometry on Drag and Flow Behaviors in a Packed Fluidized Bed
Advisor: Ahsan Choudhuri

Bachelor of Science in Mechanical Engineering 2008

Bangladesh University of Engineering and Technology (BUET)
Dhaka, Bangladesh
Thesis Title: Study of Some Mechanical Properties of Locally Available Woods
Advisor: Muhammad Mahbubul Alam

ACTIVITIES AND AWARDS

- *The George Hill, Jr. Endowed Fellowship Award* for demonstrated excellence in graduate career 2015
  The College of Engineering, Drexel University
- *Live Science*, *Drexel NOW*, and *The Guardian* news highlight for research on nano-coatings for boiling enhancement 2015
- *IMECE 2014 Poster Award* 2014
  ASME 2014 International Mechanical Engineering Congress and Exposition
  Bi-Conductive Surfaces for the Enhancement of Pool Boiling Heat Transfer
  IMECE2014-40798
- Work highlighted as a *frontispiece* in the April issue of *Advanced Materials Interfaces* titled as Biotemplates: Scalable Nanomanufacturing of Virus-templated Coatings for Enhanced Boiling (Adv. Mater. Interfaces 2/2014) 2014
- *NSF CBET Innovation Poster Award* (Co-author) 2012
  ASME 2012 International Mechanical Engineering Congress and Exposition
  Biotemplated Superhydrophobic Surfaces for Enhanced Dropwise Condensation IMECE2012-93781
- Student Member *The American Society of Mechanical Engineers* (ASME) 2011-present
- Student Member *The American Institute of Aeronautics and Astronautics* (AIAA) 2011

PUBLICATIONS

Journals

1. M. M. Rahman, and M. McCarthy, "Boiling Enhancement on Nanostructured Surfaces with Engineered Variations in Wettability and Thermal Conductivity", Heat Transfer Engineering (in press).
2. M.M. Rahman, H. Hu, H. Shabgard, P. Boettcher, Y. Sun, and M. McCarthy, "Experimental Characterization of Inward Freezing and Melting of Additive-Enhanced PCM within Millimeter-scale Cylindrical Enclosures", *ASME Journal of Heat Transfer* 2016, 138(7), pp. 072301-072301-13
3. M. M. Rahman, J. Pollack, and M. McCarthy, "Increasing Heat Transfer Using Low Conductivity Materials", Scientific Reports, 5, 13145, 2015.
4. M. M. Rahman, H. Hu, H. Shabgard, P. Boettcher, Y. Sun, and M. McCarthy, "Dendrite Growth During Freezing of Millimeter-Scale Eicosane Droplets", ASME Journal of Heat Transfer, 137 (8), 080905, 2015.
5. M. M. Rahman, E. Ölçeroğlu, and M. McCarthy, "The Role of Wickability on the Critical Heat Flux of Structured Superhydrophilic Surfaces", Langmuir, 30 (37), pp 11225–11234, 2014.
6. E. Ölçeroğlu, C.Y. Hsieh, M.M. Rahman, K.K.S Lau, and M. McCarthy, "Full-Field Dynamic Characterization of Superhydrophobic Condensation on Biotemplated Nanostructured Surfaces", Langmuir, 30 (25), pp 7556–7566, 2014.
7. M. M. Rahman, E. Ölçeroğlu, and M. McCarthy, "Scalable Nanomanufacturing of Virus-templated Coatings for Enhanced Boiling", Advanced Materials Interfaces, vol. 1, no. 2, 1300107, 2014.

Conference Publications and Presentations (presenter underlined)

1. M. M. Rahman, and M. McCarthy, "Wicking-Enhanced Critical Heat Flux for Highly Wetting Fluids", ASME Heat Transfer, Fluids Engineering, & Nanochannels, Microchannels, and Minichannels Conferences, Washington, DC, USA, July 10-14, 2016 (submitted)
2. J. Pollack, S. Ridwan, M. M. Rahman, and M. McCarthy, "Fouling and Degradation of Engineered Surfaces during Enhanced Boiling", ASME Heat Transfer, Fluids Engineering, & Nanochannels, Microchannels, and Minichannels Conferences, Washington, DC, USA, July 10-14, 2016 (submitted)
3. M. M. Rahman, Emre Ölçeroğlu, and M. McCarthy, "Boiling Heat Transfer Enhancement on Structured Surfaces with Engineered Thermal Gradients and Nucleation Sites", TFESC-12980, Proceedings of the 1st Thermal and Fluid Engineering Summer Conference (TFESC 2015), New York City, USA, August 9-12, 2015.
4. M. M. Rahman, H. Shabgard, H. Hu, P. Boettcher, Y. Sun, and M. McCarthy, "Inward Melting And Freezing of Additive-Enhanced Phase Change Materials in Small Diameter Cylinders", TFESC-12912, Proceedings of the 1st Thermal and Fluid

Engineering Summer Conference, (TFESC 2015), New York City, USA, August 9-12, 2015.

5. M. M Rahman and M. McCarthy, "Pool Boiling Heat Transfer Enhancement using Surfaces with Mixed Thermal Conductivity", ASME 2015 International Technical Conference and Exhibition on Packaging and Integration of Electronic and Photonic Microsystems and ASME 2015 13th International Conference on Nanochannels, Microchannels, and Minichannels (InterPACKICNMM 2015), July 6-9, 2015, San Francisco, California, USA.
6. M. M Rahman and M. McCarthy, "Biotemplated Nanostructures for Enhancing CHF and HTC during Pool Boiling", 9th International Conference on Boiling and Condensation Heat Transfer, Boulder, Colorado, April 26-30, 2015.
7. M. M Rahman, J. Pollack, D. Fehlinger, E. Ölçeroğlu, and M. McCarthy, "Increased Pool Boiling Heat Transfer Based On Hierarchical Microchanneled Copper Surfaces", ASME 2014 International Mechanical Engineering Congress and Exposition (IMECE 2014), Montreal, QC, Canada, November 14-20, 2014.
8. E. Ölçeroğlu, M. M Rahman, and M. McCarthy, "Factors Affecting the In-Structure Motion of Condensate Droplets on Superhydrophobic Surfaces", ASME 2014 International Mechanical Engineering Congress and Exposition (IMECE 2014), Montreal, QC, Canada, November 14-20, 2014.
9. D. Fehlinger, M. M. Rahman, E. Ölçeroğlu, and M. McCarthy, "Creating Biotemplated Nanostructured Filtration Membranes using the Tobacco mosaic virus", ASME 2014 International Mechanical Engineering Congress and Exposition (IMECE 2014), Montreal, QC, Canada, November 14-20, 2014.
10. M. M. Rahman, and M. McCarthy, "The Effect of Wickability on Pool Boiling Critical Heat Flux on Micro/Nanostructured Surfaces", proceedings of The 9th International Conference on Two-Phase Systems for Ground and Space Applications (ITTW 2014), Baltimore, MD, USA, September 22-26, 2014.
11. M. M. Rahman, E. Ölçeroğlu, and M. McCarthy, "Increased Pool Boiling HTC using Engineered Nucleation Sites on Biotemplated Nanostructured Surfaces", 12th International Conference on Nanochannels, Microchannels, and Minichannels (ICNMM 2014), Chicago, IL, USA, August 3-7, 2014.
12. E. Ölçeroğlu, M.M Rahman, and M. McCarthy, "Spatial Control of Condensate Droplets on Superhydrophobic Surfaces", 12th International Conference on Nanochannels, Microchannels, and Minichannels (ICNMM 2014), Chicago, IL, USA, August 3-7, 2014.
13. M. M. Rahman, E. Olceroglu, M. McCarthy, "Viral Nano-Templates for Investigating the Mechanisms of Pool Boiling Enhancement", ASME 2013 Summer Heat Transfer Conference (SHTC 2013), Minneapolis, MN, USA, July 14-19, 2013.
14. E. Olceroglu, M. M. Rahman, M. McCarthy, "Nucleation and Wetting of Biotemplated Surfaces for Enhanced Dropwise Condensation", ASME 2013 Summer Heat Transfer Conference (SHTC 2013), Minneapolis, MN, USA, July 14-19, 2013.
15. D. Fehlinger, E. Ölçeroğlu, M. M. Rahman, M. McCarthy, "Additive Nanomanufacturing using the Tobacco Mosaic Virus as a Nanoscale Biological Template", ASME 2013 Summer Heat Transfer Conference (SHTC 2013), Minneapolis, MN, USA, July 14-19, 2013.

16. M. M. Rahman, E. Olceroglu, M. McCarthy, "Pool Boiling Heat Flux Enhancement using Biotemplated Nanostructures", proceedings of the 12th International Workshop on Micro and Nanotechnology for Power Generation and Energy Conversion Applications (PowerMEMS '12), Atlanta, GA, USA, December 2-5, 2012.
17. M. M. Rahman, S. King, E. Olceroglu, and M. McCarthy, "Nucleate Boiling on Biotemplated Nanostructured Surfaces", proceedings of the ASME 2012 International Mechanical Engineering Congress and Exposition (IMECE 2012), Houston, TX, USA, November 9-15, 2012.
18. E. Olceroglu, S. King, M. M. Rahman, and M. McCarthy, "Biotemplated Superhydrophobic Surfaces for Enhanced Dropwise Condensation", proceedings of the ASME 2012 International Mechanical Engineering Congress and Exposition (IMECE 2012), Houston, TX, USA, November 9-15, 2012.
19. S. King, M. M. Rahman, A. Krick, L. Branco, E. Olceroglu, and M. McCarthy, "Biotemplated Nanostructured Surfaces for Enhanced Phase Change Heat Transfer", proceedings of the ASME 2012 10th International Conference on Nanochannels, Microchannels, and Minichannels (ICNMM 2012), Rio Grande, Puerto Rico, July 8-12, 2012.
20. S. King. E. Ölçeroğlu, M. M. Rahman, and M. McCarthy, "Delayed Leidenfrost Phenomena on Biotemplated Nanostructured Surfaces", proceedings of the 2012 Solid-State Sensor, Actuator, and Microsystems Workshop (Hilton Head 2012), Hilton Head Island, SC, June 3-7, 2012.
21. M. Sarker, M. M. Rahman, N. Love, and A. Choudhuri, "Effect of Bed Height, Bed Diameter, and Particle Shape on Minimum Fluidization in a Gas-Solid Fluidized Bed", proceedings of the 50th Aerospace Sciences Meeting and Exhibit, AIAA, Nashville, TN, January 6 – 9, 2012.
22. M. Ruvalcaba, M. M. Rahman, N. Love, and A. Choudhuri, "Analysis of Drag on Non-Spherical Particles in a Fluidized Bed", proceedings of 9th International Energy Conversion Engineering Conference and Exhibit, AIAA, San Diego, CA, July 31-August 3, 2011.
23. M. M. Rahman, M. Ruvalcaba, N. Love, and A. Choudhuri, "Investigation of Gas-Solid Fluidized Bed Dynamics with Spherical and Non-Spherical Particles", proceedings of the 49th Aerospace Sciences Meeting and Exhibit, AIAA, Orlando, FL, January 4 – 7, 2011.
24. M. M. Rahman, N. Love, and A. Choudhuri, "Hydrodynamic Analysis of a Fluidized Bed Operating with Spherical and Non-Spherical Particles", 1st Southwest Energy Science and Engineering Symposium, University of Texas El Paso, El Paso, TX, April 16, 2011